From histones to chromosomes: in vivo and in vitro analysis of structural changes caused by linker histone H1, histone acetylation and histone chaperone NAP1

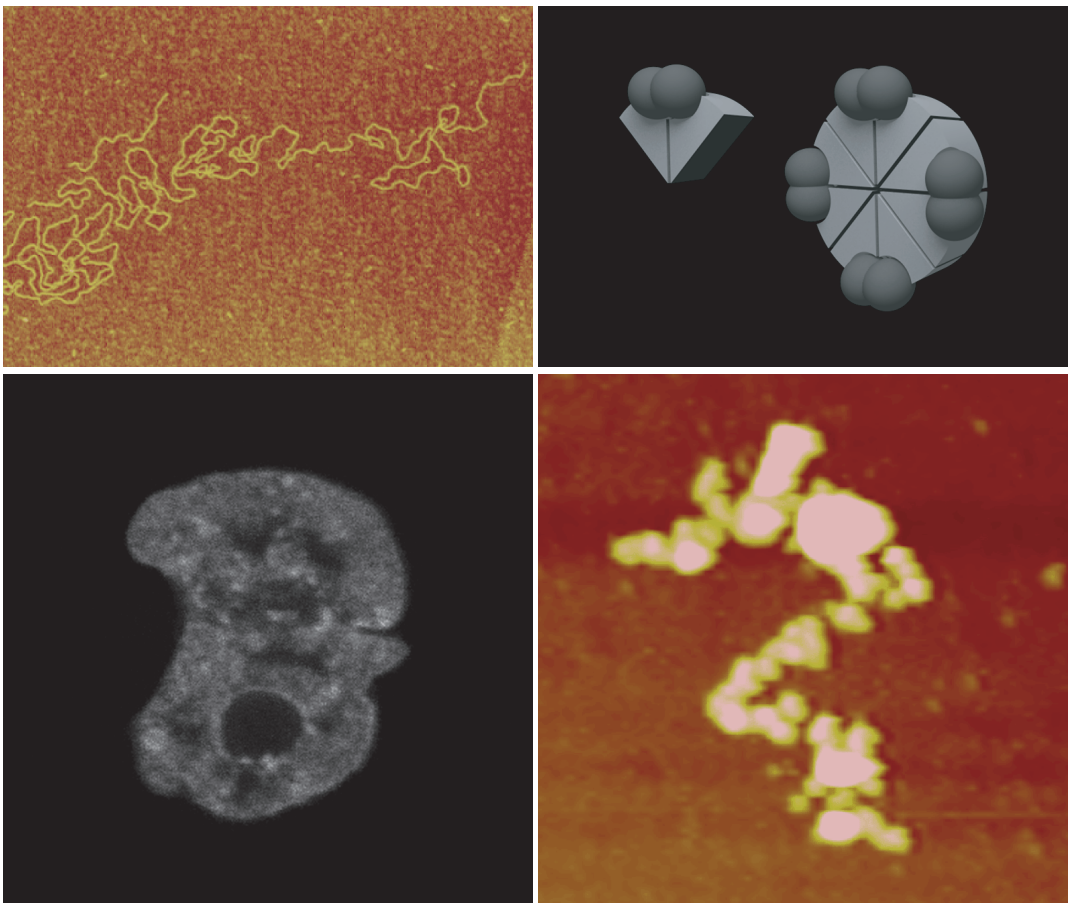

Dissertation submitted by Katalin Fejes Tóth

Dissertation
submitted to the
Combined Faculties for the Natural Sciences and for Mathematics
of the Ruperto-Carola University of Heidelberg, Germany
for the degree of
Doctor of Natural Sciences

presented by
Dr. med. Katalin Fejes Tóth
born in Budapest
Oral examination: 12th of November, 2004

From histones to chromosomes: *in vivo* and *in vitro* analysis of structural changes caused by linker histone H1, histone acetylation and histone chaperone NAP1

Referees: PD Dr. Karsten Rippe
PD Dr. Harald Herrmann

This work was carried out at the Deutsches Krebsforschungszentrum in Heidelberg in the Division of Molecular Genetics and the Kirchhoff-Institut für Physik at the Universität Heidelberg in the Division Molecular Biophysics from May 2001 to November 2004 under the scientific guidance of PD Dr. Karsten Rippe.

Publications

Kepert, J. F., Fejes Tóth, K., Caudron, M., Mücke, N., Langowski, J. & Rippe, K. (2003). Conformation of reconstituted mononucleosomes and effect of linker histone H1 binding studied by scanning force microscopy. *Biophys. J.* 85, 4012-4022.

Fejes Tóth, K., Knoch, T. A., Wachsmuth, M., Stöhr, M., Frank-Stöhr, M., Bacher, C. P., Müller, G. & Rippe, K. (2004). Trichostatin A induced histone acetylation causes decondensation of interphase chromatin. *J. Cell Sci.* 117, 4277-4287.

Fejes Tóth, K., Mazurkiewicz, J. & Rippe, K. (2004). Association states of the nucleosome assembly protein 1 and its complexes with histones, *J Biol Chem*, in press.

Kepert, J. F., Mazurkiewicz, J., Heuvelman, G., Fejes Tóth, K. & Rippe, K. (2004). Exchange of histone H2A·H2B dimer in nucleosomes and chromatin fibers by nucleosome assembly protein 1, *J Biol Chem*, under review.

Lutzmann, M., Kunze, R., Stangl, K., Stelter, P., Fejes Tóth, K., Boettcher, B. & Hurt, E. (2004). Biochemical and structural analyses of the large nucleoporins Nup157, Nup188 and Nup192, *J Biol Chem*, under review

Köszönet…

A legnagyobb hálával szüleimnek tartozom, akik közel 30 éve elviselnek és mindig mellettem állnak és támogatnak. Nélkülük és a szeretetük nélkül se ezt a munkát, se mást nem tudtam volna elérni. A szeretetük biztonságot adott még a legnehezebb helyzetekben is. Nagy köszönettel tartozom maminak is, akinek szeretete a nagy távolság ellenére is mindig jelen volt. Gézának és Anikónak köszönom, hogy okítottak és kitartóan próbálkoztak jó kutatót faragni belőlem.

Köszönet Tamásnak, aki tudományos életem kezdetétől vezetett és segített, sokszor eltűrte türelmetlen és ideges reakcióimat a kritikus megjegyzéseire és biztosította a változatosságot az életem elmúlt 3 évében. Köszönöm továbbá, hogy megajándekozott négy csodálatos gyerek szeretetével és megismertetett a repüles szépségeivel. Ha voltak is nehéz perceink, az együtt töltött idő mégis nagyon értékes marad számomra.

Eszternek, Juditnak, Julinak és T. Eszternek köszönöm, hogy a nagy távolság ellenére is kitartottak mellettem és biztos pontot jelentettek az életemben. A telefonbeszélgetések és látogatások sok magányos perctől mentettek meg.

Dankeschön…

Karsten Rippe danke ich für die Überlassung des Themas…
… außerdem für seine unermüdliche Unterstützung zu jeder Stunde. Dank seiner Begeisterung für die Biophysik habe ich mich sogar mit der analytischen Ultrazentrifuge angefreundet. Für die wunderschönen Zeiten, das viele Lachen und seine treue Freundschaft werde ich ihm immer dankbar sein.

Malte danke ich für eine sehr tiefe und enge Freundschaft, sein immer offenes Ohr und für die unschlagbaren Sprüche, auf deren Veröffentlichung ich sehnend warten werde.
Ich danke Tobi, ohne den ich jetzt nicht da wäre, wo ich jetzt bin. Die zusammen durchgearbeiteten Nächte werde ich lange in Erinnerung behalten.

Ich danke Karsten, Malte, Tobi, Peter Lichter, Tamas und Brigitte Hobrecker für ihre Unterstutzung und ihr Vertrauen. Peter werde ich ewig dankbar sein dafür, dass er mich damals in seine Arbeitsgruppe aufgenommen hat. Den Ärger und Frust, den er damit auf sich genommen hat, werde ich ein Leben lang nicht “abbezahlen” können.

Ich bedanke mich bei meinen Kollegen aus Karstens und Peters Labor für die gute Arbeitsatmosphäre, die Hilfe und gute Zusammenarbeit und für die liebevolle Aufnahme nach meinem Laborwechsel im DKFZ. Steffi danke ich für ihre unermüdliche Arbeit am LSM und ihre stets gute Laune. Für das fleissige Korrekturlesen und die Hilfe bei der Zusammenstellung dieser Arbeit danke ich Karsten, Malte, Felix und Jacek.

Mein Dank geht auch an Frank Jungmann, Margit Michaeli-MacLeod und Harald Jacobsen für ihre Hilfe bei allen formalen Angelegenheiten und Herrn Jacobsen danke ich besonders für die kontinuierliche Versorgung mit Leckereien und Lilien.

Harald Herrmann danke ich für die kompetente Betreuung meiner Arbeit und seine Hilfsbereitschaft.

Maiwen, Leticia, und Ute verdanke ich tolle Zeiten und ehrliche Gespräche, die mich immer aufgebaut und motiviert haben. Ihr Optimismus und ihre Begeisterung für die Wissenschaft und auch für die wichtigen Dinge (z.B. Coctails, Sauna oder Nutella) waren ansteckend.

Bei Gerrit Steinberg, Tobias Bäuerle, meinem Bibelkreis, besonders Annette Ebinger und Felix und Christina Wente bedanke ich mich für die tollen Dienstagabende, die netten Gespräche und die Unterstüzung in schweren Zeiten. Ihr Vertrauen auf Jesus hat mir oft Kraft geschenkt.

Dem Heidelberger Ruderklub (HRK) verdanke ich nette Freundschaften, einen tollen Ausgleich zum Laboralltag und herrliche Stunden auf dem Wasser.

“Nach dem Paper ist vor dem Paper“

(Sepp Herberger revised)

Table of content

1. Functional organization and dynamics of chromatin

1.1 Nucleosome structure and assembly

The genetic information of an organism is stored in the DNA nucleotide sequence of every cell. In bacteria the whole genome consists of 0.5-5 million base pairs (Mb) of DNA containing 500-4000 genes. In higher eukaryotes the amount of information is much larger. The human genome, for example, comprises $3.2x10^9$ nucleotides and codes for about 30 000 genes. The total length of the DNA of one human cell is about two meters but must be packed into a cell nucleus with a typical diameter of 6-10 μm, i.e. the DNA has to be tightly folded. At the same time the DNA has to be accessible for molecules and complexes of various sizes during cellular processes like transcription, replication or repair. During mitosis, where the most condensed conformation state is present, the contour length is about 10 000 times smaller. However, even during interphase when the above-mentioned biological processes take place, the DNA is already compacted about 1000fold. This enormous condensation is accomplished by specialized proteins that bind and fold the DNA. These proteins are divided into two classes: the histones and the non-histone chromosomal proteins like remodeling factors, HMG proteins, HP proteins and modifying enzymes. Together, the DNA and these histone and non-histone proteins are called chromatin.

1.1.1 The structure of histones and nucleosomes

Histones are the most abundant proteins within the cell and are responsible for the formation of the basic building block of chromatin, the nucleosome. A nucleosome consists of about 147 bp of DNA wound around an octamer of histones that comprises two molecules of each core histone H2A, H2B, H3 and H4. The nucleosomes are connected by a short stretch of DNA, called linker DNA, leading to a "beads-on-a-string" structure with a repeat length of about 200 bp in humans. The repeat length can vary from species to species from160 bp (yeast) to more than 220 bp (higher eukaryotes). This results in an approximately 7-fold length compaction (Richmond and Davey, 2003). The high-resolution structure of the nucleosome has been solved by x-ray crystallography (Argents et al., 1991; Davey et al., 2002; Lugar et al., 1997a) and reveals that the DNA is tightly wrapped 1.65 times around the disc-shaped histone core. The DNA-histone interactions are stabilized by more than 116 direct and 358 water mediated interactions (Davey et al., 2002; Lugar and Richmond, 1998).

Figure 1.1 The structure of the nucleosome. Histones have a core domain consisting of a-helices that interact to form the disc-shaped histone octamer. The DNA double helix is wound around this octamer 1.65 times. Histone tails do not possess a defined secondary structure and are therefore only partially resolved by x-ray diffraction (H2A yellow, H2B red, H3 blue, H4 green) (Luger et al., 1997a).

Histones are highly conserved, small basic proteins (11-15 kDa) consisting of two major structural units. The histone fold is required for the structural organization of the octamer and for DNA binding, while the tails are the main targets for posttranslational modifications. The histone fold consists of three α helices connected by two loops. These histone folds arrange in "handshake" form to make up the H2A·H2B dimer and the H3·H4 tetramer, respectively. Association to histone octamers takes place in the presence of DNA or at high ionic strength (> 1 M NaCl). The nucleosome has a two-fold symmetry organized along the interface of the two H3 molecules. In addition, the two H2A dimers also interact with each other and with the adjacent H3 (Fig. 1.1). Apart from these histone fold cores, each histone has a C-terminal and an N-terminal tail, which protrude from the nucleosome. Since these tails do not have a secondary structure, they can only partially be visualized by x-ray crystallography. The tails interact with linker DNA and with the other nucleosomes, thereby modulating the formation of higher order structure (Hansen, 2002; Hayes and Hansen, 2001). These interactions are influenced by posttranslational modifications, like by acetylation, phosphorylation, methylation or ubiquitination as discussed later in chapter 1.4. These modifications seem to be responsible for determining chromatin structure and transcriptional activity.

Nucleosomes have little sequence specificity. However, the bending of the DNA helix into tight turns around the nucleosome requires significant compression of the minor groove. Since AT-rich sequences are easier to compress, the nucleosome tends to position in such a way that the AT rich minor grooves are located on the inside of the DNA coil (Widom, 2001).

1.1.2 Histone variants provide additional diversity

A possibility to modulate chromatin structure results from so-called histone variants, which have a somewhat altered amino acid sequence. Unlike the basic core histones, which are only expressed in the S phase and deposited during replication, variants are expressed replication-independently and are incorporated during the whole cell cycle to fulfill special functions. As

an example, CENP-A (centromere protein A) is an H3 variant that is essential for centromere structure and function (Ahmad and Henikoff, 2002). H3.3 is used to reactivate genes that have previously been inactivated by the methylation of lysine 9 of H3 (Ahmad and Henikoff, 2002). H2A.Z is linked to gene activation while macroH2A substitutes H2A in the inactive X chromosome (Costanzi and Pehrson, 1998). Whereas H3.3 or H2A.Z differ only slightly from the basic core histones (Ahmad and Henikoff, 2002; Suto et al., 2000), macroH2A has an additional 25kDa non-histone fold domain (Costanzi and Pehrson, 1998). Up to date only variants of H2A and H3 are known. Since these two have direct contact with the same type of histone within the nucleosome, it has been proposed that it is important that only identical pairs occur within one nucleosome (Suto et al., 2000).

1.1.3 Nucleosome conformation affects chromatin structure

Nucleosome structure strongly influences the folding of chromatin. Parameters like the entry-exit angle of the DNA at the nucleosome, the exact amount of turns the DNA makes around the octamer or the length of the linker DNA influence compaction as shown in "Conformation of reconstituted mononucleosomes and effect of linker histone H1 binding studied by scanning force microscopy" and by others (Bednar et al., 1998; Kepert et al., 2003). Histone modifications or binding of other proteins like the linker histone H1 also act on this level to modulate folding. Therefore much effort has been focused on determining mononucleosome conformation. Diverse structural and biochemical methods have been used extensively. Many of these experiments were conducted with native nucleosomes from cell nuclei. However, the exact composition and modification state of native nucleosomes is not known and thus structural effects caused by posttranslational histone modifications or binding of other proteins are hard to determine. Over the last years it became possible to express the single histones recombinantly in bacteria and assemble nucleosomes by salt dialysis, or using chromatin assembly factors, allowing the reconstitution of exactly defined nucleosomes (Ito et al., 1997; Luger et al., 1997b).

1.2 Chromatin fiber folding and assembly

1.2.1 The 30 nm fiber

Unlike the structure of the nucleosome known at the atomic level, the higher order folding of chromatin is largely unknown. A schematic image of the different compaction levels is shown in Fig. 1.2.

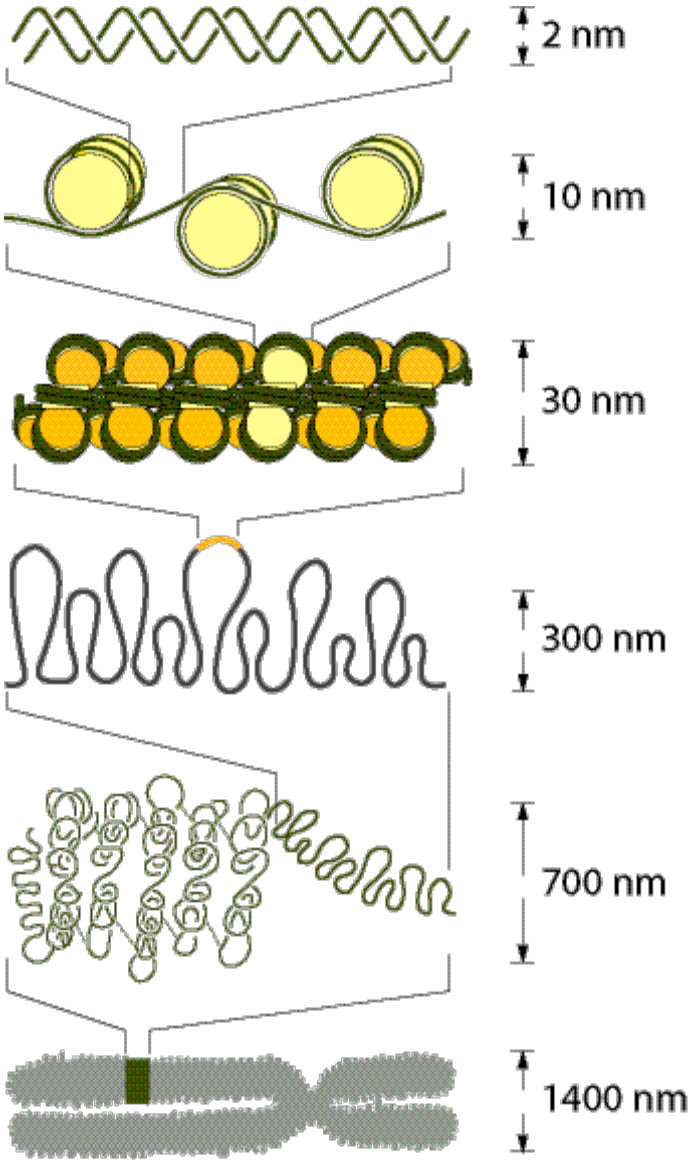

Figure 1.2 Chromatin packing. This model shows how DNA is packed into nucleosomes and further condensed to the 30 nm fiber. This fiber associates into loops or rosettes and higher order structures up to the totally condensed state found in mitotic chromosomes. However, even the structure of the 30 nm fiber is not clearly defined and folding into higher order compaction states still needs to be elucidated. (Figure adapted from (Alberts et al., 1994)).

The extended nucleosome chain termed "beads on a string" structure has a diameter of 10 nm and represents the most open state of chromatin. The next level of compaction into the so-called 30 nm fiber is not clearly defined. Two major models are proposed: in the solenoid model, six consecutive nucleosomes constitute one turn of a helix held together by histone-histone interactions with the linker DNA being bent (Fig. 1.3 A) (Finch and Klug, 1976). In the zig-zag model shown in Fig. 1.3 B the entry-exit angle of the DNA defines the relative positioning of the nucleosomes. Here alternate nucleosomes are physically closer to one

another than adjacent ones and the linker DNA is straight. Biochemical and electron microscopy studies favor the zig-zag model (vanHolde and Zlatanova, 1996).

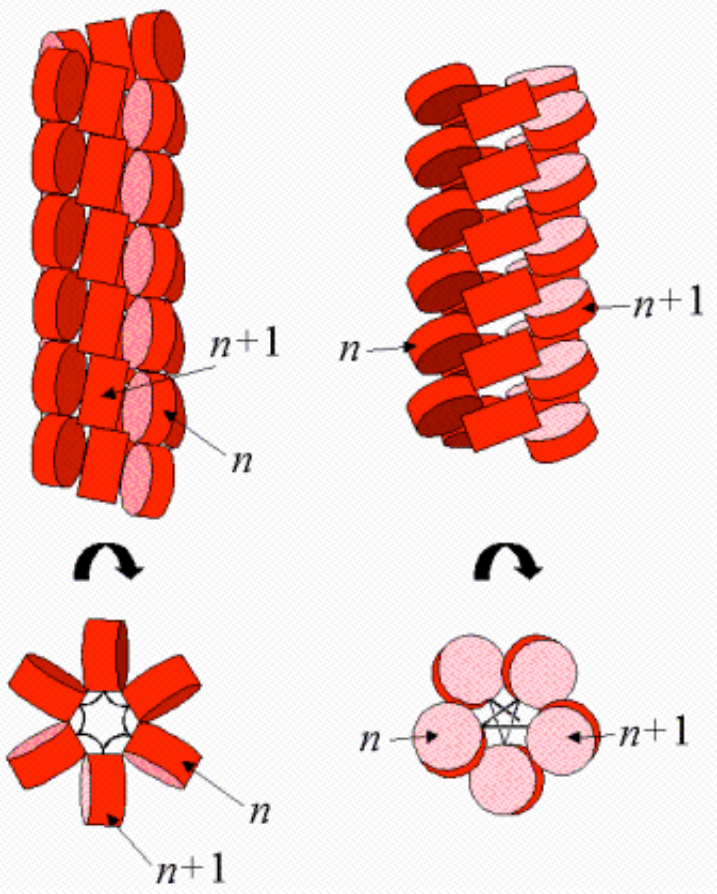

Figure 1.3 Solenoid and zig-zag model of the 30 nm fiber. Neighboring nucleosomes are indicated (n, n+1). In the solenoid model (left) it is assumed that the chain of nucleosomes forms a helical structure with the linker DNA bent in between whereas the zig-zag model (right) postulates straight DNA linkers that connect nucleosomes located on opposite sides of the fiber (image from Helmut Schiessel (Schiessel et al., 2001a).

Histones were shown to directly participate in the formation of the 30 nm fiber, since proteolytic removal of all N-terminal tails abolishes fiber formation (Schwarz et al., 1996; Tse and Hansen, 1997). Only a short stretch of the H4 N-terminus is crucial for this process (Dorigo et al., 2003), and proteolytic removal of the H3 tail does not alter association (Leuba et al., 1998). Self-association into the 30 nm fiber is stabilized by the linker histone H1 but a fiber structure forms also in the absence of linker histones.

1.2.2 Higher order chromatin structure

As indicated in Fig. 1.2, chromatin is compacted into larger loops or rosettes up to the highest form of compaction in the mitotic chromosomes. This condensed state is necessary for proper segregation of the chromosomes during cell division. During interphase a looser state is present. In microscopic images different condensation states can be observed that lead to differences in density or staining properties. A highly condensed form comprising about 10% of the genome is called heterochromatin. Most of the heterochromatin does not contain

genes and the genes that are included are usually silenced. Euchromatin is a less compact state in which most of the interphase chromatin is found, containing the transcriptionally active genes (Gilbert et al., 2004; van Holde, 1989). Some confusion is caused by the different interpretations of eu- and heterochromatin. While originally, it has been defined solely on structural or staining differences observed in the light or electron microscope, more recently the distinction has been predominantly made depending on gene activity and biochemical properties. The latter lead to a more general definition of heterochromatin: biochemical studies have revealed significant differences in the protein composition of the active and inactive states. While H1, heterochromatin proteins (e.g. HP1) and some histone variants like CENP-A have been associated with condensed, inactive chromatin or gene silencing (Ahmad and Henikoff, 2002; Cheutin et al., 2003; Park et al., 2004; Suto et al., 2000), HMG proteins or histone variants like H3.3 or H2ABbd (Barr body deficient) are related to the decondensed, transcriptionally active state (Ahmad and Henikoff, 2002; Chadwick and Willard, 2001). Histone modifications also correlate with gene activation as discussed in detail in chapter 1.4. Regions that are inactivated by heterochromatin formation are often cell cycle or tissue specific (Paro, 1990). Heterochromatin has further been subdivided into two types, the constitutive and the facultative heterochromatin. Constitutive heterochromatin is enriched in satellite DNA and is stable and conserves its heterochromatic properties during development and differentiation, whereas facultative heterochromatin can change to the euchromatic form and thus represents the part of heterochromatin that can be activated by e.g. histone modifications (Mattei, 2002). Recent studies have shown that hetero- and euchromatin are separated by borders that inhibit communication between the two chromatic states. These borders can be separated into two major groups, fixed and so-called negotiable borders. Fixed borders are established by specific DNA elements (insulators or boundary DNA elements), which define the position of the boundary and recruit specific protein complexes responsible for the isolation (West et al., 2002). They result from interactions with perinuclear substrates or loop formation (Gerasimova et al., 2000). Negotiable borders arise from the balance of opposing enzymatic activities leading to the formation of defined histone modifications (Kimura and Horikoshi, 2004; Litt et al., 2001a; Litt et al., 2001b).

Various methods have been used to analyze the higher order compaction in chromatin. Biochemical as well as microscopy methods (discussed in chapter 2 and 3) have been applied in combination with computer simulations to elucidate chromatin conformation. Nevertheless, the structure and dynamics of chromatin as it is found in the interphase nucleus are still an important subject of current research.

1.3 Chromatin remodeling and histone chaperones

1.3.1 Chromatin assembly factors

Chromatin in the interphase nucleus has a highly dynamic organization. Movements can be very fast and also cover large distances. These dynamic processes are energy-dependent and have been related to gene expression as reduced mobility has been correlated with reduced transcriptional activity (Gasser, 2002). On the nucleosomal level, these movements are due to the activity of ATP-dependent chromatin remodeling factors. They use the energy of ATP to translocate nucleosomes on the DNA, thereby allowing access to DNA sequences previously covered by the nucleosome. Both the deposition of newly synthesized histones onto naked DNA and the sliding of already assembled nucleosomes requires the activity of assembly factors. They participate in transcriptional activation and silencing, in DNA replication, repair and recombination. Through transcriptional regulation they also play a role in the regulation of cell cycle and differentiation. A great number of such complexes has been characterized and classified into four groups (Fig. 1.4).

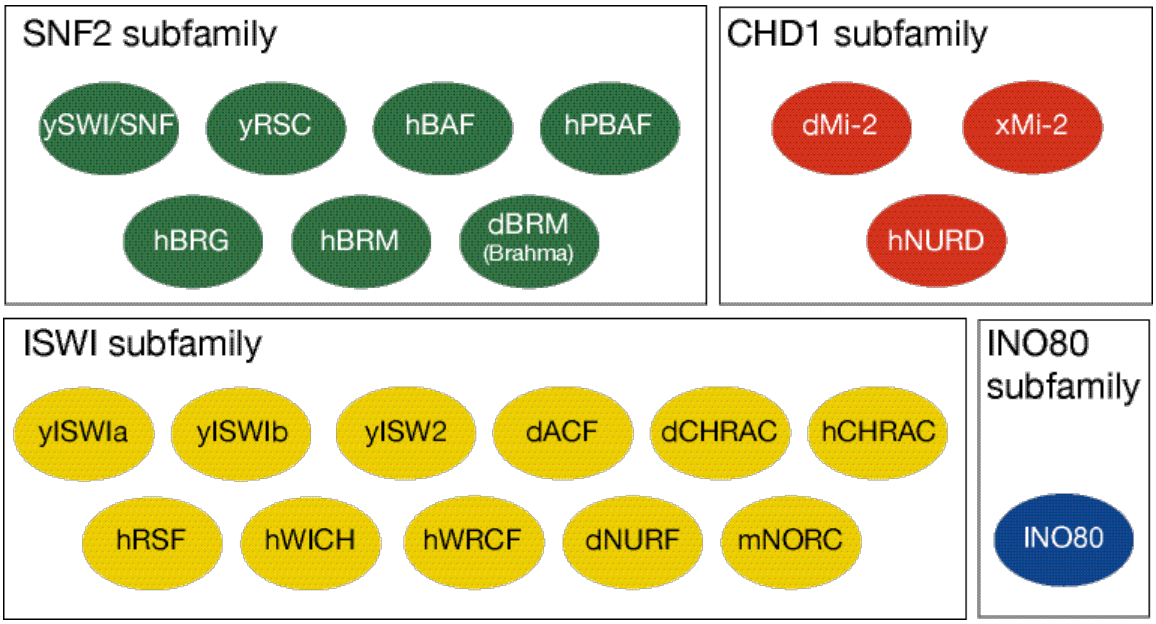

Figure 1.4 The four major subfamilies of chromatin assembly factors. Adapted from (Lusser and Kadonaga, 2003).

The two major classes, the SNF2 subfamily and ISWI subfamily differ significantly in function and structure. The SNF2 complexes are large (~ 2 MDa) with up to 12 subunits and tend to disrupt nucleosome structure. They translocate the nucleosome by 50-60 bp and their

ATPase activity is stimulated by nucleosomes as well as by DNA. The ISWI family complexes are smaller consisting of two to four subunits and tend to assemble or stabilize nucleosome structure. They shift the nucleosomes by about 10 bp and are only stimulated by nucleosomes (Lusser and Kadonaga, 2003). Interestingly a dependence of their activity on H1 has been shown for members of both families (Ramachandran et al., 2003)(J. Tamkun, personal communication). Histone acetylation is also essential for the function of chromatin assembly complexes. The activity of ISWI for example depends on the acetylation of H4 lysine16 (Clapier et al., 2001; Corona et al., 2002; Hamiche et al., 2001).

The members of the CHD1 subfamily are generally responsible for transcriptional repression and form complexes with DNA-methylases and histone deacetylases. The remodeling activity of Mi-2 depends on the methylation state of the DNA. INO80 seems to have helicase activity and participates in transcription and DNA repair. Substitution of H2A by the histone variant H2A.Z seems to depend on SWR1, an INO80 homolog.

Two mechanisms have been proposed for the movement of nucleosomes along the DNA, twisting and bulging. In the twisting model only a few histone-DNA interactions are broken at a time upon twisting of the DNA helix at the entry of the nucleosome. The detached base pairs on the surface of the nucleosome are replaced by the neighboring ones. The released base pairs propagate over the surface of the histones leading to the rotation of the DNA around the axis of the octamer (Widom, 2001). The bulging model proposes that a larger segment of DNA of about 30-35 bp detaches at the entry/exit site of the nucleosome and interaction of the free histone surface with neighboring DNA segments leads to the formation of a DNA loop, which then moves along the surface of the histones (Brower-Toland et al., 2002; Davey et al., 2002; Schiessel et al., 2001b; Widom, 1998). Remodeling complexes were shown to introduce superhelical torsion into nucleosomal DNA, suggesting a twisting mechanism (Havas et al., 2000). However, recent results are in favor of a bulging mechanism (Strohner et al., 2004). Interestingly HMGB1(a high mobility group protein discussed in chapter 1.5.2) has been shown to increase the ACF/CHRAC-dependent nucleosome remodeling activity by localizing at the entry/exit site and pre-bending the DNA (Bonaldi et al., 2002).

Chromatin assembly factors have been used for *in vitro* chromatin assembly. In this case defined components can be mixed allowing analysis of well defined chromatin substrates. Thus they are a helpful tool in examining chromatin structure *in vitro*. Activity of the enzymes can be monitored by measuring their ATPase activity using thin layer chromatography (Fig. 1.5) as their ability to hydrolyze ATP correlates with their assembly/rearrangement activity.

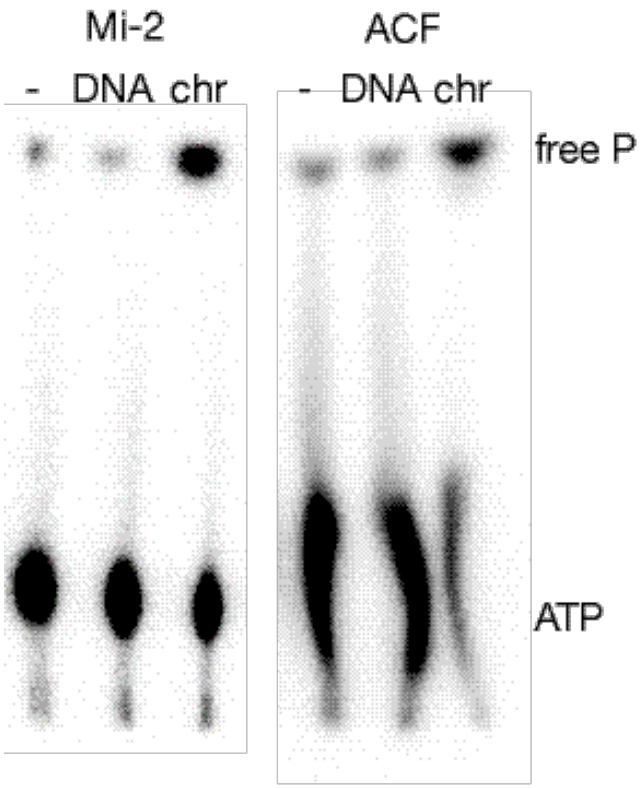

Figure 1.5 Thin layer chromatography of γ-ATP hydrolysis. Mi-2 and ACF are both chromatin assembly factors that hydrolyze ATP. Their activity and therefore ATP hydrolysis is stimulated by the presence of nucleosomes (line chr) but not by free DNA. Significant amounts of free phosphate are only produced in the presence of chromatin substrate. The ratio of free phosphate and ATP is used to determine the activity of the enzymes (K. Fejes Tóth & K. Rippe, unpublished data).

1.3.2 Histone chaperones

Histone chaperones bind histones and prevent them from nonspecific, electrostatic interactions with nucleic acids. This activity appears essential for cell viability, since mixing of histones and DNA *in vitro* in the absence of histone chaperones at physiological salt concentrations leads to rapid aggregation (Nakagawa et al., 2001). Histone chaperones are highly acidic, which is likely to mediate their interaction with the positively charged histones. They are conserved and often have special preference for given histones. CAF-1 and Asf1 bind preferentially newly synthesized H3 and H4, whereas NAP1 associates with H2A·H2B (Chang et al., 1997; Nakagawa et al., 2001). Histone chaperones are often subunits of chromatin remodeling complexes. NAP1 and nucleoplasmin, for example, cooperate with the SWI/SNF complex to mediate nucleosome disassembly (Chen et al., 1994; Cote et al., 1994). Table 1.1 summarizes the most important histone chaperones and their functions.

Chaperone	Functional roles	Binding interactions	
		histones	other factors
CAF1	histone chaperone, replication-coupled chromatin assembly, DNA repair, silencing, cell-cycle progression	H3·H4	PCNA, Asf1
Asf1	histone chaperone, replication-coupled chromatin assembly, DNA repair, silencing, cell-cycle progression	H3·H4	CAF1, Brahma, SAS-I, TAFII-250/CCG1
NAP1	histone chaperone, nuclear import of histones	H2A·H2B, (H3·H4)	Kap114, p300
HIR	histone gene regulation, histone chaperone, replication-independent chromatin assembly, silencing	H2A·H2B, H3·H4	Asf1
Nucleoplasmin	maternal storage of histones in oocytes, histone chaperone during rapid replication in early embryo	H2A·H2B, (H3·H4)	
N1/N2	maternal storage of histones in oocytes, histone chaperone during rapid replication in early embryo	H3·H4	

Table 1.1 Histone chaperones, their functions and binding partners. Adapted from (Haushalter and Kadonaga, 2003).

The best characterized histone chaperone is the chromatin assembly factor 1 (CAF1), a heterotrimer that associates with newly synthesized H3 and H4. It promotes de novo nucleosome formation on naked DNA during replication or excision repair. It participates in heterochromatin maintenance and possibly associates with heterochromatin-binding protein 1 (HP1) (Gaillard et al., 1996; Krude, 1995; Martini et al., 1998; Taddei et al., 1999; Verreault et al., 1996).

The replication coupled assembly factor (RCAF) consists of anti-silencing function 1 (Asf1) protein and specifically acetylated histones H3 and H4 (Tyler et al., 1999). Asf1 specifically interacts with CAF1 in the assembly of newly synthesized chromatin (Tyler et al., 2001). Asf1 also participates in replication independent chromatin assembly (Emili et al., 2001; Munakata et al., 2000). In addition, it also interacts with chromatin assembly proteins

(Brahma), transcription factors (TAFII-250/CCG1) and histone acetyltransferases (SAS-I) to regulate chromatin association state and gene activation (Chimura et al., 2002; Meijsing and Ehrenhofer-Murray, 2001; Moshkin et al., 2002; Osada et al., 2001).

The main transporter of the H2A·H2B dimer is NAP1 (Ishimi et al., 1984). It is involved in the import of the H2A·H2B dimer to the nucleus and the deposition of histones onto the DNA as described in several reviews (Adams and Kamakaka, 1999; Loyola and Almouzni, 2004; Tyler, 2002). NAP1 cooperates with CAF1 in de novo chromatin assembly by transporting the H2A·H2B dimer and depositing it after tetramer binding. Various lines of evidence suggest that NAP1 and the related NAP2 protein are mainly cytoplasmic during G1 and G2 phase with only a small fraction in the nucleus and translocate into the nucleus during S phase indicating their role in replication (Asahara et al., 2002; Ito et al., 1996; Miyaji-Yamaguchi et al., 2003; Rodriguez et al., 1997). A detailed analysis of the association state of NAP1 was conducted with analytical ultracentrifugation as described in "Association states of nucleosome assembly protein 1 and its complexes with histones" (Fejes Tóth et al., 2004b). Its effect on chromatin folding and its ability to capture the H2A·H2B dimer released from chromatin was analyzed by analytical ultracentrifugation and atomic force microscopy. Results are discussed in "Exchange of histone H2A·H2B dimer in nucleosomes and chromatin fibers" (Kepert et al., 2004).

Nucleoplasmin and N1/N2 are present in the xenopus oocyte and are essential for storage and deposition of histones during the rapid cycles of replication in early embryonal development (Philpott et al., 2000). Homologues of these proteins in yeast or human are not yet known. A novel factor isolated from human cell nuclei, FACT, is required for efficient transcription from chromatin templates by the RNA polymerase II. It binds the H2A·H2B dimer and seems to be responsible for disrupting nucleosome structure during transcriptional elongation (LeRoy et al., 1998; Orphanides et al., 1998; Orphanides et al., 1999).

Histone chaperones and chromatin assembly factors play a central role in regulating gene expression, cell cycle and differentiation. Thus, it is not surprising that changes in the expression of these factors correlate with severe hereditary diseases or cancer. For example it has been shown that mice lacking the SNF5 protein, a component of the SWI/SNF complex, stop developing at the peri-implantation stage. Furthermore, heterozygous mice develop nervous system and soft tissue sarcomas. In the tumors the wild type allele is lost emphasizing the tumor suppressor function of SNF5 (Klochendler-Yeivin et al., 2000). Recent studies indicate that CAF1 is a good proliferation marker and prognostic indicator in malignant and benign breast tumors (Polo et al., 2004).

1.4. Histone Modifications and DNA methylation

Both DNA and histones can be modified leading to altered gene expression. Nucleosome modification is a dynamic regulatory process accomplished by many different enzymes. These enzymes contain conserved catalytic domains, and many of them are only functional in large multisubunit complexes. The modifications of the histones include the acetylation of lysines, the methylation of lysines and arginines, the phosphorylation of serines and threonines, the ubiquitination and sumolation of lysines and the ADP-ribosylation of glutamic acids (Fischle et al., 2003a; Spencer and Davie, 1999; van Holde, 1989). In addition, DNA can be methylated (Bird and Wolffe, 1999) (Robertson, 2002). Except for methylation, all these modifications are known to be reversible (Bannister et al., 2002). A summary of the most important histone tail modifications is shown in Fig. 1.6.

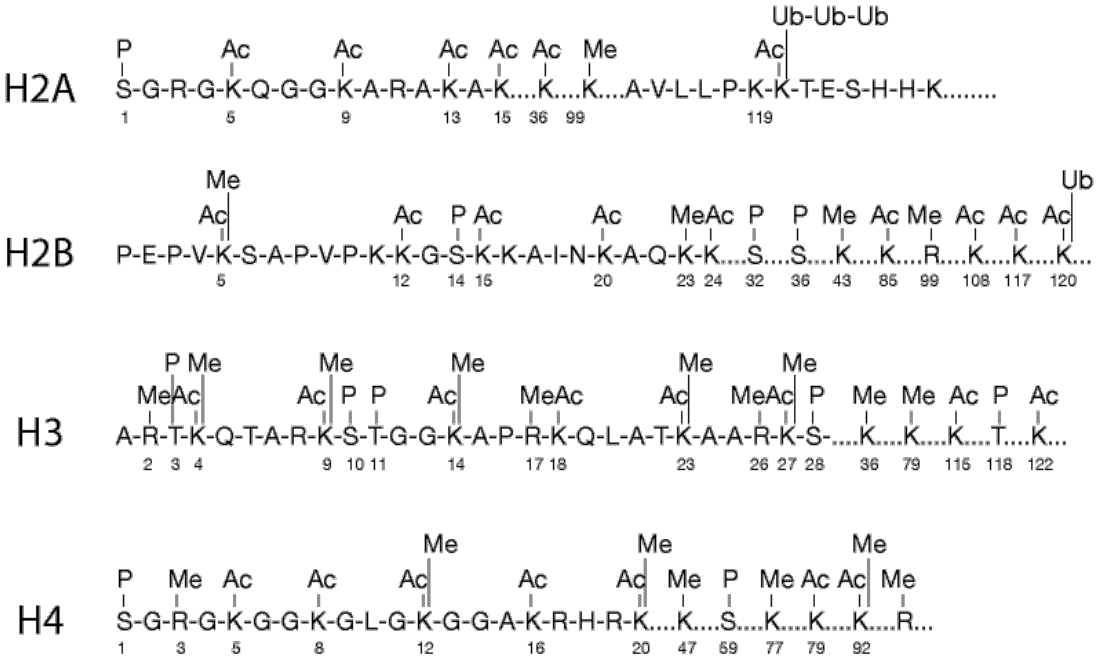

Figure 1.6 Histone modifications. Ac: acetylation, P: phosphorylation, Me: methylation, Ub: ubiquitination. (www.histone.com and (Spencer and Davie, 1999)).

1.4.1 Histone acetylation

Acetylation of histone lysines has been shown to influence transcription, DNA replication, histone deposition, higher order chromatin structure and DNA repair. Acetylation and deacetylation is performed by specific histone acetyl transferases (HAT) and deacetylases (HDAC). Histone acetylases use acetyl-CoA to add an acetyl group on the positively charged lysine residues thereby neutralizing them. In general, acetylation is thought to lead to transcriptional activation and chromatin decondensation (Dressel et al., 2000) (Richon et al.,

2000) (Kouzarides, 1999) (Allfrey et al., 1964; Fejes Tóth et al., 2004a), while deacetylation can be correlated with inactive heterochromatin (Braunstein et al., 1993). However, acetylation may in sparse cases be responsible for inactivation, while deacetylation has also been shown to activate some genes (Mariadason et al., 2000). The exact mechanism by which acetylation of histones causes decondensation is poorly understood but it is likely the result of different effects. The neutralization of the positive charge decreases the binding of the tails to DNA and adjacent histone cores while recruitment of proteins that have an acetyl-lysine binding domain, the so-called bromodomain, probably also contributes to structural changes and the alteration of gene accessibility.

Histone acetylases have been classified into two large groups, the group A or nuclear type HATs, which acetylate chromosomal histones and the group B or cytoplasmic HATs, which acetylate free histones prior to chromatin assembly (Workman and Kingston, 1998). The two major HAT B proteins are HAT1 and HAT2. They are responsible for the acetylation of newly synthesized H4 at K5 and K12, which seems to be a prerequisite for nuclear import and proper assembly. The histone chaperone CAF1 for example specifically recognizes acetylated histones and thereby transports newly synthesized histones to the replication site (Sobel et al., 1995; Workman and Kingston, 1998). HAT A are functional in the nucleus in large multisubunit complexes and involved in transcriptional regulation. The best-described HATs are Gcn5, PCAF and p300/CBP. Their main targets are H3 and H4, but some also modify histone H2A and H2B. Non-histones proteins like transcription factors, nuclear import factors or alpha-tubulin are also subject to acetylation giving an additional mechanism of transcriptional regulation (Munshi et al., 1998)(for review see (Kouzarides, 2000)). Furthermore, other histone modifications also influence acetylation. For example, the phosphorylation of H3S10 enhances K14 acetylation and together, they promote transcription (Clark et al., 1993).

Histone deacetylases can remove acetyl groups from lysines thereby causing general deactivation and chromatin condensation. Two large families with HDAC activity have been described, the SIR2 family of NAD+-dependent HDAC-s required for gene silencing in yeast and the classical HDAC family. Members of the latter are divided into two groups the class I (HDAC1, 2, 3 and 8) and class II deacetylases (HDAC4, 5, 6, 7, 9 and 10) (Bjerling et al., 2002; Braunstein et al., 1993; de Ruijter et al., 2003; Villar-Garea and Esteller, 2004). Members of the first are expressed in most cell types, while expression of the class II HDACs seems to depend on the cell type and might be relevant in differentiation and developmental processes. Most class I deacetylases are nuclear but some have been shown to be present in the cytoplasm as well, whereas class II members shuttle between the cytoplasm and the nucleus in response to certain signals (for review see (de Ruijter et al., 2003)). HDACs can be inhibited reversibly or irreversibly by many different molecules. This leads to

a global hyperacetylation of histones and has been related to transcriptional activation and decondensation (Fejes Tóth et al., 2004a; Van Lint et al., 1996). A potent HDAC inhibitor is Trichostatin A (TSA), a highly toxic fermentation product of Streptomyces, which shows its inhibitory effect in the nanomolar range. A detailed analysis of the effect of TSA on chromatin condensation state and cell cycle is described in "Trichostatin A induced histone acetylation causes decondensation of interphase chromatin" (Fejes Tóth et al., 2004a). Short-chain fatty acids such as butyrate and valproic acid form a large group of less efficient inhibitors which have already been successfully applied in cancer therapy (Archer and Hodin, 1999; Cress and Seto, 2000; Kouzarides, 1999; Mahlknecht et al., 2000).

1.4.2 Histone methylation

Methylation of histones has been associated with both gene silencing and activation. Lysine and arginine residues can be mono-, di- or trimethylated leading to different effects on chromatin condensation state and transcription. The methylation of lysine 9 in H3 leads to heterochromatin formation and gene silencing. This condensed state is stabilized by the binding of heterochromatin-binding protein HP1. Interestingly histone deacetylation is necessary prior to methylation (Nakayama et al., 2001) indicating that different histone modifications cooperate to establish a given chromatin conformation state. Another example of methylation mediated silencing is the polycomb protein, which specifically binds methylated lysine 27 of H3 (Fischle et al., 2003b). Activation is achieved by H3 K4 and K9 and H4 K40 methylation as a signal for the chromatin assembly complex Brahma. This inhibits the binding of HP1 and shifts nucleosomes to allow transcription factor binding, thus maintaining an active chromatin state (Beisel et al., 2002). Methylation of arginines in H3 and H4 also correlates with transcriptional activation (for review see (Zhang and Reinberg, 2001)).

1.4.3 Histone phosphorylation

All core histones and the linker histone H1 can be phosphorylated. This seems to be relevant in chromatin assembly, transcription, DNA repair and mitosis (Peterson and Laniel, 2004). Phosphorylation takes place at serines or threonines flanked by short stretches of basic amino acids, which probably mediate internucleosomal interactions and condensation of chromatin. Upon phosphorylation, the charge effect is disrupted resulting in the unfolding of chromatin (Dou and Gorovsky, 2000). In contrast, phosphorylation of H3 S10 has been associated with mitosis and chromatin condensation. It starts at centromeric regions during G2/M transition and spreads throughout the chromosome (Hendzel et al., 1997).

1.4.4 DNA methylation

In vertebrates methylation of cytosines seems to be an important mechanism for gene silencing. It is suggested that DNA methylation has evolved to protect the genome from transposable elements. This is fulfilled by suppressing the transcription of transposable elements and thereby limiting their spreading (Yoder et al., 1997). DNA methylation is carried out by specific DNA methylases (DNMT). So far no DNA demethylases have been identified raising the question how demethylation takes place.

DNA methylation is primarily found in transcriptionally inactive regions such as the inactive X chromosome or genes that have been turned off in certain tissues. A variety of proteins binds methylated DNA and interacts with chromatin remodeling and histone deacetylase complexes leading to the compaction and inactivation of chromatin (for review see (Leonhardt and Cardoso, 2000)). Methylation is restricted to cytosines in the sequence CG (also termed CpG), resulting in the symmetric methylation of both strands of the DNA double helix, allowing maintenance of the methylation pattern throughout replication. Some genes are only transcribed from one allele depending on their parental origin. This phenomenon is called genomic imprinting. During the formation of the germ cell imprinted genes are methylated on one allele and thus are shut off. Imprinted hypermethylated alleles are also rich in hypoacetylated histones. For their reactivation treatment with the DNA methylase inhibitor 5-azaC is not sufficient, and additional incubation with the histone deacetylase inhibitor TSA is needed (Chiurazzi et al., 1999).

Throughout the vertebrate genome regions of up to 1-2000 nucleotides with high ratio of CpG repeats, so called CpG islands, are present. In contrast to single CpGs, these islands are typically unmethylated and are found in the neighborhood of constitutively active genes (Fazzari and Greally, 2004). They seem to be responsible for maintaining an open conformation at promoters of highly expressed genes. Exceptions to this hypomethylation are CpG islands at loci undergoing genomic imprinting and X-chromosome inactivation (Li et al., 1998; Pfeifer et al., 1990). Several connections have been made between changes in the methylation pattern and tumorogenesis: genome-wide decreased DNA methylation leads to chromosomal instability. If CpG islands at promoters of tumor-suppressor genes are methylated, those are silenced, leading to subsequent tumor progression (Baylin et al., 2001; Lengauer et al., 1998). Numerous hereditary diseases have been linked to altered DNA-methylation like the Rett-syndrome or the fragile X syndrome. As an example, hypermethylation in fragile X syndrome leads to repression of the FMR1 gene (Jin and Warren, 2000; Robertson and Wolffe, 2000). This hypermethylation correlates with deacetylation of histones H3 and H4 (Coffee et al., 1999) and transcriptional inactivation

(Drouin et al., 1997). Inhibition of histone deacetylation and of DNA methylation have been shown to reactivate the transcription of the FMR1 gene (Chiurazzi et al., 1999).

1.5 Histone H1 and other chromatin associated proteins

In addition to the histones forming the core of the nucleosome, several other proteins bind to chromatin dynamically and influence higher order structure and accessibility.

1.5.1 The linker histone H1

A fifth histone, the linker histone H1, is also found in chromatin in equimolar amounts, i.e. about one per nucleosome. (van Holde, 1989). H1 has a central globular domain that can bind to the nucleosome, a long basic C-terminal region consisting mainly of lysines, alanines, serines and prolines and a short N terminus (Travers, 1999; Wolffe, 1998) . It has been suggested that the C terminus is capable of forming an α helix structure that might facilitate chromatin condensation by neutralizing the charge of the DNA backbone (Clark and Thomas, 1988; Wolffe, 1997). The globular domain binds to the linker DNA leading to reduced mobility and sliding of the nucleosomes (Varga-Weisz et al., 1995). How H1 leads to compaction into the 30 nm fiber is not completely understood, but changes of the entry-exit angle of the DNA seem to be important. We have shown that H1 stabilizes a conformation with a smaller entry-exit angle (Kepert et al., 2003), which is probably relevant in chromatin condensation. Linker histones also reduces the access of transcription factors to DNA, thus acting as global repressors (Cheung et al., 2002; Herrera et al., 2000; Zlatanova et al., 2000). They can act as general transcription regulators as they inhibit histone acetylation (Herrera et al., 2000). H1 seems to stabilize histone tail-mediated fiber interactions, which is supported by the fact that for compaction by H1, the histone tails are crucial and condensation does not occur with tailless histones (Carruthers and Hansen, 2000). Average binding-time of H1 to the chromatin is much shorter than that of core histones and rapid dissociation and association seems to be necessary for transcriptional regulation (Misteli et al., 2000). Phosphorylation of H1 has also been associated with its dissociation (Dou et al., 2002). Furthermore, acetylation of the core histone tails decreases the residence time of H1 leading to decondensation. An interesting observation that underlines the cooperativity of different factors has been obtained recently by the group of John Tamkun: they show that acetylation of lysine 16 of H4 is essential for the function of the chromatin assembly factor ISWI. The activity of ISWI in turn seems to be crucial for binding of H1 and loss of ISWI leads to the displacement of H1 from the chromatin (J. Tamkun, personal communication).

1.5.2 HMG proteins associate with active chromatin

In contrast to H1, HMG (high mobility group) proteins are mainly associated with transcriptionally active chromatin (Bustin, 2001; Thomas, 2001).Two classes of HMG proteins, the HMGB and HMGN class can be distinguished. HMGB proteins bind to DNA by recognizing specific DNA structures. They associate with the minor groove of locally distorted B-form DNA and lead to the bending of the double helix. This bending may play a role in regulating chromatin condensation. *In vitro*, H1 and HMG proteins interact and possibly a complex of the two can locally regulate condensation/decondensation processes (Ner et al., 2001; Ura et al., 1996). Competition of H1 and HMG proteins for binding sites on chromatin to modulate local chromatin fiber structure has also been described (Catez et al., 2002). HMGN proteins were shown to interact with histones H3 and H2B and to lead to decondensation (Herrera et al., 1999; Trieschmann et al., 1998). Presence of these proteins seems to be essential for polymerase II activation (Bustin et al., 1995).

1.5.3 Binding of HP1 leads to silencing

Heterochromatin binding protein 1 (HP1) is highly conserved and associates with pericentric and telomeric heterochromatin acting as a capping protein. However, it was also found at specific loci in euchromatin and might participate in gene silencing (Fanti et al., 2003; Fanti et al., 1998; Li et al., 2002; Saveliev et al., 2003). Mammals have 3 different isoforms. HP1- α and β reside predominantly in pericentric heterochromatin whereas HP1- γ is found both in hetero- and euchromatin (Minc et al., 2000). HP1s seem to play a role in heterochromatin formation, gene silencing and activation and nuclear assembly (Eissenberg and Elgin, 2000). They interact with several factors like histone methyl transferases, DNA methyl transferases (DNMT1 and 3), chromatin remodeling factors, and histone chaperones (CAF1) (Cleard et al., 1997; Fuks et al., 2003; Nielsen et al., 2002; Tschiersch et al., 1994; Vassallo and Tanese, 2002). Their tight connection to the lamin B receptor and to histones H3 and H4 suggest a possible function in docking chromatin to the nuclear envelope (Polioudaki et al., 2001).

1.5.4 Other chromatin factors

Several other factors like the Sir and the MeCP2 proteins also influence chromatin folding and connect histone modifying enzymes or chromatin assembly factors to changes in higher order chromatin structure. Recently much evidence suggests that non-coding RNAs also play a role in heterochromatin formation (Fuks et al., 2003; Hecht et al., 1995; Nan et al., 1998; Stevenson and Jarvis, 2003). Fig. 1.7 shows a possible mechanism of RNA action in transcription inactivation.

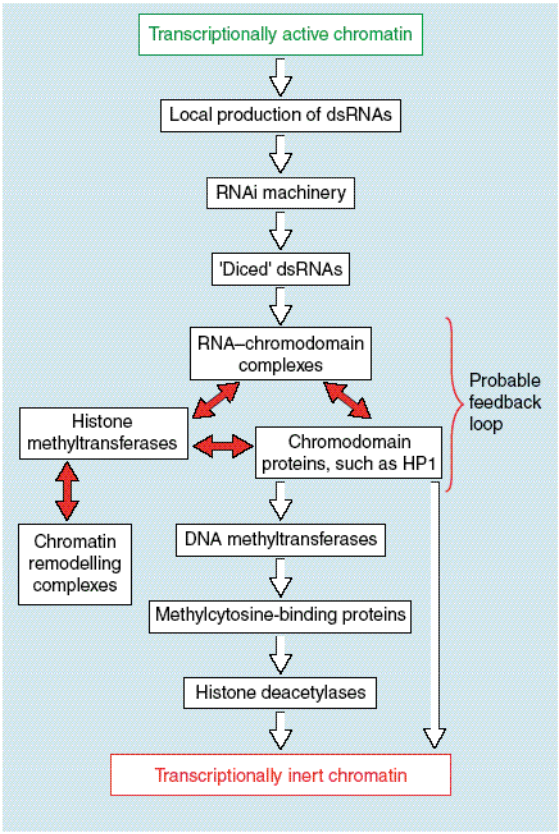

Figure 1.7 A possible way of heterochromatin formation (Stevenson and Jarvis, 2003).

1.6 Summary

Chromatin is a very dynamic structure. Its accessibility is regulated by a huge diversity of chemical modifications and protein factors. The simultaneous action of these factors is crucial for maintaining gene expression. The model depicted in Fig. 1.7 focuses on the effect of RNAi in transcriptional regulation but nevertheless shows a possible way of how all these factors might cooperate to establish a proper transcriptional state. Other factors not included in the scheme make the regulatory machinery appear even more intricate. Dysfunction of one factor might either bias the function of other proteins or be compensated by factors fulfilling similar roles. Analysis of changes in chromatin structure both *in vivo* and *in vitro* are thus essential for understanding the complex network of chromatin dependent regulatory processes.

2. Visualization and quantification of chromatin conformation changes

In the last few decades diverse methods and approaches have been applied to elucidate chromatin structure *in vivo* as well as *in vitro*. In this chapter a summary of the methods applied in this work is briefly introduced.

2.1 Biochemical approaches to examine chromatin structure

Biochemical findings from the past 30 years already indicated regularly spaced structural units of 160-220 base pairs. Several methods have been developed to analyze the protein and DNA composition, the mononucleosome structure as well as folding of the chromatin. The methods applied in this work include micrococcus nuclease (Mnase) digestion, supercoiling assays and *in vitro* reconstitution of chromatin using recombinant histones.

2.1.1 *In vitro* chromatin reconstitution

Histones can be expressed in E. coli and purified using gel filtration and ion exchange chromatography (Luger et al., 1997b). These recombinantly expressed histones are unmodified. To analyze the effect of the histone tails or their modification state they can be modified or digested with different proteases and used to reconstitute histone octamers of defined subunit composition. Subsequently, chromatin or mononucleosomes can be reconstituted by salt dialysis or using chromatin assembly factors like ACF and NAP1. *In vitro* reconstitution was used to analyze the effect of linker histone H1 on mononucleosome structure (Kepert et al., 2003).

2.1.2 Micrococcus nuclease digestion

In this method chromatin is partially digested with MNase, an enzyme that preferentially cuts DNA between the nucleosomes. This leads to the formation of mono-, di-, tri-, and higher oligonucleosomes that can be visualized on a gel as a DNA ladder after removal of the proteins. Fig. 2.1A shows an MNase digestion of chromatin reconstituted with plasmid DNA and recombinant histones with salt dialysis. If the spacing between nucleosomes is uneven, a smear is obtained on the gel, while regularly spaced nucleosomes lead to the ladder shown in Fig. 2.1A. Thus the quality of *in vitro* reconstituted chromatin can be determined.

2.1.3 Supercoiling assay

This approach utilizes that plasmid DNA is negatively supercoiled. Assembly of nucleosomes leads to positive supercoiling and thus counteracts the negative coils. In

eukaryotes enzymes called topoisomerases remove superhelical tension. When a supercoiled plasmid is treated with topoisomerase the number of supercoils is decreased. However, the presence of chromatin already compensates the negative supercoils and the enzyme has no further effect. Upon removal of the nucleosomes the superhelicity returns. This method is applied to analyze the efficiency of *in vitro* chromatin assembly by visualizing the topoisomers of chromatin-containing plasmids after Topoisomerase I (Topo I) treatment (Fig 2.1B).

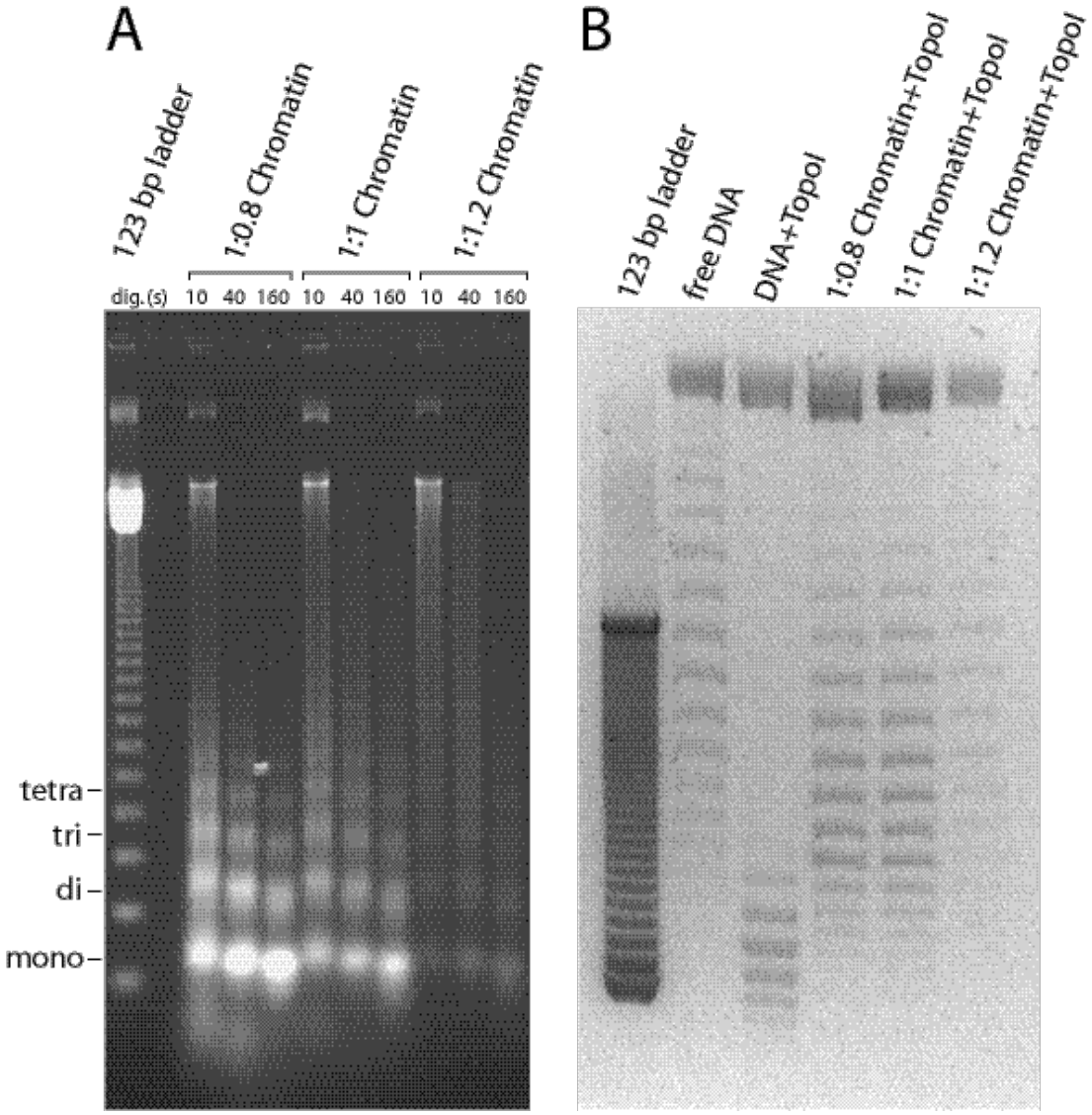

Figure 2.1 Biochemical analysis of Chromatin. (A) MNase digestion of chromatin reconstituted by salt dialysis with plasmid DNA and different ratios of DNA to recombinant histone octamer from 1:0.8 to 1:1.2. MNase treatment was conducted for 10, 40 and 160 seconds and DNA was run on a 1% agarose gel. Bands correspond to mono-, di-, and higher oligonucleosomes as indicated. (B) Supercoiling assay conducted with the same substrates as in (A). When free DNA is treated with topoisomerase I, the number of supercoils decreases. However presence of nucleosomes reduces or abolishes the effect of topo I. Single bands correspond to different topoisomers of the plasmid DNA. (K. Fejes Tóth & K. Rippe, unpublished data).

2.2 Analytical Ultracentrifugation

Analytical ultracentrifugation (AUC) is a versatile and powerful technique for characterizing the behavior of macromolecules in solution. Using modern data analysis methods, analytical ultracentrifugation experiments can be used to characterize assembly of biomolecular complexes, to determine subunit stoichiometries, to detect and characterize macromolecular conformational changes (size, shape, structure), and to measure equilibrium constants and thermodynamic parameters (free energies, enthalpies, entropies). The basic physical property used in AUC is mass or density, respectively. The sample is visualized utilizing absorbance of the particles in real time during sedimentation, allowing very accurate determination of hydrodynamic and thermodynamic parameters. In contrast to many other techniques, biomolecules are characterized in their native state under physiological solution conditions. The experiments are performed in free solution and are not obscured by interactions with surfaces like in gel filtration or surface plasmon resonance biosensors.

Fig. 2.2 shows the basic experimental setup. The instrument spins the sample under vacuum at a defined speed and temperature while it records the concentration distribution. The actual sample is placed in a sector-shaped cavity between two quartz windows to allow absorbance measurements during centrifugation. Double sector cells are used to be able to correct for the absorbance of the sample solvent. With the help of a monochromator the wavelength is freely selectable making examination of a wide range of sample concentrations possible.

Here, AUC was applied in numerous ways. The effect of histone chaperone NAP1 on chromatin conformation (Kepert et al., 2004), the association state and histone binding properties of NAP1 (Fejes Tóth et al., 2004b), the effect of H1 on nucleosome structure (Kepert et al., 2003) and the association state of the nucleoporin Nup145N (Lutzmann and Boettcher, 2004) were analyzed. For these experiments two basic types of AUC experiments, the sedimentation velocity and sedimentation equilibrium measurements, were used.

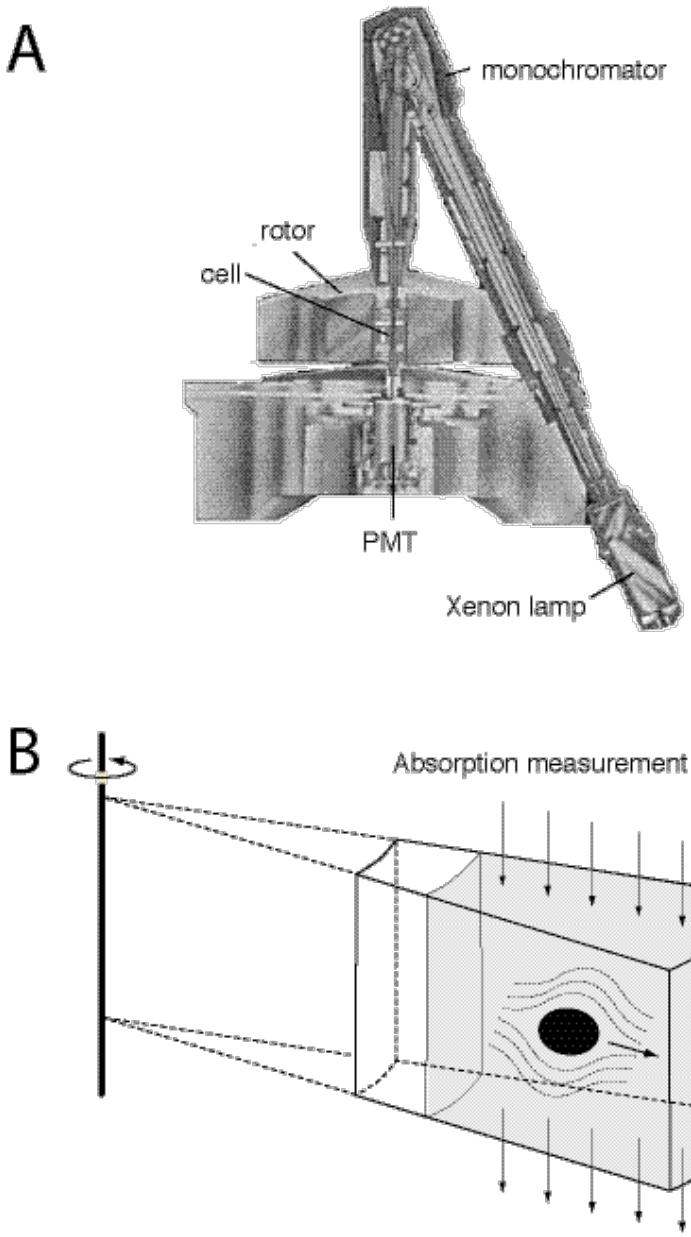

Figure 2.2 The analytical ultracentrifuge. (A) Samples are centrifuged at a constant speed, while light absorption is measured throughout the cell. (B) Due to the centrifugal force molecules are moving towards the outside of the cell depending on their form and molecular weight. As time passes less molecules are in the center, while the concentration increases at the outside leading to an absorption gradient that is detected and plotted in dependence of the radial distance.

2.2.1 Sedimentation velocity measurement

In sedimentation velocity experiments, an initially uniform solution is centrifuged with a sufficiently high angular velocity to cause relatively rapid sedimentation of the solute towards the cell bottom. This leads to the depletion of solute near the center of the cell and a sharp boundary between the depleted region and the uniform concentration of sedimenting solute (Fig 2.3).

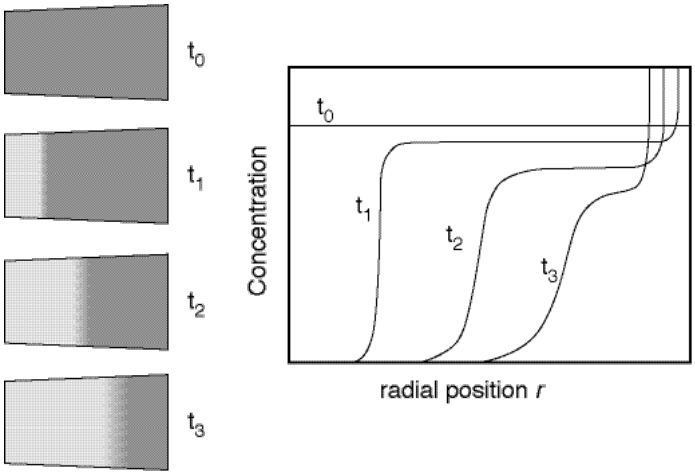

Figure 2.3 Movement of the boundary in a sedimentation velocity experiment. As the boundary progresses down the cell, the concentration in the plateau region decreases due to radial dilution and the boundary broadens due to diffusion. From the boundary movement the sedimentation coefficient, and from the broadening the diffusion coefficient is obtained.

The rate of movement of this boundary is measured and from this the sedimentation coefficient s is determined. The sedimentation coefficient is independent of the nature of the molecule and simply gives a measure for how rapidly a particle will move in a given field of gravity or centrifugal force. This depends directly on the mass of the particle and inversely on the frictional coefficient, which in turn is a measure of the molecules size and shape. The sedimentation coefficient of a particle with given molar mass, density and shape is also dependent on solvent density and solvent viscosity as seen in eq. 2.1:

$$\frac{M(1-\bar{v}\rho)}{N_A f} = \frac{v}{\omega^2 r} = s \qquad (2.1)$$

where M is the molar weight of the particle, N_A the Avogado number, f the frictional coefficient, $\bar{v}$ the partial specific volume of the particle, ρ the solvent density, v the velocity with which the band is moving and $\omega^2 r$ the centrifugal acceleration. The partial specific volume can be determined from the protein or DNA sequence, while the density of a solvent depends on its buffer composition. The sedimentation coefficient has the unit seconds and since the values are typically about 10^{-13} sec they are expressed in Svedberg (S) with 1 S=10^{-13} sec.

The Einstein-Sutherland equation gives the relation of the diffusion coefficient, D and the friction coefficient f:

$$D = \frac{RT}{N_A f} \qquad (2.2)$$

where R is the gas constant and T the absolute temperature. The diffusion coefficient can be directly determined from the sedimentation velocity runs by measuring the rate of boundary spreading. thus, the frictional coefficient in eq. 2.1 can be substituted and from the ratio of

the sedimentation and diffusion coefficient the molecular weight of the particles is calculated according to the Svedberg equation:

$$M = \frac{sRT}{D(1-\bar{v}\rho)} \qquad (2.3)$$

For the experimental determination of sedimentation and diffusion coefficient from the sedimentation velocity data the Lamm equation has been used:

$$\frac{dc}{dt} = \left(D\frac{d^2c}{dr^2} + \frac{1}{r}\cdot\frac{dc}{dr} \right) - s\cdot\omega^2\left(r\cdot\frac{dc}{dr} + 2c \right) \qquad (2.4)$$

The Lamm equation describes the observed changes of the concentration gradient in dependence of sedimentation time. No general analytical solution has been derived. However, solving the equation numerically has become possible recently with sophisticated analysis software like the SEDPHAT program (Schuck, 2003). This approach has been applied here to solve the complex equilibrium system of different association states adopted by NAP1 (Fejes Tóth et al., 2004b).

2.2.2 Sedimentation equilibrium measurement

A sedimentation equilibrium measurement is applied to determine molecular masses. A moderate, constant angular velocity is used until a dynamic equilibrium of sedimentation and diffusion is obtained. At first, the centrifugal field causes the material to sediment towards the cell bottom, increasing the local solute concentration. This causes increased back diffusion, opposing the centrifugal field. After sufficient time, a stationary condition is reached. Figure 2.5 shows a typical exponential concentration profile of histone H2A in sedimentation-diffusion-equilibrium. From this profile, a weight-averaged molecular mass is calculated. For a one component system the molecular weight can be determined by the function:

$$A_r = A_0 \exp\left(\frac{M(1\text{-}\nu\rho)\omega^2\left(r^2 - r_0^2\right)}{2RT} \right) + E \qquad (2.5)$$

where A_r is the measured absorption at a radial position r, A_0 the absorption at a reference point, r_0 and E the baseline. This equation can be modified for more complex systems containing more components or associating molecules. From such experiments the association constants of reactions can be derived.

As shown in eq. 2.3, molecular masses can be obtained from a sedimentation velocity experiment, with the advantage of being much faster and yielding molecular mass distributions rather than mass averages. However, this evaluation requires knowledge of the

frictional properties of the particle, because transport processes are involved. In the equilibrium experiments transport processes are eliminated. Therefore the resulting concentration gradient does not depend on molecular shape and is more reliable for determining the molecular mass.

For a typical experiment only 130 μl of a protein sample with an OD at 280 nm of 0.3 is needed. For an average protein this corresponds to about 50 μg. If the protein is detected at 230 nm, where the amide bond absorbs, typically 8-10fold lower concentrations are sufficient. The obtained molecular weight is usually within 5% of the calculated value determined from the protein sequence and the method is applicable over a wide range of molecular weights from approximately 2.5 kDa up to 1.5 MDa.

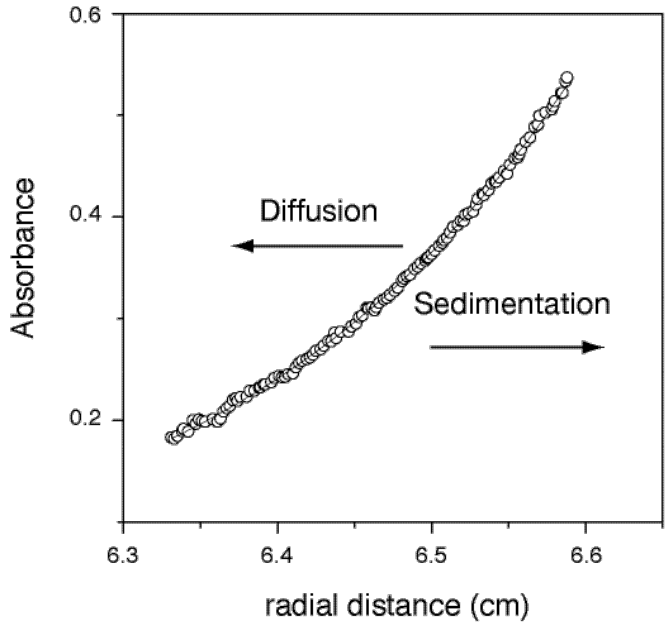

Figure 2.4 Sedimentation equilibrium run of histone H2A. Samples are centrifuged with moderate speed (here 20000 rpm) until an equilibrium between sedimentation and diffusion is reached. The flow of solute due to sedimentation increases with radial distance, which in equilibrium is counteracted by diffusion that increases with the concentration gradient. In equilibrium, the resulting concentration distribution is exponential with the square of the radial position. From the shape of the curve the molecular weight of the particles can be determined according to equation 3.4. Here a molecular weight of 15.3 kDa was obtained for recombinant H2A. (K. Fejes Tóth & K. Rippe, unpublished data).

2.2.3 Self-associating systems

Reversible interactions of proteins are among the fundamental principles that govern their role and organization. Self-association is frequently coupled to heterogeneous protein-protein interactions, and often represents an integral part of the reaction mechanism. This highlights the importance of methods that allow the characterization of the thermodynamic properties of self-associating proteins in solution. AUC is appropriate for determining monomer molecular weight, the extent of oligomerization and association/dissociation constants of self-associating systems. For this multiple measurements at different concentrations and speeds are required. Data analysis is often difficult and suitable analysis software has only become available in the past years. Velocity runs were analyzed by SEDPHAT, while for the analysis

of the equilibrium runs the Ultrascan software (http://www.ultrascan.uthscsa.edu) from Borries Demeler was found to be most appropriate.

2.3 Scanning force microscopy (SFM)

Scanning force microscopy (SFM) or atomic force microscopy (AFM) is used to image biomolecules without further fixing or staining with high resolution (reviewed in ref. (Bustamante and Rivetti, 1996)). For this purpose the molecules are bound to an even surface. An ultrafine sensor tip with a typical curvature radius of 5-15 nm is mounted on a flexible cantilever and moved in x and y direction over the surface by a piezo scanner. A schematic view showing the SFM setup for air and liquid is shown in Fig. 2.5A and B. In the "tapping mode" used in this work, the cantilever is oscillating up and down with a given amplitude while it is scanning (Hansma et al., 1993). The tip makes transient contacts with the sample leading to a reduction of the amplitude. Changes in sample height lead to variations of the cantilever amplitude, which are detected with a four quadrant photodiode by monitoring a laser beam reflected from the back of the cantilever. Variation of the amplitude are corrected by moving the piezo scanner and thus the sample in *z* direction up or down until the original amplitude is reestablished. Thus, the force between tip and sample is held constant and a topographic image of the surface is obtained from the movements of the scanner in *z*-direction. To image samples in liquid a fluid cell is used (Fig. 2.5B) where an O-ring seals the cell with the sample surface creating a fluid sample volume. Solutions can be exchanged by flushing them through the cell via a micropipetter connected to the cell allowing controlled exchange of the buffer solution. This enables the analysis of the effect of different buffer compositions or the addition of protein factors during measurements.
The lateral resolution and the apparent size of an object d in the SFM image is limited mostly by the curvature radius r of the scanning tip (Fig. 2.5C). The resolution in x-y direction also depends on the minimal height Δz that can be reliably measured and on the height difference Δh of the two objects as given in equation 2.6:

$$d = \sqrt{2r}\left(\sqrt{\Delta z} + \sqrt{\Delta z + \Delta h}\right) \qquad (2.6)$$

Typical resolutions obtained are around 5-10 nm laterally and 2 Å horizontally (Bustamante and Rivetti, 1996).

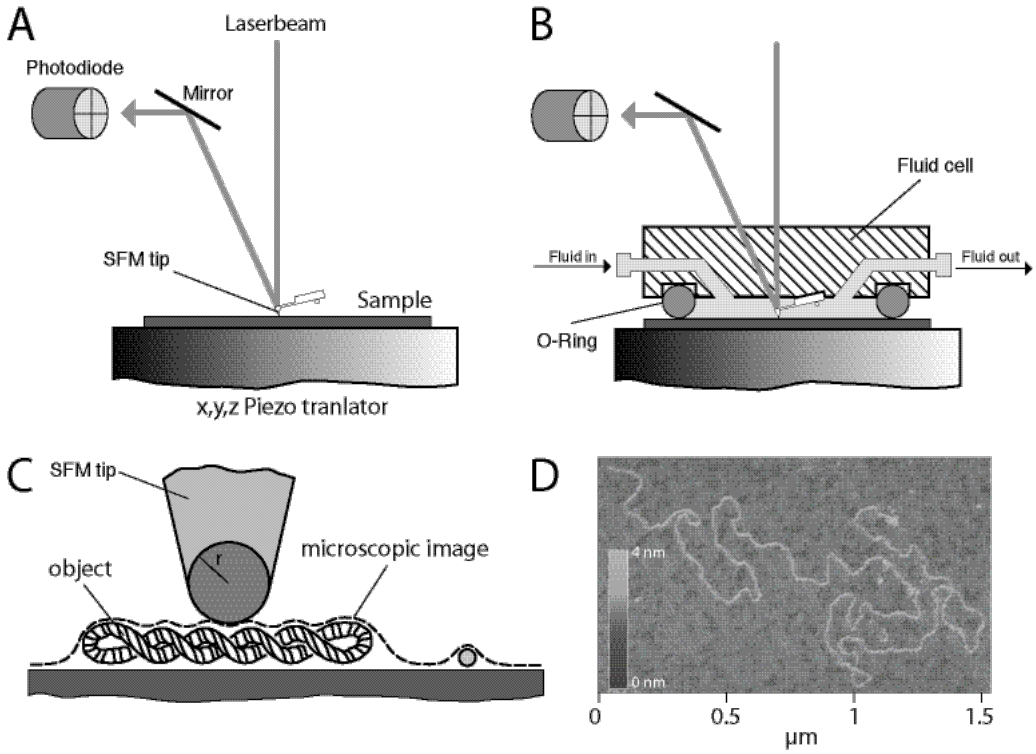

Figure 2.5 Schematic view of the SFM and image acquisition. (A) In the so-called "tapping mode", the cantilever is oscillating up and down above the sample. The tip makes transient contacts with the sample leading to a reduction of the oscillation amplitude. This is detected by monitoring a laser beam that is reflected on the back of the cantilever with a four quadrant photodiode. (B) For measurements in buffer a fluid cell is sealed by an O-ring to establish a buffer floated area. (C) The resolution largely depends on the geometry of the tip. The obtained microscopic image of a DNA is shown as a dashed line in the scheme. (D) SFM image of lambda DNA. The DNA is bound to the surface and shown as a long fiber. Height differences are indicated on the false-colour scale. Images (A) and (B) adapted and modified from (Rippe et al., 1997).

We have applied AFM to analyze DNA alone and in complex with histones (Kepert et al., 2003) or other proteins. As an example Fig. 2.6 shows images of free DNA, mononucleosomes, native chromatin and chromatin reconstituted with recombinant histones. Recombinant chromatin was reconstituted with salt dialysis as described in chapter 2.1.1 using recombinant histones and 1 DNA Single nucleosomes can not be differentiated probably due to formation of higher order structure or unspecific aggregation. 1 DNA is linear and has a length of over 40 kb. Up to date no other images of recombinantly reconstituted fiber have been published.

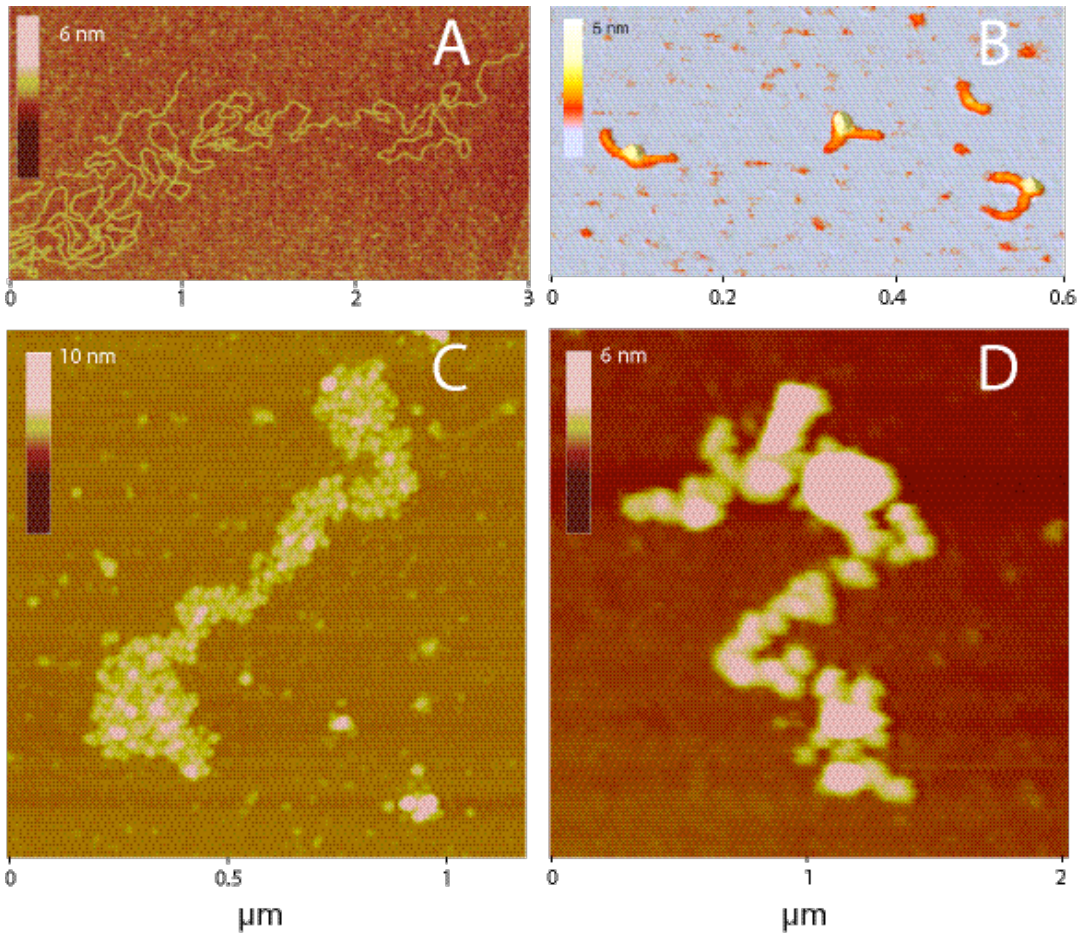

Figure 2.6 AFM images of DNA and chromatin. (A) λ DNA, (B) mononucleosomes reconstituted on a 614 bp DNA with salt dialysis using recombinant histones, (C) native chromatin isolated from HeLa cell nuclei, (D) chromatin reconstituted by salt dialysis using λ DNA and recombinant histones. Nucleosomes emerge from the surface and are seen as white spheres. In image (D) higher order structure seems to be present therefore single nucleosomes can not be distinguished. Lateral resolution is in the nm range and vertical is in the Å range resolution as indicated by the false-colour scale. Images (A) and (D) K. Fejes Tóth & K. Rippe, unpublished data, image (B) (Kepert et al., 2003), (C) (Kepert et al., 2004).

2.4 Epifluorescence microscopy and confocal laser scanning microscopy (CLSM)

Living cells can be observed by light microscopy. Light microscopy has a resolution limit of around 0.2 μm, i.e. about half the wavelength of light, and allows the observation of numerous cellular organelles. The cell nucleus, for example, was described for the first time nearly 200 years ago by Brown (1833). Different methods can be used to study unstained cells: the phase contrast microscope and the differential-interference-contrast (DIC) microscope use the interference effects resulting when light rays have passed different areas of the cell and thus differ in phase. The dark field microscope detects light that is scattered by the various components of the cell, and the cell appears as a bright object against a dark background.

Another way of increasing contrast and visualizing structures that cannot be distinguished in conventional light microscopy is fluorescence microscopy. Here only light of a wavelength in the excitation range of the fluorophores used for labeling reaches the specimen and only light of wavelengths in the corresponding emission range is allowed to reach the detector. This results in an image where the labeled structures are visualized against a black background and thus very little fluorescence is sufficient to give an image rich in contrast.
In epifluorescence microscopy light is not only collected from the focal plane but also from underneath and above, leading to loss in depth discrimination. This problem can be reduced in two ways. Deconvolution uses the point spread function of the optical system, i.e., the image one gets from infinitely small spots to reconstruct the real fluorescence distribution with an improved 3D resolution. The other approach is confocal microscopy. Figure 2.7 shows how resolution is improved using CLSM.

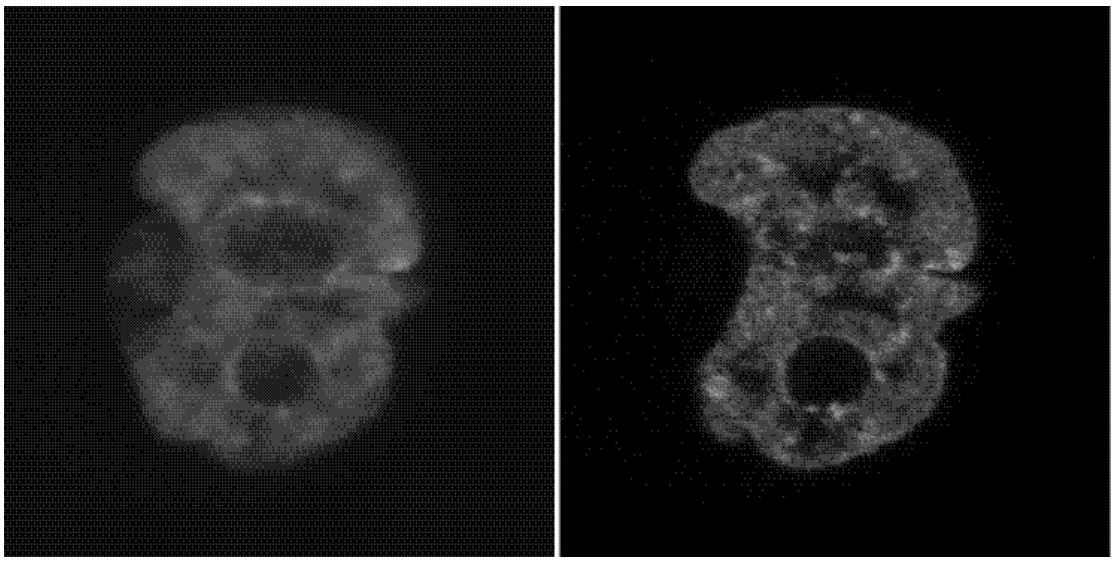

Figure 2.7 Comparison of epifluorescent and confocal microscope images. Image of a HeLa cell nucleus stably expressing the fusion protein of histone H2A and yellow fluorescent protein (H2A-YFP). The epifluorescent microscope image (left) was reconstructed by mean intensity projection of a stack obtained by CLSM resulting in an unsharp image with loss of fine structure and depth information. A single slice obtained by confocal microscopy (right) leads to high resolution in both xy and z direction.

2.4.1 Imaging with a confocal microscope

When an epifluorescence microscope is used to image a particular focal plane of a 3D object, parts of the object from above and below the focal plane are also illuminated and the light coming from these regions contributes to the image as out-of-focus signal, or blur. This can obscure fine structures and make a detailed interpretation of the image very hard. In a confocal microscope, coherent laser light is focused onto a diffraction limited spot at a

specific 3D position in the specimen using the objective lens. The fluorescence emitted from the illuminated object is collected using the same optics and guided to the detector, usually a photomultiplier tube (PMT). A pinhole in the optical path allows only light emitted from the illuminated spot to pass and reach the detector, while light from other spots in the same or another plane is rejected by the pinhole. (Fig. 2.8). This increases image contrast and depth discrimination. By varying the pinhole diameter, the degree of confocality can be adapted to practical requirements. To obtain a two-dimensional image, data from each point in the plane of the focus are collected sequentially by scanning the field of interest in a raster pattern. This way a CLSM can image a thin optical slice out of a thick specimen, a method known as optical sectioning. Under suitable conditions, the thickness (Z dimension) of such a slice may be less than 500 nm.

In addition to the observation of a single slice of a thick specimen with good contrast, optical sectioning allows the subsequent imaging of neighboring slices by moving the specimen along the optical axis. This results in a 3D data set, which provides information about the topological structure of the object. CLSM has been used to in this work to resolve the arrangement of chromatin and to analyze the effect of Trichostatin A, a potent histone deacetylase inhibitor on chromatin conformation in the nucleus.

For confocal microscopy the sample needs to be fluorescently labeled. This can be achieved on fixed cells by immunostaining or FISH (fluorescent *in situ* hybridisation) or *in vivo* by fusing the protein of interest to an autofluorescent protein. The most commonly used constructs contain spectral variants of green fluorescent protein (GFP) derived from jellyfish (for review see (Lippincott-Schwartz and Patterson, 2003)). When using proteins with different spectral properties colocalisation or interaction of different molecules can be observed *in vivo*.

A field of growing importance is the investigation of living specimens that show dynamic changes even in the range of milliseconds. Here the acquisition of time-resolved confocal image series (known as time series) provides a way to visualize and quantify the changes.

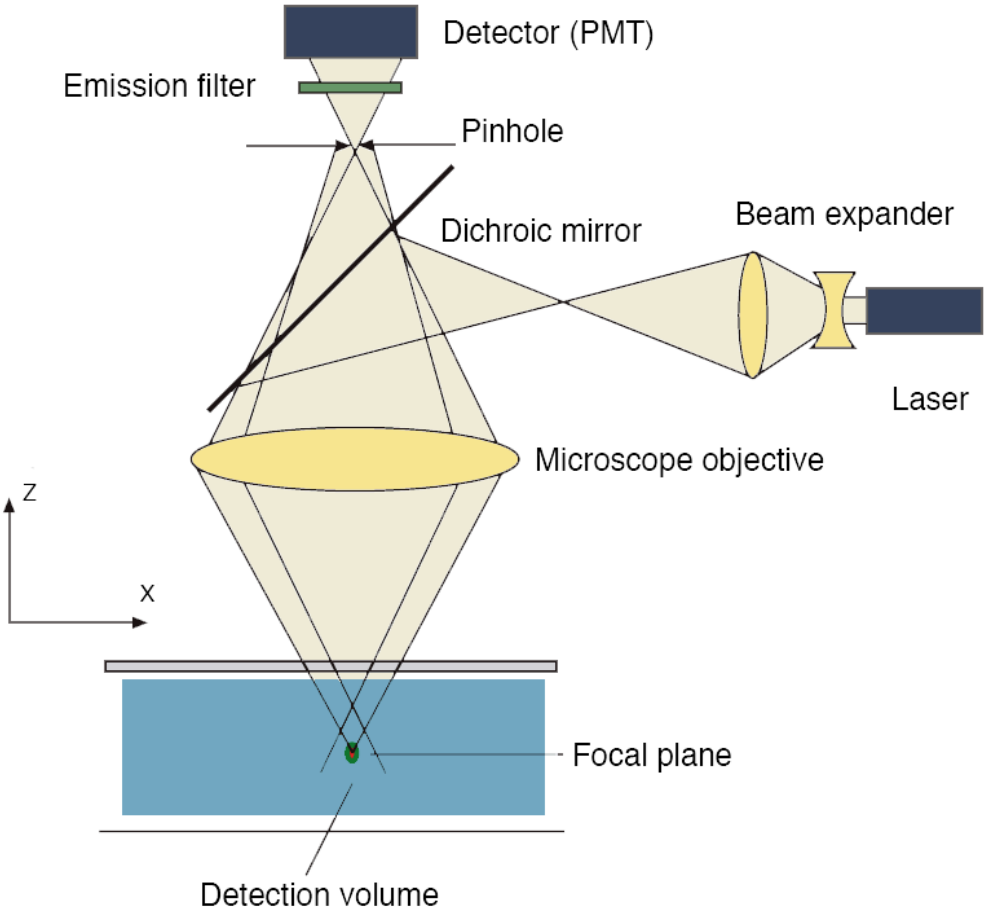

Figure *2.8* Beam path in a CLSM. A microscope objective lens is used to focus a laser beam onto the specimen, where it excites fluorescence. The fluorescence emission is collected by the objective and guided to the detector via a dichroic beamsplitter. The wavelength range of interest of the fluorescence spectrum is selected by an emission filter, which also acts as a barrier blocking the excitation laser line. The pinhole is arranged in front of the detector, on a plane conjugated to the focal plane of the objective. Light coming from above or below the focal plane or beside the focal spot is out of focus and thus blocked by the pinhole and therefore does not contribute to image formation.

2.4.2 Analyzing mobility of macromolecules

In recent years the interest in the mobility of macromolecules in living cell has grown significantly. The mobility is determined by diffusion, directed/active transport, and association/dissociation processes with related immobilization and can be addressed by numerous methods that have been developed. Combining confocal microscopy and *in vivo* fluorescent labeling techniques opens up a broad range of methods for the analysis of macromolecular dynamics. Two of them, fluorescence recovery/redistribution after photobleaching (FRAP), and fluorescence correlation spectroscopy (FCS) have been applied in this work to analyze the mobility of histones and the effect of the histone deacetylase inhibitor TSA on mobility (Fejes Tóth et al., 2004a).

The most commonly used one is fluorescence recovery after photobleaching (FRAP), (for review see(Wouters et al., 2001)). The scheme of a typical FRAP experiment is shown in Fig. 2.9. A non-equilibrium distribution is induced by bleaching an area of interest with high laser intensity. Subsequently the redistribution of fluorescent molecules from neighboring areas is recorded. Depending on the interaction with other molecules the amount of redistributed molecules and the kinetics of this process can vary. Proteins that associate with relatively immobile cellular structures have a slower recovery compared to freely mobile molecules.

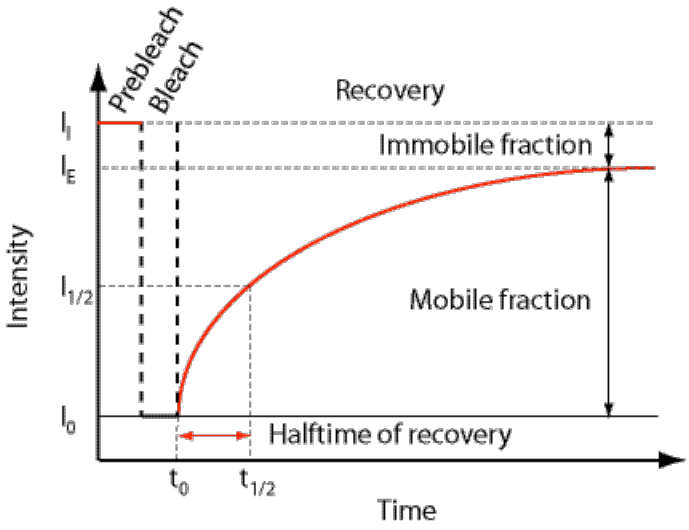

Figure 2.9 Fluorescence recovery after photobleaching (FRAP). A selected area within a cell is bleached and recovery of fluorescence within the area due to its redistribution is measured. Recovery kinetics depend on the transport/diffusion properties and on association/dissociation to immobile structures. I_i: initial intensity; I_0: intensity at time point t_0 (first post bleach intensity); I_E: end value of the recovered intensity; $I_{1/2}$: half recovered intensity ($I_{1/2} = (I_E - I_0) / 2$); $t_{1/2}$: halftime of recovery corresponding to $I_{1/2}$.

The time resolution of FRAP is in the range of milliseconds to seconds, faster movements cannot be resolved. For faster processes fluorescence correlation spectroscopy (FCS) with a time resolution in the microsecond range is more appropriate. FCS is not an imaging method but analyzes the movement of single molecules within the confocal volume of less than a femtoliter at a fixed position in the sample. When fluorescently labeled molecules cross the focus by Brownian motion, corresponding signal fluctuations are recorded on the detector. In order to determine the number and the mean dwell time of the molecules in the focus a autocorrelation analysis of the time-dependent fluorescence signal is applied. Small unbound molecules diffuse fast, generating short intensity fluctuations. The intensity correlation function thus decreases rapidly resulting in a short diffusional correlation time. Large or bound molecules move slowly and generate long fluctuations, leading to long correlation times (Fig. 2.10).

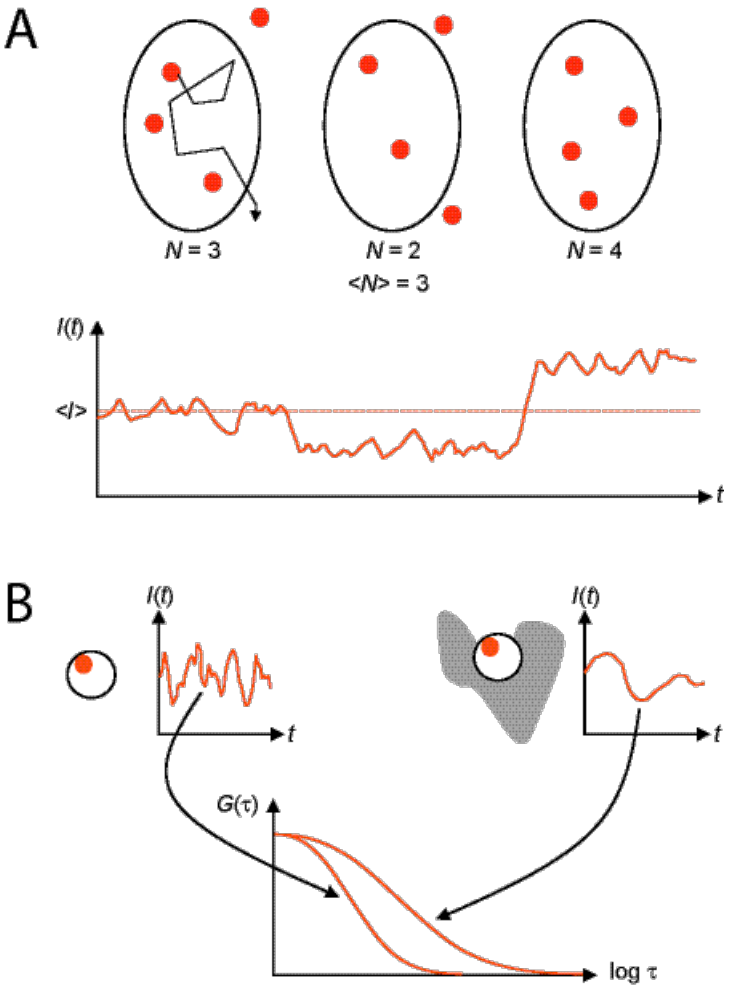

Figure 2.10 Fluorescence correlation spectroscopy (FCS). A: diffusion induces fluctuation of the number of molecules in the focus and thus fluctuations in fluorescence intensity. B: Small molecules generate short fluctuations and rapidly decaying correlation functions, while larger complexes generate longer fluctuations and slowly decaying correlation functions.

An additional method to analyze interactions of two molecules (not applied in this work) is fluorescence resonance energy transfer (FRET). Here two molecules of interest are labeled with different fluorophores, chosen in such a way that the emission spectrum of one fluorophore (the donor) overlaps with the absorption spectrum of the other (the acceptor). If the two molecule species bind to each other, and the two fluorophores are brought into close proximity (within 1-10 nm), the energy of the absorbed light can be transferred directly the donor to the acceptor. Thus, when the complex is illuminated at the excitation wavelength of the donor, light is emitted at the emission wavelength of the acceptor. This approach can be applied to monitor the assembly of the transcription machinery or the binding of histone-modifying enzymes (Day et al., 2001) (Yamagoe et al., 2003).

2.4.3 Quantification of structural changes

Structural changes of cellular components due to cell cycle, apoptosis or treatment with drugs can often be visualized, but the detection of small changes or the evaluation of its statistical relevance require quantification with sophisticated image analysis methods. Two methods have been applied in this work to analyze structural changes of interphase chromatin, namely

image correlation spectroscopy (ICS) and spatially resolved scaling analysis (SRSA) (Fejes Tóth et al., 2004a).

Image correlation spectroscopy is based on the same principle as FCS. However, the correlation analysis is carried out in space and not in time. Thus, large objects defined by a certain fluorescence intensity level have longer correlation lengths, while small objects lead to shortly decaying correlation function (Fig. 2.11). This method is appropriate to determine the characteristic size of statistically organized objects.

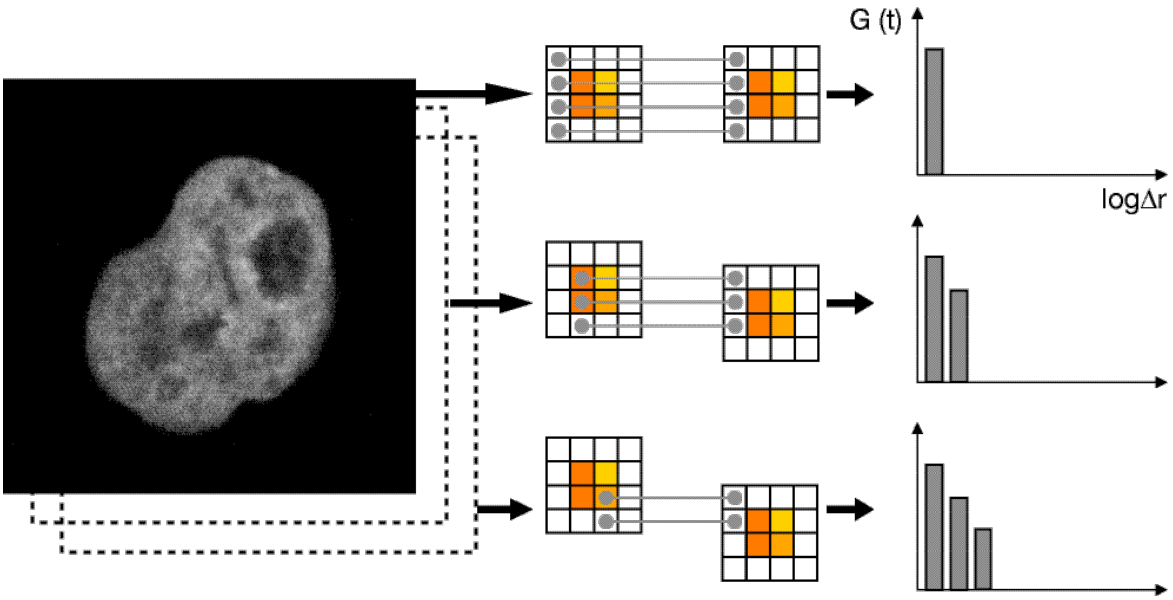

Figure 2.11 Image correlation spectroscopy (ICS). Confocal images of HeLa cell nuclei stably expressing H2A-YFP were used to calculate the correlation length of chromatin structures within the nucleus. The intensity of each pixel of an image is multiplied with the intensity of the overlaying pixel of a duplicate image and the sum of all products from one image is computed and plotted. Then the image is shifted pixel by pixel and overlaying intensities are multiplied again. As the distance increases the intensity correlation decreases (Fejes Tóth et al., 2004a).

Spatially resolved scaling analysis describes the local fractal dimension D_f, i.e., how the mass/intensity inside an area grows with increasing size of this area. A more homogeneous mass distribution leads to a higher fractal dimension, as the mass increases with a higher exponent of the side length of the area. The determination of the fractal dimension of two pixels within one image is shown in Fig. 2.12. By visual inspection no difference can be seen, however, the fractal dimensions differ significantly. Thus small structural changes can be detected.

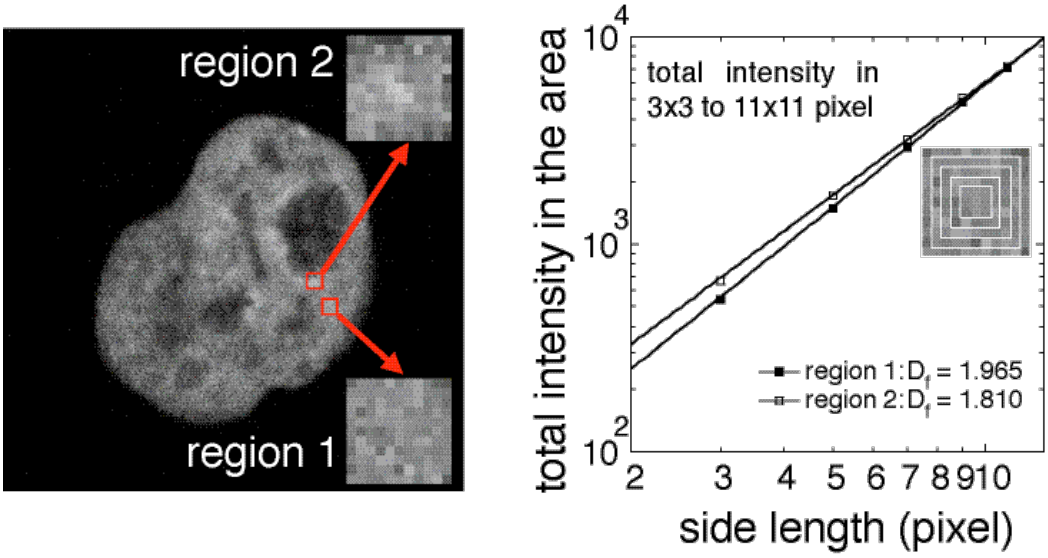

Figure 2.12 Spatially resolved scaling analysis (SRSA) describes how the mass/intensity inside an area grows with increasing size of the area: Boxes of different side lengths are analyzed around each pixel and the total intensity inside the boxes is plotted in dependence of the side length on a double logarithmic plot. Data points are fitted linearly and the slope of the line gives the fractal dimension of the given pixel. i.e. the exponent with which the mass depends on the box side length (Fejes Tóth et al., 2004a).

2.5 Summary

Taken together, there is a large variety of methods both *in vitro* and *in vivo* to analyze chromatin structure. Most of the methods used in this work possess many advantages that make them indispensable in elucidating *in vivo* chromatin structure. AFM has a high resolution comparable to electron microscopy but can be applied under physiological buffer conditions without further fixation or staining procedures. Molecules nevertheless need to be attached on the surface to be able to visualize them. AUC is a versatile method for determining the shape and weight of molecules in physiological buffers and can be used to analyze structural changes caused by changes in buffer composition, pH or by addition of other molecules. Analysis and interpretation of the data required a sophisticated software, which has been developed in the past few years. While conformational changes of the chromatin fiber can be detected by AUC, the method lacks the molecular resolution provided by AFM. Thus, by combining the two techniques, complementary information on chromatin conformation can be obtained (Kepert et al., 2004). Both AUC and AFM are *in vitro* methods. To study the *in vivo* conformation, non-invasive fluorescence microscopy using autofluorescently labeled proteins have been used. For *in vivo* measurements confocal microscopy possesses the necessary resolution to analyze subnuclear structures. This allows the application of methods to analyze mobility and association of macromolecules and nuclear structures and to determine fine structural changes using image analysis methods.

Summary

In eukaryotes, the DNA is packed by small basic proteins called histones. An octamer consisting of two copies of each histone H2A, H2B, H3, and H4 forms a protein core around which 147 base pairs of DNA are wrapped 1.65 times. This complex is termed the nucleosome. The nucleosomes are connected through the DNA and associate under physiological conditions into a compact fiber with approximately 30 nm diameter. In the nucleus, this 30 nm fiber is organized into higher order structures. Different factors and processeslike histone modifications, linker histone H1, histone chaperones and chromatin assembly factors influence the level of compaction of the nucleosome chain, which in turn regulates gene expression. In this work different aspects of processes and factors and their impact on chromatin conformation were analyzed.

First, it was found using atomic or scanning force microscopy (AFM/SFM) that binding of the linker histone H1to chromatin stabilizes a smaller entry-exit angle of the DNA at the nucleosome. This change could lead to a compaction of the 30 nm fiber resulting in transcriptional repression.

Secondly, as a process leading to decondensation of chromatin and to transcriptional activation, the acetylation of the N-terminal histone tails was analyzed. For this purpose the interphase chromatin structure was analyzed in vivo by confocal laser scanning microscopy and quantitative image analysis methods. After incubation with the histone deacetylase inhibitor Trichostatin A (TSA), the increased histone acetylation induces a reversible global decondensation and a more homogeneous chromatin distribution.

In a third part of the work, the interaction of the histone chaperone NAP1 (nucleosome assembly factor 1) with histones was analyzed. NAP1 is involved in nuclear import and the ordered deposition of the histone H2A·H2B dimer on DNA. In addition, it has been related to changes of the chromatin conformation during transcription. Therefore, the functional association state of NAP1 and its effect on chromatin structure were analyzed using analytical ultracentrifugation (AUC). Under physiological salt and protein concentrations, NAP1 forms a dimer-octamer equilibrium and binds histones with a 1:1 stoichiometry. If NAP1 is incubated with chromatin, it removes H2A·H2B dimers leading to decondensation of chromatin by increasing the length of the linker DNA.

In connection with the protein transport through nuclear pores, as in the case of NAP1 carrying the H2A·H2B dimer, the association state of the nucleoporin Nup145N was analyzed in collaboration with the laboratory of Prof. Ed Hurt. Using AUC it could be shown that Nup145N is present as a monomer.

Zusammenfassung

In Eukaryonten ist die DNA mit Hilfe von Komplexen kleiner basischer Proteine verpackt, die als Histone bezeichnet werden. Ein Oktamer aus jeweils zwei Kopien der Histone H2A, H2B, H3 und H4 bildet einen Proteinkern, um den 147 Basenpaare DNA 1.65 mal gewunden sind. Dieser Komplex wird als Nukleosom bezeichnet. Die Nukleosomen sind durch die DNA verbunden und assoziieren unter physiologischen Bedingungen zu einer kompakten Faser mit etwa 30 nm Durchmesser. Diese 30-Nanometer-Faser ist im Zellkern in weiteren, nicht genau bekannten Strukturen organisiert. Verschiedene Faktoren und Prozesse wie Histon-Modifikationen, Linker-Histon H1, Histon-Chaperone und Chromatin-Assemblierungsfaktoren beeinflußen den Kompaktierungsgrad der Nukleosomenkette, der wiederum die Genexpression steuert. In dieser Arbeit wurden verschiedene Aspekte dieser Faktoren und Prozesseund ihr Einfluss auf die Chromatinkonformation untersucht.

Zuerst konnte durch Rasterkraftmikroskopie (AFM/SFM) festgestellt werden, dass die Bindung von H1 die Stabilisierung eines kleineren Eintritts-Austritts-Winkels der DNA am Nukleosom bewirkt. Diese Winkeländerung könnte zu einer kompakteren 30-Nanometer-Faser und dadurch zu einer Repression der Transkription führen.

Zweitens wurde als ein Prozess, der zu einem Übergang des Chromatins in eine offene und transkriptionsaktive Konformation führt die Modifikation der N-terminalen Histon-Schwänze durch Acetylierung untersucht. Dazu wurde die Interphase-Chromatinstruktur *in vivo* mit konfokaler Fluoreszenzmikroskopie und quantitativer Bildanalyse untersucht. Nach Inkubation mit dem Histondeacetylaseinhibitor Trichostatin A (TSA) und erhöhter Histonacetylierung zeigte sich eine reversibele globale Dekondensierung und gleichmässigere Verteilung des Chromatins.

In einem dritten Teil der Arbeit wurden die Wechselwirkungen des Histon-Chaperons NAP1 (Nucleosome Assembly Factor 1) mit Histonen untersucht. NAP1 spielt beim nuklearen Import und bei der geordneten Deposition des Histon-H2A·H2B-Dimers auf die DNA eine Rolle. Außerdem wird es mit Änderungen der Chromatinkonformation bei der Transkription in Verbindung gebracht. Deshalb wurde der funktionelle Assoziationszustand von NAP1 und seine Wirkung auf die Chromatinstruktur mit analytischer Ultrazentrifugation (AUZ) untersucht. Unter physiologischen Salzbedingungen und Proteinkonzentrationen bildet NAP1 ein Dimer-Oktamer-Gleichgewicht und bindet Histone mit einer 1:1-Stöchiometrie. Wenn NAP1 mit Chromatin inkubiert wird, entfernt es einzelne H2A·H2B-Dimere und bewirkt dadurch eine Dekondensierung des Chromatins, durch eine Verlängerung der Linkerlänge.

In Verbindung mit dem Transport von Proteinen durch Kernporen in den Zellkern, wie ihn NAP1 für das H2A·H2B-Dimer durchführt, wurde in einem Kollaborationsprojekt mit der Arbeitsgruppe von Prof. Ed Hurt der Assoziationszustand des Nukleoporin Nup145N untersucht. Dabei konnte mittels AUZ gezeigt werden, dass Nup145N als Monomer vorliegt.

Schwarz, P. M., Felthauser, A., Fletcher, T. M., and Hansen, J. C. (1996). Reversible oligonucleosome self-association: dependence on divalent cations and core histone tail domains. *Biochemistry* 35, 4009-4015.

Sobel, R. E., Cook, R. G., Perry, C. A., Annunziato, A. T., and Allis, C. D. (1995). Conservation of deposition-related acetylation sites in newly synthesized histones H3 and H4. *Proc Natl Acad Sci U S A* 92, 1237-1241.

Spencer, V. A., and Davie, J. R. (1999). Role of covalent modifications of histones in regulating gene expression. *Gene* 240, 1-12.

Stevenson, D. S., and Jarvis, P. (2003). Chromatin silencing: RNA in the driving seat. *Curr Biol* 13, R13-15.

Strohner, R., Wachsmuth, M., Dachauer, K., Mazurkiewicz, J., Rippe, K., and Längst, G. (2004). A 'loop recapture' mechanism for nucleosome remodelling by ISWI containing complexes. *manuscript submitted.*

Suto, R. K., Clarkson, M. J., Tremethick, D. J., and Luger, K. (2000). Crystal structure of a nucleosome core particle containing the variant histone H2A.Z. *Nat Struct Biol* 7, 1121-1124.

Taddei, A., Roche, D., Sibarita, J. B., Turner, B. M., and Almouzni, G. (1999). Duplication and maintenance of heterochromatin domains. *J Cell Biol* 147, 1153-1166.

Thomas, J. O. (2001). HMG1 and 2: architectural DNA-binding proteins. *Biochem Soc Trans* 29, 395-401.

Travers, A. (1999). The location of the linker histone on the nucleosome. *Trends Biochem Sci* 24, 4-7.

Trieschmann, L., Martin, B., and Bustin, M. (1998). The chromatin unfolding domain of chromosomal protein HMG-14 targets the N-terminal tail of histone H3 in nucleosomes. *Proc Natl Acad Sci USA* 95, 5468-5473.

Tschiersch, B., Hofmann, A., Krauss, V., Dorn, R., Korge, G., and Reuter, G. (1994). The protein encoded by the Drosophila position-effect variegation suppressor gene Su(var)3-9 combines domains of antagonistic regulators of homeotic gene complexes. *Embo J* 13, 3822-3831.

Tse, C., and Hansen, J. C. (1997). Hybrid trypsinized nucleosomal arrays: identification of multiple functional roles of the H2A/H2B and H3/H4 N-termini in chromatin fiber compaction. *Biochemistry* 36, 11381-11388.

Tyler, J. K. (2002). Chromatin assembly. Cooperation between histone chaperones and ATP-dependent nucleosome remodeling machines. *Eur J Biochem* 269, 2268-2274.

Tyler, J. K., Adams, C. R., Chen, S. R., Kobayashi, R., Kamakaka, R. T., and Kadonaga, J. T. (1999). The RCAF complex mediates chromatin assembly during DNA replication and repair. *Nature* 402, 555-560.

References

Adams, C. R., and Kamakaka, R. T. (1999). Chromatin assembly: biochemical identities and genetic redundancy. *Curr Opin Genet Dev* 9, 185-190.

Ahmad, K., and Henikoff, S. (2002). Histone H3 variants specify modes of chromatin assembly. *Proc Natl Acad Sci USA* 99 Suppl 4, 16477-16484.

Alberts, B., Bray, D., Lewis, J., Raff, M., Roberts, K., and Watson, J. D. (1994). Molecular biology of the cell, 3rd Edition edn (New York & London, Garland Publishing, Inc.).

Allfrey, V. G., Faulkner, R., and Mirsky, A. E. (1964). Acetylation and methylation of histones and their possible role in the regulation of RNA synthesis. *Proc Natl Acad Sci USA* 51, 786-794.

Archer, S. Y., and Hodin, R. A. (1999). Histone acetylation and cancer. *Curr Opin Genet Dev* 9, 171-174.

Arents, G., Burlingame, R. W., Wang, B.-C., Love, W. E., and Moudrianakis, E. N. (1991). The nucleosomal core histone octamer at 3.1 Å resolution: A triparatite protein assembly and a left-handed superhelix. *Proc Natl Acad Sci USA* 88, 10148-10152.

Asahara, H., Tartare-Deckert, S., Nakagawa, T., Ikehara, T., Hirose, F., Hunter, T., Ito, T., and Montminy, M. (2002). Dual roles of p300 in chromatin assembly and transcriptional activation in cooperation with nucleosome assembly protein 1 in vitro. *Mol Cell Biol* 22, 2974-2983.

Bannister, A. J., Schneider, R., and Kouzarides, T. (2002). Histone methylation: dynamic or static? *Cell* 109, 801-806.

Baylin, S. B., Esteller, M., Rountree, M. R., Bachman, K. E., Schuebel, K., and Herman, J. G. (2001). Aberrant patterns of DNA methylation, chromatin formation and gene expression in cancer. *Hum Mol Genet* 10, 687-692.

Bednar, J., Horowitz, R. A., Grigoryev, S. A., Carruthers, L. M., Hansen, J. C., Koster, A. J., and Woodcock, C. L. (1998). Nucleosomes, linker DNA, and linker histone form a unique structural motif that directs the higher-order folding and compaction of chromatin. *Proc Natl Acad Sci USA* 95, 14173-14178.

Beisel, C., Imhof, A., Greene, J., Kremmer, E., and Sauer, F. (2002). Histone methylation by the Drosophila epigenetic transcriptional regulator Ash1. *Nature* 419, 857-862.

Bird, A. P., and Wolffe, A. P. (1999). Methylation-induced repression — belts, braces, and chromatin. *Cell* 99, 451-454.

Bjerling, P., Silverstein, R. A., Thon, G., Caudy, A., Grewal, S., and Ekwall, K. (2002). Functional divergence between histone deacetylases in fission yeast by distinct cellular localization and in vivo specificity. *Mol Cell Biol* 22, 2170-2181.

Bonaldi, T., Langst, G., Strohner, R., Becker, P. B., and Bianchi, M. E. (2002). The DNA chaperone HMGB1 facilitates ACF/CHRAC-dependent nucleosome sliding. *Embo J* 21, 6865-6873.

Braunstein, M., Rose, A. B., Holmes, S. G., Allis, C. D., and Broach, J. R. (1993). Transcriptional silencing in yeast is associated with reduced nucleosome acetylation. *Genes Dev* 7, 592-604.

Brower-Toland, B. D., Smith, C. L., Yeh, R. C., Lis, J. T., Peterson, C. L., and Wang, M. D. (2002). Mechanical disruption of individual nucleosomes reveals a reversible multistage release of DNA. *Proc Natl Acad Sci U S A* 99, 1960-1965.

Bustamante, C., and Rivetti, C. (1996). Visualizing Protein-Nucleic Acid Interactions on a Large-Scale with the Scanning Force Microscope. *Annu Rev Biophys Biomol Struct* 25, 395-429.

Bustin, M. (2001). Chromatin unfolding and activation by HMGN(*) chromosomal proteins. *Trends Biochem Sci* 26, 431-437.

Bustin, M., Trieschmann, L., and Postnikov, Y. V. (1995). The HMG-14/-17 chromosomal protein family: architectural elements that enhance transcription from chromatin templates. *Semin Cell Biol* 6, 247-255.

Carruthers, L. M., and Hansen, J. C. (2000). The Core Histone N-termini function independently of linker histones during chromatin condensation. *J Biol Chem* 275, 37285-37290.

Catez, F., Brown, D. T., Misteli, T., and Bustin, M. (2002). Competition between histone H1 and HMGN proteins for chromatin binding sites. *EMBO Rep* 3, 760-766.

Chadwick, B. P., and Willard, H. F. (2001). A novel chromatin protein, distantly related to histone H2A, is largely excluded from the inactive X chromosome. *J Cell Biol* 152, 375-384.

Chang, L., Loranger, S. S., Mizzen, C., Ernst, S. G., Allis, C. D., and Annunziato, A. T. (1997). Histones in transit: cytosolic histone complexes and diacetylation of H4 during nucleosome assembly in human cells. *Biochemistry* 36, 469-480.

Chen, H., Li, B., and Workman, J. L. (1994). A histone-binding protein, nucleoplasmin, stimulates transcription factor binding to nucleosomes and factor-induced nucleosome disassembly. *Embo J* 13, 380-390.

Cheung, E., Zarifyan, A. S., and Kraus, W. L. (2002). Histone H1 represses estrogen receptor alpha transcriptional activity by selectively inhibiting receptor-mediated transcription initiation. *Mol Cell Biol* 22, 2463-2471.

Cheutin, T., McNairn, A. J., Jenuwein, T., Gilbert, D. M., Singh, P. B., and Misteli, T. (2003). Maintenance of stable heterochromatin domains by dynamic HP1 binding. *Science* 299, 721-725.

Chimura, T., Kuzuhara, T., and Horikoshi, M. (2002). Identification and characterization of CIA/ASF1 as an interactor of bromodomains associated with TFIID. *Proc Natl Acad Sci U S A* 99, 9334-9339.

Chiurazzi, P., Pomponi, M. G., Pietrobono, R., Bakker, C. E., Neri, G., and Oostra, B. A. (1999). Synergistic effect of histone hyperacetylation and DNA demethylation in the reactivation of the FMR1 gene. *Hum Mol Genet* 8, 2317-2323.

Clapier, C. R., Langst, G., Corona, D. F., Becker, P. B., and Nightingale, K. P. (2001). Critical role for the histone H4 N terminus in nucleosome remodeling by ISWI. *Mol Cell Biol* 21, 875-883.

Clark, D. J., and Thomas, J. O. (1988). Differences in the binding of H1 variants to DNA. Cooperativity and linker-length related distribution. *Eur J Biochem* 178, 225-233.

Clark, I. D., MacManus, J. P., Banville, D., and Szabo, A. G. (1993). A study of sensitized lanthanide luminescence in an engineered calcium-binding protein. *Anal Biochem* 210, 1-6.

Cleard, F., Delattre, M., and Spierer, P. (1997). SU(VAR)3-7, a Drosophila heterochromatin-associated protein and companion of HP1 in the genomic silencing of position-effect variegation. *Embo J* 16, 5280-5288.

Coffee, B., Zhang, F., Warren, S. T., and Reines, D. (1999). Acetylated histones are associated with FMR1 in normal but not fragile X-syndrome cells. *Nat Genet* 22, 98-101.

Corona, D. F., Clapier, C. R., Becker, P. B., and Tamkun, J. W. (2002). Modulation of ISWI function by site-specific histone acetylation. *EMBO Rep* 3, 242-247.

Costanzi, C., and Pehrson, J. R. (1998). Histone macroH2A1 is concentrated in the inactive X chromosome of female mammals. *Nature* 393, 599-601.

Cote, J., Quinn, J., Workman, J. L., and Peterson, C. L. (1994). Stimulation of GAL4 derivative binding to nucleosomal DNA by the yeast SWI/SNF complex. *Science* 265, 53-60.

Cress, W. D., and Seto, E. (2000). Histone deacetylases, transcriptional control, and cancer. *J Cell Physiol* 184, 1-16.

Davey, C. A., Sargent, D. F., Luger, K., Maeder, A. W., and Richmond, T. J. (2002). Solvent mediated interactions in the structure of the nucleosome core particle at 1.9 Å resolution. *J Mol Biol* 319, 1097-1113.

Day, R. N., Periasamy, A., and Schaufele, F. (2001). Fluorescence resonance energy transfer microscopy of localized protein interactions in the living cell nucleus. *Methods* 25, 4-18.

de Ruijter, A. J., van Gennip, A. H., Caron, H. N., Kemp, S., and van Kuilenburg, A. B. (2003). Histone deacetylases (HDACs): characterization of the classical HDAC family. *Biochem J* 370, 737-749.

Dorigo, B., Schalch, T., Bystricky, K., and Richmond, T. J. (2003). Chromatin Fiber Folding: Requirement for the Histone H4 N-terminal Tail. *J Mol Biol* 327, 85-96.

Dou, Y., Bowen, J., Liu, Y., and Gorovsky, M. A. (2002). Phosphorylation and an ATP-dependent process increase the dynamic exchange of H1 in chromatin. *J Cell Biol* 158, 1161-1170.

Dou, Y., and Gorovsky, M. A. (2000). Phosphorylation of linker histone H1 regulates gene expression in vivo by creating a charge patch. *Mol Cell* 6, 225-231.

Dressel, U., Renkawitz, R., and Baniahmad, A. (2000). Promoter specific sensitivity to inhibition of histone deacetylases: implications for hormonal gene control, cellular differentiation and cancer. *Anticancer Res* 20, 1017-1022.

Drouin, R., Angers, M., Dallaire, N., Rose, T. M., Khandjian, W., and Rousseau, F. (1997). Structural and functional characterization of the human FMR1 promoter reveals similarities with the hnRNP-A2 promoter region. *Hum Mol Genet* 6, 2051-2060.

Eissenberg, J. C., and Elgin, S. C. (2000). The HP1 protein family: getting a grip on chromatin. *Curr Opin Genet Dev* 10, 204-210.

Emili, A., Schieltz, D. M., Yates, J. R., 3rd, and Hartwell, L. H. (2001). Dynamic interaction of DNA damage checkpoint protein Rad53 with chromatin assembly factor Asf1. *Mol Cell* 7, 13-20.

Fanti, L., Berloco, M., Piacentini, L., and Pimpinelli, S. (2003). Chromosomal distribution of heterochromatin protein 1 (HP1) in Drosophila: a cytological map of euchromatic HP1 binding sites. *Genetica* 117, 135-147.

Fanti, L., Giovinazzo, G., Berloco, M., and Pimpinelli, S. (1998). The heterochromatin protein 1 prevents telomere fusions in Drosophila. *Mol Cell* 2, 527-538.

Fazzari, M. J., and Greally, J. M. (2004). Epigenomics: beyond CpG islands. *Nat Rev Genet* 5, 446-455.

Fejes Tóth, K., Knoch, T. A., Wachsmuth, M., Stöhr, M., Frank-Stöhr, M., Bacher, C. P., Müller, G., and Rippe, K. (2004a). Trichostatin A induced histone acetylation causes decondensation of interphase chromatin. *J Cell Sci* 117, 4277-4287.

Fejes Tóth, K., Mazurkiewicz, J., and Rippe, K. (2004b). Association states of the nucleosome assembly protein 1 and its complexes with histones. submitted.

Finch, J. T., and Klug, A. (1976). Solenoidal model for superstructure in chromatin. *Proc Natl Acad Sci USA* 73, 1897-1901.

Fischle, W., Wang, Y., and Allis, C. D. (2003a). Histone and chromatin cross-talk. *Curr Opin Cell Biol* 15, 172-183.

Fischle, W., Wang, Y., Jacobs, S. A., Kim, Y., Allis, C. D., and Khorasanizadeh, S. (2003b). Molecular basis for the discrimination of repressive methyl-lysine marks in histone H3 by Polycomb and HP1 chromodomains. *Genes Dev* 17, 1870-1881.

Fuks, F., Hurd, P. J., Deplus, R., and Kouzarides, T. (2003). The DNA methyltransferases associate with HP1 and the SUV39H1 histone methyltransferase. *Nucleic Acids Res* 31, 2305-2312.

Gaillard, P. H., Martini, E. M., Kaufman, P. D., Stillman, B., Moustacchi, E., and Almouzni, G. (1996). Chromatin assembly coupled to DNA repair: a new role for chromatin assembly factor I. *Cell* 86, 887-896.

Gasser, S. M. (2002). Visualizing chromatin dynamics in interphase nuclei. *Science* 296, 1412-1416.

Gerasimova, T. I., Byrd, K., and Corces, V. G. (2000). A chromatin insulator determines the nuclear localization of DNA. *Mol Cell* 6, 1025-1035.

Gilbert, N., Boyle, S., Fiegler, H., Woodfine, K., Carter, N. P., and Bickmore, W. A. (2004). Chromatin architecture of the human genome; gene-rich domains are enriched in open chromatin fibers. *Cell* 118, 555-566.

Hamiche, A., Kang, J. G., Dennis, C., Xiao, H., and Wu, C. (2001). Histone tails modulate nucleosome mobility and regulate ATP-dependent nucleosome sliding by NURF. *Proc Natl Acad Sci U S A* 98, 14316-14321.

Hansen, J. C. (2002). Conformational dynamics of the chromatin fiber in solution: determinants, mechanisms, and functions. *Annu Rev Biophys Biomol Struct* 31, 361-392.

Hansma, H. G., Sinsheimer, R. L., Groppe, J., Bruice, T. C., Elings, V., Gurley, G., Bezanilla, M., Mastrangelo, I. A., Hough, P. V. C., and Hansma, P. K. (1993). Recent advances in atomic force microscopy of DNA. *Scanning* 15, 296-299.

Haushalter, K. A., and Kadonaga, J. T. (2003). Chromatin assembly by DNA-translocating motors. *Nat Rev Mol Cell Biol* 4, 613-620.

Havas, K., Flaus, A., Phelan, M., Kingston, R., Wade, P. A., Lilley, D. M., and Owen-Hughes, T. (2000). Generation of superhelical torsion by ATP-dependent chromatin remodeling activities. *Cell* 103, 1133-1142.

Hayes, J. J., and Hansen, J. C. (2001). Nucleosomes and the chromatin fiber. *Current Opinion in Genetics & Development* 11, 124-129.

Hecht, A., Laroche, T., Strahl-Bolsinger, S., Gasser, S. M., and Grunstein, M. (1995). Histone H3 and H4 N-termini interact with SIR3 and SIR4 Proteins: A molecular model for the formation of heterochromatin in yeast. *Cell* 80, 583-592.

Hendzel, M. J., Wei, Y., Mancini, M. A., Van Hooser, A., Ranalli, T., Brinkley, B. R., Bazett-Jones, D. P., and Allis, C. D. (1997). Mitosis-specific phosphorylation of histone H3 initiates primarily within pericentromeric heterochromatin during G2 and spreads in an ordered fashion coincident with mitotic chromosome condensation. *Chromosoma* 106, 348-360.

Herrera, J. E., Sakaguchi, K., Bergel, M., Trieschmann, L., Nakatani, Y., and Bustin, M. (1999). Specific acetylation of chromosomal protein HMG-17 by PCAF alters its interaction with nucleosomes. *Mol Cell Biol* 19, 3466-3473.

Herrera, J. E., West, K. L., Schiltz, R. L., Nakatani, Y., and Bustin, M. (2000). Histone H1 is a specific repressor of core histone acetylation in chromatin. *Mol Cell Biol* 20, 523-529.

Ishimi, Y., Hirosumi, J., Sato, W., Sugasawa, K., Yokota, S., Hanaoka, F., and Yamada, M. (1984). Purification and initial characterization of a protein which facilitates assembly of nucleosome-like structure from mammalian cells. *Eur J Biochem* 142, 431-439.

Ito, T., Bulger, M., Kobayashi, R., and Kadonaga, J. T. (1996). Drosophila NAP-1 is a core histone chaperone that functions in ATP- facilitated assembly of regularly spaced nucleosomal arrays. *Mol Cell Biol* 16, 3112-3124.

Ito, T., Tyler, J. K., and Kadonaga, J. T. (1997). Chromatin assembly factors: a dual function in nucleosome formation and mobilization? *Genes Cells* 2, 593-600.

Jin, P., and Warren, S. T. (2000). Understanding the molecular basis of fragile X syndrome. *Hum Mol Genet* 9, 901-908.

Kepert, J. F., Fejes Tóth, K., Caudron, M., Mücke, N., Langowski, J., and Rippe, K. (2003). Conformation of reconstituted mononucleosomes and effect of linker histone H1 binding studied by scanning force microscopy. *Biophys J* 85, 4012-4022.

Kepert, J. F., Mazurkiewicz, J., Heuvelman, G., Fejes Tóth, K., and Rippe, K. (2004). Exchange of histone H2A·H2B dimer in nucleosomes and chromatin fibers by nucleosome assembly protein 1. submitted.

Kimura, A., and Horikoshi, M. (2004). Partition of distinct chromosomal regions: negotiable border and fixed border. *Genes Cells* 9, 499-508.

Klochendler-Yeivin, A., Fiette, L., Barra, J., Muchardt, C., Babinet, C., and Yaniv, M. (2000). The murine SNF5/INI1 chromatin remodeling factor is essential for embryonic development and tumor suppression. *EMBO Rep* 1, 500-506.

Kouzarides, T. (1999). Histone acetylases and deacetylases in cell proliferation. *Curr Opin Genet Dev* 9, 40-48.

Kouzarides, T. (2000). Acetylation: a regulatory modification to rival phosphorylation? *Embo J* 19, 1176-1179.

Krude, T. (1995). Chromatin assembly factor 1 (CAF-1) colocalizes with replication foci in HeLa cell nuclei. *Exp Cell Res* 220, 304-311.

Lengauer, C., Kinzler, K. W., and Vogelstein, B. (1998). Genetic instabilities in human cancers. *Nature* 396, 643-649.

Leonhardt, H., and Cardoso, M. C. (2000). DNA methylation, nuclear structure, gene expression and cancer. *J Cell Biochem Suppl* Suppl, 78-83.

LeRoy, G., Orphanides, G., Lane, W. S., and Reinberg, D. (1998). Requirement of RSF and FACT for transcription of chromatin templates in vitro. *Science* 282, 1900-1904.

Leuba, S. H., Bustamante, C., Zlatanova, J., and van Holde, K. (1998). Contributions of linker histones and histone H3 to chromatin structure: scanning force microscopy studies on trypsinized fibers. *Biophys J* 74, 2823-2829.

Li, G., Chandler, S. P., Wolffe, A. P., and Hall, T. C. (1998). Architectural specificity in chromatin structure at the TATA box in vivo: nucleosome displacement upon beta-phaseolin gene activation [In Process Citation]. *Proc Natl Acad Sci U S A* 95, 4772-4777.

Li, Y., Kirschmann, D. A., and Wallrath, L. L. (2002). Does heterochromatin protein 1 always follow code? *Proc Natl Acad Sci U S A* 99 Suppl 4, 16462-16469.

Lippincott-Schwartz, J., and Patterson, G. H. (2003). Development and use of fluorescent protein markers in living cells. *Science* 300, 87-91.

Litt, M. D., Simpson, M., Gaszner, M., Allis, C. D., and Felsenfeld, G. (2001a). Correlation between histone lysine methylation and developmental changes at the chicken beta-globin locus. *Science* 293, 2453-2455.

Litt, M. D., Simpson, M., Recillas-Targa, F., Prioleau, M. N., and Felsenfeld, G. (2001b). Transitions in histone acetylation reveal boundaries of three separately regulated neighboring loci. *Embo J* 20, 2224-2235.

Loyola, A., and Almouzni, G. (2004). Histone chaperones, a supporting role in the limelight. *Biochim Biophys Acta* 1677, 3-11.

Luger, K., Mäder, A. W., Richmond, R. K., Sargent, D. F., and Richmond, T. J. (1997a). Crystal structure of the nucleosome core particle at 2.8 Å resolution. *Nature* 389, 251-260.

Luger, K., Rechsteiner, T. J., Flaus, A. J., Waye, M. M., and Richmond, T. J. (1997b). Characterization of nucleosome core particles containing histone proteins made in bacteria. *J Mol Biol* 272, 301-311.

Luger, K., and Richmond, T. J. (1998). DNA binding within the nucleosome core. *Curr Opin Struct Biol* 8, 33-40.

Lusser, A., and Kadonaga, J. T. (2003). Chromatin remodeling by ATP-dependent molecular machines. *Bioessays* 25, 1192-1200.

Lutzmann, M. K., R.; Stangl, K.; Stelter, P.; Fejes Tóth, K.; , and Boettcher, B. H., E. (2004). Biochemical and structural analyses of the large nucleoporins Nup157, Nup188 and Nup192 (Heidelberg).

Mahlknecht, U., Ottmann, O. G., and Hoelzer, D. (2000). When the band begins to play: histone acetylation caught in the crossfire of gene control. *Mol Carcinog* 27, 268-271.

Mariadason, J. M., Corner, G. A., and Augenlicht, L. H. (2000). Genetic reprogramming in pathways of colonic cell maturation induced by short chain fatty acids: comparison with trichostatin A, sulindac, and curcumin and implications for chemoprevention of colon cancer. *Cancer Res* 60, 4561-4572.

Martini, E., Roche, D. M., Marheineke, K., Verreault, A., and Almouzni, G. (1998). Recruitment of phosphorylated chromatin assembly factor 1 to chromatin after UV irradiation of human cells. *J Cell Biol* 143, 563-575.

Mattei, M.-G., Luciani, J. (2002). Heterochromatin, from Chromosome to Protein. *wwwbiologiaunibait/eca/NEWSLETTER/NS-11/02-Articlehtml*.

Meijsing, S. H., and Ehrenhofer-Murray, A. E. (2001). The silencing complex SAS-I links histone acetylation to the assembly of repressed chromatin by CAF-I and Asf1 in Saccharomyces cerevisiae. *Genes Dev* 15, 3169-3182.

Minc, E., Courvalin, J. C., and Buendia, B. (2000). HP1gamma associates with euchromatin and heterochromatin in mammalian nuclei and chromosomes. *Cytogenet Cell Genet* 90, 279-284.

Misteli, T., Gunjan, A., Hock, R., Bustin, M., and Brown, D. T. (2000). Dynamic binding of histone H1 to chromatin in living cells. *Nature* 408, 877-881.

Miyaji-Yamaguchi, M., Kato, K., Nakano, R., Akashi, T., Kikuchi, A., and Nagata, K. (2003). Involvement of nucleocytoplasmic shuttling of yeast Nap1 in mitotic progression. *Mol Cell Biol* 23, 6672-6684.

Moshkin, Y. M., Armstrong, J. A., Maeda, R. K., Tamkun, J. W., Verrijzer, P., Kennison, J. A., and Karch, F. (2002). Histone chaperone ASF1 cooperates with the Brahma chromatin-remodelling machinery. *Genes Dev* 16, 2621-2626.

Munakata, T., Adachi, N., Yokoyama, N., Kuzuhara, T., and Horikoshi, M. (2000). A human homologue of yeast anti-silencing factor has histone chaperone activity. *Genes Cells* 5, 221-233.

Munshi, N., Merika, M., Yie, J., Senger, K., Chen, G., and Thanos, D. (1998). Acetylation of HMG I(Y) by CBP turns off IFN beta expression by disrupting the enhanceosome. *Mol Cell* 2, 457-467.

Nakagawa, T., Bulger, M., Muramatsu, M., and Ito, T. (2001). Multistep chromatin assembly on supercoiled plasmid DNA by nucleosome assembly protein-1 and ATP-utilizing chromatin assembly and remodeling factor. *J Biol Chem* 276, 27384-27391.

Nakayama, J., Rice, J. C., Strahl, B. D., Allis, C. D., and Grewal, S. I. (2001). Role of histone H3 lysine 9 methylation in epigenetic control of heterochromatin assembly. *Science* 292, 110-113.

Nan, X., Cross, S., and Bird, A. (1998). Gene silencing by methyl-CpG-binding proteins. *Novartis Found Symp* 214, 6-16.

Ner, S. S., Blank, T., Perez-Paralle, M. L., Grigliatti, T. A., Becker, P. B., and Travers, A. A. (2001). HMG-D and histone H1 interplay during chromatin assembly and early embryogenesis. *J Biol Chem* 276, 37569-37576.

Nielsen, A. L., Sanchez, C., Ichinose, H., Cervino, M., Lerouge, T., Chambon, P., and Losson, R. (2002). Selective interaction between the chromatin-remodeling factor BRG1 and the heterochromatin-associated protein HP1alpha. *Embo J* 21, 5797-5806.

Orphanides, G., LeRoy, G., Chang, C. H., Luse, D. S., and Reinberg, D. (1998). FACT, a factor that facilitates transcript elongation through nucleosomes. *Cell* 92, 105-116.

Orphanides, G., Wu, W. H., Lane, W. S., Hampsey, M., and Reinberg, D. (1999). The chromatin-specific transcription elongation factor FACT comprises human SPT16 and SSRP1 proteins. *Nature* 400, 284-288.

Osada, S., Sutton, A., Muster, N., Brown, C. E., Yates, J. R., 3rd, Sternglanz, R., and Workman, J. L. (2001). The yeast SAS (something about silencing) protein complex contains a MYST-type putative acetyltransferase and functions with chromatin assembly factor ASF1. *Genes Dev* 15, 3155-3168.

Park, Y. J., Dyer, P. N., Tremethick, D. J., and Luger, K. (2004). A new FRET approach demonstrates that the histone variant H2AZ stabilizes the histone octamer within the nucleosome. *J Biol Chem.*

Paro, R. (1990). Imprinting a determined state into the chromatin of Drosophila. *Trends Genet* 6, 416-421.

Peterson, C. L., and Laniel, M. A. (2004). Histones and histone modifications. *Curr Biol* 14, R546-551.

Pfeifer, G. P., Tanguay, R. L., Steigerwald, S. D., and Riggs, A. D. (1990). In vivo footprint and methylation analysis by PCR-aided genomic sequencing: comparison of active and inactive X chromosomal DNA at the CpG island and promoter of human PGK-1. *Genes Dev* 4, 1277-1287.

Philpott, A., Krude, T., and Laskey, R. A. (2000). Nuclear chaperones. *Semin Cell Dev Biol* 11, 7-14.

Polioudaki, H., Kourmouli, N., Drosou, V., Bakou, A., Theodoropoulos, P. A., Singh, P. B., Giannakouros, T., and Georgatos, S. D. (2001). Histones H3/H4 form a tight complex with the inner nuclear membrane protein LBR and heterochromatin protein 1. *EMBO Rep* 2, 920-925.

Polo, S. E., Theocharis, S. E., Klijanienko, J., Savignoni, A., Asselain, B., Vielh, P., and Almouzni, G. (2004). Chromatin assembly factor-1, a marker of clinical value to distinguish quiescent from proliferating cells. *Cancer Res* 64, 2371-2381.

Ramachandran, A., Omar, M., Cheslock, P., and Schnitzler, G. R. (2003). Linker histone H1 modulates nucleosome remodeling by human SWI/SNF. *J Biol Chem* 278, 48590-48601.

Richmond, T. J., and Davey, C. A. (2003). The structure of DNA in the nucleosome core. *Nature* 423, 145-150.

Richon, V. M., Sandhoff, T. W., Rifkind, R. A., and Marks, P. A. (2000). Histone deacetylase inhibitor selectively induces p21WAF1 expression and gene-associated histone acetylation. *Proc Natl Acad Sci USA* 97, 10014-10019.

Rippe, K., Mücke, N., and Langowski, J. (1997). Molecules in motion: Imaging DNA with the scanning force microscope in aqueous solutions. *Bioforum International* 1, 42-44.

Robertson, K. D. (2002). DNA methylation and chromatin - unraveling the tangled web. *Oncogene* 21, 5361-5379.

Robertson, K. D., and Wolffe, A. P. (2000). DNA methylation in health and disease. *Nat Rev Genet* 1, 11-19.

Rodriguez, P., Munroe, D., Prawitt, D., Chu, L. L., Bric, E., Kim, J., Reid, L. H., Davies, C., Nakagama, H., Loebbert, R., *et al.* (1997). Functional characterization of human nucleosome assembly protein-2 (NAP1L4) suggests a role as a histone chaperone. *Genomics* 44, 253-265.

Saveliev, A., Everett, C., Sharpe, T., Webster, Z., and Festenstein, R. (2003). DNA triplet repeats mediate heterochromatin-protein-1-sensitive variegated gene silencing. *Nature* 422, 909-913.

Schiessel, H., Gelbart, W. M., and Bruinsma, R. (2001a). DNA folding: Structural and mechanical properties of the two- angle model for chromatin. *Biophys J* 80, 1940-1956.

Schiessel, H., Widom, J., Bruinsma, R. F., and Gelbart, W. M. (2001b). Polymer reptation and nucleosome repositioning. *Phys Rev Lett* 86, 4414-4417.

Schuck, P. (2003). On the analysis of protein self-association by sedimentation velocity analytical ultracentrifugation. *Anal Biochem* 320, 104-124.

Tyler, J. K., Collins, K. A., Prasad-Sinha, J., Amiott, E., Bulger, M., Harte, P. J., Kobayashi, R., and Kadonaga, J. T. (2001). Interaction between the Drosophila CAF-1 and ASF1 chromatin assembly factors. *Mol Cell Biol* 21, 6574-6584.

Ura, K., Nightingale, K., and Wolffe, A. P. (1996). Differential association of HMG1 and linker histones B4 and H1 with dinucleosomal DNA: structural transitions and transcriptional repression. *Embo J* 15, 4959-4969.

van Holde, K. E. (1989). Chromatin (Heidelberg, Springer).

van Holde, K., and Zlatanova, J. (1996). What determines the folding of the chromatin fiber? *Proceedings of the National Academy of Sciences of the United States of America* 93, 10548-10555.

Van Lint, C., Emiliani, S., and Verdin, E. (1996). The expression of a small fraction of cellular genes is changed in response to histone hyperacetylation. *Gene Expr* 5, 245-253.

Varga-Weisz, P. D., Blank, T. A., and Becker, P. B. (1995). Energy-dependent chromatin accessibility and nucleosome mobility in a cell-free system. *Embo J* 14, 2209-2216.

Vassallo, M. F., and Tanese, N. (2002). Isoform-specific interaction of HP1 with human TAFII130. *Proc Natl Acad Sci U S A* 99, 5919-5924.

Verreault, A., Kaufman, P. D., Kobayashi, R., and Stillman, B. (1996). Nucleosome assembly by a complex of CAF-1 and acetylated histones H3/H4. *Cell* 87, 95-104.

Villar-Garea, A., and Esteller, M. (2004). Histone deacetylase inhibitors: Understanding a new wave of anticancer agents. *Int J Cancer* 112, 171-178.

West, A. G., Gaszner, M., and Felsenfeld, G. (2002). Insulators: many functions, many mechanisms. *Genes Dev* 16, 271-288.

Widom, J. (1998). Structure, dynamics, and function of chromatin in vitro. *Annu Rev Biophys Biomol Struc* 27, 285-327.

Widom, J. (2001). Role of DNA sequence in nucleosome stability and dynamics. *Quart Rev Biophys* 34, 269-324.

Wolffe, A. (1998). Chromatin: Structure and Function, 2 edn (London, Academic Press).

Wolffe, A. P. (1997). Histone H1. *Int J Biochem Cell Biol* 29, 1463-1466.

Workman, J. L., and Kingston, R. E. (1998). Alteration of nucleosome structure as a mechanism of transcriptional regulation. *Annu Rev Biochem* 67, 545-579.

Wouters, F. S., Verveer, P. J., and Bastiaens, P. I. (2001). Imaging biochemistry inside cells. *Trends Cell Biol* 11, 203-211.

Yamagoe, S., Kanno, T., Kanno, Y., Sasaki, S., Siegel, R. M., Lenardo, M. J., Humphrey, G., Wang, Y., Nakatani, Y., Howard, B. H., and Ozato, K. (2003). Interaction of histone acetylases and deacetylases in vivo. *Mol Cell Biol* 23, 1025-1033.

Yoder, J. A., Walsh, C. P., and Bestor, T. H. (1997). Cytosine methylation and the ecology of intragenomic parasites. *Trends Genet* 13, 335-340.

Zhang, Y., and Reinberg, D. (2001). Transcription regulation by histone methylation: interplay between different covalent modifications of the core histone tails. *Genes Dev* 15, 2343-2360.

Zlatanova, J., Caiafa, P., and Van Holde, K. (2000). Linker histone binding and displacement: versatile mechanism for transcriptional regulation. *FASEB J* 14, 1697-1704.

JCS ePress online publication date 3 August 2004

Trichostatin A-induced histone acetylation causes decondensation of interphase chromatin

Katalin Fejes Tóth[1,2], Tobias A. Knoch[1,3], Malte Wachsmuth[1], Monika Frank-Stöhr[4], Michael Stöhr[4], Christian P. Bacher[5], Gabriele Müller[6] and Karsten Rippe[1,2,*]

[1]Kirchhoff-Institut für Physik, AG Molekulare Biophysik, Ruprecht-Karls-Universität Heidelberg, Im Neuenheimer Feld 227, 69120 Heidelberg, Germany
[2]Molekulare Genetik, [3]Biomedizinische Strukturanalyse, [4]Cytometrie, [5]Intelligente Bioinformatiksysteme and [6]Genregulation und DNA-Topologie, Deutsches Krebsforschungszentrum, Im Neuenheimer Feld 280, 69120 Heidelberg, Germany
*Author for correspondence (e-mail: karsten.rippe@kip.uni-heidelberg.de)

Accepted 26 April 2004
Journal of Cell Science 117, 4277-4287 Published by The Company of Biologists 2004
doi:10.1242/jcs.01293

Summary

The effect of trichostatin A (TSA)-induced histone acetylation on the interphase chromatin structure was visualized in vivo with a HeLa cell line stably expressing histone H2A, which was fused to enhanced yellow fluorescent protein. The globally increased histone acetylation caused a reversible decondensation of dense chromatin regions and led to a more homogeneous distribution. These structural changes were quantified by image correlation spectroscopy and by spatially resolved scaling analysis. The image analysis revealed that a chromatin reorganization on a length scale from 200 nm to >1 μm was induced consistent with the opening of condensed chromatin domains containing several Mb of DNA. The observed conformation changes could be assigned to the folding of chromatin during G1 phase by characterizing the effect of TSA on cell cycle progression and developing a protocol that allowed the identification of G1 phase cells on microscope coverslips. An analysis by flow cytometry showed that the addition of TSA led to a significant arrest of cells in S phase and induced apoptosis. The concentration dependence of both processes was studied.

Key words: TSA, Histone deacetylase, Image correlation spectroscopy, Fractal dimension, Cell cycle

Introduction

The reversible (de)acetylation of the N-terminal histone tails by specific histone acetylases and deacetylases (HDAC) is involved in the regulation of gene expression. A correlation of histone acetylation with enhanced transcription was described 40 years ago (Allfrey et al., 1964). For a number of genes, a direct connection with gene expression has been demonstrated (Coffee et al., 1999; Dressel et al., 2000; Grunstein, 1997; Kouzarides, 1999; Richon et al., 2000; Sambucetti et al., 1999), and dysfunction of histone acetylases and HDACs has been associated with different types of cancer (Archer and Hodin, 1999; Cress and Seto, 2000; Kouzarides, 1999; Mahlknecht et al., 2000). Various HDAC inhibitors (HDACi) have been described that induce cell cycle arrest, differentiation, and apoptosis in cell lines. Many of these have potent antitumor activities in vivo (reviewed by Marks et al., 2001; Marks et al., 2000). One of the most effective and best studied HDAC inhibitor is trichostatin A (TSA) (Yoshida et al., 1995; Yoshida et al., 1990). A crystallographic analysis of TSA and a histone deacetylase homologue indicates that TSA interacts reversibly with the HDAC catalytic site preventing binding of the substrate (Finnin et al., 1999; Marks et al., 2001; Marks et al., 2000).

It is widely accepted that histone acetylation is essential to establish a transcriptionally competent state of chromatin (Kadonaga, 1998; Strahl and Allis, 2000; Tse et al., 1998; Zhang et al., 1998). However, the relation between chromatin conformation and histone acetylation is complex and three different effects could be important (Hansen, 2002; Hansen et al., 1998). (1) Acetylation might modulate interactions between histone tails and the DNA. Nonacetylated histone tails carry a large number of positively charged lysine and arginine residues (≈100 per nucleosome) that interact with the negatively charged phosphate groups of the DNA backbone in vitro (Allan et al., 1982; Fletcher and Hansen, 1995; Hansen, 2002; Hansen et al., 1998; van Holde, 1989). However, these electrostatic interactions are highly dependent on ion concentration, and it has been shown that core histone N-termini do not bind stably to DNA at physiological ionic strength (Fletcher and Hansen, 1995; Lee and Hayes, 1998; Usachenko et al., 1994). (2) The histone tails could affect internucleosomal association (Hansen, 2002; Hansen et al., 1998; Luger and Richmond, 1998). An interaction between the positive N-terminal H4 tail and a highly negative region on the exposed H2A-H2B surface has been identified in the crystal structure of the nucleosome (Luger et al., 1997). Again, acetylation of the corresponding lysine residues is likely to weaken this interaction. (3) The histone tail acetylation might also serve as a marker for the binding of other chromosomal proteins that subsequently induce a more open and transcriptionally competent conformation. Binding to histone tails has been described for a number of proteins like NURF, SWI/SNF and RSC (Georgel et al., 1997; Logie et al., 1999), Bdf1 (Ladurner et al., 2003) and NAP-1 (McQuibban et al.,

1998). Furthermore, the acetylation state of histone tails seems to influence both the binding of histone variants (Alvelo-Ceron et al., 2000; Waterborg and Kapros, 2002) and of linker histones (Zlatanova et al., 2000).

In vitro studies of chromatin fiber fragments by analytical ultracentrifugation and electron microscopy demonstrated that histone acetylation induced only moderate conformation changes. At approximately physiological salt concentrations but in the absence of divalent cations the sedimentation coefficient of hyperacetylated fibers was 11-15% smaller (Wang et al., 2001) and the fiber diameter was somewhat reduced (22.1±5.1 nm versus 28.1±5.8 nm) (Annunziato et al., 1988). Although it is frequently assumed or speculated that histone acetylation affects chromatin structure in vivo to create a more 'open' chromatin conformation, direct evidence for this concept is missing. Furthermore, it is currently an open question whether changes in the histone acetylation state on the nucleosome level will affect the higher order organization of the chromatin fiber. Previous in vivo studies show that upon inhibition of acetylation heterochromatin binding protein HP1 reversibly disperses within the nucleus (Maison et al., 2002). However, it is unclear whether this diffuse localization is due to weaker binding of HP1 to heterochromatic regions or if it is correlated with changes in chromatin distribution.

We have studied the effect of TSA-induced histone acetylation on the interphase chromatin conformation by confocal laser scanning microscopy (CLSM). The studies were conducted with HeLa cells stably expressing a fusion protein of histone H2A and enhanced yellow fluorescent protein (H2A-YFP). H2A-YFP is incorporated into chromatin and provides an in vivo fluorescent label that reflects the DNA density as previously demonstrated for H2B-GFP (Bestvater et al., 2002; Kanda et al., 1998; Kimura and Cook, 2001; Weidemann et al., 2003). A reversible decondensation of dense chromatin regions due to histone acetylation was detected. To quantify this effect, two advanced image analysis methods were introduced, namely image correlation spectroscopy (ICS) and spatially resolved scaling analysis (SRSA). They revealed a chromatin reorganization at the micrometer scale consistent with the opening of condensed chromatin domains over several Mb of DNA.

Materials and Methods

Cell culture

The HeLa cell line with autofluorescent histone H2A-YFP was constructed as described (Tobias A. Knoch, Approaching the three-dimensional organisation of the human genome, PhD thesis, Ruprecht-Karls-Universität Heidelberg, 2002). The human histone gene for H2A (GeneBank accession number 83549) was amplified by PCR and inserted into the *Eco*RI-*Bam*HI site of the promoterless plasmid pECFP-1 (Clontech). The *Hin*dIII fragment of simian virus 40 (SV40) was inserted in reverse direction into the *Hin*dIII site of the multiple cloning site of pECFP-1 and the ECFP sequence was replaced with EYFP. The resulting construct pSV-HIII-H2A-EYFP expresses a 376 amino acid fusion protein from the early SV40 promoter and consists of the human H2A gene, a seven amino acid linker and the C-terminal EYFP domain. This plasmid was introduced into HeLa (ATCC: CCL 2) cells with Lipofectamin (Life Technologies, Rockville, MD, USA) and a stable monoclonal cell line was selected with 500 μg/ml G418 (Life Technologies). The same untransfected HeLa cell line was used for control experiments and fluorescence-activated cell sorting (FACS) analysis of the cell cycle. Cells were grown in RPMI 1640 (Life Technologies) supplemented with 10% FCS in a humidified atmosphere under 5% CO_2 at 37°C. Cells were allowed to attach for at least 24 hours before treatment with TSA (Sigma-Aldrich, St Louis, MO, USA).

Western blot analysis

Treatment was conducted for 2, 6, 12 and 24 hours with final TSA concentrations of 12.5, 25, 50, 100, 200 ng/ml, respectively. Cells were washed and lysed by incubation on ice for 30 minutes in a PBS buffer supplemented with 1% NP-40, 0.5% sodium desoxycholate, 0.1% SDS and protease inhibitors. The lysate was centrifuged at >10,000 ***g*** and the protein concentration of the supernatant determined by ELISA (enzyme-linked immunosorbent assay) using BCA Protein Assay Reagent (Pierce, Rockford, IL, USA). Equal amounts of total protein were loaded on a 12% SDS-polyacrylamide gel, blotted, and detected with anti-GFP antibody (Abcam, Cambridge, UK) that also binds to the YFP domain and anti-lamin antibody (Santa Cruz, Santa Cruz, CA, USA).

Flow cytometry

For FACS (fluorescence-activated cell sorting) analysis cells were incubated with 0, 50, or 100 ng/ml TSA for 12 hours or 24 hours, trypsinized and washed twice with PBS containing 0.02% (w/v) EDTA. Cells were fixed with ethanol, stored at –20°C for at least one day, and stained with a solution containing 5 μM DAPI (4,6-diamidino-2-phenylindole; Serva, Heidelberg, Germany) and 5 μM SR101 (sulforhodamine 101; Eastman Kodak, Rochester, USA) as a protein counterstain (Stoehr et al., 1976). The FACS analysis of cell cycle and apoptosis was carried out on a Cytofluorograph System 30-L (Ortho Diagnostics Systems Inc., Westwood, MA, USA) using the UV lines (351-364 nm) of an argon laser as described previously (Dean and Jett, 1974; Stoehr et al., 1976). The dependence of apoptosis on the concentration of TSA was analyzed by assuming that the percentage of cells in apoptosis (a) goes linear with the fractional saturation (θ) of HDACs with TSA according to Eqn 1. The baseline (b) corresponds to the percentage of apoptotic cells present in the absence of TSA and (c) is the proportionality constant:

$$a = c \times \theta + b \,. \quad (1)$$

The parameter θ is calculated from the binding equilibrium given by Eqn 2 with a dissociation constant K_d and cooperativity factor α:

$$\theta = \frac{[\mathrm{TSA}]^{\alpha}}{K_d^{\alpha} + [\mathrm{TSA}]^{\alpha}} \,. \quad (2)$$

For H2A-YFP fluorescence intensity measurements by flow cytometry, cells were resuspended in medium after trypsinisation and measured with a Profile I flow cytometer (Coulter Corporation, Hialeah, FL, USA). Excitation was carried out with the 488 nm line of an argon laser and emission was measured with a band pass filter at 515-535 nm.

Fluorescence microscopy analysis

For CLSM (confocal laser scanning microscopy) cells expressing H2A-YFP were seeded on modified cell culture dishes that had an etched grid of 175 μm spacing fixed onto the bottom of the dish. Three-dimensional stack images of living cells were acquired in the presence and absence of TSA with a Leica TCS SP2 confocal laser scanning microscope (Leica Microsystems, Mannheim, Germany) using a HCXPlApo 63×1.32 oil objective lens. An Argon laser was used for excitation at 514 nm and emission was detected at 526-651 nm. For DAPI imaging excitation was carried out with a laser diode at 405 nm and emission was recorded at 420-480 nm. Images of 512×512 pixels in stacks of about 70 frames with a pixel size of

70×70×210 nm and 12 bit intensity resolution were taken with four times averaging. For in vivo imaging, cells were held in a humid incubation chamber with temperature and CO_2 control (PeCon, Erbach-Bach, Germany). FRAP (fluorescence recovery after photobleaching) experiments were conducted using the Leica software. Small regions of the cell nuclei were bleached at maximal intensity at 514 nm four times and postbleach images were taken every 2 seconds for 2 minutes. The intensity in an arbitrary area within the bleached region was plotted against time. The freely mobile fraction R of H2A-YFP was determined from the fluorescence in the bleached region after a plateau was reached (F_∞) and the fluorescence before (F_i) and after (F_0) bleaching according to Eqn 3. The fluorescence intensity outside the bleached region decreased to approximately 80% during the postbleach observation time. This was corrected by dividing F_∞ by the correction factor γ=0.8:

$$R = \frac{F_\infty/\gamma - F_0}{F_i - F_0}. \quad (3)$$

For cell cycle analysis on coverslips, cells were fixed in 4% paraformaldehyde with 2% sucrose for 15 minutes, permeabilized with 0.5% Triton X-100 for 5 minutes, and blocked with 4% BSA/PBS for 20 minutes at room temperature. Staining was conducted with 5.0 μM DAPI, 180 mM Tris-HCl pH 7.5 and 50% (v/v) glycerol for ⩾24 hours at 4°C. Images were taken with an Axiovert S100 TV wide-field fluorescence microscope (Zeiss, Jena, Germany). The image acquisition and processing was performed on about 4000 cells per coverslip with OpenLab software (Improvision, Lexington, MA, USA) in a procedure similar to that described previously (Bestvater et al., 2002). For image analysis the background was subtracted and a threshold was set to allow recognition of cell nuclei and calculation of a binary mask. Objects of a size and intensity below that of intact nuclei were disregarded. The DNA content of each nucleus was determined from the integrated DAPI intensity and plotted in a histogram to derive the cell cycle stage. The fluorescence lifetime of H2A-YFP in the absence and presence of TSA was measured as described previously (Hanley et al., 2002).

Image segmentation

For the quantitative analysis by spatially resolved scaling analysis (SRSA) the region of the nucleus was segmented from the CLSM stacks using the image processing software Tikal developed by C. Bacher and M. Gebhard. A 3D anisotropic diffusion filter that uses an 'edge stopping' function based on Tuckey's biweight error norm was applied (Black et al., 1998). This algorithm preserves object boundaries sharper than ordinary Gaussian filters. After noise reduction by 3D anisotropic diffusion, segmentation of the cells based on a global threshold method was conducted. The outlines of nuclei were obtained by Canny edge detection on the previously segmented images (Canny, 1986). For image correlation spectroscopy the segmentation was carried out by setting a threshold after Gaussian smoothing, which resulted in a binary mask leaving the nuclei blank.

Image correlation spectroscopy (ICS)

The typical length of spatial chromatin density fluctuations and their amplitude were determined by calculating the radial spatial autocorrelation function of pixel intensities in CLSM images. Only intensities from pixels in the nuclei were taken. Based on the two-dimensional autocorrelation function according to

$$G(\Delta x,\Delta y) = \frac{\langle I(x+\Delta x, y+\Delta y) I(x,y)\rangle}{\langle I(x,y)\rangle^2} - 1 \quad (4)$$

[see Petersen (Petersen, 2001) for a review of ICS theory and applications] the radial correlation function $G(r)$ was computed by averaging over all displacements with $r=\sqrt{\Delta x^2+\Delta y^2}$. The resulting spectra were fitted with Gaussian functions using Origin (OriginLab, Northampton, MA, USA). The full width at half maximum of the shortest decay was identified as the correlation length of chromatin subcompartments while the $G(0, 0)$ value from the fit was used as normalized variance of the chromatin density fluctuations.

Spatially resolved scaling analysis (SRSA)

The local and thus spatially resolved behavior of the chromatin mass distribution in three-dimensional CLSM image stacks was investigated by computing the weighted local fractal dimension D_f (Kaye, 1989; Tobias A. Knoch, Approaching the three-dimensional organisation of the human genome, PhD thesis, Ruprecht-Karls-Universität Heidelberg, 2002; Rodríguez-Iturbe and Rinaldo, 1997). D_f is the exponent that related the mass or pixel intensity $M(l)$ of a cubic measurement volume to the side length l of this volume:

$$M(l) \sim l^{D_f}. \quad (5)$$

Each image stack with a pixel size of 70×70×210 nm was placed in a grid of 70×70×70 nm for isotropic spatial measurements. The intensity values were summed up for three-dimensional boxes with up to l=11 grid elements around all image pixels belonging to the segmented nucleus. To account for pixels in the box not belonging to the segmented volume, the total intensity in the box was weighted with the fraction of nuclear pixels. D_f was calculated by linear regression for $3 \leqslant l \leqslant 11$.

Results

TSA cell cycle effects were dependent on concentration and incubation time

Cell cycle effects were examined by FACS analysis to determine the total DNA content per cell after DAPI staining. Thirteen independent experiments each in triplicate were averaged. Upon treatment with TSA for 12 hours a weak arrest in G1 (increase by 11.4±8.2% at 50 ng/ml TSA and 10.6±6.3% at 100 ng/ml TSA) and an arrest in the G2/M (increase by 29.7±29.2% at 50 ng/ml TSA and 59.4±28.8% at 100 ng/ml TSA) stage was observed (Fig. 1A,B). By contrast, after 24 hours incubation, TSA caused a strong arrest in S phase in a concentration-dependent manner (increase by 42.4±16.8% at 50 ng/ml TSA and 73±24% at 100 ng/ml TSA) (Fig. 1C,D). Upon longer incubation, cells continued to progress through the cell cycle indicating that TSA induced an arrest but did not block the cells at a specific cell cycle position. The HeLa control cells and the HeLa-H2A-YFP cell line were indistinguishable with respect to the effect of TSA on cell cycle progression.

Simultaneous inhibition of different HDACs induced apoptosis

Effects of TSA on apoptosis were also analyzed by FACS using DAPI staining. The fraction of apoptotic cells was quantified at different TSA concentrations (Fig. 2). The data showed a concentration dependence with a maximal fraction of apoptotic cells of about 20% at TSA concentrations ⩾200 ng/ml (660 nM). A fit of the data to a simple binding equilibrium was conducted according to Eqns 1 and 2 with α=1. In this model only one class of TSA binding sites exists and the percentage of apoptotic cells is dependent on the saturation of these sites

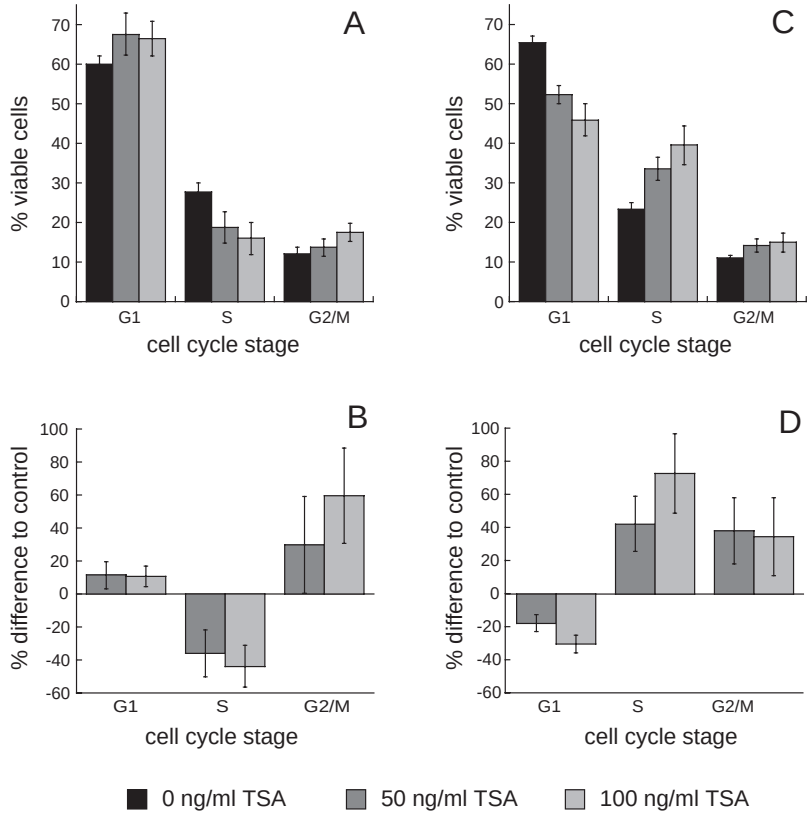

Fig. 1. Effect of TSA on the cell cycle as analyzed by FACS. Black bars, control cells; dark gray bars, cells treated with 50 ng/ml TSA; light gray bars, cells treated with 100 ng/ml TSA. The overall changes in the distribution after (A) 12 hours and (C) 24 hours, and the change weighted with the fraction of cells in the given cell cycle stage after (B) 12 hours and (D) 24 hours are shown.

with TSA (dashed line in Fig. 2). The scaling factor c in Eqn 1 accounts for the detachment of apoptotic cells from the culture dish so that a plateau value at 20% is reached. It is assumed that the probability of an apoptotic cell to detach from the dish is independent of the TSA concentration and that the time course of apoptosis is significantly shorter than the TSA incubation time of 24 hours. Furthermore, cellular uptake of TSA and equilibration to its concentration in the medium are fast on this time scale as inferred from the kinetics of TSA effects on gene expression (Mariadason et al., 2000). In Fig. 2, the fit with α=1 showed systematic deviations from the data with a value for the apparent dissociation constant of K_d=700 nM. If α was allowed to vary, the fit was significantly better and values of K_d=310 nM and α=3.2 were obtained (continuous line in Fig. 2). Thus, the concentration dependence of TSA-induced apoptosis was not simply proportional to the saturation of HDACs with TSA, but showed a rather sharp transition around a concentration of ≈300 nM (≈100 ng/μl) TSA. This behavior suggests an induction of apoptosis by TSA that would require simultaneous inhibition of three HDACs.

TSA increased the amount of H2A-YFP incorporated into chromatin

A quantitative analysis by flow cytometry revealed that the TSA-treated cells showed an up to two-fold increase of H2A-YFP fluorescence intensity that correlated with the TSA concentration as expected for a simple binding equilibrium (Fig. 3A, Eqn 2 with α=1). The apparent dissociation constant was K_d=500 nM (150 ng/ml) reflecting the TSA concentration at which the fluorescence intensity reached half of the maximum value. At a concentration of 100 ng/ml TSA, as used for imaging, a 40±3% higher fluorescence intensity was observed compared to the control cells. The differences in the cell cycle distribution for control cells (G1: 65.4±5.2%, S: 23.4±5.0%, G2/M 11.0±2.3%) and TSA-treated cells (G1: 45.9±11.0%, S: 39.5±13.6%, G2/M: 15.0±6.4%) can only partly account for this effect: assuming a DNA content of 1 n (G1), 1.5 n (S) and 2 n (G2M) the average DNA content and fluorescence per cell would only increase by ≈10%. Measurements by in vivo fluorescence lifetime imaging experiments yielded almost identical fluorescence lifetimes of 2.92±0.18 nseconds and 2.89±0.37 nseconds in the absence and presence of TSA, respectively. Therefore, the increased fluorescence is due to a higher H2A-YFP concentration and not related to changes of the photophysical properties of the YFP-tag. Indeed, a western blot analysis showed that the total amount of H2A-YFP increased significantly (Fig. 3B). From a quantification of band intensities, a twofold increase at 100 ng/ml TSA and 24 hours incubation time is estimated. However, it should be noted that the western blot signal does

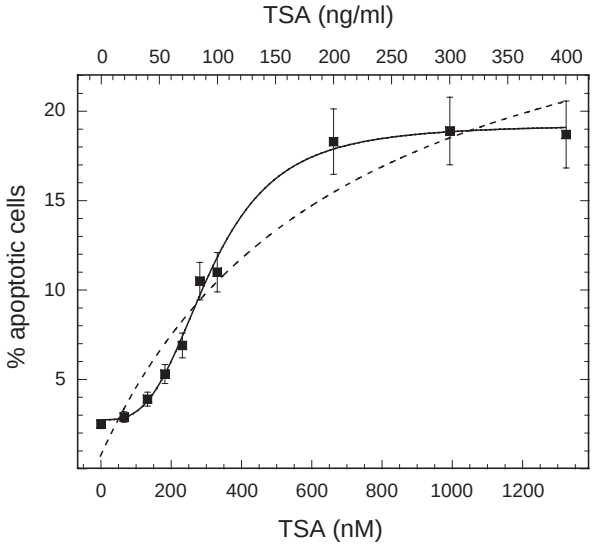

Fig. 2. Concentration dependence of TSA induced apoptosis. TSA caused an increase in apoptosis in a concentration-dependent manner after incubation for 24 hours, as revealed by the FACS analysis. A fit of the data to a model in which apoptosis reflects the binding of TSA to a single class of independent binding sites (Eqn 2, α=1) showed a systematic error (dashed line). By contrast, a good fit of the data was obtained with a cooperativity factor of α=3.2 (solid line).

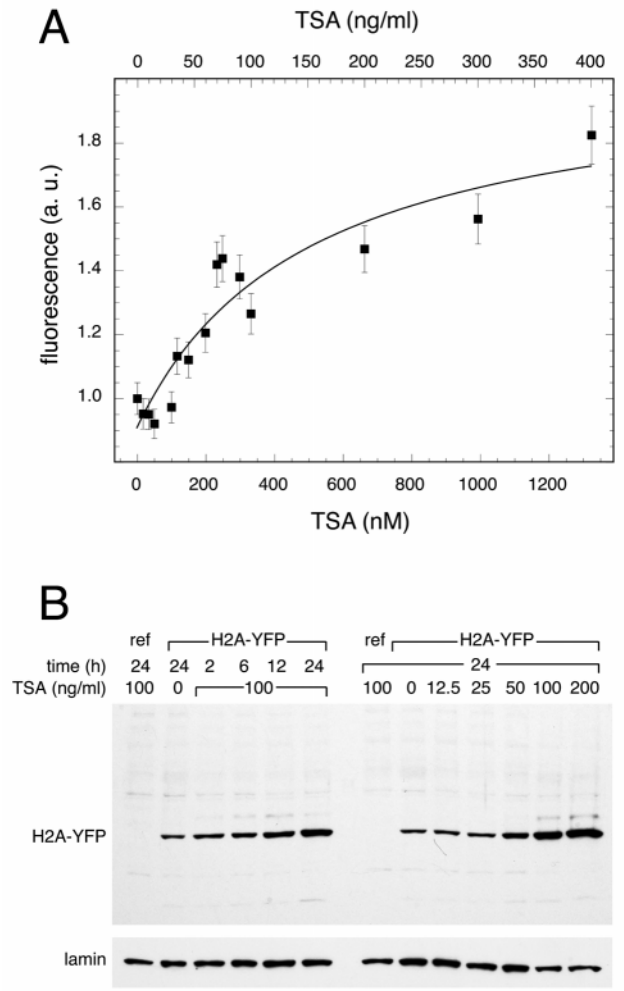

Fig. 3. Effects of TSA on H2A-YFP expression. (A) H2A-YFP fluorescence intensity increased upon TSA treatment. Cells were incubated with the indicated TSA concentrations for 24 hours and H2A-YFP fluorescence was measured by FACS analysis. The fluorescence intensity of untreated cells was set to 1 and the relative fluorescence increase was plotted. (B) Western blot analysis of H2A-YFP protein expression relative to that of lamin. The H2A-YFP concentration increased with longer incubation times (left) and higher TSA concentrations (right).

not display a linear response to concentration and that the 40% increase in H2A-YFP fluorescence determined by FACS analysis is more reliable. The FRAP analysis of the cells revealed that TSA had no significant effect on the ratio of incorporated to free H2A-YFP. Average values for the fraction of free H2A-YFP determined according to Eqn 3 for 15 cells were 11.1±4.5% (control) and 17.1±5.9% (100 ng/ml TSA, 24 hours). Thus, the TSA-treated cells had an approximately 30% higher concentration of chromatin-incorporated H2A-YFP, when differences in the cell cycle stage distribution were taken into consideration and the concentration of H2A-YFP in the cytosol was assumed to be constant.

TSA induced a reversible decondensation of interphase chromatin

The effect of TSA was studied with H2A-YFP-expressing cells by CLSM to detect a reorganization of interphase chromatin. Cells were incubated with 100 ng/ml TSA for 24 hours. Under these conditions a significant increase of acetylation of histone H4 was visible on Triton-acid urea gels (data not shown) as described previously (Hoshikawa et al., 1994). The cell density was reduced to about 50%. On the CLSM images of the control cells dense chromatin regions are seen as brighter areas around the nucleolus and close to the nuclear membrane because of a higher local density of H2A-YFP. Upon TSA treatment these dense regions vanished and a more homogeneous chromatin distribution was observed (Fig. 4A,C). To confirm that the observed changes correlate with changes in the DNA distribution, DAPI images of the same cells were taken after fixation. Cells showed a somewhat altered structure probably a result of fixation but the more homogeneous distribution of DNA upon TSA treatment was still apparent (Fig. 4B,D). DAPI-stained images of control HeLa cells were also studied. In these cells TSA had a similar effect on the DNA distribution as in the H2A-YFP-expressing cells. Thus, it can be excluded that an increased incorporation of H2A-YFP (see above) caused decondensation of the chromatin.

To test whether the conformational changes induced by TSA were reversible and on which time scale they occurred, the effect of adding and removing TSA was studied (Fig. 5). After TSA addition cells were imaged every 30 minutes. Significant changes were detected after about 4 hours (Fig. 5B). Upon removal of TSA dense chromatin areas reappeared after further incubation for 4 hours (Fig. 5C). This indicates that TSA, inhibits HDACs reversibly and that chromatin recondenses again if the TSA concentration is sufficiently reduced.

Determining the cell cycle stage on coverslips

Since the significant increase of S phase cells upon TSA treatment could obscure a comparison of the interphase chromatin conformation, a method was developed to identify the cell cycle stage of a given cell on microscopic images. Cell were grown on coverslips with an etched grid, and living cells were imaged with CLSM using H2A-YFP as a chromatin marker (Fig. 6A). Their positions on the grid were recorded for later identification and cells were fixed and stained with DAPI. Phase contrast (Fig. 6B) and DAPI (Fig. 6C) images were acquired with an inverse epifluorescence microscope. Integrated DAPI intensities per nucleus of ≈4000 cells were plotted (Fig. 6D). Then the cell cycle stage of single cells was determined from their position in the histogram. For the quantitative image analysis only cells within the full width at half maximum from the G1 peak were used.

Quantification of changes in chromatin morphology

The structural differences of the interphase chromatin conformation due to TSA-induced histone acetylation were quantified by image correlation spectroscopy (ICS) and by spatially resolved scaling analysis (SRSA). Both methods revealed a significant effect of increased histone acetylation on the nuclear structure and allowed a quantitative description of the interphase chromatin distribution. About 30 cells treated with TSA and 60 control cells were evaluated. The ICS analysis based on images of the YFP fluorescence from living cells (Fig. 4) yielded correlation lengths of 2.56±0.07 μm

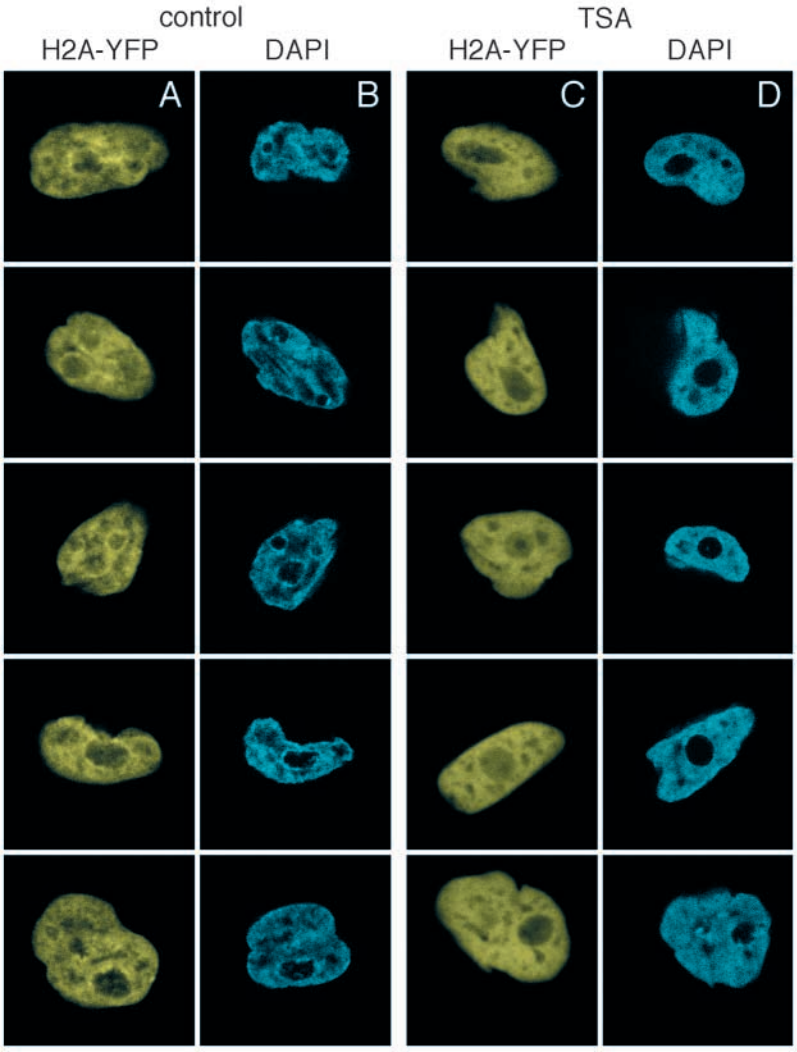

Fig. 4. TSA-induced changes of interphase chromatin morphology. HeLa cells stably expressing H2A-YFP were treated with 100 ng/ml TSA for 24 hours. 28 μm×28 μm (400×400 pixel) images are shown. Image intensities were normalized to the same average value. (A) Nuclei of control cells imaged in vivo with H2A-YFP. Dense chromatin areas were seen as brighter spots around the nucleolus and close to the nuclear membrane. (B) Fixed and DAPI-stained images of the same nuclei as in A. (C) TSA-treated cells imaged in vivo with H2A-YFP. The chromatin distribution was more homogeneous and most of the dense chromatin disappeared. (D) Fixed and DAPI-stained images of the same nuclei as in C.

(+TSA) and 1.27±0.07 μm (control) and an intensity variance of 0.045±0.004 (+TSA) and 0.055±0.003 (control) (Fig. 7). Thus, in TSA-treated cells chromatin density fluctuations on distances >1 μm were significantly longer and with a lower intensity variance, indicative of a more homogeneous distribution. This qualitative difference was also found in DAPI images of fixed H2A-YFP-expressing cells (Fig. 4B,D) with correlation lengths of 1.22±0.07 μm (+TSA) and 0.75±0.07 μm (control). The same HeLa cell line but without H2A-YFP displayed similar values of 1.49±0.07 μm (+TSA) and 0.88±0.07 μm (control) showing that decondensation did not result from the higher incorporation of H2A-YFP. The about two-fold longer correlation length obtained for the in vivo H2A-YFP images might be due to fast chromatin movements during imaging and/or artifacts induced by the fixation of cells.

On a local scale <800 nm, i.e. below the above-mentioned correlation lengths, the SRSA histograms based on images of the H2A-YFP fluorescence from living cells showed clear peaks at 2.815 (+TSA) and 2.415 (control, Fig. 8). The distributions had a standard deviation of σ=0.046 (+TSA) and 0.065 (control) around the peak when fit with a Gaussian function. The rather large differences indicate that because of decondensation of chromatin, the local chromatin density distribution of TSA-treated cells was more similar to a homogeneously filled volume for which one would get a fractal dimension of 3. Again very similar results were obtained for the local fractal dimension when analyzing the DNA distribution in DAPI-stained images of fixed H2A-YFP cells (Fig. 4B,D). Peaks at 2.823 (+TSA) and 2.537 (control) were observed, which had widths of σ=0.032 (+TSA) and 0.071 (control).

Discussion

TSA affects cell cycle progression

It has been reported that TSA induces an arrest in G1 or G2/M phase (Hoshikawa et al., 1994; Inokoshi et al., 1999; Yamashita et al., 2003; Yoshida and Beppu, 1988). While a moderate arrest of cells in G1 and G2/M was observed in our experiments after an incubation time of 12 hours at 50 and 100 ng/ml, a more pronounced arrest in S phase was apparent if cells were incubated for 24 hours in the presence of the same TSA concentrations. Thus, for certain combinations of TSA concentrations and incubation times, a previously not observed strong arrest in S phase was induced. The HeLa cells studied here required about 18.5 hours to complete one cell cycle (Tobias A. Knoch, Approaching the three-dimensional organisation of the human genome, PhD thesis, Ruprecht-Karls-Universität Heidelberg, 2002), which is fast compared to other cell lines. Experiments conducted with a slower growing HeLa cell line showed no significant arrest in S phase after 24 hours (data not shown) the effect of TSA on cell cycle progression might be related to the growth rate.

The above results indicate that it was important to select cells in G1 phase for the image analysis in order to separate differences in cell cycle progression from structural changes in interphase chromatin. While the cell cycle stage can be determined by immunostaining using cell cycle-specific marker proteins, a more direct and reliable method is determining the DNA content. This was done for single cells on the coverslip by calculating the integrated DAPI intensities after fixation. It allowed the assignment of the cell cycle stage to single cells previously imaged in vivo. As compared to the FACS analysis a broadening of the distribution was observed (Fig. 3D). The differences to the FACS histograms are probably related to the potentially

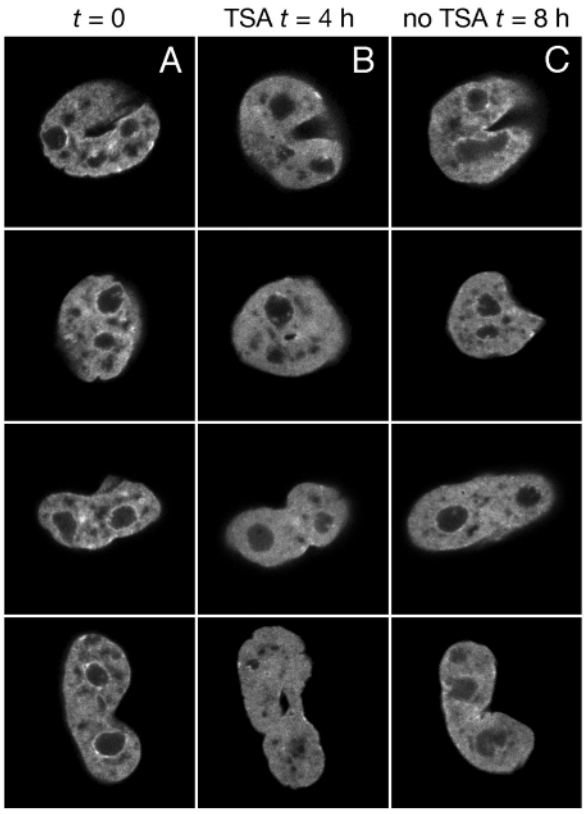

Fig. 5. Reversibility of TSA-induced chromatin decondensation. CLSM images of the same cell nuclei before treatment with TSA (A), after incubation with 100 ng/ml TSA for 4 hours (B), and after changing to a medium without TSA and incubation for another 4 hours (C). The effect of TSA is reversible since dense chromatin regions reappeared after washing out TSA.

incomplete or reduced excitation of nuclear regions outside the focal plane, the fixation procedure (paraformaldehyde versus ethanol) and the different algorithm used for the analysis. Nevertheless, the method applied here allows the analysis of the cell cycle stage and the reliable identification of G1 phase cells in the microscope by a direct determination of the DNA content.

TSA-induced apoptosis and H2A-YFP expression

Previous studies suggest that apoptosis caused by TSA treatment is preceded by histone hyperacetylation (Lee et al., 1996) and requires new protein synthesis (Medina et al., 1997). The concentration-dependent effects of TSA on apoptosis deviated significantly from a simple model, in which the number of apoptotic cells reflects the saturation of a single HDAC by TSA (Fig. 2). However, an excellent fit of the apoptosis data was obtained for a model that assumes a cooperative concentration dependence of TSA on HDAC activity. Since the structural analysis of the catalytic HDAC center shows only the reversible binding of one TSA molecule (Finnin et al., 1999) this apparent cooperativity cannot be explained by the facilitated binding of multiple TSA molecules to a single HDAC protein. Therefore, the results indicate that induction of apoptosis requires the simultaneous inhibition of different HDACs. From the data in Fig. 2 a cooperativity factor of α=3.2 was derived, which suggests that the simultaneous inhibition of HDAC activity at three different targets can lead to apoptosis. To date 17 human genes have been identified encoding HDACs. Eleven of these genes – members of so-called class I and II are inhibited by TSA (Johnstone, 2002). Thus, the simultaneous involvement of multiple HDACs in a complex cellular process such as apoptosis seems very possible.

In the presence of 100 ng/ml TSA the average H2A-YFP intensity per cell increased by about 40% after 24 hours (Fig. 6A) without any detectable change in the fluorescence properties as inferred from fluorescence lifetime measurements. This effect is mainly due to an increased expression of H2A-YFP protein as demonstrated by western blot analysis (Fig. 6B) and would correspond to an approximately 30% higher H2A-YFP concentration in the nucleus when accounting for differences in the cell cycle distribution. It has been shown that a number of viral promoters such as SV40, MMTV, CMV or MLP are induced by TSA up to three- to fourfold. (Dressel et al., 2000). Thus, a moderate TSA dependent induction of H2A-YFP expression is not surprising.

Within the accuracy of the measurement, the fraction of free H2A-YFP did not increase significantly as shown by FRAP experiments, indicating that the additional H2A-YFP protein is either incorporated into chromatin or that the concentration of H2A-YFP in the cytosol is increased. Since the analysis of DAPI-stained HeLa control cells without H2A-YFP showed a similar TSA-dependent decondensation as the HeLa H2A-YFP cell line, it can be excluded that the small difference in the H2A-YFP expression level contributes to the observed chromatin reorganization.

Histone acetylation and large scale chromatin decondensation

The TSA concentration at which the HDAC activity is reduced by 50%, the IC_{50} value, has been measured in vitro to be between 1.4 to 38 nM for different HDACs (Buggy et al., 2000; Furumai et al., 2001; Hoffmann et al., 2001; Yoshida et al., 1990). We have used concentrations about one order of magnitude above the IC_{50} values (100 ng/ml or 330 nM TSA) to assure a significant inhibition of HDAC activity. Treatment of the cells for several hours resulted in a visible decondensation of bona fide heterochromatic areas and led to a more homogeneous distribution of chromatin. Upon removal of TSA the effect was almost completely reversed after about 4 hours. This is consistent with previous findings that TSA binds reversibly to the active center of HDACs and acts as a competitive inhibitor (Finnin et al., 1999; Yoshida et al., 1995; Yoshida et al., 1990).

Effects of TSA on histone acetylation and gene expression have been observed within 30 minutes indicating that the uptake of TSA into the nucleus is fast on the time scale of the experiments conducted here (Mariadason et al., 2000). Previous studies demonstrated that two histone fractions exist with different kinetics of acetylation and deacetylation (Covault and Chalkley, 1980; Sun et al., 2001; Sun et al., 2003; Zhang and Nelson, 1988). About 10-15% of the histones are

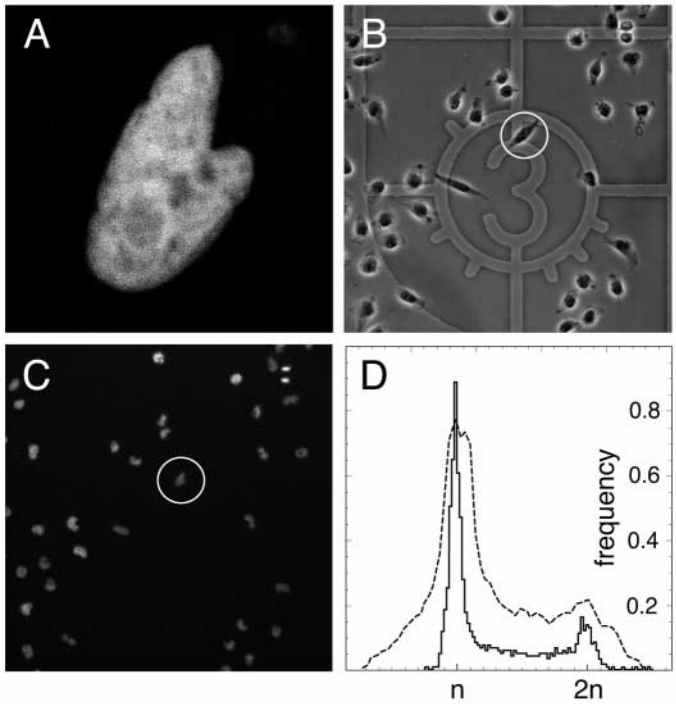

Fig. 6. Determination of the cell cycle stage of investigated cells. (A) In vivo CLSM images of HeLa cell nuclei expressing H2A-YFP. (B) Phase contrast image of fixed, DAPI-stained cells were taken with an inverse fluorescence microscope. The white circle shows the cell imaged in A. (C) DAPI image of the same area as in B. (D) Comparative histogram of cells analyzed by FACS (solid line) and on coverslips (dashed line). DAPI intensities of the imaged nuclei were plotted and the cell cycle stage of single cells was determined from their position in the histogram.

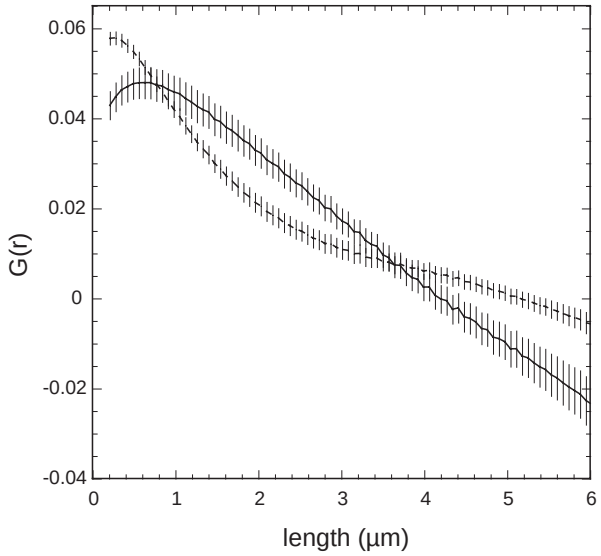

Fig. 7. ICS analysis of TSA-induced decondensation. Both for and The spatial radial autocorrelation function was calculated and averaged over 60 control cells (dashed line) and 30 TSA-treated cells (solid line).

acetylated and deacetylated with a half-time ($t_{1/2}$) of about 3-8 minutes, whereas for the bulk of histones acetylation has a $t_{1/2}$ between 200 and 400 minutes, and deacetylation a $t_{1/2}$ of 30-150 minutes. From the kinetics of the reversible chromatin conformation changes observed here it appears that for complete (de)condensation the fraction of histones with a slower rate on the time scale of several hours has to be acetylated or deacetylated.

Acetylation of histone tails appears to have only moderate effects on the conformation of the 30 nm chromatin fiber in vitro and a small reduction of sedimentation coefficient and fiber diameter has been reported (Annunziato et al., 1988; Wang et al., 2001). Other more indirect effects would involve modulating the binding of chromatin-associated proteins like HP1 (Maison et al., 2002), the recruitment of chromatin remodeling complexes (Georgel et al., 1997; Logie et al., 1999) or the exchange of regular core histones with histone variants like histone H3.3, H2AX and macroH2A (Ausio et al., 2001; Hazzouri et al., 2000; Janicki et al., 2004). The chromatin reorganization described here consists of structural changes up to the μm range and must therefore reflect the three-dimensional arrangement of the chromatin fiber in the nucleus rather than its local structure. It is of interest to know whether changes in the mass density or flexibility of the 30 nm fiber would have significant effects on its higher order folding, and we are currently examining this question by computer simulations.

Quantification of confocal images by ICS and SRSA

The ICS analysis evaluates the spatial distribution of the pixel intensity from the computation of the correlation function given in Eqn 4. In general, a specific chromatin compaction state is characterized by a non-random distribution of regions with higher and/or lower chromatin densities at certain average distances in the nucleus. This will lead to a corresponding correlation and/or anticorrelation of the intensity values, and the dimensions of given chromatin substructures can be derived from the decomposition of the correlation function in Fig. 7. The most prominent feature is the correlation length of the smallest component for which values of 2.56 μm (+ TSA) and 1.27 μm (control) were determined. Thus, on lengths above 1 μm a decondensation of chromatin upon TSA treatment was demonstrated with ICS. The correlation length of density fluctuations can be assigned to the average size of chromatin subcompartments in the order of 1.3 μm for control cells. In TSA-treated cells the length increased by a factor of two while the fluctuations showed a lower intensity variance of 0.045 as compared to 0.055 in the control. This behavior reflects the dissolution of dense chromatin domains that contain several Mb of DNA.

In the second approach introduced here for a quantitative description of the chromatin condensation state, the local fractal dimension over the whole nucleus is calculated. This method, designated as spatially resolved scaling analysis or SRSA, determines the exponent D_f, i.e. the fractal dimension, with which the sum of all pixel intensities increases with the side length l of an observation cube around a given pixel. For a completely homogenous distribution D_f=3 will be obtained, since the volume of a cube increases with the third power of its length. However, if structures exist that have intensity fluctuations in the order of the length scale studied, the sum of all pixel intensities will increase with an exponent of D_f<3 when plotted against the length l of the observation cube. Thus, by

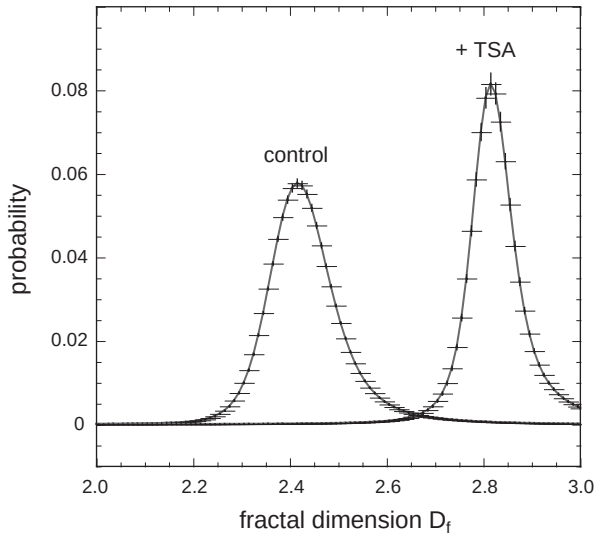

Fig. 8. Spatially resolved scaling analysis (SRSA) of TSA-induced chromatin decondensation. The averaged distribution of the local fractal dimension D_f was computed for both control and TSA-treated cells.

analyzing the average fractal dimension D_f of the density distribution on a local scale between the optical resolution limit of 200 nm and 800 nm, the chromatin organization in general and the decondensation of chromatin after TSA treatment can be characterized. The observed increase of D_f from 2.415 (control) to 2.815 (+TSA) suggests that the topology of chromatin changes significantly in the 0.2 to 0.8 μm scale with respect to loop size and/or folding pattern upon hyperacetylation (Cremer and Cremer, 2001; Tobias A. Knoch, Approaching the three-dimensional organisation of the human genome, PhD thesis, Ruprecht-Karls-Universität Heidelberg, 2002; Knoch, 2003).

ICS and SRSA clearly identify a large chromatin decondensation by TSA from averaging an ensemble of cells in G1 phase. They are complementary in the sense that the ICS analysis reveals the decondensation of chromatin subcompartments with a correlation length of 1.3 μm upon increased histone acetylation, while the SRSA results demonstrate that a more homogeneous chromatin distribution is also induced on a length scale between 0.2 to 0.8 μm. Both methods are suitable for the quantification of a wide range of structural changes not only of chromatin but also of other cellular structures. In addition, they provide an approach to quantitatively compare simulated chromatin arrangements with experimentally determined distributions from microscopic images.

Concluding remarks

By in vivo labeling of specific chromatin loci with an autofluorescent Lac repressor it has been demonstrated that transcriptional activation is accompanied by a large-scale unfolding of chromatin (Janicki et al., 2004; Tumbar et al., 1999). It is often assumed or speculated that histone acetylation induces such an opening of chromatin. However, direct in vivo experimental support for this model has been missing. We have demonstrated here that increased histone acetylation leads to a reversible decondensation of dense chromatin subcompartments within a range of 0.2 to >1 μm in length in living G1 phase HeLa cells. This result is consistent with the recent observation that the HDAC inhibitor suberoylanilide hydroxamic acid (SAHA) increased the DNase I sensitivity and restriction enzyme accessibility of the p21WAF1 promoter region (Gui et al., 2004).

Since the effect of acetylation per se on the conformation of the 30 nm chromatin fiber appears from in vitro studies to be moderate, it is currently an open question whether these local changes would translate into significant differences of the higher order folding of the fiber. Alternatively, acetylation might serve as a marker to recruit chromatin-remodeling complexes and/or other chromosomal proteins that change the higher order conformation of the chromatin fiber. It is anticipated that the combination of in vivo microscopy and quantitative image analysis by ICS and SRSA introduced here will prove to be useful for further studies in two aspects. First, it now becomes possible to relate high resolution images of chromatin to 3D models of the chromatin fiber folding into specific subcompartments. Second, the chromatin conformation can be reliably evaluated in cell lines in which the expression or activity of certain proteins is inhibited, for example by RNAi approaches. This would allow the in vivo identification of proteins that are essential for establishing an open chromatin structure.

The support of Peter Lichter is gratefully acknowledged. We would like to thank Stephanie Fesser, Sabine Görisch, Karsten Richter, Eberhard Spiess, Andreas Ladurner, Quentin Hanley and Tom Jovin for their help, and Waldemar Waldeck and Jan Ellenberg for valuable discussions. The project was supported by the Volkswagen Foundation in the program 'Junior Research Groups at German Universities'.

References

Allan, J., Harborne, N., Rau, D. C. and Gould, H. (1982). Participation of core histone "tails" in the stabilization of the chromatin solenoid. *J. Cell Biol.* **93**, 285-297.

Allfrey, V. G., Faulkner, R. and Mirsky, A. E. (1964). Acetylation and methylation of histones and their possible role in the regulation of RNA synthesis. *Proc. Natl. Acad. Sci. USA* **51**, 786-794.

Alvelo-Ceron, D., Niu, L. and Collart, D. G. (2000). Growth regulation of human variant histone genes and acetylation of the encoded proteins. *Mol. Biol. Rep.* **27**, 61-71.

Annunziato, A. T., Frado, L. L., Seale, R. L. and Woodcock, C. L. (1988). Treatment with sodium butyrate inhibits the complete condensation of interphase chromatin. *Chromosoma* **96**, 132-138.

Archer, S. Y. and Hodin, R. A. (1999). Histone acetylation and cancer. *Curr. Opin. Genet. Dev.* **9**, 171-174.

Ausio, J., Abbott, D. W., Wang, X. and Moore, S. C. (2001). Histone variants and histone modifications: a structural perspective. *Biochem. Cell Biol.* **79**, 693-708.

Bestvater, F., Knoch, T. A., Langowski, J. and Spiess, E. (2002). Construct conversions caused by simultaneous co-transfection: "GFP-walking". *Biotechniques* **32**, 848-850.

Black, M. J., Sapiro, G., Marimont, D. H. and Heger, D. (1998). Robust anisotropic diffusion. *IEEE Trans. Image Process.* **7**, 421-431.

Buggy, J. J., Sideris, M. L., Mak, P., Lorimer, D. D., McIntosh, B. and Clark, J. M. (2000). Cloning and characterization of a novel human histone deacetylase HDAC8. *Biochem. J.* **350**, 199-205.

Canny, J. F. (1986). A computational approach to edge detection. *IEEE Trans. Pattern Anal. Mach. Intell.* **8**, 679-698.

Coffee, B., Zhang, F., Warren, S. T. and Reines, D. (1999). Acetylated histones are associated with FMR1 in normal but not fragile X-syndrome cells. *Nat. Genet.* **22**, 98-101.

Covault, J. and Chalkley, R. (1980). The identification of distinct populations of acetylated histone. *J. Biol. Chem.* **255**, 9110-9116.

Cremer, T. and Cremer, C. (2001). Chromosome territories, nuclear architecture and gene regulation in mammalian cells. *Nat. Rev. Genet.* **2**, 292-301.

Cress, W. D. and Seto, E. (2000). Histone deacetylases, transcriptional control, and cancer. *J. Cell. Physiol.* **184**, 1-16.

Dean, P. N. and Jett, J. H. (1974). Mathematical analysis of DNA distributions derived from flow microfluorometry. *J. Cell Biol.* **60**, 523-527.

Dressel, U., Renkawitz, R. and Baniahmad, A. (2000). Promoter specific sensitivity to inhibition of histone deacetylases: implications for hormonal gene control, cellular differentiation and cancer. *Anticancer Res.* **20**, 1017-1022.

Finnin, M. S., Donigian, J. R., Cohen, A., Richon, V. M., Rifkind, R. A., Marks, P. A., Breslow, R. and Pavletich, N. P. (1999). Structures of a histone deacetylase homologue bound to the TSA and SAHA inhibitors. *Nature* **401**, 188-193.

Fletcher, T. M. and Hansen, J. C. (1995). Core histone tail domains mediate oligonucleosome folding and nucleosomal DNA organization through distinct molecular mechanisms. *J. Biol. Chem.* **270**, 25359-25362.

Furumai, R., Komatsu, Y., Nishino, N., Khochbin, S., Yoshida, M. and Horinouchi, S. (2001). Potent histone deacetylase inhibitors built from trichostatin A and cyclic tetrapeptide antibiotics including trapoxin. *Proc. Natl. Acad. Sci. USA* **98**, 87-92.

Georgel, P. T., Tsukiyama, T. and Wu, C. (1997). Role of histone tails in nucleosome remodeling by *Drosophila* NURF. *EMBO J.* **16**, 4717-4726.

Grunstein, M. (1997). Histone acetylation in chromatin structure and transcription. *Nature* **389**, 349-352.

Gui, C. Y., Ngo, L., Xu, W. S., Richon, V. M. and Marks, P. A. (2004). Histone deacetylase (HDAC) inhibitor activation of p21WAF1 involves changes in promoter-associated proteins, including HDAC1. *Proc. Natl. Acad. Sci. USA* **101**, 1241-1246.

Hanley, Q. S., Arndt-Jovin, D. J. and Jovin, T. M. (2002). Spectrally resolved fluorescence lifetime imaging microscopy. *Appl. Spectrosc.* **56**, 155-166.

Hansen, J. C. (2002). Conformational dynamics of the chromatin fiber in solution: determinants, mechanisms, and functions. *Annu. Rev. Biophys. Biomol. Struct.* **31**, 361-392.

Hansen, J. C., Tse, C. and Wolffe, A. P. (1998). Structure and function of the core histone N-termini: more than meets the eye. *Biochemistry* **37**, 17637-17641.

Hazzouri, M., Pivot-Pajot, C., Faure, A. K., Usson, Y., Pelletier, R., Sele, B., Khochbin, S. and Rousseaux, S. (2000). Regulated hyperacetylation of core histones during mouse spermatogenesis: involvement of histone deacetylases. *Eur. J. Cell Biol.* **79**, 950-960.

Hoffmann, K., Heltweg, B. and Jung, M. (2001). Improvement and validation of the fluorescence-based histone deacetylase assay using an internal standard. *Arch. Pharm.* **334**, 248-252.

Hoshikawa, Y., Kwon, H. J., Yoshida, M., Horinouchi, S. and Beppu, T. (1994). Trichostatin A induces morphological changes and gelsolin expression by inhibiting histone deacetylase in human carcinoma cell lines. *Exp. Cell Res.* **214**, 189-197.

Inokoshi, J., Katagiri, M., Arima, S., Tanaka, H., Hayashi, M., Kim, Y. B., Furumai, R., Yoshida, M., Horinouchi, S. and Omura, S. (1999). Neuronal differentiation of neuro 2a cells by inhibitors of cell cycle progression, trichostatin A and butyrolactone I. *Biochem. Biophys. Res. Commun.* **256**, 372-376.

Janicki, S. M., Tsukamoto, T., Salghetti, S. E., Tansey, W. P., Sachidanandam, R., Prasanth, K. V., Ried, T., Shav-Tal, Y., Bertrand, E., Singer, R. H. et al. (2004). From silencing to gene expression: real-time analysis in single cells. *Cell* **116**, 683-698.

Johnstone, R. W. (2002). Histone-deacetylase inhibitors: novel drugs for the treatment of cancer. *Nat. Rev. Drug. Discov.* **1**, 287-299.

Kadonaga, J. T. (1998). Eukaryotic transcription: an interlaced network of transcription factors and chromatin-modifying machines. *Cell* **92**, 307-313.

Kanda, T., Sullivan, K. F. and Wahl, G. M. (1998). Histone-GFP fusion protein enables sensitive analysis of chromosome dynamics in living mammalian cells. *Curr. Biol.* **8**, 377-85.

Kaye, B. H. (1989). *A Random Walk Through Fractal Dimensions*. New York, NY: VCH.

Kimura, H. and Cook, P. R. (2001). Kinetics of core histones in living human cells: little exchange of H3 and H4 and some rapid exchange of H2B. *J. Cell Biol.* **153**, 1341-1353.

Knoch, T. A. (2003). Towards a hollistic understanding of the human genome by determination and integration of its sequential and three-dimensional organization. In *High Performance Computing in Science and Engineering* (ed. E. Krause, W. Jäger and M. Resch), pp. 421-440. Heidelberg, Germany: Springer.

Kouzarides, T. (1999). Histone acetylases and deacetylases in cell proliferation. *Curr. Opin. Genet. Dev.* **9**, 40-48.

Ladurner, A. G., Inouye, C., Jain, R. and Tjian, R. (2003). Bromodomains mediate an acetyl-histone encoded antisilencing function at heterochromatin boundaries. *Mol. Cell* **11**, 365-376.

Lee, K. M. and Hayes, J. J. (1998). Linker DNA and H1-dependent reorganization of histone-DNA interactions within the nucleosome. *Biochemistry* **37**, 8622-8628.

Lee, E., Furukubo, T., Miyabe, T., Yamauchi, A. and Kariya, K. (1996). Involvement of histone hyperacetylation in triggering DNA fragmentation of rat thymocytes undergoing apoptosis. *FEBS Lett.* **395**, 183-187.

Logie, C., Tse, C., Hansen, J. C. and Peterson, C. L. (1999). The core histone N-terminal domains are required for multiple rounds of catalytic chromatin remodeling by the SWI/SNF and RSC complexes. *Biochemistry* **38**, 2514-2522.

Luger, K. and Richmond, T. J. (1998). DNA binding within the nucleosome core. *Curr. Opin. Struct. Biol.* **8**, 33-40.

Luger, K., Mäder, A. W., Richmond, R. K., Sargent, D. F. and Richmond, T. J. (1997). Crystal structure of the nucleosome core particle at 2.8 Å resolution. *Nature* **389**, 251-260.

Mahlknecht, U., Ottmann, O. G. and Hoelzer, D. (2000). When the band begins to play: histone acetylation caught in the crossfire of gene control. *Mol. Carcinog.* **27**, 268-271.

Maison, C., Bailly, D., Peters, A. H., Quivy, J. P., Roche, D., Taddei, A., Lachner, M., Jenuwein, T. and Almouzni, G. (2002). Higher-order structure in pericentric heterochromatin involves a distinct pattern of histone modification and an RNA component. *Nat. Genet.* **30**, 329-334.

Mariadason, J. M., Corner, G. A. and Augenlicht, L. H. (2000). Genetic reprogramming in pathways of colonic cell maturation induced by short chain fatty acids: comparison with trichostatin A, sulindac, and curcumin and implications for chemoprevention of colon cancer. *Cancer Res.* **60**, 4561-4572.

Marks, P. A., Richon, V. M. and Rifkind, R. A. (2000). Histone deacetylase inhibitors: inducers of differentiation or apoptosis of transformed cells. *J. Natl. Cancer Inst.* **92**, 1210-1216.

Marks, P. A., Richon, V. M., Breslow, R. and Rifkind, R. A. (2001). Histone deacetylase inhibitors as new cancer drugs. *Curr. Opin. Oncol.* **13**, 477-483.

McQuibban, G. A., Commisso-Cappelli, C. N. and Lewis, P. N. (1998). Assembly, remodeling, and histone binding capabilities of yeast nucleosome assembly protein 1. *J. Biol. Chem.* **273**, 6582-6590.

Medina, V., Edmonds, B., Young, G. P., James, R., Appleton, S. and Zalewski, P. D. (1997). Induction of caspase-3 protease activity and apoptosis by butyrate and trichostatin A (inhibitors of histone deacetylase): dependence on protein synthesis and synergy with a mitochondrial/cytochrome c-dependent pathway. *Cancer Res.* **57**, 3697-3707.

Petersen, N. O. (2001). FCS and spatial correlations on biological surfaces. In *Fluorescence Correlation Spectroscopy – Theory and Applications*, (ed. R. Rigler and E. S. Elson), pp. 162-184. Heidelberg, Germany: Springer.

Richon, V. M., Sandhoff, T. W., Rifkind, R. A. and Marks, P. A. (2000). Histone deacetylase inhibitor selectively induces p21WAF1 expression and gene-associated histone acetylation. *Proc. Natl. Acad. Sci. USA* **97**, 10014-10019.

Rodríguez-Iturbe, I. and Rinaldo, A. (1997). *Fractal River Basins – Chance and Self-organization*. Cambridge, UK: Cambridge University Press.

Sambucetti, L. C., Fischer, D. D., Zabludoff, S., Kwon, P. O., Chamberlin, H., Trogani, N., Xu, H. and Cohen, D. (1999). Histone deacetylase inhibition selectively alters the activity and expression of cell cycle proteins leading to specific chromatin acetylation and antiproliferative effects. *J. Biol. Chem.* **274**, 34940-34947.

Stoehr, M., Gebhardt, U. and Goerttler, K. (1976). Computer assistance in multiparameter flow microphotometry of mammalian cells. *Biotechnol. Bioeng.* **18**, 1057-1074.

Strahl, B. D. and Allis, C. D. (2000). The language of covalent histone modifications. *Nature* **403**, 41-45.

Sun, J. M., Chen, H. Y. and Davie, J. R. (2001). Effect of estradiol on histone acetylation dynamics in human breast cancer cells. *J. Biol. Chem.* **276**, 49435-49442.

Sun, J. M., Spencer, V. A., Chen, H. Y., Li, L. and Davie, J. R. (2003).

Measurement of histone acetyltransferase and histone deacetylase activities and kinetics of histone acetylation. *Methods* **31**, 12-23.

Tse, C., Georgieva, E. I., Ruiz-Garcia, A. B., Sendra, R. and Hansen, J. C. (1998). Gcn5p, a transcription-related histone acetyltransferase, acetylates nucleosomes and folded nucleosomal arrays in the absence of other protein subunits. *J. Biol. Chem.* **273**, 32388-32392.

Tumbar, T., Sudlow, G. and Belmont, A. S. (1999). Large-scale chromatin unfolding and remodeling induced by VP16 acidic activation domain. *J. Cell Biol.* **145**, 1341-1354.

Usachenko, S. I., Bavykin, S. G., Gavin, I. M. and Bradbury, E. M. (1994). Rearrangement of the histone H2A C-terminal domain in the nucleosome. *Proc. Natl. Acad. Sci. USA* **91**, 6845-6849.

van Holde, K. E. (1989). *Chromatin*. Heidelberg, Germany: Springer.

Wang, X. Y., He, C., Moore, S. C. and Ausio, J. (2001). Effects of histone acetylation on the solubility and folding of the chromatin fiber. *J. Biol. Chem.* **276**, 12764-12768.

Waterborg, J. H. and Kapros, T. (2002). Kinetic analysis of histone acetylation turnover and Trichostatin A induced hyper- and hypoacetylation in alfalfa. *Biochem. Cell Biol.* **80**, 279-293.

Weidemann, T., Wachsmuth, M., Knoch, T. A., Müller, G., Waldeck, W. and Langowski, J. (2003). Counting nucleosomes in living cells with a combination of fluorescence correlation spectroscopy and confocal imaging. *J. Mol. Biol.* **334**, 229-240.

Yamashita, Y., Shimada, M., Harimoto, N., Rikimaru, T., Shirabe, K., Tanaka, S. and Sugimachi, K. (2003). Histone deacetylase inhibitor trichostatin A induces cell-cycle arrest/apoptosis and hepatocyte differentiation in human hepatoma cells. *Int. J. Cancer* **103**, 572-576.

Yoshida, M. and Beppu, T. (1988). Reversible arrest of proliferation of rat 3Y1 fibroblasts in both the G1 and G2 phases by trichostatin A. *Exp. Cell Res.* **177**, 122-131.

Yoshida, M., Kijima, M., Akita, M. and Beppu, T. (1990). Potent and specific inhibition of mammalian histone deacetylase both in vivo and in vitro by trichostatin A. *J. Biol. Chem.* **265**, 17174-17179.

Yoshida, M., Horinouchi, S. and Beppu, T. (1995). Trichostatin A and trapoxin: novel chemical probes for the role of histone acetylation in chromatin structure and function. *BioEssays* **17**, 423-430.

Zhang, D. E. and Nelson, D. A. (1988). Histone acetylation in chicken erythrocytes. Rates of deacetylation in immature and mature red blood cells. *Biochem. J.* **250**, 241-245.

Zhang, W., Bone, J. R., Edmondson, D. G., Turner, B. M. and Roth, S. Y. (1998). Essential and redundant functions of histone acetylation revealed by mutation of target lysines and loss of the Gcn5p acetyltransferase. *EMBO J.* **17**, 3155-3167.

Zlatanova, J., Caiafa, P. and van Holde, K. (2000). Linker histone binding and displacement: versatile mechanism for transcriptional regulation. *FASEB J.* **14**, 1697-1704.

THE JOURNAL OF BIOLOGICAL CHEMISTRY
Vol. 280, No. 16, Issue of April 22, pp. 15690–15699, 2005

Printed in U.S.A.

Association States of Nucleosome Assembly Protein 1 and Its Complexes with Histones*

Received for publication, November 26, 2004, and in revised form, January 10, 2005
Published, JBC Papers in Press, January 31, 2005, DOI 10.1074/jbc.M413329200

Katalin Fejes Tóth‡§, Jacek Mazurkiewicz‡, and Karsten Rippe‡¶

From the ‡Kirchhoff-Institut für Physik, AG Molekulare Biophysik, Ruprecht-Karls-Universität Heidelberg, Im Neuenheimer Feld 227 and the §Deutsches Krebsforschungszentrum, Abt. Molekulare Genetik (B060), Im Neuenheimer Feld 280, D-69120 Heidelberg, Germany

The histone chaperone NAP1 is a carrier of histones during nuclear import, nucleosome assembly, and chromatin remodeling. Analytical ultracentrifugation was used to determine the association states of NAP1 alone and in complexes with core histones. In addition, the concentration dependence of the association was quantified by determining the equilibrium dissociation constant between different NAP1 species. At physiological protein and salt concentrations the prevalent species were the NAP1 dimer and octamer. These were also the association states found to interact with histones in a stoichiometry of one NAP1 monomer per histone. Based on these results a model for a cell cycle-dependent shift of the NAP1 dimer-octamer equilibrium is proposed that reflects different biological functions of NAP1.

In eukaryotes the DNA is packed into nucleosomes consisting of 147 bp of DNA wrapped around an octamer of small basic histone proteins (1–4). This octamer consists of two copies of histones H2A, H2B, H3, and H4, respectively. The nucleosome constitutes the basic repeating unit of chromatin, and formation of a regularly spaced nucleosome chain during chromatin assembly is a prerequisite to maintain the biological activity of chromatin. This requires ATP-dependent chromatin assembly factors as well as so-called histone chaperones (5–10). Histone chaperones bind histone proteins and prevent nonspecific, charge-based interaction with nucleic acids. This activity appears essential to cell viability, because simple mixing of histones and DNA *in vitro* at physiological salt concentrations leads to the rapid formation of poorly defined insoluble aggregates (11, 12). One of these chaperones, the nucleosome assembly protein 1 (NAP1)[1] (13, 14), is involved in the transport of the histone H2A·H2B dimer from the cytoplasm to the nucleus and the deposition of histones onto the DNA as described in several reviews (5–7, 10). NAP1 is highly acidic, which is likely to mediate its interaction with the positively charged histone proteins. It is thought to function in large chromosomal domains rather than at local restricted sites (5), and in yeast loss of NAP1 leads to an altered gene expression of about 10% of the genome (15). NAP1 is present at micromolar concentrations throughout the cell cycle, and an increase of the NAP1 concentration during S-phase has been reported for some NAP1 homologues in higher eukaryotes (16–19). Various lines of evidence indicate that NAP1 and the related NAP2 protein are mainly cytoplasmic during G_1 and G_2 phase with only a small fraction in the nucleus and translocate into the nucleus during S phase (14, 19–21).

In vivo experiments show coimmunoprecipitation of NAP1 with the histones H2A and H2B but not with H3 and H4 (11, 22). In contrast, NAP1 is capable of binding all four core histones *in vitro* (13, 14, 23–25). Several studies focused on the determination of the association state of NAP1, which in yeast has a monomer molecular mass of 47.9 kDa. By gel filtration or gradient centrifugation very different molecular masses ranging from 120 to 600 kDa and sedimentation coefficients from 1.5 S up to 7 S were reported. In a recent study it was concluded based on analytical ultracentrifugation experiments that yNAP1 exists as complex mixture of species with *s* values between 4.5 and 12 S at physiological salt concentrations (75 and 150 mM NaCl). In the presence of 500 mM NaCl concentration a 4.5 S NAP1 dimer was identified (26). It appears that upon mixing NAP1 with histones distinct complexes are formed, which sediment around 5–6 S, 8 S, and 10–12 S, respectively (13, 23, 24). Within the 12 S complex all four histones cosedimented in nearly equal amounts, and upon addition of DNA nucleosomes were formed. The 5–6 S complex was assigned to a NAP1 complex with the H2A·H2B dimer and the 8 S complex to a complex that contains NAP1 and the $(H3{\cdot}H4)_2$ tetramer (13, 23, 24). Hence, the biologically highly relevant interaction of NAP1 with histones appears to be tightly connected to the NAP1 association state. In particular, the nature of the different NAP1 complexes observed previously at physiological ionic strength and their relation to specific NAP1 activities remain to be elucidated.

Here, we have used analytical ultracentrifugation (AUC) to determine the different association states of NAP1 on its own and in complexes with histones. AUC is very useful for the identification of the oligomeric state and the stoichiometry of proteins, and to characterize their thermodynamic and hydrodynamic properties in solution (27, 28). The concentration dependence of the equilibrium between different NAP1 species was quantified in terms of the corresponding dissociation constants. At physiological protein and salt concentrations the dominating species were the NAP1 dimer and octamer, which were also the association states found to interact with histones. Based on these results and estimates of the intracellular concentration of NAP1 we propose a model, in which the transport/exchange of H2A·H2B dimers in G_1 and G_2 phase is mediated by NAP1 dimers. The accumulation of NAP1 in the nucleus during S phase induces the association of NAP1 into an octamer complex. This species has eight histone binding sites so that it could act as a carrier for multiple histone dimers as required for the *de novo* assembly of nucleosomes.

* The costs of publication of this article were defrayed in part by the payment of page charges. This article must therefore be hereby marked "*advertisement*" in accordance with 18 U.S.C. Section 1734 solely to indicate this fact.

¶ To whom correspondence should be addressed. Tel.: 49-6221-54-9270; Fax: 49-6221-54-9112; E-mail: Karsten.Rippe@kip.uni-heidelberg.de.

[1] The abbreviations used are: NAP1, nucleosome assembly protein 1; AUC, analytical ultracentrifugation; *s*, sedimentation coefficient; *D*, diffusion coefficient.

EXPERIMENTAL PROCEDURES

Expression and Purification of NAP1—Yeast NAP1 was expressed from plasmid pET28-yNAP1 from Toshio Tsukiyama with a N-terminal His tag. The plasmid corresponds to *Saccharomyces cerevisiae* NAP1 with a T7 tag cloned into the NdeI site of pET28a. The His tag is followed by a thrombin cleavage site. The expressed NAP1 protein has a calculated molecular mass of 52.4 kDa with the His tag and 49.5 kDa after thrombin cleavage. Protein overexpression from pET28-yNAP1 was in *Escherichia coli* BL21(DE3) carrying the pLysS plasmid. For purification, cells were suspended in lysis buffer (20 mM Tris-HCl, pH 7.5, 500 mM KCl, 20 mM imidazole, 5 mM mercaptoethanol, 15% glycerol, 1 mM EDTA, 0. 1% Nonidet P-40, 1 mM Pefabloc), sonicated, and centrifuged. Nickel-agarose beads were equilibrated with lysis buffer and added to the supernatant after supplementing $MgCl_2$ to a final concentration of 2 mM. Binding was allowed for 3–4 h at 4 °C, and beads were washed twice with lysis buffer and twice with washing buffer (20 mM Tris-HCl, pH 7.5, 100 mM KCl, 20 mM imidazole, 5 mM mercaptoethanol, 15% glycerol, 0.01% Nonidet P-40, 1 mM Pefabloc). Elution was conducted with washing buffer supplemented with 0.5 M imidazole. The eluate was dialyzed against buffer A (20 mM Tris-HCl, pH 7.5, 100 mM M KCl, 1 mM dithiothreitol, 10% glycerol, 0.1 mM EDTA). The protein was further purified on a Mono-Q column and eluted with a KCl gradient from 0.1 to 1 M in buffer A. Fractions were checked on SDS-PAGE, and NAP1-containing fractions were pooled and dialyzed against buffer A. DNase activity was tested by incubating NAP1 with supercoiled plasmid DNA over 2 days. For some experiments the His tag was removed by binding purified NAP1 to nickel-agarose and incubating with biotin-tagged thrombin for 2 h at 20 °C using the thrombin cleavage kit according to the specifications given by the manufacturer (Novagen, Madison, WI). Thrombin was subsequently removed with streptavidin beads. Using the program SEDNTERP[2] (29) the monomer extinction coefficient of NAP1 was calculated from the amino acid sequence to be $\epsilon_{280} = 37{,}000\ M^{-1}\cdot cm^{-1}$. From the absorbance spectrum of the protein we derived the corresponding value of $\epsilon_{230} = 293{,}000\ M^{-1}\cdot cm^{-1}$.

Preparation and Gel Electrophoresis Analysis of Fluorescent Histone Complexes—Recombinant *Xenopus laevis* histones H2A12C, H2B, H3C110A, and H4K5C were overexpressed from pET plasmids in *E. coli* as described previously (30, 31). The H2A12C and H4K5C proteins contain a cysteine substitution, allowing specific labeling with thiol-reactive probes (32, 33). In Histone H3C110A the cysteine is substituted against alanine to hinder modification of this residue, which could lead to functional impairment. Histones H2A12C and H2B or H3C110A and H4K5C were dissolved in unfolding buffer containing 7 M guanidinium chloride, 20 mM Tris-HCl, pH 7.5, 1 mM EDTA, and 5 mM mercaptoethanol at equimolar ratios and a total protein concentration of 1 mg/ml. Refolding was by dialysis into the same buffer but without guanidinium chloride. A reducing agent was removed by repeated concentration and dilution of histone proteins in freshly degassed labeling buffer (20 mM Tris-HCl, pH 7.2, 0.1 mM EDTA) using Vivaspin 20 concentrators (Vivascience, Hannover, Germany). Labeling was carried out at a histone monomer concentration of ~60 μM with a 1.5 times molar excess of Alexa Fluor 488 C5 maleimide (Molecular Probes Europe BV, Leiden, Netherlands) for 1 h. The reaction was stopped by adding 10 mM dithiothreitol and incubating for 30 min on ice. Labeled histone complexes were then purified from misfolded histone and free dye using BioRex 70 resin (Bio-Rad Laboratories GmbH) as described before (32). Concentration of labeled histones and labeling efficiency were assessed by absorbance spectroscopy using an excitation coefficient of $\epsilon_{496} = 72{,}000\ M^{-1}\cdot cm^{-1}$ for the Alexa 488 label (34) and the published values for the histones at a wavelength of 276 nm (30) after subtracting the contribution of Alexa 488 at this wavelength. A labeling efficiency of 70% was routinely reached for H2A12C and 50% for H4K5C, and the labeled histones behaved identically to the wild type in terms of association state. Agarose gel electrophoresis of NAP1 complexes with labeled histones was conducted on 1% agarose gels in 0.11× TBE (10 mM Tris, 10 mM boric acid, 0.22 mM EDTA) supplemented with 10 mM KCl. NAP1 and histones were mixed prior to loading in 10 mM Tris-HCl, pH 7.5, 150 mM KCl and incubated for at least 10 min at room temperature. Bands were visualized by illumination with a UV-light box at 302 nm and detection by using a charge-coupled device camera.

Analytical Ultracentrifugation—Analytical sedimentation equilibrium ultracentrifugation was carried out at 20 °C on a Beckman Optima XL-A analytical ultracentrifuge equipped with absorbance optics and an An60 Ti rotor. The partial specific volume $\bar{v}$ at this temperature was determined from the amino acid composition to be $0.726\ ml\cdot g^{-1}$ for NAP1, $0.746\ ml\cdot g^{-1}$ for the histones, and $0.730\ ml\cdot g^{-1}$ for the NAP1-histone complexes using the program SEDNTERP version 1.05[2] (29). Hydration values of 0.44 g of H_2O per g of NAP1, 0.39 g of H_2O per g of histone, and 0.43 g of H_2O per g of NAP1·histone complex were calculated as described previously (35). Proteins were dialyzed against buffer containing 10 mM Tris-HCl, pH 7.5, 5% (v/v) glycerol and 10 or 100 mM KCl prior to analysis. The density ρ of the buffer was $1.0133\ g\cdot ml^{-1}$ (10 mM KCl) and $1.0176\ g\cdot ml^{-1}$ (100 mM KCl), and the viscosity η was 1.1680 mPa·s (10 mM KCl) and 1.1667 mPa·s (100 mM KCl) at 20 °C as calculated with SEDNTERP.

Sedimentation equilibrium ultracentrifugation runs were performed with NAP1 concentrations ranging between 0.5 and 32 μM and at speeds of 5,000, 7,000, and 10,000 rpm and for some runs also at 3,000 and 15,000 rpm. The NAP1-H2A^f·H2B complexes were studied with 3 μM H2A^f·H2B dimer (6 μM histone monomer) and 6 μM NAP1. In addition, experiments were conducted, in which the NAP1 concentration was varied from 3 to 12 μM. NAP1 and H3·H4^f were mixed at a 1:1 monomer ratio using 8.6 μM H3·H4^f dimer and 17.3 μM NAP1. Equilibrium was obtained after 24–30 h as judged from a comparison of scans recorded at intervals of 4 h. Absorbance data were collected at 230 and 280 nm by averaging 10 scans with radial increments of 0.001 cm in step mode. Absorbance values above 1.3 were not included in the analysis. The sedimentation equilibrium data were analyzed by global fitting of all data sets of a given sample with the software UltraScan version 6.2 (www.ultrascan.uthscsa.edu) from Borries Demeler. A monomer-dimer, dimer-octamer, or dimer-octamer-hexadecamer model was used as described in the text. Other models that involved a NAP1 dimer as basic building block and included tetramers or hexamers were also tested but did not lead to good fits. All fits derived according to Reactions 1–4 had a fit quality of 35% or higher, with a value of >30% being considered as an adequate model for the data.

Analytical sedimentation velocity studies were conducted at 20 °C and at 35,000 and 42,000 rpm in epon double-sector cells and in the same buffer used for the equilibrium runs. The NAP1 concentration was between 1 and 4 μM for the analysis of NAP1 complexes. For experiments with histones 3 μM H2A·H2B dimer (6 μM histone monomer) and 6 μM NAP1 monomer or 20 μM NAP1 and 10 μM H3·H4^f dimer (20 μM histone monomer) were used. Data were collected at 230, 280, or 496 nm using a spacing of 0.03 cm in a continuous scan mode. A global analysis of the sedimentation velocity experiments was conducted with the program SEDPHAT version 2.0 (www.analyticalultracentrifugation.com) (36). The local residual mean square deviation was between 0.006 and 0.011 for single and global fits. The same models as in the equilibrium runs were used with an instantaneous equilibrium between different association states corresponding to kinetic off-rate constants that are equal or faster than 0.1/s.

RESULTS

NAP1 Associates into Dimer, Octamer, and Hexadecamer—Yeast NAP1 was expressed in *Escherichia coli* and purified by His tag affinity and ion exchange chromatography (Fig. 1*A*). A contaminating DNase activity present in the eluate from the nickel-chelating resin was removed by a second chromatography step on a Mono-Q ion exchange column. After the final purification step the protein was more than 95% pure and the preparation had no detectable DNase activity as tested by incubation with supercoiled plasmid substrate at 37 °C over several days and analysis by agarose gel electrophoresis (data not shown). For some AUC experiments the His tag of NAP1 was removed by thrombin digestion to test if the tag effects the association state. The His tag was cut off quantitatively under appropriate conditions with hardly any additional degradation of the protein (Fig. 1*B*). NAP1 preparations equivalent to those obtained after 6–22 h of digestion were used in subsequent AUC experiments.

Binding of NAP1 to histones was studied with histone H2A·H2B and H3·H4 complexes that were reconstituted from overexpressed and purified recombinant histones (30). The heterodimer/tetramer complexes were prepared with the fluorescent dye Alexa 488 covalently attached to either H2A or to H4 in a site-specific manner (see "Experimental Procedures"). These labeled H2A^f or H4^f histones displayed an additional

[2] J. Philo, D. Hayes, and T. Laue, available at www.jphilo.mailway.com/download.htm.

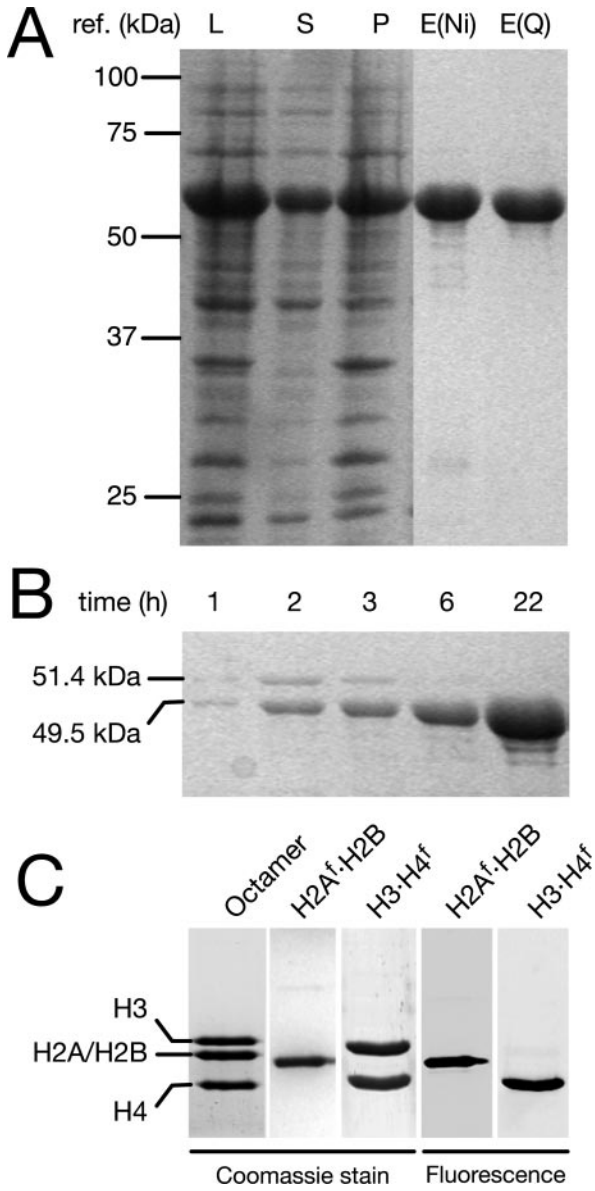

FIG. 1. *A*, purification of NAP1 protein from *E. coli* with nickel-affinity and ion exchange chromatography. Due to its high number of negative charges the NAP1 protein displays a somewhat reduced mobility on SDS gels with an apparent molecular mass of ≈60 kDa. *L*, lysate; *S*, supernatant; *P*, pellet; *E(Ni)*, eluate after affinity purification with nickel-agarose beads; *E(Q)*, eluate from Mono-Q ion exchange column. *B*, cleavage of His tag from NAP1. NAP1 was bound to nickel-agarose beads, and thrombin cleavage was conducted for the times indicated. Increasing amounts of tag-free NAP1 were released to the supernatant. At extended incubation times unspecific cleavage by thrombin resulted in faster moving bands. *C*, gel electrophoretic analysis of reconstituted and purified $H2A^f$·H2B dimer and $(H3{\cdot}H4^f)_2$ tetramer. An SDS-gel is shown with visualization of the protein by Coomassie staining in comparison to the $H2A^f$ and $H4^f$ fluorescence signal of the same lanes. As a reference, a histone octamer is included that has been reconstituted from purified recombinant histones as described previously (31). Histones $H2A^f$ and H2B are not separated on the gel.

absorbance maximum at 496 nm and a fluorescence maximum at about 520 nm allowing specific detection of NAP1-histone complexes by absorbance and fluorescence measurements. Fig. 1*C* shows a Coomassie-stained SDS-gel with the purified histone $H2A^f$·H2B and H3·$H4^f$ complexes and a reconstituted histone octamer preparation as a reference. The SDS-gel demonstrates that the histone preparations are highly purified and that $H2A^f$ and the $H4^f$ displayed the expected fluorescence signal upon excitation of the Alexa 488 fluorophore. The recombinant histones H2A und H2B from *X. laevis* have a very similar mobility under standard electrophoretic conditions and are hardly separated (37).

The association states of NAP1 in absence of histones were determined by sedimentation equilibrium ultracentrifugation. Typical data sets are displayed in Fig. 2(*A* and *B*), and the results are summarized in Table I. Initial runs at approximately physiological salt concentrations (100 mM KCl, 2 mM $MgCl_2$) revealed a complex multispecies equilibrium. To identify the basic building blocks of the NAP1 multimers the salt concentration was varied from 10 mM to 1 M KCl. At 10 mM KCl an excellent fit of the data was obtained over a concentration range from 0.5 to 13.4 μM NAP1 with a monomer-dimer model and a monomer molecular mass constrained to 51.3 kDa as calculated from the amino acid composition (Fig. 2*A*) according to Reaction 1.

$$2\ \mathrm{NAP1} \rightleftarrows (\mathrm{NAP1})_2$$

REACTION 1

A dissociation constant of $K_{d1-2} = 0.2 \times 10^{-6}$ M was determined. At NAP1 concentrations well above the dissociation constant (measurements at 6.7, 8.1, and 13.4 μM) the data could be described well with a single component fit. A molecular mass of 104 ± 4 kDa was obtained with the molecular mass being the only fit parameter and using the calculated values for the partial specific volume $\bar{v} = 0.726\ \mathrm{ml{\cdot}g^{-1}}$ of NAP1 and a buffer density of $\rho = 1.0133\ \mathrm{g{\cdot}ml^{-1}}$ (see "Experimental Procedures"). This result is in excellent agreement with the calculated value of 102.7 kDa for the NAP1 dimer. Thus, NAP1 forms a dimer in low salt buffer, which is the building block for the oligomers formed at physiological salt concentrations. This finding confirms a previous study, in which the NAP1 dimer was identified as the basic association state (26). Accordingly, the molecular mass of the NAP1 dimer of 102.7 kDa was used in further experiments as a fixed parameter to determine the higher association states at physiological buffer conditions and in complexes with histones.

At 100 mM KCl concentration the association of NAP1 into larger complexes was evident from a comparison of the molecular weight averages. For example at ≈2 μM protein concentration average values of 81 ± 4 kDa (10 mM KCl) and 169 ± 9 kDa (100 mM KCl) were determined when fitting the data to a single component model. However, in these experiments systematic deviations from a one or two component model were observed in the residuals of the fits, indicating a more complex equilibrium state. A detailed analysis revealed that the data at 100 mM KCl were best described by a dimer-octamer-hexadecamer equilibrium (Reaction 2).

$$8(\mathrm{NAP1})_2 \rightleftarrows 2(\mathrm{NAP1})_8 \rightleftarrows (\mathrm{NAP1})_{16}$$

REACTION 2

Other models that involve the NAP1 dimer as the smallest unit (*e.g.* formation of tetramer or hexamer) did not lead to good fits. Fig. 2*B* shows a representative data set at 100 mM KCl with a fit to a dimer-octamer-hexadecamer equilibrium and the dimer molecular mass constrained to 102.7 kDa. Very good fits to this model were obtained over a concentration range from 0.5 μM to 32 μM NAP1 monomer with data recorded at 230 and 280 nm. Values for the dissociation constant of $K_{d2-8} = (5.8 \pm 3.9) \times 10^{-18}\ \mathrm{M^3}$ and $K_{d8-16} = (1.2 \pm 0.3) \times 10^{-6}$ M were determined. The concentration at which the ratio of NAP1 in the dimeric and octameric state is 1:1 is $(K_{d2-8})^{1/3} = (1.8 \pm 0.4) \times 10^{-6}$ M. At salt concentrations of 150 mM KCl, 100 mM KCl plus 2 mM $MgCl_2$, or 10 mM KCl plus 2 mM $MgCl_2$ (Table I) the data were also best described with a dimer-octamer-hexadecamer equilib-

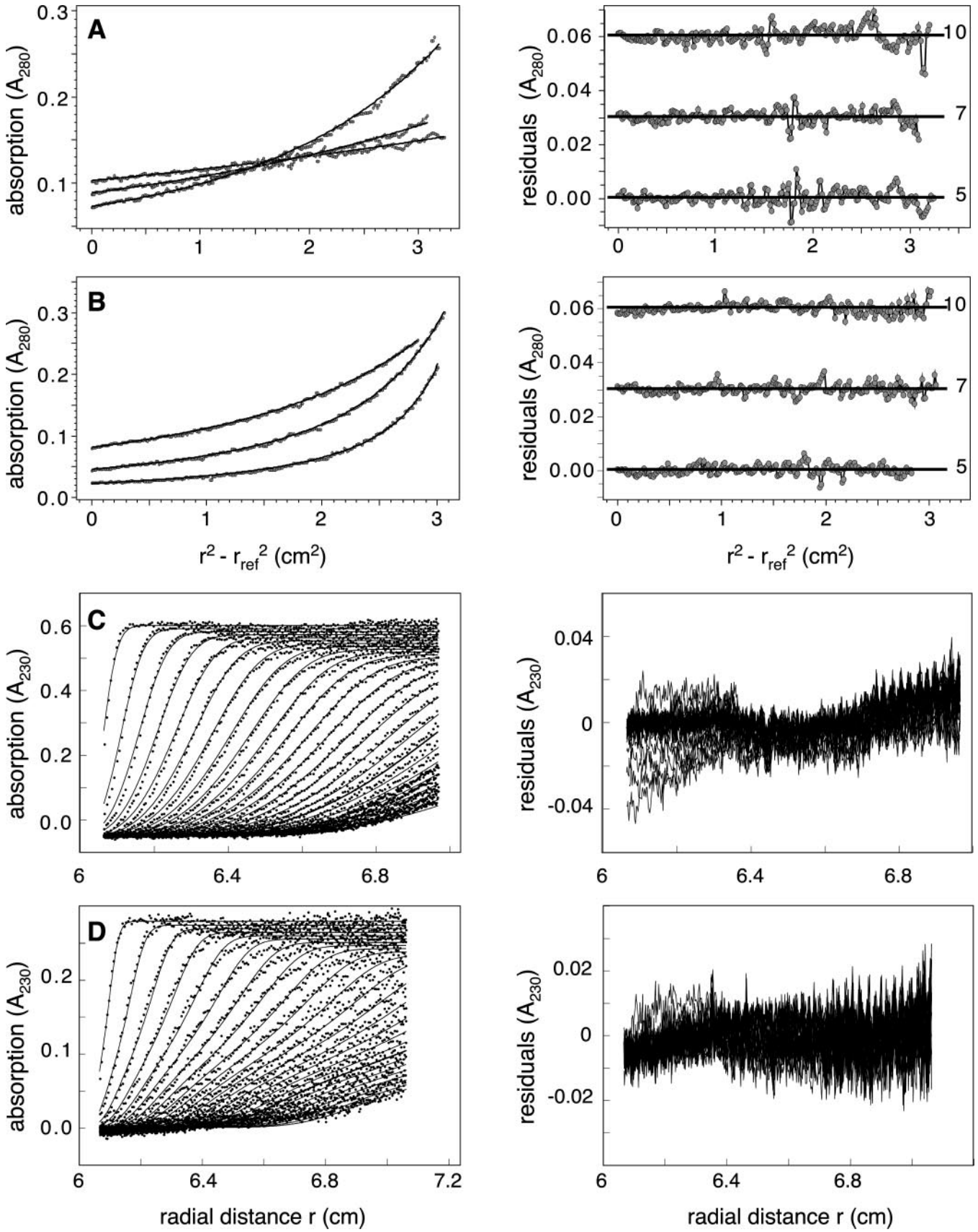

FIG. 2. **Analytical ultracentrifugation of NAP1.** The *left panel* shows the experimental data and the fitted curves in dependence of the radial position. On the *right* the residuals of the fits are plotted. Equilibrium centrifugation experiments were carried out at 20 °C and at 5,000, 7,000, and 10,000 rpm as shown in *A* and *B*. Representative sedimentation velocity runs conducted at 35,000 rpm (*C*) and 42,000 rpm (*D*) are shown with every fifth scan being included in the plot. *A* and *C*, NAP1 in buffer containing 10 mM KCl was fitted with a monomer-dimer equilibrium (Reaction 1) with the molecular mass of the monomer fixed at 51.3 kDa. *B* and *D*, NAP1 in buffer containing 100 mM KCl fitted with a dimer-octamer-hexadecamer equilibrium (Reaction 2).

TABLE I
Association states of NAP1, histones, and NAP1-histone complexes determined by sedimentation equilibrium analysis

KCl (mM)	Basic association state	Abbreviation	M_{fit}[a] (*kDa*)	Equilibrium complexes
10	NAP1 monomer	NAP1	51.3[b]	Monomer·dimer[b]
100	NAP1 dimer	$(NAP1)_2$	102.7	Dimer-octamer-hexadecamer
10 + $MgCl_2$[c]	NAP1 dimer	$(NAP1)_2$	102.7	Dimer-octamer-hexadecamer
100 + $MgCl_2$[c]	NAP1 dimer	$(NAP1)_2$	102.7	Dimer-octamer-hexadecamer
10/100	H2A·H2B dimer	$(H2Af{\cdot}H2B)_1$	28.5[d]	Dimer[d]
10/100	NAP1 dimer with H2A·H2B dimer	$(NAP1)_2$-$(H2A^f{\cdot}H2B)_1$	131.2	Dimer-octamer
10/100	H3·H4 dimer	$(H3{\cdot}H4^f)_1$	27.2[e]	Dimer[e]
10/100	NAP1 dimers with H3·H4 dimer	$(NAP1)_2$-$(H3{\cdot}H4^f)_1$	129.8	Dimer-tetramer-octamer

[a] Molecular masses were fixed in the analysis with equilibrium association models at these values calculated from the amino acid sequence.
[b] A molecular mass of 103.8 ± 1 kDa demonstrating the formation of a dimer was determined from a one component fit for NAP1 at concentrations of 6.7 μM and higher.
[c] $MgCl_2$ was added at a concentration of 2 mM.
[d] A molecular mass of 27.5 ± 4 kDa was determined for H2Af·H2B dimer from measurements at 10 mM and 100 mM KCl with a one-component fit.
[e] Under the conditions of the experiments most of the H3·H4 was present in the dimer state. A molecular mass of 29.7 ± 5 kDa was determined in equilibrium runs at 10 and 100 mM KCl from a one-component fit.

rium with no apparent changes of the dissociation constants. Raising the KCl concentration above 0.5 M led to the dissociation of the complex into increasing amounts of monomeric NAP1 indicating that the formation of the NAP1 dimer involves predominantly electrostatic interactions that are weakened by high salt concentrations. At 500 mM KCl NAP1 was present almost completely as a dimer in agreement with results reported recently (26).

The possible effect of the His tag on the NAP1 association was examined by cleavage of the tag with thrombin (Fig. 1*B*). This construct was studied by equilibrium analytical ultracentrifugation experiments at 100 mM KCl and at NAP1 monomer concentrations of 2, 4, 8, 12, 16, and 32 μM. Within the accuracy of measurement no differences were observed in the average molecular weight or multimer equilibrium distribution (data not shown). Best fits were also obtained with a dimer-octamer-hexadecamer equilibrium and similar dissociation constants as those determined for the His-tagged NAP1. Thus, the His tag had no detectable effect on the association properties of NAP1. Because a significant fraction of the protein was lost during the additional purification after thrombin digestion of NAP1, the subsequent experiments were conducted with His-tagged NAP1.

NAP1 complexes were also studied by sedimentation velocity analysis to determine the sedimentation coefficient and hydrodynamic shape of the complexes. The salt-dependent association of NAP1 was clearly evident in the sedimentation velocity analysis when computing the weight average sedimentation coefficient. At a protein concentration of 2 μM values of 3.8 ± 0.3 S at 10 mM KCl and 6.5 ± 0.6 S at 100 mM KCl were determined. Again the data were indicative of the presence of several species. The sedimentation coefficients of the single components in the NAP1 multispecies equilibrium system according to Reaction 1 or Reaction 2 were determined with the program SEDPHAT from Peter Schuck (36). The resulting values of the sedimentation coefficients *s* measured at 20 °C are given in Table II. Representative sedimentation velocity plots are shown for 10 mM KCl (Fig. 2*C*) and 100 mM KCl (Fig. 2*D*). The sedimentation coefficients of the monomer and dimer were determined at 10 mM KCl using a monomer-dimer equilibrium model (Reaction 1). The monomer had an *s* value of 2.4 ± 0.2 S, whereas the dimer yielded 4.4 ± 0.2 S. At 100 mM KCl a dimer-octamer-hexadecamer equilibrium (Reaction 2) was used and sedimentation coefficients of 11.4 ± 0.8 S (octamer) and 21.3 ± 0.5 S (hexadecamer) were measured.

NAP1 Binds Histones in a 1:1 Stoichiometry—Initial attempts to analyze the association of NAP1 with recombinant histones H2A·H2B and H3·H4 by analytical ultracentrifugation yielded no clear results. The complex dimer-octamer-hexadecamer equilibrium of NAP1 precluded the identification of additional species with bound histones. Therefore, recombinant histone complexes were prepared with the fluorescent dye Alexa 488 covalently attached to either H2A or to H4 in a site-specific manner. These labeled histones $H2A^f$ or $H4^f$ allowed a specific detection of NAP1·histone complexes both by absorbance and fluorescence measurements.

The initial characterization of complex formation of $H2A^f{\cdot}H2B$ and $H3{\cdot}H4^f$ with NAP1 was conducted using electrophoresis mobility shift assays. Increasing amounts of NAP1 were mixed with labeled histone complexes ($H2A^f{\cdot}H2B$ or $H3{\cdot}H4^f$) and analyzed on agarose gels exploiting the $H2A^f$ or $H4^f$ fluorescence signal (Fig. 3). Free histones migrate into the opposite direction due to their highly positive charge. Accordingly, they were not visible in the gel, except for nonspecific, hardly migrating aggregates in samples, in which an excess of histones was present (Fig. 3, *lanes* with 0, 0.4, and 0.8 μM NAP1). Upon addition of NAP1 to histones, a specific complex formed and reached saturation at a ratio of approximately one NAP1 monomer per histone, both for $H2A^f{\cdot}H2B$ (Fig. 3*A*) and $H3{\cdot}H4^f$ (Fig. 3*B*). Thus, one NAP1 protein binds one histone in good agreement with previous studies (25). It is further noted that NAP1-$H2A^f{\cdot}H2B$ and NAP1-$H3{\cdot}H4^f$ complexes migrated at an apparent identical height, indicative for the formation of complexes of similar size and charge.

NAP1 Dimer and Octamer Form Complexes with H2A·H2B Dimers—The AUC analysis was conducted with absorbance data recorded at 496 nm. Thus, only the species containing $H2A^f{\cdot}H2B$ dimer was detected. For the $H2A^f{\cdot}H2B$ dimer alone a molecular mass of 29 ± 4 kDa was determined in equilibrium runs, which is in very good agreement with the 28.5 kDa derived from the amino acid sequence. NAP1 and histone dimer were mixed at different molar ratios. Only at a ratio of one NAP1 monomer per histone monomer a good fit could be obtained with a dimer-octamer model for sedimentation equilibrium and velocity experiments at both 10 mM and 100 mM KCl according to Reaction 3 (Fig. 4).

$$4(NAP1)_2\text{-}(H2A{\cdot}H2B)_1 \rightleftarrows (NAP1)_8\text{-}(H2A{\cdot}H2B)_4$$

REACTION 3

A NAP1 hexadecamer species with $H2A^f{\cdot}H2B$ was not detected in the experiments. Using a dimer-octamer-hexadecamer model did not improve the fit, and the K_{d8-16} values indicated negligible amounts of hexadecamer. Interestingly, already at 10 mM KCl the octamer complex was present, suggesting a stabilization of the NAP1 octamer upon histone binding at this

TABLE II
Hydrodynamic parameters of NAP1 complexes

	s^a	Molecular mass[b]	$f/f_o{}^c$	$D \times 10^{7d}$	Model fit Reaction[a]
	S	*kDa*		$cm^2\ s^{-1}$	
NAP1	2.4 ± 0.2	51.3	1.80 ± 0.16	4.1 ± 0.4	1
$(NAP1)_2$	4.4 ± 0.2	102.6	1.56 ± 0.07	3.8 ± 0.4	1, 2
$(NAP1)_8$	11.4 ± 0.8	410.4	1.52 ± 0.10	2.5 ± 0.2	2
$(NAP1)_{16}$	21.3 ± 0.5	820.8	1.29 ± 0.05	2.3 ± 0.1	2
$(NAP1)_2$-$(H2A{\cdot}H2B)_1$	5.5 ± 0.7	131.1	1.45 ± 0.16	3.8 ± 0.4	3
$(NAP1)_8$-$(H2A{\cdot}H2B)_4$	16.6 ± 2.2	524.4	1.21 ± 0.14	2.8 ± 0.4	3
$(NAP1)_2$-$(H3{\cdot}H4)_1$	5.5 ± 0.7	129.8	1.44 ± 0.16	3.8 ± 0.4	4
$(NAP1)_4$-$(H3{\cdot}H4)_2$	10.9 ± 1.6	259.6	1.15 ± 0.14	3.8 ± 0.5	4
$(NAP1)_8$-$(H3{\cdot}H4)_4$	16.6 ± 2.2	519.2	1.19 ± 0.14	2.9 ± 0.4	4

[a] The sedimentation coefficient at standard conditions (20 °C, H_2O) as determined from single and global fits to models described by Reactions 1–4 as indicated using SEDPHAT. Standard deviations were determined from averaging results from single fits.
[b] Calculated molecular masses are included as a fixed parameter in the analysis of sedimentation velocity runs.
[c] Ratio of the measured friction coefficient f to the friction coefficient f_o of a sphere with the same volume, including hydration.
[d] Diffusion constants at standard conditions (20 °C, H_2O) determined from the friction coefficient (35).

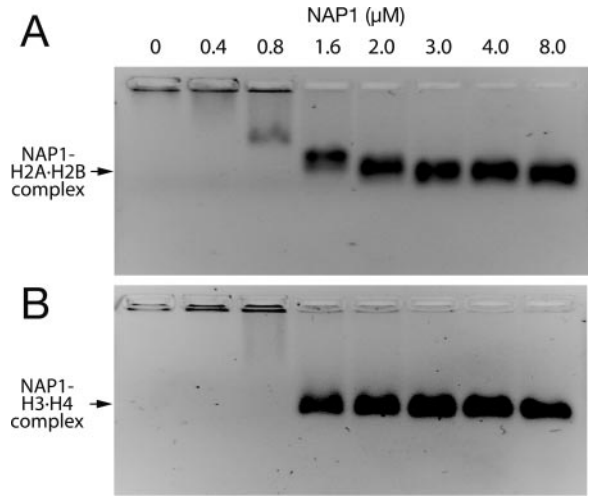

FIG. 3. **Gel shift analysis of NAP1 with the H2A·H2B dimer and the $(H3{\cdot}H4)_2$ tetramer.** *A*, increasing concentrations of NAP1 were mixed with 1.0 μM $H2A^f{\cdot}H2B$ dimer. NAP1 was completely saturated with histones at a ratio of ≈1 NAP1 monomer per histone. *B*, increasing concentrations of NAP1 were mixed with 1.0 μM $H3{\cdot}H4^f$ dimer. At a ratio of ≈1 NAP1 monomer per histone NAP1 was completely saturated with histones.

salt concentration. A value of $K_{d2-8} = 5 \times 10^{-16}$ M^3 and $(K_{d2-8})^{1/3} = 8 \times 10^{-6}$ M was measured. At 100 mM KCl the multimerization occurred with $K_{d2-8} = 3 \times 10^{-18}$ M^3 and $(K_{d2-8})^{1/3} = 1.4 \times 10^{-6}$ M. This is very similar to the NAP1 dimer-octamer equilibrium in the absence of histones showing that the binding of $H2A^f{\cdot}H2B$ dimer had little effect on the formation of the NAP1 octamer at 100 mM KCl. The Histone $H2A^f{\cdot}H2B$ dimer interacted with NAP1 with high affinity, because no indication for the presence of free $H2A^f{\cdot}H2B$ dimer was found at a 1:1 stoichiometry of NAP1 and histone. This is consistent with a NAP1·histone dissociation constant of 20 nM at 0.1 M ionic strength as estimated from affinity blotting experiments (38).

To determine the sedimentation coefficients of the NAP1-$H2A^f{\cdot}H2B$ complexes sedimentation velocity runs were performed and analyzed according to Reaction 3. A representative fit at 10 mM KCl is shown in Fig. 4*C*. The sedimentation coefficient of the $(NAP1)_2$-$(H2A^f{\cdot}H2B)_1$ dimer complex was measured to be 5.5 ± 0.7 S and for the $(NAP1)_8$-$(H2A^f{\cdot}H2B)_4$ octamer complex a value of $s = 16.6 \pm 2.2$ S was determined (Table II).

NAP1 Dimer and Octamer Form Complexes with H3·H4—The analysis of NAP1 complexes in the presence of H3·H4 was also conducted at 496 nm to detect only histone-containing species. For $H3{\cdot}H4^f$ alone a molecular mass of 29.7 ± 5 kDa was determined in equilibrium runs at 10 and 100 mM KCl with a good fit to a one component model. This value is very close to the molecular mass of 27.2 kDa calculated for the dimer, and the fit to a monomer-dimer equilibrium indicated that under these experimental conditions only a small fraction (<15%) associates into the $(H3{\cdot}H4^f)_2$ tetramer. This is consistent with previous studies that reported the dissociation of $(H3{\cdot}H4)_2$ tetramer into dimers at low ionic strength and protein concentration in the micromolar range (39, 40). The formation of a stable $(H3{\cdot}H4)_2$ tetramer would require higher protein and salt concentrations than those used here (40).

NAP1 and histones were mixed in equimolar amounts and examined by sedimentation equilibrium (Fig. 5*A*) and velocity centrifugation (Fig. 5*B*) at 10 mM and 100 mM KCl. All data sets showed a good fit to a dimer-tetramer-octamer model with a fixed molecular mass of 129.8 kDa for the $(NAP1)_2$-$(H3{\cdot}H4^f)_1$ dimer complex as described in Reaction 4.

$$4(NAP1)_2\text{-}(H3{\cdot}H4)_1 \rightleftarrows 2(NAP1)_4\text{-}(H3{\cdot}H4)_2 \rightleftarrows (NAP1)_8\text{-}(H3{\cdot}H4)_4$$

REACTION 4

Thus, $H3{\cdot}H4^f$ behaves very similar to $H2A^f{\cdot}H2B$ in its interaction with NAP1 but in addition to the dimer and octamer complex an association state forms, in which two NAP1 dimers stabilize the $(H3\text{-}H4^f)_2$ tetramer complex. At 10 mM KCl this complex was the prevalent species, and little octamer complex was present, whereas at 100 mM KCl the concentration of the $(NAP1)_4$-$(H3{\cdot}H4^f)_2$ complex was low and the $(NAP1)_8$-$(H3{\cdot}H4^f)_4$ complex formed with a dissociation constant of $K_{d2-8} = 2 \times 10^{-17}$ M^3 and $(K_{d2-8})^{1/3} = 3 \times 10^{-6}$ M.

Sedimentation coefficients for the $(NAP1)_2$-$(H3{\cdot}H4^f)$ and $(NAP1)_8$-$(H3{\cdot}H4^f)_4$ complexes were found to be equivalent to those of the corresponding complexes with $H2A^f{\cdot}H2B$ within the accuracy of the measurement. Accordingly, the values for these association states were averaged resulting in $s = 5.5 \pm 0.7$ S (dimer) and $s = 16.6 \pm 2.2$ S (octamer). The sedimentation coefficient of the $(NAP1)_4$-$(H3{\cdot}H4^f)_2$ complex was determined to be 10.9 ± 1.6 S (Table II).

Conformations of NAP1 Complexes Are Derived from Hydrodynamic Measurements—From the sedimentation coefficients measured for the NAP1 complexes the ratio of the friction coefficient f to that of a sphere with the same volume and friction coefficient f_o was calculated (Table II). The relatively high f/f_o ratios indicate that the conformation of NAP1 dimer and octamer differ significantly from a sphere for which f/f_o would equal one. Upon binding of histones to NAP1 dimer only a small decrease of the friction coefficient ratio was observed from 1.52 ± 0.10 to 1.45 ± 0.16 for the $(NAP1)_2$-$(H2A{\cdot}H2B)_1$

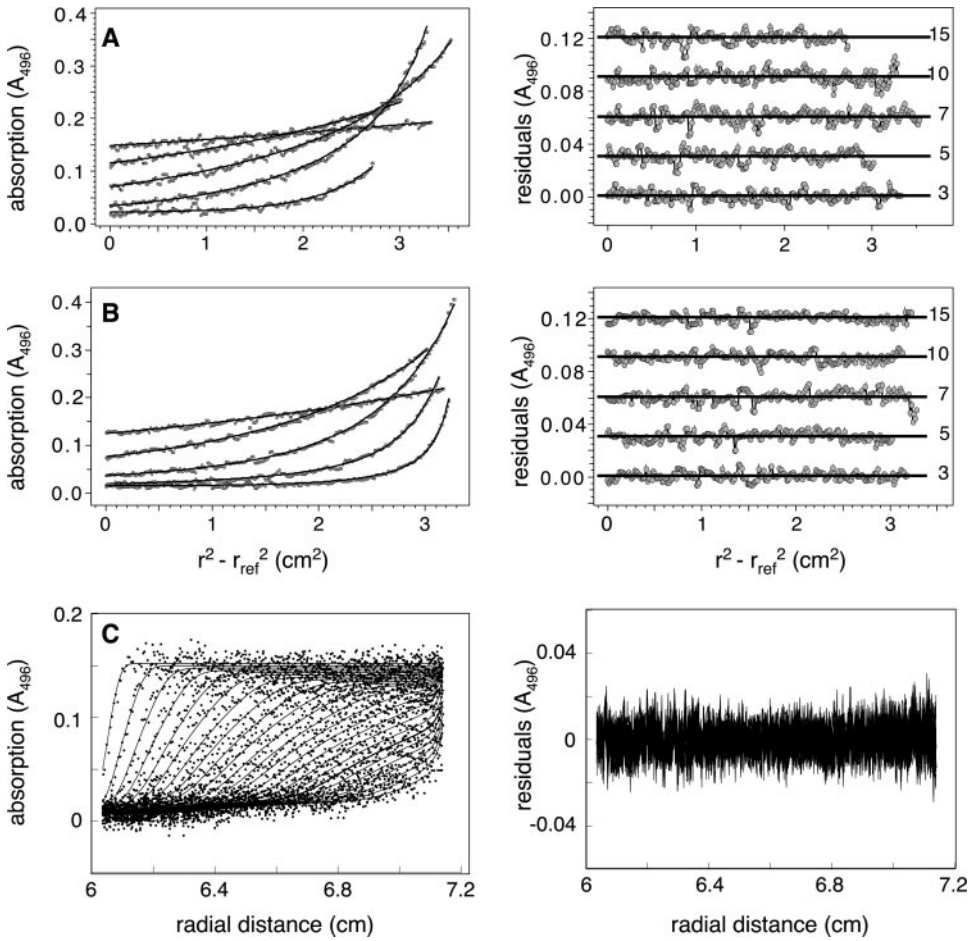

FIG. 4. **Analytical ultracentrifugation of NAP1 complexes with histone H2A^f·H2B dimer.** Experiments were recorded at 496 nm. The *left panel* shows the experimental data and the fitted curves in dependence of the normalized radial position. On the *right* the residuals of the fits are plotted. Runs were fitted to the model given in Reaction 3 with the molecular mass of the $(NAP1)_2$-$(H2A{\cdot}H2B)_1$ species constrained to 131.2 kDa. Data acquired at 10 mM KCl (*A*) and 100 mM KCl (*B*) are shown. *C*, sedimentation velocity run at 10 mM and a NAP1/histone ratio of 1:1. Only every fifth scan is shown.

and to 1.44 ± 0.16 for the $(NAP1)_2$-$(H3{\cdot}H4)_1$ species. In contrast the NAP1 octamer complex adopted a more globular shape when associated with histones, because the value of f/f_o decreased significantly. In analogy to the stacked annular pentamer-decamer structure formed by the histone chaperone nucleoplasmin (9, 10, 41) we propose the model depicted in Fig. 6*A*. It is consistent with the hydrodynamic parameters derived from the sedimentation velocity analysis, but it is noted also that other arrangements of NAP1 subunits would be compatible with the measured friction coefficient ratios. In our model the NAP1 octamer forms an annular structure, which can stack to form a hexadecamer. The disk-shaped structure of the depicted octamer has a relatively high friction coefficient, and stacking of two octamers would lead to a reduction of the f/f_o ratio as observed in the sedimentation velocity runs, which yielded values of $f/f_o = 1.52 \pm 0.10$ (octamer) and $f/f_o = 1.29 \pm 0.05$ (hexadecamer) (Table II). Upon histone binding the NAP1 octamer undergoes a transition to a more compact association state as indicated in Fig. 6*A* by an accompanying decrease of the central cavity.

The friction coefficients and the known molecular weights can be used to calculate the diffusion constant *D*. The values for *D* in pure water are listed in Table II. From mobility measurements of other proteins like GFP it is estimated that in the cell the corresponding *in vivo* value would be 3 to 4 times lower due to the higher viscosity in the absence of any topological constraints to the mobility imposed by chromatin or other cellular structures (42).

NAP1 Octamer Formation Could Be Induced in Vivo during S Phase by NAP1 Accumulation in the Nucleus—The number of NAP1 monomers in haploid yeast cells has been determined to be around 8070 molecules in microarray experiments (43). During G_1 phase NAP1 is mostly excluded from the nucleus (21, 44). A haploid yeast cell has an average cell volume of 32 μm^3 (45). Estimating that about half of the cell volume is occupied by organelles like nucleus, vacuole, mitochondria, and the Golgi apparatus that are inaccessible to NAP1 this would correspond to a concentration of ≈1 μM NAP1 monomer or ≈0.5 μM NAP1 dimer. From the dissociation constants K_{d2-8} and K_{d8-16} determined in the AUC experiments it can be concluded that during G_1 phase NAP1 is present in the cytoplasm mostly as a dimer. As plotted in Fig. 6*B* the fraction of NAP1 present in the dimer, octamer, and hexadecamer state would be 94:6:0.1%.

During S phase dephosphorylation of NAP1 leads to its accumulation in the nucleus (14, 19) with some increase in the expression level (18) resulting in a significantly higher NAP1 concentration. The yeast nucleus has a total volume of ~3.6 μm^3 of which not more than 2.9 μm^3 are estimated to be accessible for NAP1 (46, 47). Without considering any increase in the expression level a concentration of 4 μM NAP1 monomer could be reached if 80% of NAP1 would be localized in the nucleus. This would favor the association of NAP1 dimer into octamer and hexadecamer. For a 2 μM NAP1 dimer concentration the ratio of dimer:octamer:hexadecamer is 50:38:12% (Fig. 6*B*). Taking into consideration that upon histone binding the

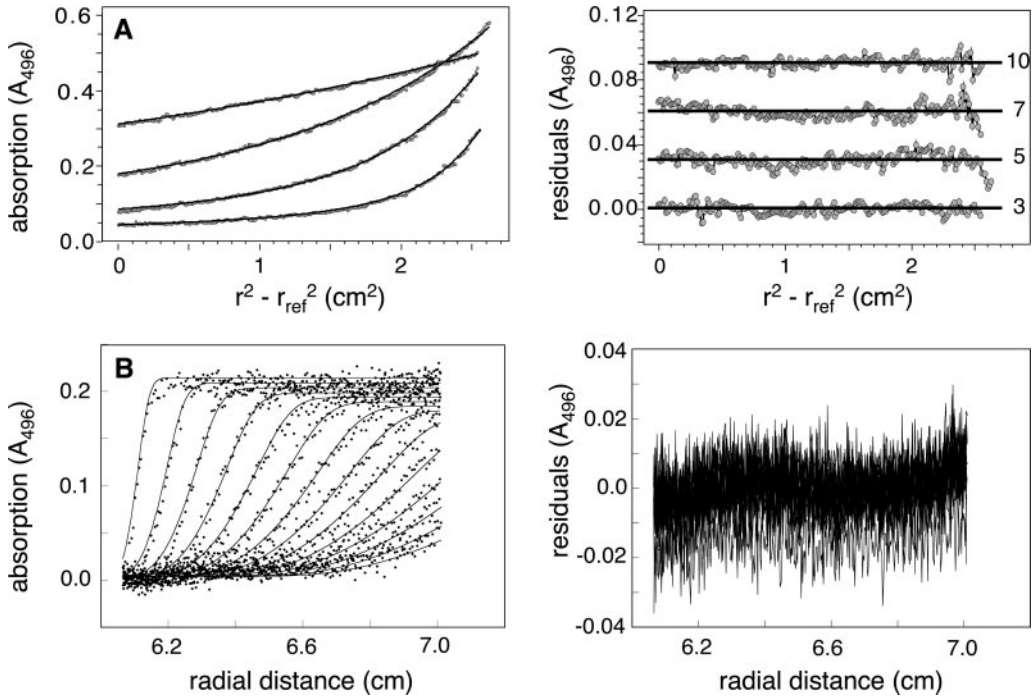

FIG. 5. **Analytical ultracentrifugation of NAP1 complexes with histone $(H3{\cdot}H4^f)_2$ tetramer.** Experiments were recorded at 496 nm. The *left panel* shows the experimental data and the fitted curves in dependence of the normalized radial position. On the *right* the residuals of the fits are plotted. Equilibrium runs were fitted to the model given in Reaction 4 with the molecular mass of the $(NAP1)_2$-$(H3{\cdot}H4^f)_1$ species constrained to 129.8 kDa. The data sets shown were acquired at 100 mM KCl by equilibrium sedimentation (*A*) and velocity sedimentation (*B*), where only every fifth scan is shown.

hexadecamer was destabilized and not detected in the AUC experiments the fraction of NAP1 in dimeric and octameric complexes would be 53:47%.

DISCUSSION

NAP1 mediates various important biological activities like the rearrangement of nucleosomes during transcription, the shuttling of the histone H2A·H2B dimer from the cytoplasm to the nucleus, and the assembly of newly synthesized DNA into chromatin (see Refs. 5–7, 10 for reviews). These diverse functions of NAP1 are likely to differ with respect to the number and type of histones found in complexes with NAP1. An understanding of the different NAP1 association states is therefore an essential prerequisite for any mechanistic studies of NAP1 activities. Considerable efforts have been made to characterize the multimer equilibrium of NAP1 alone and in complexes with histones (13, 14, 23, 25, 26). However, the physiologically relevant association states adopted by NAP1 remained to be elucidated. Here analytical ultracentrifugation was used to identify the complexes of NAP1 alone and with core histones, and to characterize these with respect to their thermodynamic stability and hydrodynamic shape.

The NAP1 monomer was only observed at unphysiologically low ionic strength and associates into a dimer with high affinity if the salt concentration is raised. At physiological ionic strength an equilibrium between NAP1 dimer, octamer, and hexadecamer was present (Table I). The measured sedimentation coefficients of the monomer (2.4 ± 0.2 S) and dimer (4.4 ± 0.2 S) determined in our analysis are in good agreement with the values measured recently in the presence of 500 mM KCl and 1.8 M guanidinium hydrochloride (26). In addition, a NAP1 octamer and hexadecamer were identified here with *s* values of 11.4 ± 0.8 and 21.3 ± 0.5 (Table II). The data summarized in Tables I and II lead to the model shown in Fig. 6*A*, in which the NAP1 dimer associates into a disk-shaped annular octamer. The hexadecamer is formed by stacking two octamers on top of each other. This conformation is consistent with the large reduction of the friction coefficient ratio from f/f_o = 1.52 ± 0.10 (octamer) to f/f_o = 1.29 ± 0.05 (hexadecamer). Because these conformations are similar to the pentamer-decamer structure formed by the histone chaperone nucleoplasmin (9, 10, 41), they appear the most likely, although other shapes and arrangements of NAP1 subunits would also be compatible with the observed friction coefficient ratios.

The interactions between NAP1 and core histones were investigated first in gel shift experiments, and a stoichiometry of 1:1 for NAP1-histone complexes was measured, which confirms the results reported previously (25). The NAP1-histone complexes have been described to sediment between 5 and 12 S (13, 14, 23, 24). Here, the species that predominantly form under physiological salt and protein concentrations were identified as a NAP1 dimer bound to a histone dimer (5.5 ± 0.7 S) and a NAP1 octamer-histone complex (16.6 ± 2.2 S) (Table II). No significant shifts in the equilibrium between the NAP1 dimer and the NAP1 octamer were observed upon histone binding under these conditions.

Based on AUC results and estimates of the intracellular concentration of NAP1 the model shown in Fig. 7 was devised for the cell cycle-dependent formation of different NAP1 association states. During transcription chromatin regions have to adopt a more open conformation. Removal of one H2A·H2B dimer from the histone octamer seems to be essential for transcription elongation through nucleosomes (48, 49), and NAP1 and other histone chaperones stimulate the binding of transcription factors to chromatin templates (50, 51). In addition, the histone H2A·H2B dimer exchanges more rapidly than the H3·H4 tetramer *in vivo* (52, 53). It has been shown that NAP1 is present in complexes with SWR1 that catalyzed the exchange of H2A·H2B dimer to a dimer variant in yeast (54). Thus, as shown in Fig. 7, mediating the dissociation and rebinding of single H2A·H2B dimers during transcription in G_1 phase is a likely function of NAP1 dimers that could explain its effect on gene expression (15). During DNA replication in S

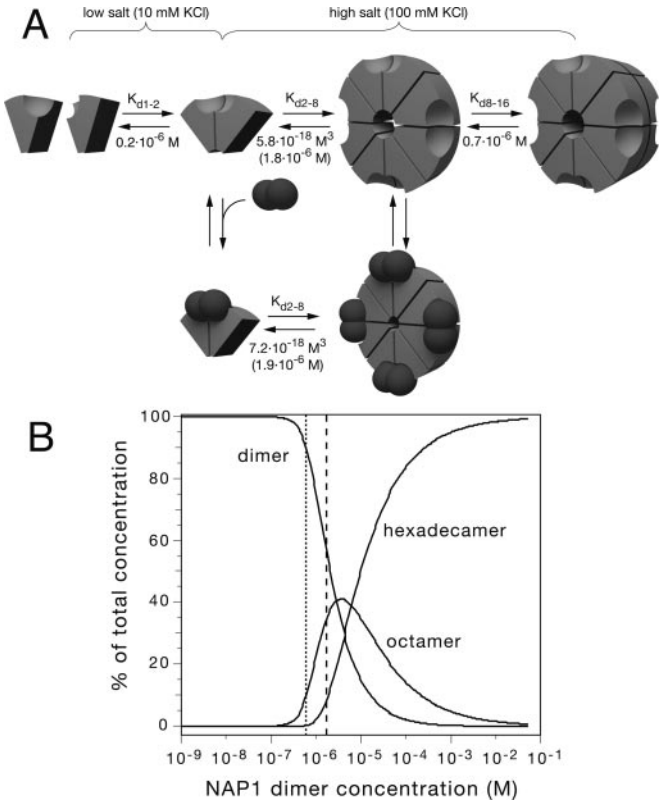

FIG. 6. *A*, model of association states of NAP1. At low salt concentration (10 mM KCl) NAP1 is present as a monomer and a dimer. At higher salt concentration (100 mM) the smallest association state is the NAP1 dimer. This associates further to an octamer and a hexadecamer with the indicated K_d values. The values in *parentheses* refer to $(K_{d2-8})^{1/3}$, the concentration at which the ratio of NAP1 in the dimeric and octameric state is 1:1. The K_d values for multimerization of complexes with histones are similar to those of free NAP1. However, no hexadecamer was detected in the presence of histones. The NAP1 octamer-histone complex adopts a more compact conformation than the free NAP1 octamer as inferred from the hydrodynamic analysis. H3·H4 behaves essentially as H2A·H2B except for an additional intermediate complex formed predominantly at 10 mM KCl as described in Reaction 4. *B*, dependence of the three NAP1 species on total NAP1 concentration. At 1 μM NAP1 monomer concentration the protein is mostly present as a dimer with a ratio of dimer:octamer:hexadecamer of 94:6:0.1 (*dotted line*). In contrast, at around 4 μM NAP1 monomer half of the protein is in larger complexes with relative dimer:octamer:hexadecamer fractions of 50:38:12 (*dashed line*).

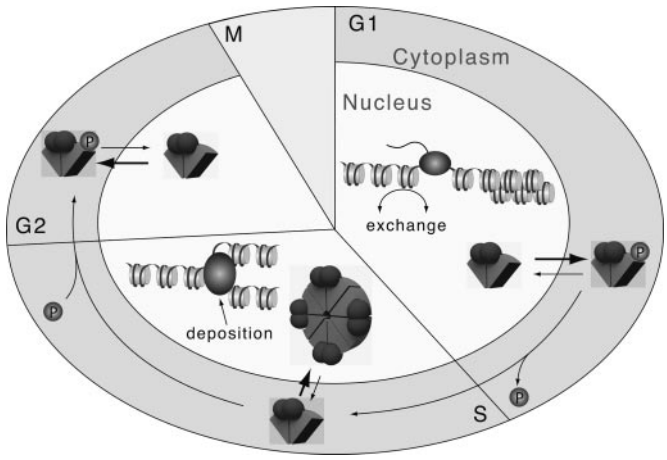

FIG. 7. **Hypothetical model for the cell cycle-dependent association states of NAP1.** During G_1 phase NAP1 is mainly phosphorylated and thus cytoplasmic. Low concentrations of NAP1 present as dimers in the nucleus participate in chromatin rearrangement during transcription regulation and bind free H2A·H2B dimers. For this function a dimer that can carry the H2A·H2B dimer would be sufficient. During transition into S phase NAP1 is dephosphorylated and accumulates in the nucleus leading to higher concentrations. This induces the association of NAP1 into the octameric state, which is able to carry multiple H2A·H2B dimers and possibly also H3·H4 dimers to the replication sites. At the end of S phase NAP1 gets phosphorylated again, is exported to the cytoplasm, and dissociates to a dimer.

phase histones are needed in large quantities in the nucleus. Upon dephosphorylation during the G_1/S transition NAP1 shuttles histones into the nucleus (14, 19–21, 55). In some cases also a higher expression of NAP1 was observed during S-phase (16, 18). Due to the accumulation of NAP1 in the nucleus its local concentration increases, leading to a significant increase of the NAP1 octamer complex fraction (Fig. 6*B*). Based on these results, it is estimated that for a concentration of 2 μM NAP1 dimer in the nucleus ~50% would be present in the octamer complex. The actual fraction of the NAP1 octamers might be higher *in vivo* due to excluded volume effects that are referred to as macromolecular crowding (56). Furthermore, the NAP1 dimer-octamer equilibrium could be directly affected by post-translational modifications like polyglutamylation (57), phosphorylation, or acetylation. Acetylation of NAP1 by p300 was shown to promote its ability to assemble chromatin and facilitates the transfer of H2A·H2B from nucleosomes to NAP1. Acetylation occurs in a cell cycle-dependent manner (19, 58) suggesting a possible regulatory function in histone binding and complex assembly. Here it is proposed that during S-phase the nuclear NAP1 complex is present mostly as an octamer (Figs. 6 and 7). This complex has eight histone binding sites, which could facilitate the *de novo* assembly of nucleosomes by binding two H2A·H2B dimers and two H3·H4 dimers, sufficient for the assembly of a complete histone octamer. It is noted that the *in vitro* experiments presented here and in the literature show high affinity binding of NAP1 to all core histones (13, 14, 23–25). However, an *in vivo* interaction of NAP1 with histones H3·H4 has not been demonstrated and only NAP1-H2A·H2B complexes have been isolated by immunoprecipitation experiments (11, 14, 22). This suggests that the NAP1 interaction with H3·H4 is prevented by the association of H3·H4 dimers with histone chaperone CAF-1 (5, 39, 59) and/or DNA. However, NAP1 is sufficient for the *in vitro* assembly of nucleosomes and can serve as a carrier for all four core histones in the reaction (60). This process is of considerable interest for the reconstitution of chromatin with defined histone composition. It is also conceivable that the NAP1-mediated assembly of complete nucleosomes is taking place *in vivo* under specific conditions that remain to be identified.

In summary, NAP1 has various important activities like the import of H2A·H2B into the nucleus and the assembly of two H2A·H2B dimers and possibly also H3·H4 into nucleosomes during replication. Furthermore, it interacts with the histone H2A·H2B dimer during transcription and histone exchange. These processes differ with respect to the number of histones involved. Thus, the quantitative description of the association states of NAP1 alone and in complexes with histones presented here provides new insights into the mechanisms by which NAP1 can exert its different biological functions.

Acknowledgments—The support of Peter Lichter is gratefully acknowledged. We thank Felix Kepert, Malte Wachsmuth, Lutz Ehrhardt, and Borries Demeler for help and Tamas Fischer for valuable discussions. We are grateful to Karolin Luger, Gernot Laengst, and Tom Owen-Hughes for providing plasmid vectors. The project was supported by the Volkswagen Foundation in the program "Junior Research Groups at German Universities."

REFERENCES

1. Arents, G., Burlingame, R. W., Wang, B.-C., Love, W. E., and Moudrianakis, E. N. (1991) *Proc. Natl. Acad. Sci. U. S. A.* **88,** 10148–10152
2. Luger, K., Mäder, A. W., Richmond, R. K., Sargent, D. F., and Richmond, T. J.

(1997) *Nature* **389,** 251–260
3. Davey, C. A., Sargent, D. F., Luger, K., Maeder, A. W., and Richmond, T. J. (2002) *J. Mol. Biol.* **319,** 1097–1113
4. Harp, J. M., Hanson, B. L., Timm, D. E., and Bunick, G. J. (2000) *Acta Crystallogr. D Biol. Crystallogr.* **56,** 1513–1534
5. Loyola, A., and Almouzni, G. (2004) *Biochim. Biophys. Acta* **1677,** 3–11
6. Tyler, J. K. (2002) *Eur. J. Biochem.* **269,** 2268–2274
7. Adams, C. R., and Kamakaka, R. T. (1999) *Curr. Opin. Genet. Dev.* **9,** 185–190
8. Haushalter, K. A., and Kadonaga, J. T. (2003) *Nat. Rev. Mol. Cell. Biol.* **4,** 613–620
9. Prado, A., Ramos, I., Frehlick, L. J., Muga, A., and Ausio, J. (2004) *Biochem. Cell Biol.* **82,** 437–445
10. Akey, C. W., and Luger, K. (2003) *Curr. Opin. Struct. Biol.* **13,** 6–14
11. Nakagawa, T., Bulger, M., Muramatsu, M., and Ito, T. (2001) *J. Biol. Chem.* **276,** 27384–27391
12. van Holde, K. E. (1989) *Chromatin*, p. 416, Springer, Heidelberg
13. Ishimi, Y., Hirosumi, J., Sato, W., Sugasawa, K., Yokota, S., Hanaoka, F., and Yamada, M. (1984) *Eur. J. Biochem.* **142,** 431–439
14. Ito, T., Bulger, M., Kobayashi, R., and Kadonaga, J. T. (1996) *Mol. Cell. Biol.* **16,** 3112–3124
15. Ohkuni, K., Shirahige, K., and Kikuchi, A. (2003) *Biochem. Biophys. Res. Commun.* **306,** 5–9
16. Dong, A., Zhu, Y., Yu, Y., Cao, K., Sun, C., and Shen, W. H. (2003) *Planta* **216,** 561–570
17. Zimmerman, Z. A., and Kellogg, D. R. (2001) *Mol. Biol. Cell* **12,** 201–219
18. Mortensen, E. M., McDonald, H., Yates, J., 3rd, and Kellogg, D. R. (2002) *Mol. Biol. Cell* **13,** 2091–2105
19. Asahara, H., Tartare-Deckert, S., Nakagawa, T., Ikehara, T., Hirose, F., Hunter, T., Ito, T., and Montminy, M. (2002) *Mol. Cell. Biol.* **22,** 2974–2983
20. Rodriguez, P., Munroe, D., Prawitt, D., Chu, L. L., Bric, E., Kim, J., Reid, L. H., Davies, C., Nakagama, H., Loebbert, R., Winterpacht, A., Petruzzi, M. J., Higgins, M. J., Nowak, N., Evans, G., Shows, T., Weissman, B. E., Zabel, B., Housman, D. E., and Pelletier, J. (1997) *Genomics* **44,** 253–265
21. Miyaji-Yamaguchi, M., Kato, K., Nakano, R., Akashi, T., Kikuchi, A., and Nagata, K. (2003) *Mol. Cell. Biol.* **23,** 6672–6684
22. Chang, L., Loranger, S. S., Mizzen, C., Ernst, S. G., Allis, C. D., and Annunziato, A. T. (1997) *Biochemistry* **36,** 469–480
23. Ishimi, Y., Sato, W., Kojima, M., Sugasawa, K., Hanaoka, F., and Yamada, M. (1985) *Cell Struct. Funct.* **10,** 373–382
24. Fujii-Nakata, T., Ishimi, Y., Okuda, A., and Kikuchi, A. (1992) *J. Biol. Chem.* **267,** 20980–20986
25. McBryant, S. J., Park, Y. J., Abernathy, S. M., Laybourn, P. J., Nyborg, J. K., and Luger, K. (2003) *J. Biol. Chem.* **278,** 44574–44583
26. McBryant, S. J., and Peersen, O. B. (2004) *Biochemistry* **43,** 10592–10599
27. Laue, T. M., and Stafford, W. F., 3rd. (1999) *Annu. Rev. Biophys. Biomol. Struct.* **28,** 75–100
28. Lebowitz, J., Lewis, M. S., and Schuck, P. (2002) *Protein Sci.* **11,** 2067–2079
29. Laue, T. M., Shah, B. D., Ridgeway, T. M., and Pelletier, S. L. (1992) in *Analytical Ultracentrifugation in Biochemistry and Polymer Science* (Harding, S. E., Rowe, A. J., and Horton, J. C., eds) pp. 90–125, Royal Society of Chemistry, Cambridge
30. Luger, K., Rechsteiner, T. J., and Richmond, T. J. (1999) *Methods Enzymol.* **304,** 3–19
31. Kepert, J. F., Fejes Tóth, K., Caudron, M., Mücke, N., Langowski, J., and Rippe, K. (2003) *Biophys. J.* **85,** 4012–4022
32. Lee, K. M., and Hayes, J. J. (1997) *Proc. Natl. Acad. Sci. U. S. A.* **94,** 8959–8964
33. Bruno, M., Flaus, A., Stockdale, C., Rencurel, C., Ferreira, H., and Owen-Hughes, T. (2003) *Mol. Cell* **12,** 1599–1606
34. Haugland, R. P. (2004) *Handbook of Fluorescent Probes and Research Chemicals*, 9th Ed., pp. 20–36, Molecular Probes, Eugene, OR
35. Rippe, K., Mücke, N., and Schulz, A. (1998) *J. Mol. Biol.* **278,** 915–933
36. Schuck, P. (2003) *Anal. Biochem.* **320,** 104–124
37. Luger, K., Rechsteiner, T. J., Flaus, A. J., Waye, M. M., and Richmond, T. J. (1997) *J. Mol. Biol.* **272,** 301–311
38. McQuibban, G. A., Commisso-Cappelli, C. N., and Lewis, P. N. (1998) *J. Biol. Chem.* **273,** 6582–6590
39. Tagami, H., Ray-Gallet, D., Almouzni, G., and Nakatani, Y. (2004) *Cell* **116,** 51–61
40. Baxevanis, A. D., Godfrey, J. E., and Moudrianakis, E. N. (1991) *Biochemistry* **30,** 8817–8823
41. Dutta, S., Akey, I. V., Dingwall, C., Hartman, K. L., Laue, T., Nolte, R. T., Head, J. F., and Akey, C. W. (2001) *Mol. Cell* **8,** 841–853
42. Wachsmuth, M., Waldeck, W., and Langowski, J. (2000) *J. Mol. Biol.* **298,** 677–689
43. Ghaemmaghami, S., Huh, W. K., Bower, K., Howson, R. W., Belle, A., Dephoure, N., O'Shea, E. K., and Weissman, J. S. (2003) *Nature* **425,** 737–741
44. Rodriguez, P., Pelletier, J., Price, G. B., and Zannis-Hadjopoulos, M. (2000) *J. Mol. Biol.* **298,** 225–238
45. Johnston, G. C., Ehrhardt, C. W., Lorincz, A., and Carter, B. L. (1979) *J. Bacteriol.* **137,** 1–5
46. Ostashevsky, J. (2002) *Mol. Biol. Cell* **13,** 2157–2169
47. Weidemann, T., Wachsmuth, M., Knoch, T. A., Muller, G., Waldeck, W., and Langowski, J. (2003) *J. Mol. Biol.* **334,** 229–240
48. Studitsky, V. M., Walter, W., Kireeva, M., Kashlev, M., and Felsenfeld, G. (2004) *Trends Biochem. Sci.* **29,** 127–135
49. Belotserkovskaya, R., Oh, S., Bondarenko, V. A., Orphanides, G., Studitsky, V. M., and Reinberg, D. (2003) *Science* **301,** 1090–1093
50. Walter, P. P., Owen-Hughes, T. A., Cote, J., and Workman, J. L. (1995) *Mol. Cell. Biol.* **15,** 6178–6187
51. Chen, H., Li, B., and Workman, J. L. (1994) *EMBO J.* **13,** 380–390
52. Kimura, H., and Cook, P. R. (2001) *J. Cell Biol.* **153,** 1341–1353
53. Levchenko, V., and Jackson, V. (2004) *Biochemistry* **43,** 2359–2372
54. Mizuguchi, G., Shen, X., Landry, J., Wu, W. H., Sen, S., and Wu, C. (2004) *Science* **303,** 343–348
55. Li, M., Strand, D., Krehan, A., Pyerin, W., Heid, H., Neumann, B., and Mechler, B. M. (1999) *J. Mol. Biol.* **293,** 1067–1084
56. Ellis, R. J. (2001) *Trends Biochem. Sci* **26,** 597–604
57. Regnard, C., Desbruyeres, E., Huet, J. C., Beauvallet, C., Pernollet, J. C., and Edde, B. (2000) *J. Biol. Chem.* **275,** 15969–15976
58. Ito, T., Ikehara, T., Nakagawa, T., Kraus, W. L., and Muramatsu, M. (2000) *Genes Dev.* **14,** 1899–1907
59. Smith, S., and Stillman, B. (1989) *Cell* **58,** 15–25
60. Ito, T., Levenstein, M. E., Fyodorov, D. V., Kutach, A. K., Kobayashi, R., and Kadonaga, J. T. (1999) *Genes Dev.* **13,** 1529–1539

Conformation of Reconstituted Mononucleosomes and Effect of Linker Histone H1 Binding Studied by Scanning Force Microscopy

Jochen Felix Kepert,* Katalin Fejes Tóth,*† Maïwen Caudron,‡ Norbert Mücke,§ Jörg Langowski,§ and Karsten Rippe*†

*Kirchhoff-Institut für Physik, AG Molekulare Biophysik (F15), Ruprecht-Karls-Universität Heidelberg, D-69120 Heidelberg, Germany; †Deutsches Krebsforschungszentrum, Molekulare Genetik (B060), D-69120 Heidelberg, Germany; ‡European Molecular Biology Laboratory, Karsenti Group, 69117 Heidelberg, Germany; and §Deutsches Krebsforschungszentrum, Biophysik der Makromoleküle (B040), D-69120 Heidelberg, Germany

ABSTRACT The conformation of mononucleosome complexes reconstituted with recombinant core histones on a 614-basepair-long DNA fragment containing the *Xenopus borealis* 5S rRNA nucleosome positioning sequence was studied by scanning/atomic force microscopy in the absence or presence of linker histone H1. Imaging without prior fixation was conducted with air-dried samples and with mononucleosomes that were injected directly into the scanning force microscopy fluid cell and visualized in buffer. From a quantitative analysis of ~1,700 complexes, the following results were obtained: i), In the absence of H1, a preferred location of the nucleosome at the *X. borealis* 5S rRNA sequence in the center of the DNA was detected. From the distribution of nucleosome positions, an energy difference of binding to the 5S rRNA sequence of $\Delta\Delta G \approx 3$ kcal mol^{-1} as compared to a random sequence was estimated. Upon addition of H1, a significantly reduced preference of nucleosome binding to this sequence was observed. ii), The measured entry-exit angles of the DNA at the nucleosome in the absence of H1 showed two maxima at 81 ± 29° and 136 ± 18° (air-dried samples), and 78 ± 25° and 137 ± 25° (samples imaged in buffer solution). In the presence of H1, the species with the smaller entry-exit angle was stabilized, yielding average values of 88 ± 34° for complexes in air and 85 ± 10° in buffer solution. iii), The apparent contour length of the nucleosome complexes was shortened by 34 ± 13 nm as compared to the free DNA due to wrapping of the DNA around the histone octamer complex. Considering an 11 nm diameter of the nucleosome core complex, this corresponds to a total of 145 ± 34 basepairs that are wound around the nucleosome.

INTRODUCTION

In eukaryotes, the DNA is packaged by histone proteins into a chain of nucleosomes, in which 146 or 147 basepairs of DNA are wrapped in 1.67 turns of a left-handed superhelix around a histone octamer complex (Davey et al., 2002; Hansen, 2002; Luger et al., 1997a; Ramakrishnan, 1997b; Richmond and Widom, 2000; van Holde, 1989). This protein core consists of two copies each of the four histones, H2A, H2B, H3, and H4. The nucleosome is the basic building block of the chromatin fiber and changes of its conformation are likely to modulate the organization of the fiber. The structure of the free histone octamer and that of the nucleosome complex has been determined by high resolution x-ray diffraction (Arents et al., 1991; Davey et al., 2002; Harp et al., 2000; Luger et al., 1997a). The nucleosome has a cylindrical shape with a diameter of ~11 nm and a height of 5.5 nm.

A fifth histone, the so-called linker histone H1 or H5, binds to the nucleosome core complex (Graziano et al., 1994; Ramakrishnan, 1997a; Zhou et al., 1998; Zlatanova and van Holde, 1996). Although its exact binding site and orientation are still unknown, it seems to affect the trajectory of the DNA at the nucleosome. It has been proposed that H1 binding constrains the entry-exit angle of the DNA at the nucleosome and thus contributes to the formation of higher order chromatin structure (Bednar et al., 1998; Furrer et al., 1995; Hamiche et al., 1996; Leuba et al., 1998a,b; Ramakrishnan, 1997a; Tóth et al., 2001; Travers, 1999; Zlatanova et al., 1998). The linker histones can modulate gene transcription (Zlatanova et al., 2000). For example, it has been shown that histone H1 can selectively repress the transcription of oocytic 5S rDNA in *Xenopus borealis* (Buttinelli et al., 1999). Linker histones can also act as general transcription regulators as they play a role in inhibition of histone acetylation (Herrera et al., 2000).

We have applied scanning force microscopy (SFM, also termed atomic force microscopy) to determine the structural parameters of unfixed mononucleosomes reconstituted with recombinant core histone proteins DNA and linker histone H1. The recombinant histones allow the analysis of highly purified and well-defined nucleosomes in the absence of any posttranslational modifications or contaminations with other chromosomal proteins (Luger et al., 1997a,b). SFM can be used for imaging DNA and protein-DNA complexes without further fixing or staining of the sample, and imaging can be conducted in physiological buffer solutions. Accordingly, the technique is especially suited to study the native conformation of nucleosome complexes with minimal disturbance of the sample. Over the past years, SFM has been applied successfully in various studies of chromatin samples including oligonucleosomes, chromatin fibers, and whole metaphase chromosomes (Allen et al., 1993; Bash et al., 2003, 2001; Fritzsche and Henderson, 1996; Fritzsche et al., 1994; Karymov et al., 2001; Leuba et al., 1998a,b, 1994; Martin et al., 1995; Wang et al., 2002; Yodh et al., 1999,

Received June 24, 2003, and accepted for publication August 11, 2003.

Address reprint requests to Karsten Rippe, Tel.: +49-6221-549270; Fax: +49-6221-42524676; E-mail: Karsten.Rippe@kip.uni-heidelberg.de.

0006-3495/03/12/4012/11 $2.00

2002; Zlatanova et al., 1998). Results from the SFM chromatin analysis as well as technical aspects of these studies have been described in a number of reviews (Bustamante et al., 1997; Fritzsche et al., 1997, 1995; Leuba and Bustamante, 1999).

As proposed previously, essential determinants of the chromatin fiber structure are the entry-exit angle of the nucleosomal DNA and the rotational orientation and distance of neighboring nucleosomes, which depend on the linker DNA length (Leuba et al., 1994; Woodcock et al., 1993; Yang et al., 1994). In a series of articles, these parameters have been defined by SFM imaging and electron cryomicroscopy of chromatin fibers isolated from chicken erythrocytes (Bednar et al., 1998; Horowitz et al., 1994; Leuba et al., 1998a,b, 1994; Woodcock et al., 1993; Yang et al., 1994; Zlatanova et al., 1998). Here, we present an SFM study of unfixed recombinant nucleosome core particles with special focus on the effect of linker histone H1 binding. The samples were imaged either after air-drying or in a buffer solution that preserves the native hydration state, and a quantitative analysis of different conformational states was conducted. We find that binding of H1 stabilizes a nucleosome conformation with a smaller entry-exit angle and reduces the binding preference to the high affinity 5S rRNA sequence from *X. borealis*.

MATERIALS AND METHODS

Expression and purification of recombinant histone proteins

Overexpression and purification of recombinant histone proteins as well as reconstitution of histone octamers and mononucleosomes were essentially conducted as described (Luger et al., 1997b, 1999) using a slightly different chromatography procedure scheme on a fast protein liquid chromatography system (Amersham Biosciences, Freiburg, Germany). The supernatant from the resolubilized histone protein inclusion bodies was filtered and loaded on a 5 × 60-cm Sephacryl S-200 high resolution gel filtration column equilibrated with 1.5 column volumes of SAU-1000 buffer (7 M deionized urea, 20 mM sodium acetate, pH 5.2, 1 mM EDTA, 1 M KCl, 5 mM 2-mercaptoethanol). The column was run at room temperature at a flow rate of 3 ml/min. Elution of proteins was monitored by the absorbance at 280 nm. Fractions were analyzed on an 18% SDS-acrylamide gel and by ultraviolet spectroscopy. Pooled fractions were dialyzed against water containing 5 mM 2-mercaptoethanol overnight at 4°C using 6000–8000 MWCO dialysis bags (Spectrum Laboratories, Rancho Dominguez, CA). Proteins were lyophilized and stored at −20°C. For further purification, the probes were redissolved in SAU-50 buffer (7 M deionized urea, 20 mM sodium acetate, pH 5.2, 1 mM EDTA, 50 mM KCl, 5 mM 2-mercaptoethanol) and the protein solution was applied to a Mono S HR 5/5 cation exchange column equilibrated with the same buffer. Histones were eluted by linearly increasing the KCl concentration in 20 column volumes to 0.6 M.

Reconstitution of histone octamers was done as described previously (Luger et al., 1997b, 1999). The final purification of the octamers was conducted with a Superdex 200 HR 10/10 column equilibrated with refolding buffer (2 M KCl, 10 mM Tris-HCl, pH 7.5, 0.1 mM EDTA, 5 mM 2-mercaptoethanol). The flow rate was 0.6 ml/min. The stoichiometry of the octamer complex was checked on an 18% SDS-acrylamide gel, and fractions with equimolar amounts of the four histones were pooled and stored at −20°C in refolding buffer supplemented with glycerol to a final concentration of 50%. Octamer concentrations were determined using an extinction coefficient at 276 nm $\varepsilon_{276} = 38\ 400\ M^{-1}\cdot cm^{-1}$ (Luger et al., 1999).

Preparation of linker histone H1

Full-length histone protein H1 from calf thymus was obtained from Roche Diagnostics (Mannheim, Germany) and further purified. 5 mg of lyophilized protein were dissolved in 1 ml 1× TE buffer overnight. The protein was loaded on a 1 ml Sepharose SP-Fast Flow column and washed with 1× TE buffer supplemented with 0.3 M NaCl and 0.5 mM PMSF. Then the protein was eluted in a step gradient of 1 ml 1 × TE, 0.5 M NaCl, 0.5 mM PMSF followed by 1.4 ml of 1 × TE, 2 M NaCl, 0.5 mM PMSF. The last fractions of ~0.8 ml that showed the highest absorption at 280 nm were pooled. The protein was desalted on a NAP-5 column (Amersham Biosciences, Freiburg, Germany) previously equilibrated with H_2O. The H1-containing fraction was concentrated with Vivaspin 500 centrifugal concentrators (10000 MWCO, Sartorius, Göttingen, Germany) to a volume of 0.5 ml. This fraction was loaded on a second NAP-5 column equilibrated with 1× TE and eluted with 1 ml 1× TE. The DNA-binding activity of the purified H1 preparation was determined by analytical ultracentrifugation and fluorescence anisotropy measurements of H1 binding to a 20 bp DNA duplex under conditions of stoichiometric binding.

Reconstitution of nucleosomes

For reconstitution of nucleosomes, 100 nM of DNA fragment and 100–130 nM histone octamer were incubated for 30 min at room temperature in a buffer containing 10 mM Tris-HCl pH 7.5 and 2 M KCl. Two different DNA fragments were used: a 146-bp-long palindromic sequence derived from human α-satellite DNA studied previously (Luger et al., 1997a) was assembled by ligating the HPLC-purified synthetic oligonucleotides ATC AAT ATC CAC CTG CAG ATT CTA CCA AAA GTG TAT TTG GAA ACT GCT CCA TCA AAA GGC ATG TTC AGC T (N1), ATT CAG CTG AAC ATG CCT TTT GAT GGA GCA GTT TCC AAA TAC ACT TTT GGT AGA ATC TGC AGG TGG ATA TTG AT (N2), GAA TTC AGC TGA ACA TGC CTT TTG ATG GAG CAG TTT CCA AAT ACA CTT TTG GTA GAA TCT GCA GGT GGA TAT TGA T (N3) and ATC AAT ATC CAC CTG CAG ATT CTA CCA AAA GTG TAT TTG GAA ACT GCT CCA TCA AAA GGC ATG TTC AGC TGA (N4) (PE-Applied Biosystems, Weiterstadt, Germany) under standard conditions. The ligation product of the N1·N2 and the N3·N4 duplex was purified by HPLC chromatography using an ion-exchange Gen-Pak Fax column (Millipore, Milford, MA). The gradient was 0–0.5 NaCl (10 min) followed by 0.5–1.0 M NaCl (20 min) at 0.75 ml/min flow rate. The buffer contained 20 mM Tris-HCl, pH 7.6 and 0.1 mM EDTA. For the SFM imaging, mononucleosomes were reconstituted with a 614-bp-long DNA fragment, which was amplified by polymerase chain reaction from the plasmid pXP-10. It contains a nucleosome positioning sequence from the *X. borealis* 5S rRNA gene in the center. The polymerase chain reaction product was purified from a 1% TBE agarose gel using a gel extraction kit according to the protocol provided by the manufacturer (Qiagen, Hilden, Germany).

Formation of the octamer-DNA complex was done by salt dialysis with two different methods that yielded equivalent results. According to the first protocol, the KCl concentration was decreased from 2 M to zero in 10 mM Tris-HCl pH 7.5 buffer in a continuous gradient overnight at 4°C. The second protocol involved a stepwise reduction of the salt concentration at 4°C (Gottesfeld et al., 2001). Six different buffers with 10 mM Tris-HCl pH 7.5 and 1.5, 1, 0.8, 0.67, 0.2 M, or no KCl were used. In each dialysis step, the sample was incubated for at least 1 h. In the reconstitutions with linker histone H1, the protein was added at a ratio of 1.1 molecule H1 per nucleosome in the dialysis step with 0.67 M KCl.

After dialysis, the samples were incubated for ~2 h at 37° to equilibrate the distribution of binding positions (Luger et al., 1999), and then stored at 4°C. Reconstituted mononucleosomes were analyzed on an 8% polyacrylamide gel (29:1) or on a 1% agarose gel in 1× TBE buffer. Bands were

visualized by ethidium bromide staining. To compare the amount of free DNA relative to mononucleosomes, it should be noted that the intensity of ethidium bromide fluorescence is ~1.4 times higher for free DNA than for nucleosomal DNA (McMurray et al., 1991).

Analytical ultracentrifugation

Analytical ultracentrifugation experiments were carried out on a Beckmann Coulter (Palo Alto, CA) Optima XL-A with absorbance optics. Mononucleosome solutions of $A_{260} \approx 0.4$ were centrifuged at 20 C°. The buffer solution contained 20 mM Tris-HCl, pH 7.5, 0.1 mM EDTA, 0.1 mM DTT. For the histone octamer, a molecular mass $M = 108$ kDa and a partial specific volume $\bar{v} = 0.744$ ml·g^{-1} at 20°C was derived from the sequence with the program SEDNTERP V1.05 by J. Philo, D. Hayes, and T. Laue. The same program was used to calculate a buffer density $\rho = 0.999$ g·ml^{-1} and a viscosity $\eta = 1.008$ mPa s at 20°C. For the 146 bp DNA, a partial specific volume $\bar{v} = 0.55$ ml·g^{-1} at 20°C (Durchschlag, 1986) and a calculated molecular mass $M = 116$ kDa (Dorigo et al., 2003) was used so that nucleosome values of $M = 224$ kDa and $\bar{v} = 0.655$ ml·g^{-1} were derived. The sedimentation velocity data were recorded at 260 nm with 42,000 rpm using a spacing of 0.003 cm in the continuous scan mode. Data were analyzed by computing the g (s*) distribution (Stafford 1992, 1997) with the program DCDT+ version 1.13 by John Philo according to the algorithm described (Philo, 2000).

SFM imaging

SFM images in air and in fluid were obtained with a Multimode Scanning Probe Microscope and a Nanoscope IIIa controller from Veeco Instruments (Woodbury, NY) operating in the ''tapping mode''. The SFM samples were prepared according to the following protocols:

Imaging of air dried samples

10 μl of a solution of 2–10 nM nucleosomes in 5 mM Hepes-KOH pH 7.5, 10 mM Mg-acetate, and 50 mM K-acetate was deposited onto freshly cleaved mica (Plano, Wetzlar, Germany) and immediately washed with distilled water. The mica was then dried with a constant stream of nitrogen. Images were recorded in air at ambient humidity using etched Si-probes type ''Nanosensor'' (LOT Oriel, Darmstadt, Germany) with a force constant 17–64 N/m, a thickness of 3.5–5.0 μm, a resonance frequency between 250 and 400 kHz, and a tip curvature radius of ≈10 nm (specifications given by the manufacturer).

Imaging in buffer solutions

A solution of 60–80 μl of a buffer containing 10 mM Hepes-KOH 8.0, 30 mM NaCl, 10 mM $MgCl_2$, and nucleosomes at a concentration between 0.4 and 0.8 nM was pipetted onto a freshly cleaved mica disk. In this buffer, complexes were barely visible, most likely due to weak adhesion to the surface as observed previously, e.g., Rippe et al. (1997a,b). To increase the binding affinity of the complexes to the mica surface, $NiCl_2$ was added to a final Ni^{2+} concentration of ~10 mM (Hansma and Laney, 1996; Schulz et al., 1998). Images were recorded with NP-S Tips (Veeco Instruments) with a force constant of 0.32 N/m, a nominal tip radius curvature of 5–40 nm, and a resonance frequency ~8.7 kHz.

Image analysis

Only molecules with a single nucleosome not obstructed by other DNA fragments or protein molecules were analyzed. Complexes with the protein being bound at the end of the DNA were not included into the analysis. DNA contour length, DNA entry-exit angles, and nucleosome positions were measured with the installed Nanoscope Software and with the program Image SXM version 1.67 by Steve Barrett based on NIH Image Software from the National Institutes of Health (Bethesda, MD). The data were plotted and fitted with the program Kaleidagraph (Synergy Software, Reading, PA). The error bars correspond to the square root of the number of samples within each bin. At least four independent experiments were analyzed for the complexes studied in fluid and in air.

Analysis of nucleosome binding sites

The location of the bound nucleosome was determined by measuring the DNA contour length from the middle of the nucleosome complex to the free end of the DNA fragment that was nearer. This length was divided by the total contour length of the complex leading to values of the ratio r between 0 and 0.5. Since the *X. borealis* 5S rRNA sequence was located in the middle of the fragment, a value of $r = 0.5$ would correspond to a nucleosome at this position.

Measurement of DNA entry-exit angles

The DNA entry-exit angles at the octamer were measured with Image SXM by drawing lines through the DNA axes on both sides of the nucleosome and measuring the angle at their intersection.

Measurements of apparent contour length

The contour length was determined by drawing a curved line through the middle of the DNA contour from one end of the molecule to the other end. For the protein-DNA complexes, the curve was drawn through the center of the protein from the DNA entry and exit points.

RESULTS

Reconstitution of mononucleosomes

Recombinant histone proteins were overexpressed and purified as described (Luger et al., 1997b, 1999). Fig. 1 *A* shows a Coomassie-stained SDS gel with the purified single histones H2A, H2B, H3, and H4 and the reconstituted histone octamer. The SDS gel demonstrates that the single proteins are highly purified except for a minor shorter contaminant in the H4 preparations that was removed during further purification of the octamer. The recombinant histones H2A und H2B from *Xenopus laevis* have a very similar mobility under standard electrophoretic conditions and are hardly separated in the octamer sample (Luger et al., 1997b).

With the octamer preparation shown in Fig. 1 *A*, mononucleosomes were reconstituted by salt dialysis. Fig. 1 *B* displays a nondenaturing polyacrylamide gel of mononucleosomes assembled on a 146-bp-long palindromic sequence derived from human α-satellite DNA. This complex corresponds to the one used in previous crystallographic studies (Luger et al., 1997a, 1999). As compared to the free DNA, the octamer-DNA complex shows a strongly reduced mobility in the gel. An analysis of purified mononucleosomes on the 146 bp DNA by analytical ultracentrifugation yielded a sedimentation coefficient of $s = 11.7 \pm 0.4$ S (20°C, water) and a diffusion coefficient of $D = 3.5 \times 10^{-7}$ cm^2 s^{-1} corresponding to a molecular mass

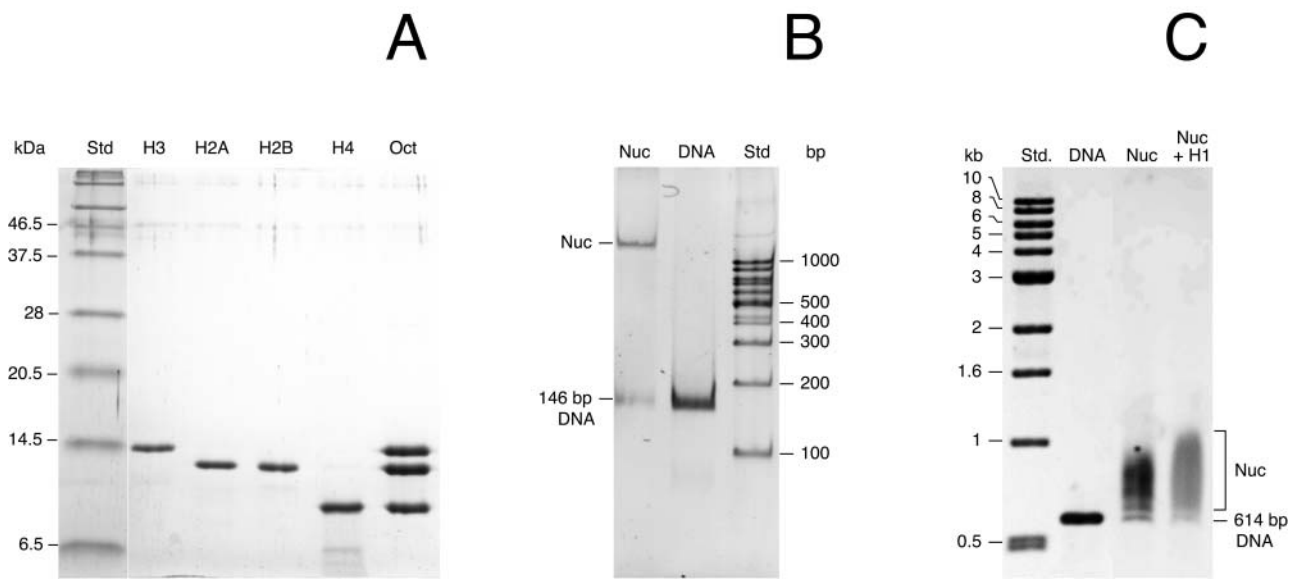

FIGURE 1 Gel-electrophoretic analysis of mononucleosomes reconstituted with recombinant histone proteins. (*A*) SDS gel of purified recombinant histones H2A, H2B, H3, and H4, and reconstituted histone octamers (lane *Oct*). (*B*) Nondenaturing polyacrylamide gel of mononucleosomes reconstituted with a 146 bp DNA fragment used previously for crystallography (Luger et al., 1997a). As compared to the free DNA, the octamer-DNA complex (*Nuc*) showed a strongly reduced mobility (Luger et al., 1999). (*C*) Agarose gel of mononucleosomes reconstituted with a 614 bp DNA fragment.

of $M = 240 \pm 30$ kDa. The expected sedimentation coefficient calculated from the crystal structure coordinates (Davey et al., 2002) using the program HYDROPRO (Garcia de la Torre et al., 2000) is $s = 11.1 \pm 0.3$ S.

For the SFM imaging, mononucleosomes were reconstituted on a 614 bp DNA. A longer fragment was chosen to visualize the DNA entering and leaving the nucleosome so that the entry-exit angle and contour length could be measured. The reconstituted complexes were analyzed on a 1% agarose gel. The sample typically contained a small fraction of free DNA (10–20%) and most of the complexes carried only a single nucleosome. Formation of the nucleosome resulted in the expected shift to lower gel-electrophoretic mobility. However, in contrast to the preparation obtained with the 146 bp DNA (Fig. 1 *B*), no distinct bands were observed, but the mobility was reduced over a rather broad range (Fig. 1 *C*). This reflects binding of the nucleosome complex to various positions on the DNA-fragment (Hamiche et al., 1996).

Images of mononucleosomes

Representative images obtained by SFM with nucleosomes assembled on the 614 bp fragment are displayed in Fig. 2. The DNA and protein complexes imaged in air (Fig. 2, *A* and *B*) and fluid (Fig. 2 *C*) had typical dimensions of 6 nm width and 0.5 nm height (DNA) and 16 nm width and 2 nm height (nucleosome). The true dimensions of the DNA are a diameter of 2.4 nm whereas the nucleosome has a cylindrical shape of 11 nm diameter and 5.5 nm height. The observed broadening of the sample can be attributed to the finite dimensions of the scanning tip. Conversely, the measured height is somewhat lower than the expected dimensions of 2.4 nm (DNA) and 5.5 nm (nucleosome) most likely due to interaction of the tip and the sample as discussed previously (e. g., Rippe et al. (1997b); Schulz et al. (1998)).

The magnification (600 × 400 nm) of single complexes given in Fig. 3 demonstrates that the protein-complex and the DNA were clearly visible so that a detailed quantitative analysis of the conformation of the complexes could be conducted as described below.

Nucleosome binding positions

The measured distribution of the nucleosome binding position as expressed by the value of r is given in Fig. 4. The analysis of air-dried samples (Fig. 4, *A* and *B*) and those imaged in buffer yielded similar results (Fig. 4, *C* and *D*). The contour length measurements of the complexes showed a standard deviation of ~10% in air and in fluid. Given this accuracy for the contour length determination, a Gaussian distributions of $r = 0.50 \pm 0.07$ would be expected for a sample that had all the nucleosomes bound at the 5S rRNA sequence. However, in the absence of H1, the experimentally determined values for r of 0.49 ± 0.18 (Fig. 4 *A*, air) and 0.44 ± 0.17 (Fig. 4 *C*, fluid) displayed a larger standard deviation. This indicates that a significant number of nucleosomes were also positioned at other sites of the DNA template. The difference between the measured width of the distribution and that expected for a sample with all nucleosomes located at the 5S rRNA sequence indicated that both in air and in fluid, ~40% of the nucleosomes are bound to the 5S rRNA sequence.

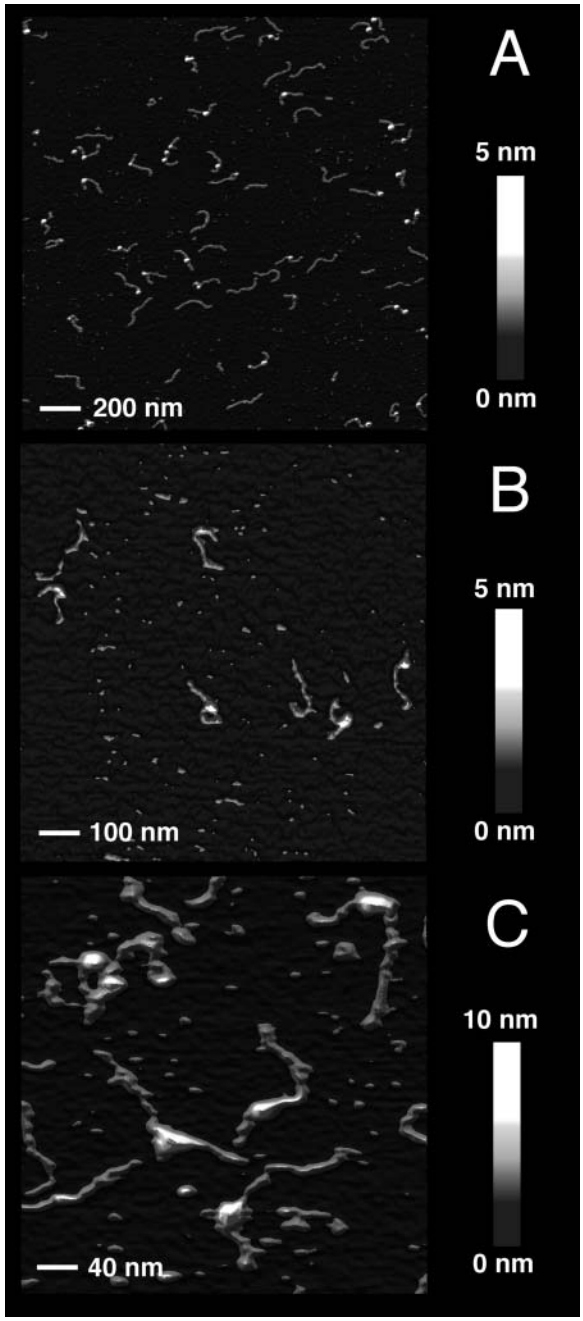

FIGURE 2 Scanning force microscopy images of mononucleosomes reconstituted with a 614 bp DNA fragment. (*A*) Image of a 2 × 2 μm area of a sample without H1 scanned in air. (*B*) A 1 × 1 μm scan of air-dried mononucleosomes reconstituted with linker histone H1. (*C*) SFM scan in buffer of a 400 × 400 nm area of complexes without H1.

According to the Boltzmann equation, the probability P_i to find a complex with energy E_i is described by

$$P_i \propto g_i \times \exp\left(\frac{-E_i}{kT}\right) \quad (1)$$

with g_i being the number of states with energy E_i. The octamer binding site covers 147 basepairs of DNA, so that on a 614-basepair-long DNA, there are $614 - 146 = 468$ binding sites. Only nucleosomes were analyzed in which both free DNA ends were detectable, i.e., $r \geq 0.11$. Accordingly, complexes bound at the terminal 70 basepairs were not included in the analysis. This reduces the effective value of the unspecific binding sites by 140 and $g_{un} = 328$. From Eq. 1, the energy difference ΔE between specific and unspecific complexes can be calculated from the experimental ratio of unspecific to specific complexes $P_{un}/P_{sp} = 1.5$ given in Eq. 2:

$$\frac{P_{un}}{P_{sp}} = \frac{g_{un}}{g_{sp}} \exp\left(\frac{\Delta E}{kT}\right). \quad (2)$$

The resulting energy difference for nucleosome binding to the specific positioning sequence in the *X. borealis* 5S rRNA as compared to a random sequence is ~5 *kT*. The corresponding free energy $\Delta\Delta G$ is 3 kcal mol^{-1}.

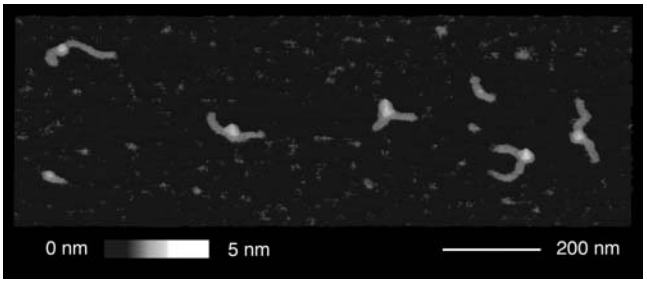

FIGURE 3 Magnified view of single mononucleosome complexes. An area of 600 × 400 nm from an SFM image of mononucleosomes acquired in air is shown in a three-dimensional representation.

Upon addition of the linker histone H1, the distribution profile changed significantly (Fig. 4, *B* and *D*). The distribution was rather broad and little preference of nucleosome binding to the *X. borealis* 5S rRNA sequence was observed. Again, the samples with H1 imaged in air (Fig. 4 *B*) and in buffer (Fig. 4 *D*) were undistinguishable within the accuracy of the measurement.

DNA contour length

The apparent DNA contour length of the mononucleosomes was determined in air and in fluid (Fig. 5) as described previously (Schulz et al., 1998). For the free DNA fragments, a length of 190 ± 9 nm was measured (air-dried samples, 691 fragments analyzed). This corresponds to a value of 0.31 ± 0.015 nm/bp, which is slightly smaller than the canonical value for DNA of 0.34 nm per basepair. As discussed previously, the DNA contour length determined by SFM is frequently found to be somewhat shorter than that expected for B-DNA (Rivetti and Codeluppi, 2001). The contour length of mononucleosomes without H1 was 156 ± 14 nm in air (Fig. 5 *A*) and 156 ± 22 nm in fluid (Fig. 5 *C*). Mononucleosomes with H1 yielded a contour length of 154 ± 11 nm in air (Fig. 5 *B*) and 157 ± 16 nm in fluid (Fig. 5 *D*).

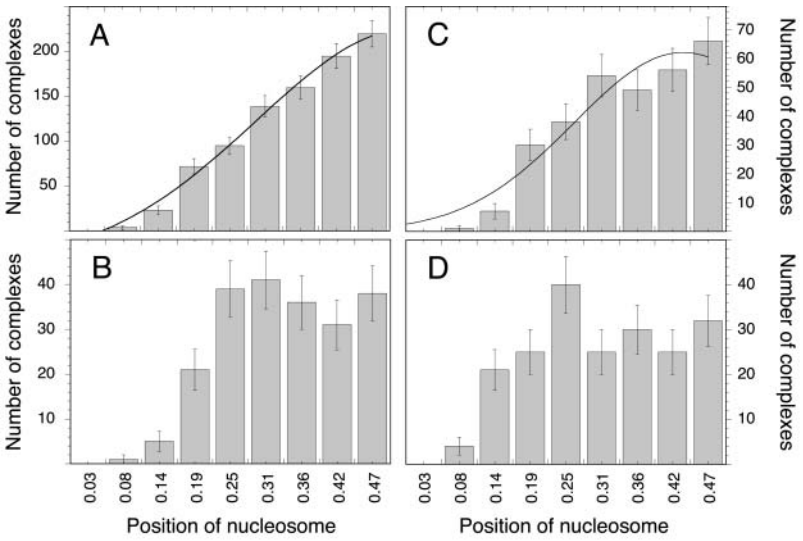

FIGURE 4 Histogram of the nucleosome binding position on the 614 bp DNA fragment. Images were recorded in air and in buffer in the absence or presence of linker histone H1. (*A*) Air, without H1; (*B*) air, with H1; (*C*) fluid, without H1; and (*D*) fluid, with H1.

No significant differences between measurements in air (Fig. 5, *A* and *B*) and in buffer (Fig. 5, *C* and *D*) were apparent. In addition, no effect of the addition of linker histone H1 was detected except for a slightly smaller standard deviation of the distribution (Fig. 5). In the complexes studied, the apparent DNA contour length was reduced on an average by 34 ± 13 nm as compared to the free DNA. This shortening would correspond to ~110 bp of DNA with a contour length of 0.31nm/bp. To determine the amount of DNA that is wrapped around the nucleosome, one has to take into account that the part of the measured contour length of the mononucleosomes traced through the nucleosome complex itself should be subtracted from the total contour length (Hamiche et al., 1996). Since the true dimensions of this part could not be determined directly on the SFM images, a value of 11 nm for the diameter of the nucleosome was taken (Davey et al., 2002; Luger et al., 1997a). This leads to a total of 45 nm or 145 ± 34 bp that are wrapped around the histone octamer complex.

DNA entry-exit angle at the nucleosome

The histogram of DNA entry-exit angles at the nucleosome complexes displayed a bimodal distribution for complexes without H1 (Fig. 6, *A* and *C*). In air, two maxima at 81 ± 29° and 136 ± 18° were observed (Fig. 6 *A*). For measurements in fluid, the values were similar with 78 ± 25° and 137 ± 25° (Fig. 6 *C*). These data were derived by fitting the distributions with a sum of two Gaussian functions. Addition of the linker histone H1 led to a significant increase in the amount of complexes that displayed smaller DNA entry-exit angles (Fig. 6, *B* and *D*). The population centered around 136° was reduced whereas a corresponding increase of the species with the smaller DNA entry-exit angle was evident.

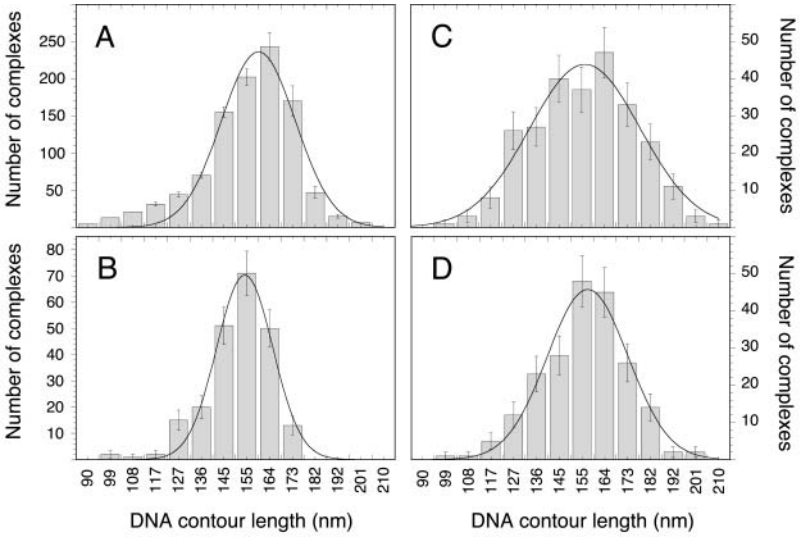

FIGURE 5 Histogram of contour length measurements. The free 614 bp DNA fragment displayed a 190 ± 9 nm contour length. (*A*) Air, without H1; (*B*) air, with H1; (*C*) fluid, without H1; and (*D*) fluid, with H1.

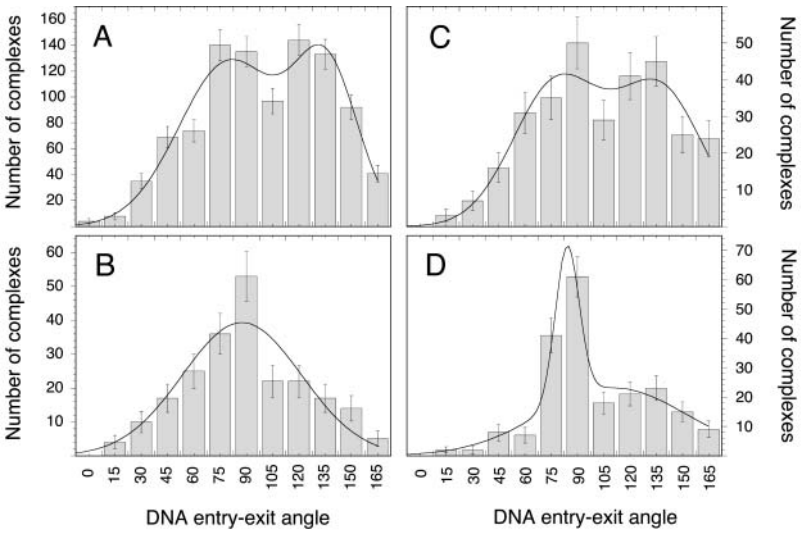

FIGURE 6 Histogram of DNA entry-exit angles at the octamer. (*A*) Air, without H1; (*B*) air, with H1; (*C*) fluid, without H1; and (*D*) fluid, with H1.

A mean value of 88 ± 34° was measured for the air-dried samples (Fig. 6 *B*). In fluid, a maximum at 85 ± 10° and a rather small amount of complexes at 132 ± 22° were detected (Fig. 6 *D*).

DISCUSSION

To our knowledge, we present in this report the first quantitative microscopy analysis of nucleosomes containing recombinant core histone proteins. These histone proteins lack any posttranslational modifications and are completely free of other chromosomal proteins. Therefore, they are particularly suitable to examine the nucleosome conformation under defined conditions and the effect of linker histone H1 binding. Recently, glutaraldehyde fixed nucleosome arrays were visualized successfully by SFM imaging in water with good resolution, and conformation changes due to the DNA sequence or the solution conditions were revealed (Bash et al., 2003; Wang et al., 2002). Furthermore, it has been shown by SFM that air-dried protein-DNA complexes may adopt a conformation that is different from that observed in buffer (Schulz et al., 1998). Thus, SFM provides a valuable contribution to the imaging of biological samples and their conformation changes under conditions where the native hydration state is preserved. Our quantitative comparison of unfixed nucleosomes imaged in air and in buffer yielded essentially the same results. Although the composition of the two deposition buffers was somewhat different (see Materials and Methods), both contained millimolar concentrations of divalent cations and the total ionic strength was very similar. It corresponded to nearly physiological concentrations (84 and 97 mM). Thus, the results obtained here indicate that with respect to the structural features quantitated (binding position of nucleosome, apparent contour length, and DNA entry-exit angle), drying of the samples did not induce changes of the nucleosome conformation, and the differences in buffer composition had no effect. This is in agreement with previous studies of mono- and oligonucleosomes, in which no structural changes have been observed for an ionic strength between 40 and 100 mM (reviewed in van Holde and Zlatanova (1996)).

Reconstitution with the 146 bp DNA according to the published protocols (Luger et al., 1997b, 1999) produced a homogenous population of mononucleosomes and a well-defined band on the polyacrylamide gel (Fig. 1 *B*). The sedimentation velocity analysis by analytical ultracentrifugation yielded an s value of 11.7 ± 0.4 S that is in good agreement with the value of 12.0 S for mononucleosomes from chicken erythrocytes (Butler and Thomas, 1998) and a theoretically determined value of $s = 11.1 \pm 0.3$ S from the crystal structure. The measured molecular mass of 240 ± 30 kDa in the velocity sedimentation analysis compares favorably with the calculated value of 224 kDa for the complex and demonstrates the integrity of our mononucleosome preparations.

After mononucleosome reconstitution on a 614 bp DNA, the gel electrophoretic mobility of the complex varied over a relatively large range on a 1% agarose gel (Fig. 1 *C*). This reflects the distribution of different nucleosome binding positions on the DNA fragment. A similar gel mobility of mononucleosomes has been observed previously with a shorter DNA fragment (Hamiche et al., 1996). Since the DNA entry-exit angles at the nucleosome are significantly smaller than 180°, the electrophoretic mobility will be lowest for nucleosomes bound at the center of the DNA. The effect of gel retardation due to DNA bending is reduced the more the bent region is located at the end of the fragment (Koo and Crothers, 1988). Accordingly, both the distribution of binding sites and the magnitude of the DNA entry-exit angle will determine the electrophoretic mobility. These effects cannot be distinguished in the comparison of the samples with and without linker histone H1 by gel-electrophoresis (Fig. 1 *C*). However, the SFM image analysis conducted here

clearly demonstrates that both parameters are changed by H1 binding. This effect of H1 is due to interaction of the protein with the nucleosome since nonspecific H1 binding to free DNA can be excluded under the conditions of the SFM imaging. As determined by fluorescence anisotropy measurements, H1 binds to a 20 basepair DNA with a dissociation constant of $K_d \approx 10^{-7}$ M in SFM buffer (F. Kepert and K. Rippe, unpublished). Thus, at nanomolar DNA and H1 concentrations as in the SFM experiments, the fraction of H1 complexed with free DNA is neglectable.

Position of the bound nucleosomes

In the absence of linker histone H1, ~40% of the nucleosomes were bound at the *X. borealis* 5S rRNA positioning sequence, which is located in the center of the 614 bp DNA. In agreement with other studies, a significant amount of nucleosomes was also located at other positions (Dong et al., 1990; Karymov et al., 2001; Meersseman et al., 1991; Panetta et al., 1998). It has been shown that the related 208 bp 5 S rRNA sequence from the sear urchin *Lytechinus variegatus* contains additional minor binding sites so that ≈50% of the nucleosomes are bound at a unique position (Dong et al., 1990; Karymov et al., 2001; Meersseman et al., 1991). Previously, values of 0.84–2.2 *kT* or 0.7–1.3 *kT* have been estimated for the energy difference of this five S rRNA sequence considering either four or more (Dong et al., 1990) or only two alternative (Karymov et al., 2001) nucleosome binding positions. However, it is usually assumed for the analysis of unspecific binding of a ligand to DNA that every basepair constitutes a possible start of a binding site so that a sequence of length L has L–146 possible locations for the histone octamer (McGhee and von Hippel, 1974; Widom, 2001). Accordingly, a 208 bp sequence contains $208 - 146 = 62$ binding positions. In the analysis presented above (Eq. 2) this would correspond to an energy difference of 4 *kT* or $\Delta\Delta G = 2.4$ kcal mol^{-1} for binding to the sea urchin 5 S rRNA high affinity site within the 208 bp DNA fragment. This energy difference is similar to the value of $\Delta\Delta G \approx 3$ kcal mol^{-1} measured here for the corresponding sequence from *X. borealis*. Numerous experiments in which nucleosomes are successfully reconstituted with regular spacing on 12 tandemly arranged 208-bp fragments of the 5 S rRNA gene of *L. variegatus* (reviewed in Hansen (2002)) also support the view that this sequence has a binding energy that is several *kT* higher than a random sequence.

Remarkably, the unfavorable cost of DNA bending around the nucleosome has been calculated to be as high as ≈76 kcal mol^{-1} (Widom, 2001). Thus, the histone-DNA interaction energy has to be quite large and a free energy difference of ≈3 kcal mol^{-1} between different sites is easily conceivable. It can be estimated from the data given by Cotton and Hamkalo (1981) that at approximately physiological salt concentrations (150 mM NaCl), the average dissociation constant of DNA in mononucleosomes isolated from a mouse cell line is 2 nM ($\Delta G \approx 12$ kcal mol^{-1}). For chicken erythrocytes, a value of 3.6 nM ($\Delta G = 11.4$ kcal mol^{-1}) at 100 mM NaCl has been measured (Ausio et al., 1984). Nucleosome core particle reconstituted on 146 bp sequences containing the human α-satellite DNA or the *L. variegatus* 5S DNA showed K_d*s* of 0.03 and 0.06 nM, respectively, at 50 mM NaCl, indicating that complexes with these sequences were ~2 kcal mol^{-1} more stable than those formed with bulk DNA (Gottesfeld and Luger, 2001). An up to 1000-fold range in relative affinities between certain sequences has been demonstrated that corresponds to a >4 kcal mol^{-1} range in $\Delta\Delta G$ (Lowary and Widom, 1997; Widom, 2001). However, in the later studies, a comparison of the *L. variegatus* 5S rRNA with bulk chicken genomic DNA showed only a relatively modest free-energy difference of 0.5 kcal mol^{-1}. This value is similar in magnitude to that of the thermal fluctuations $RT \approx 0.6$ kcal mol^{-1}, and therefore too small to explain the preferred binding observed here. According to Eq. 2, <1% of the complexes would be bound to the central 5S rRNA sequence of the template studied here if the binding affinity difference to this site would only be 0.5 kcal mol^{-1}. Thus, to explain the experimental results presented in Fig. 4, *A* and *C*, as well as the previously observed binding preference to the related *L. variegatus* 5 S rRNA sequence (Dong et al., 1990; Karymov et al., 2001; Meersseman et al., 1991) a higher binding energy difference of $\Delta\Delta G = 2$–3 kcal mol^{-1} as compared to random sites is required. This $\Delta\Delta G$ value is also consistent with a thermodynamic analysis of nucleosome dissociation constants (Gottesfeld and Luger, 2001).

The addition of linker histone H1 led to a distribution of binding positions that displayed little preference for the 5S rRNA positioning sequence (Fig. 4, *B* and *D*). This suggests that in the presence of H1, the free-energy difference between binding positions is reduced to values of ~2 *RT* (1.2 kcal mol^{-1}) or lower, which would not result in a significant increase of occupancy at the central 5 S rRNA sequence considering the accuracy of the measurement. And alternative explanation would be that the effect of H1 addition is mostly on the kinetics of nucleosome movement. Although various reports indicate that in the absence of H1, considerable rearrangement of histone octamers can occur on the DNA, it appears that H1 inhibits the short-range mobility of histone octamers on DNA and traps the nucleosomes at a certain position (Panetta et al., 1998; Pennings et al., 1994). If this is the case, a broader distribution of binding sites might be observed despite a significant energy difference to the 5 S rRNA positioning sequence if an equilibrium is not reached.

DNA contour length

From x-ray crystallography studies it is known that 146 bp (Luger et al., 1997a) or 147 bp (Davey et al., 2002) of DNA are wrapped around the histone octamer core complex. Our

results yield a similar value of 145 ± 34 bp from the SFM contour length measurements of the same recombinant histone samples but reconstituted on a longer DNA fragment (Fig. 5). However, the value for the amount of DNA wrapping determined from SFM images displayed a rather large standard deviation. Although the contour length measurements of the free DNA had a standard deviation of ≈5%, the corresponding value for the nucleosome complexes was twice as high. This indicates that some heterogeneity with respect to the amount of DNA wrapped into the nucleosome is present. It is also possible that the binding of the nucleosome to the surface introduces some broadening of the measured contour length distributions. The addition of linker histone H1 has little effect on the apparent DNA contour length except for a small narrowing of the distribution, the significance of which is unclear (Fig. 5). Binding of H1 has been reported to protect another 20 bp in addition to the 146/147 bp wrapped around the octamer (Travers, 1999). This would correspond to a length of only 6 nm or 4% of the total contour length. It is likely that an additional shortening of this magnitude or less would not be detected in our analysis as a significant reduction.

DNA entry-exit angles at the nucleosome

For mononucleosomes without linker histone H1, two maxima in the distribution of bending angles at ~80° and at 136° were identified, indicating that two species with a different DNA geometry were present (Fig. 6, *A* and *C*). Upon binding of H1 to the nucleosome, the complexes with angles ≥120° mostly disappeared (Fig. 6, *B* and *D*), and the first maximum ~85° became more pronounced. Thus, the linker histone seems to stabilize the conformation of nucleosomes in which the DNA entry-exit angle is ~85°. A reduction of the entry-exit angles has also been observed by SFM, electron microscopy (EM), and electron cryomicroscopy (cryo-EM) studies of native nucleosome preparations (Bednar et al., 1998; Hamiche et al., 1996; Leuba et al., 1998a,b; Zlatanova et al., 1998). Thus, in support of previous results, we conclude from our experiments that histone H1 stabilizes a certain DNA geometry at the nucleosome, in which the DNA entry-exit angle is significantly reduced as compared to the linker histone free nucleosome.

Studies of chromatin isolated mostly from chicken erythrocytes but also from other sources indicate that the DNA flanking the nucleosome core and the linker histone can interact to form a so called stem motif (Bednar et al., 1998; Hamiche et al., 1996; Zlatanova et al., 1998). In this structure, the two DNA segments leaving the nucleosome core particle associate ~8 nm from the nucleosome center and remain in contact for 3–5 nm before diverging (Bednar et al., 1998). On the SFM images in the presence of H1, we did not observe any complexes that had a nucleosome stem motif. This could be partly attributed to an insufficient resolution to examine the trajectory of the DNA directly at the nucleosome. Obviously, detection of a stem motif would require that the region in which the two DNA segments associate is separated well from the nucleosome core. However, also the small DNA entry-exit angle characteristic for a nucleosome stem (Bednar et al., 1998; Hamiche et al., 1996) was not apparent upon quantitative inspection of the samples. Only a very small fraction of the complexes had angles <45° (Fig. 6, *B* and *D*). Thus, it appears also conceivable that the formation of a stem structure with recombinant core histone proteins might require additional components/modifications besides the simple addition of linker histone H1 that are not present in our in vitro system.

By cryo-EM imaging of native chromatin fibers, mean DNA entry-exit angles between ≈30° (80 mM salt) to ≈90° (5 mM salt) have been estimated (Bednar et al., 1995, 1998; Woodcock et al., 1993; Woodcock and Horowitz, 1995). In another cryo-EM study on reconstituted chicken erythrocyte mononucleosomes without H1, average values of 58 ± 42° were determined but there was also a significant population of complexes with angles ≥120° (Furrer et al., 1995). In general, the values for the DNA entry-exit angle determined by cryo-EM appear to be significantly lower than those measured by SFM (Leuba et al., 1998a,b; Zlatanova et al., 1998). Since resolution and contrast are different for the two imaging techniques, the relative location of the measured bending angle with respect to the nucleosome core might vary. Effects of sample preparation and effective salt concentration have also to be considered. For the SFM imaging, the samples are bound to a surface. It has been previously argued that no systematic error is introduced in the mean DNA bending angle that exists in solution under the conditions of deposition used here (Erie et al., 1994; Rees et al., 1993; Rivetti et al., 1996). Furthermore, the conventional EM imaging of surface bound mononucleosomes also shows small entry-exit angles in the presence of linker histone, although no quantitative analysis is given (Hamiche et al., 1996). However, an effect of binding the complexes on the surface cannot be excluded, and the absolute DNA entry-exit angles determined by SFM might not be directly comparable to those obtained by true solution methods such as analysis of DNA labeled mononucleosomes by fluorescence resonance energy transfer (Tóth et al., 2001). Nevertheless, the relative changes of the angle distribution observed here upon addition of linker histone H1 provide reliable evidence that H1 stabilizes a smaller entry-exit angle.

Previous SFM studies of fixed chromatin fibers yielded average values of 100 ± 40° in the presence and 130 ± 40° in the absence of linker histones (Leuba et al., 1998a,b; Zlatanova et al., 1998). These data are consistent with the distribution of angles between 70 and 150° determined here for nucleosome core particles and DNA entry-exit angles of 85 ± 10° (air) and 88 ± 34° (buffer) for nucleosome complexes with H1 (Fig. 6). The agreement suggests that the entry-exit angle is predominantly determined on the level of a single nucleosome by the binding or dissociation of the

linker histone, which in turn is expected to affect the compaction of the whole chromatin fiber.

We emphasize that the experiments described here were conducted in a well-defined system with highly purified protein components and recombinant proteins. Thus, the approach can be extended to study the effect of posttranslational histone modifications as well as the binding of other chromosomal proteins. Furthermore, it could be demonstrated that unfixed mononucleosomes can be studied in their native hydration state by SFM. This is a specific advantage of the technique that will prove to be useful in studies of the higher order chromatin organization.

We gratefully acknowledge the support of Tom Jovin and Peter Lichter, and thank Gudrun Heim and Nathalie Brun for their help, Karolin Luger for providing the histone expression vectors, and Jacek Mazurkiewicz for critical reading of the manuscript. Part of the work by J.F.K., K.F.T., and K.R., and the work of M.C., was done at the Division Biophysics of Macromolecules of the Deutsches Krebsforschungszentrum. J.F.K. did some of the SFM imaging at the Department of Molecular Biology at the Max-Planck-Institut für biophysikalische Chemie in Göttingen.

The project was supported by the Volkswagen Foundation in the program ''Junior Research Groups at German Universities''.

REFERENCES

Allen, M. J., X. F. Dong, T. E. O'Neill, P. Yau, S. C. Kowalczykowski, J. Gatewood, R. Balhorn, and E. M. Bradbury. 1993. Atomic force microscope measurements of nucleosome cores assembled along defined DNA sequences. *Biochemistry.* 32:8390–8396.

Arents, G., R. W. Burlingame, B.-C. Wang, W. E. Love, and E. N. Moudrianakis. 1991. The nucleosomal core histone octamer at 3.1 Å resolution: a triparatite protein assembly and a left-handed superhelix. *Proc. Natl. Acad. Sci. USA.* 88:10148–10152.

Ausio, J., D. Seger, and H. Eisenberg. 1984. Nucleosome core particle stability and conformational change. Effect of temperature, particle and NaCl concentrations, and crosslinking of histone H3 sulfhydryl groups. *J. Mol. Biol.* 176:77–104.

Bash, R., H. Wang, J. Yodh, G. Hager, S. M. Lindsay, and D. Lohr. 2003. Nucleosomal arrays can be salt-reconstituted on a single-copy MMTV promoter DNA template: their properties differ in several ways from those of comparable 5S concatameric arrays. *Biochemistry.* 42:4681–4690.

Bash, R. C., J. Yodh, Y. Lyubchenko, N. Woodbury, and D. Lohr. 2001. Population analysis of subsaturated 172-12 nucleosomal arrays by atomic force microscopy detects nonrandom behavior that is favored by histone acetylation and short repeat length. *J. Biol. Chem.* 276:48362–48370.

Bednar, J., R. A. Horowitz, J. Dubochet, and C. L. Woodcock. 1995. Chromatin conformation and salt-induced compaction: Three-dimensional structural information from cryoelectron microscopy. *J. Cell Biol.* 131:1365–1376.

Bednar, J., R. A. Horowitz, S. A. Grigoryev, L. M. Carruthers, J. C. Hansen, A. J. Koster, and C. L. Woodcock. 1998. Nucleosomes, linker DNA, and linker histone form a unique structural motif that directs the higher-order folding and compaction of chromatin. *Proc. Natl. Acad. Sci. USA.* 95:14173–14178.

Bustamante, C., G. Zuccheri, S. H. Leuba, G. L. Yang, and B. Samori. 1997. Visualization and analysis of chromatin by scanning force microscopy. *Methods.* 12:73–83.

Butler, P. J., and J. O. Thomas. 1998. Dinucleosomes show compaction by ionic strength, consistent with bending of linker DNA. *J. Mol. Biol.* 281:401–407.

Buttinelli, M., G. Panetta, D. Rhodes, and A. Travers. 1999. The role of histone H1 in chromatin condensation and transcriptional repression. *Genetica.* 106:117–124.

Cotton, R. W., and B. A. Hamkalo. 1981. Nucleosome dissociation at physiological ionic strengths. *Nucleic Acids Res.* 9:445–457.

Davey, C. A., D. F. Sargent, K. Luger, A. W. Maeder, and T. J. Richmond. 2002. Solvent mediated interactions in the structure of the nucleosome core particle at 1.9 Å resolution. *J. Mol. Biol.* 319:1097–1113.

Dong, F., J. C. Hansen, and K. E. van Holde. 1990. DNA and protein determinants of nucleosome positioning on sea urchin 5S rRNA gene sequences in vitro. *Proc. Natl. Acad. Sci. USA.* 87:5724–5728.

Dorigo, B., T. Schalch, K. Bystricky, and T. J. Richmond. 2003. Chromatin fiber folding: requirement for the histone H4 N-terminal tail. *J. Mol. Biol.* 327:85–96.

Durchschlag, H. 1986. Specific volumes of biological macromolecules and some other molecules of biological interest. *In* Thermodynamic Data for Biochemistry and Biotechnology. H.-J. Hinz, editor. Springer-Verlag, Berlin. 45–128.

Erie, D. A., G. Yang, H. C. Schultz, and C. Bustamante. 1994. DNA bending by Cro protein in specific and nonspecific complexes: implications for protein site recognition and specificity. *Science.* 266:1562–1566.

Fritzsche, W., and E. Henderson. 1996. Scanning force microscopy reveals ellipsoid shape of chicken erythrocyte nucleosomes. *Biophys. J.* 71: 2222–2226.

Fritzsche, W., A. Schaper, and T. M. Jovin. 1994. Probing chromatin with the scanning force microscope. *Chromosoma.* 103:231–236.

Fritzsche, W., L. Takac, and E. Henderson. 1997. Application of atomic force microscopy to visualization of DNA, chromatin, and chromosomes. *Crit. Rev. Eukaryot. Gene Expr.* 7:231–240.

Fritzsche, W., J. Vesenka, and E. Henderson. 1995. Scanning force microscopy of chromatin. *Scanning Microsc.* 9:729–739.

Furrer, P., J. Bednar, J. Dubochet, A. Hamiche, and A. Prunell. 1995. DNA at the entry-exit of the nucleosome observed by cryoelectron microscopy. *J. Struct. Biol.* 114:177–183.

Garcia de la Torre, J., M. L. Huertas, and B. Carrasco. 2000. Calculation of hydrodynamic properties of globular proteins from their atomic-level structure. *Biophys. J.* 78:719–730.

Gottesfeld, J. M., and K. Luger. 2001. Energetics and affinity of the histone octamer for defined DNA sequences. *Biochemistry.* 40:10927–10933.

Gottesfeld, J. M., C. Melander, R. K. Suto, H. Raviol, K. Luger, and P. B. Dervan. 2001. Sequence-specific recognition of DNA in the nucleosome by pyrrole-imidazole polyamides. *J. Mol. Biol.* 309:615–629.

Graziano, V., S. E. Gerchman, D. K. Schneider, and V. Ramakrishnan. 1994. Histone H1 is located in the interior of the chromatin 30-nm filament. *Nature.* 368:351–354.

Hamiche, A., P. Schultz, V. Ramakrishnan, P. Oudet, and A. Prunell. 1996. Linker histone-dependent DNA structure in linear mononucleosomes. *J. Mol. Biol.* 257:30–42.

Hansen, J. C. 2002. Conformational dynamics of the chromatin fiber in solution: determinants, mechanisms, and functions. *Annu. Rev. Biophys. Biomol. Struct.* 31:361–392.

Hansma, H. G., and D. E. Laney. 1996. DNA binding to mica correlates with cationic radius: assay by atomic force microscopy. *Biophys. J.* 70: 1933–1939.

Harp, J. M., B. L. Hanson, D. E. Timm, and G. J. Bunick. 2000. Asymmetries in the nucleosome core particle at 2.5 Å resolution. *Acta Crystallogr. D Biol. Crystallogr.* 56:1513–1534.

Herrera, J. E., K. L. West, R. L. Schiltz, Y. Nakatani, and M. Bustin. 2000. Histone H1 is a specific repressor of core histone acetylation in chromatin. *Mol. Cell. Biol.* 20:523–529.

Horowitz, R. A., D. A. Agard, J. W. Sedat, and C. L. Woodcock. 1994. The three-dimensional architecture of chromatin in situ: electron tomography reveals fibers composed of a continuously variable zig-zag nucleosomal ribbon. *J. Cell Biol.* 125:1–10.

Karymov, M. A., M. Tomschik, S. H. Leuba, P. Caiafa, and J. Zlatanova. 2001. DNA methylation-dependent chromatin fiber compaction in vivo and in vitro: requirement for linker histone. *FASEB J.* 15:2631–2641.

Koo, H.-S., and D. M. Crothers. 1988. Calibration of DNA curvature and a unified description of sequence-directed bending. *Proc. Natl. Acad. Sci. USA.* 85:1763–1767.

Leuba, S. H., and C. Bustamante. 1999. Analysis of chromatin by scanning force microscopy. *Methods Mol. Biol.* 119:143–160.

Leuba, S. H., C. Bustamante, K. van Holde, and J. Zlatanova. 1998a. Linker histone tails and N-tails of histone H3 are redundant: scanning force microscopy studies of reconstituted fibers. *Biophys. J.* 74:2830–2839.

Leuba, S. H., C. Bustamante, J. Zlatanova, and K. van Holde. 1998b. Contributions of linker histones and histone H3 to chromatin structure: scanning force microscopy studies on trypsinized fibers. *Biophys. J.* 74: 2823–2829.

Leuba, S. H., G. Yang, C. Robert, B. Samori, K. van Holde, J. Zlatanova, and C. Bustamante. 1994. Three-dimensional structure of extended chromatin fibers as revealed by tapping-mode scanning force microscopy. *Proc. Natl. Acad. Sci. USA.* 91:11621–11625.

Lowary, P. T., and J. Widom. 1997. Nucleosome packaging and nucleosome positioning of genomic DNA. *Proc. Natl. Acad. Sci. USA.* 94:1183–1188.

Luger, K., A. W. Mäder, R. K. Richmond, D. F. Sargent, and T. J. Richmond. 1997a. Crystal structure of the nucleosome core particle at 2.8 Å resolution. *Nature.* 389:251–260.

Luger, K., T. J. Rechsteiner, A. J. Flaus, M. M. Waye, and T. J. Richmond. 1997b. Characterization of nucleosome core particles containing histone proteins made in bacteria. *J. Mol. Biol.* 272:301–311.

Luger, K., T. J. Rechsteiner, and T. J. Richmond. 1999. Preparation of nucleosome core particle from recombinant histones. *Methods Enzymol.* 304:3–19.

Martin, L. D., J. P. Vesenka, E. Henderson, and D. L. Dobbs. 1995. Visualization of nucleosomal substructure in native chromatin by atomic force microscopy. *Biochemistry.* 34:4610–4616.

McGhee, J. D., and P. H. von Hippel. 1974. Theoretical aspects of DNA-protein interactions: co-operative and non-co-operative binding of large ligands to a one-dimensional homogenous lattice. *J. Mol. Biol.* 86:469–489.

McMurray, C. T., E. W. Small, and K. E. van Holde. 1991. Binding of ethidium to the nucleosome core particle. Internal and external binding modes. *Biochemistry.* 30:5644–5652.

Meersseman, G., S. Pennings, and E. M. Bradbury. 1991. Chromatosome positioning on assembled long chromatin. Linker histones affect nucleosome placement on 5 S rDNA. *J. Mol. Biol.* 220:89–100.

Panetta, G., M. Buttinelli, A. Flaus, T. J. Richmond, and D. Rhodes. 1998. Differential nucleosome positioning on Xenopus oocyte and somatic 5 S RNA genes determines both TFIIIA and H1 binding: a mechanism for selective H1 repression. *J. Mol. Biol.* 282:683–697.

Pennings, S., G. Meersseman, and E. M. Bradbury. 1994. Linker histones H1 and H5 prevent the mobility of positioned nucleosomes. *Proc. Natl. Acad. Sci. USA.* 91:10275–10279.

Philo, J. S. 2000. A method for directly fitting the time derivative of sedimentation velocity data and an alternative algorithm for calculating sedimentation coefficient distribution functions. *Anal. Biochem.* 279:151–163.

Ramakrishnan, V. 1997a. Histone H1 and chromatin higher-order structure. *Crit. Rev. Eukaryot. Gene Expr.* 7:215–230.

Ramakrishnan, V. 1997b. Histone structure and the organization of the nucleosome. *Annu. Rev. Biophys. Biomol. Struct.* 26:83–112.

Rees, W. A., R. W. Keller, G. Y. Vesenka, and C. Bustamante. 1993. Evidence of DNA bending in transcription complexes imaged by scanning force microscopy. *Science.* 260:1646–1649.

Richmond, T. J., and J. Widom. 2000. Nucleosome and chromatin structure. *In* Chromatin Structure and Gene Expression, Frontiers in Molecular Biology. S. Elgin and J. L. Workman, editors. Oxford University Press, Oxford, UK. 328–351.

Rippe, K., N. Mücke, and J. Langowski. 1997a. Molecules in motion: Imaging DNA with the scanning force microscope in aqueous solutions. *Bioforum International.* 1:42–44.

Rippe, K., N. Mücke, and J. Langowski. 1997b. Superhelix dimensions of a 1868 base pair plasmid determined by scanning force microscopy in air and in aqueous solution. *Nucleic Acids Res.* 25:1736–1744.

Rivetti, C., and S. Codeluppi. 2001. Accurate length determination of DNA molecules visualized by atomic force microscopy: evidence for a partial B- to A-form transition on mica. *Ultramicroscopy.* 87:55–66.

Rivetti, C., M. Guthold, and C. Bustamante. 1996. Scanning force microscopy of DNA deposited onto mica: equilibration versus molecular kinetic trapping studied by statistical polymer chain analysis. *J. Mol. Biol.* 264:919–932.

Schulz, A., N. Mücke, J. Langowski, and K. Rippe. 1998. Scanning force microscopy of *E. coli* RNA polymerase·σ^{54} holoenzyme complexes with DNA in buffer and in air. *J. Mol. Biol.* 283:821–836.

Stafford, W. F. 1992. Boundary analysis in sedimentation transport experiments: a procedure for obtaining sedimentation coefficient distributions using the time derivative of the concentration profile. *Anal. Biochem.* 203:295–301.

Stafford, W. F. 1997. Sedimentation velocity spins a new weave for an old fabric. *Curr. Opin. Biotechnol.* 8:14–24.

Tóth, K., N. Brun, and J. Langowski. 2001. Trajectory of nucleosomal linker DNA studied by fluorescence resonance energy transfer. *Biochemistry.* 40:6921–6928.

Travers, A. 1999. The location of the linker histone on the nucleosome. *Trends Biochem. Sci.* 24:4–7.

van Holde, K., and J. Zlatanova. 1996. What determines the folding of the chromatin fiber. *Proc. Natl. Acad. Sci. USA.* 93:10548–10555.

van Holde, K. E. 1989. Chromatin. Springer, Heidelberg.

Wang, H., R. Bash, J. G. Yodh, G. L. Hager, D. Lohr, and S. M. Lindsay. 2002. Glutaraldehyde modified mica: a new surface for atomic force microscopy of chromatin. *Biophys. J.* 83:3619–3625.

Widom, J. 2001. Role of DNA sequence in nucleosome stability and dynamics. *Quart. Rev. Biophys.* 34:269–324.

Woodcock, C. L., S. A. Grigoryev, R. A. Horowitz, and N. Whitaker. 1993. A chromatin folding model that incorporates linker variability generates fibers resembling the native structures. *Proc. Natl. Acad. Sci. USA.* 90: 9021–9025.

Woodcock, C. L., and R. A. Horowitz. 1995. Chromatin organization reviewed. *Trends Cell Biol.* 5:272–277.

Yang, G., S. H. Leuba, C. Bustamante, J. Zlatanova, and K. van Holde. 1994. Role of linker histones in extended chromatin fibre structure. *Nat. Struct. Biol.* 1:761–763.

Yodh, J. G., Y. L. Lyubchenko, L. S. Shlyakhtenko, N. Woodbury, and D. Lohr. 1999. Evidence for nonrandom behavior in 208-12 subsaturated nucleosomal array populations analyzed by AFM. *Biochemistry.* 38:15756–15763.

Yodh, J. G., N. Woodbury, L. S. Shlyakhtenko, Y. L. Lyubchenko, and D. Lohr. 2002. Mapping nucleosome locations on the 208-12 by AFM provides clear evidence for cooperativity in array occupation. *Biochemistry.* 41:3565–3574.

Zhou, Y. B., S. E. Gerchman, V. Ramakrishnan, A. Travers, and S. Muyldermans. 1998. Position and orientation of the globular domain of linker histone H5 on the nucleosome. *Nature.* 395:402–405.

Zlatanova, J., P. Caiafa, and K. Van Holde. 2000. Linker histone binding and displacement: versatile mechanism for transcriptional regulation. *FASEB J.* 14:1697–1704.

Zlatanova, J., S. H. Leuba, and K. van Holde. 1998. Chromatin fiber structure: morphology, molecular determinants, structural transitions. *Biophys. J.* 74:2554–2566.

Zlatanova, J., and K. van Holde. 1996. The linker histones and chromatin structure: new twists. *Prog. Nucleic Acid Res. Mol. Biol.* 52:217–259.

THE JOURNAL OF BIOLOGICAL CHEMISTRY VOL. 280, NO. 40, pp. 34063–34072, October 7, 2005

NAP1 Modulates Binding of Linker Histone H1 to Chromatin and Induces an Extended Chromatin Fiber Conformation*[S]

Received for publication, July 6, 2005, and in revised form, August 11, 2005 Published, JBC Papers in Press, August 16, 2005, DOI 10.1074/jbc.M507322200

J. Felix Kepert, Jacek Mazurkiewicz, Gerrit L. Heuvelman, Katalin Fejes Tóth, and Karsten Rippe[1]

From the Kirchhoff-Institut für Physik, Molecular Biophysics Group, Ruprecht-Karls-Universität Heidelberg, Im Neuenheimer Feld 227, D-69120 Heidelberg, Germany

NAP1 (nucleosome assembly protein 1) is a histone chaperone that has been described to bind predominantly to the histone H2A·H2B dimer in the cell during shuttling of histones into the nucleus, nucleosome assembly/remodeling, and transcription. Here it was examined how NAP1 interacts with chromatin fibers isolated from HeLa cells. NAP1 induced a reversible change toward an extended fiber conformation as demonstrated by sedimentation velocity ultracentrifugation experiments. This transition was due to the removal of the linker histone H1. The H2A·H2B dimer remained stably bound to the native fiber fragments and to fibers devoid of linker histone H1. This was in contrast to mononucleosome substrates, which displayed a NAP1-induced removal of a single H2A·H2B dimer from the core particle. The effect of NAP1 on the chromatin fiber structure was examined by scanning/atomic force microscopy. A quantitative image analysis of ~36,000 nucleosomes revealed an increase of the average internucleosomal distance from 22.3 ± 0.4 to 27.6 ± 0.6 nm, whereas the overall fiber structure was preserved. This change reflects the disintegration of the chromatosome due to binding of H1 to NAP1 as chromatin fibers stripped from H1 showed an average nucleosome distance of 27.4 ± 0.8 nm. The findings suggest a possible role of NAP1 in chromatin remodeling processes involved in transcription and replication by modulating the local linker histone content.

The dynamic organization of chromatin in the eukaryotic nucleus is tightly connected to transcription (1–3). Transcribed chromatin is thought to be in a more open conformation with a higher accessibility to DNase I or micrococcal nuclease (4–7). On the other hand, highly compacted and dense chromatin regions, referred to as heterochromatin, are often transcriptionally inactive and contain a reduced number of genes (3, 7, 8). Several factors have been identified that promote a transition between a transcriptionally active and a more dense/inactive chromatin conformation. These include linker histones (9–11), DNA methylation (2, 12), histone modifications (13–15), and the incorporation of histone variants (16–19). The dynamic nature of chromatin manifests itself by continuous rearrangements of its three-dimensional structure. These changes involve the activity of histone chaperones that mediate the ordered deposition and the removal and exchange of histones (20–23). The central carrier of the histone H2A·H2B dimer in the cell is NAP1 (nucleosome assembly protein 1) (24). NAP1 is involved in the transport of the histone H2A·H2B dimer from the cytoplasm to the nucleus and the deposition of histones onto the DNA as described in several reviews (20–23). NAP1 and other histone chaperones stimulate the binding of transcription factors to chromatin templates (25, 26). In yeast, loss of NAP1 leads to an altered gene expression of about 10% of the genome (27), and several lines of evidence suggest that NAP1 has activities related to transcription. First, it has been shown that NAP1 is present in complexes with SWR1, which catalyzes the substitution of the nucleosomal H2A·H2B dimer against the variant H2A.Z·H2B dimer (18). In addition, it has been demonstrated that NAP1 is capable of removing H2A·H2B dimers from mononucleosomes and exchanging these with the histone variant H2A.Z·H2B (28), the incorporation of which has important effects on gene expression *in vivo* (29). Second, Ito *et al.* (30) showed that upon histone acetylation of nucleosomal arrays with p300, H2A·H2B dimers are transferred to NAP1 in the presence of the transcriptional activator protein GalVP16. Third, the transcription by RNA polymerase II is facilitated by elongation factors like the FACT complex that possess histone chaperone activity (19, 31–33). As NAP1 is similar to FACT in its affinity to the H2A·H2B dimer while being present at much higher concentrations, it has been proposed to play a role in remodeling nucleosomes at the promoter or during elongation (34). Recently, a new link between NAP1 and the linker histones has been emerged. It has been shown that NAP1 acts as a linker histone chaperone in *Xenopus* eggs (35). In addition, the NAP1-related protein nucleoplasmin is capable of extracting linker histones from chromatin (36).

Despite its obvious importance to gene expression, the direct effect of NAP1 on the chromatin fiber conformation has not been characterized. In particular, it is not clear if NAP1 alone is sufficient for the extraction of the histone H2A·H2B dimer from the nucleosome in the context of the chromatin fiber as it has been reported for a mononucleosomal template (28). Because the protein composition of native chromatin fibers is complex, a variety of potential interaction partners for NAP1 exists. In particular, an interaction with linker histones has to be considered based on recent reports (35, 36). Furthermore, structural changes due to NAP1 binding to chromatin cannot be excluded.

Here the influence of NAP1 on the chromatin conformation and protein composition was investigated by analytical ultracentrifugation (AUC),[2] scanning/atomic force microscopy, and biochemical methods. AUC experiments describe the unperturbed, global conformation of chromatin fibers under physiological conditions (37–46), and SFM allows it to identify changes of the fiber geometry at the single nucleosomal level (47–57). By using a combination of these two biophysical techniques in conjunction with biochemical characterizations, it is

* This work was supported by the Volkswagen Foundation Program "Junior Research Groups at German Universities" and Deutsche Forschungsgemeinschaft Research Training Group "Molecular Imaging Methods for the Analysis of Gene and Protein Expression" Grant GRK 886/1. The costs of publication of this article were defrayed in part by the payment of page charges. This article must therefore be hereby marked "*advertisement*" in accordance with 18 U.S.C. Section 1734 solely to indicate this fact.

[S] The on-line version of this article (available at http://www.jbc.org) contains supplemental Fig. S1.

[1] To whom correspondence should be addressed. Tel.: 49-6221-549270; Fax: 49-6221-549112; E-mail: Karsten.Rippe@kip.uni-heidelberg.de.

[2] The abbreviations used are: AUC, analytical ultracentrifugation; H1, linker histone H1; SFM, scanning force microscopy; *s*, sedimentation coefficient; nt, nucleotide; MNase, micrococcal nuclease.

shown here that NAP1 mediates the reversible removal of the linker histones from chromatin fibers. This process does not disrupt the overall fiber organization but causes a more open structure due to an increase in the average distance between two nucleosomes. These observations suggest a new potential role for NAP1 in the establishment of a transcriptionally active chromatin conformation.

EXPERIMENTAL PROCEDURES

Preparation of Chromatin Fibers, NAP1, and Histones—HeLa cells were grown in RPMI (PAA Laboratories, Pasching, Austria) supplemented with 10% fetal calf serum. Cells were washed twice with an isotonic Tris-HCl buffer (IT) containing 25 mM Tris-HCl, pH 7.5, 137 mM NaCl, 5 mM KCl, 0.3 mM Na_2HPO_4, 0.5 mM $MgCl_2$, and 0.7 mM $CaCl_2$, detached from the surface using a cell scraper, and collected in IT buffer. Nonidet P-40 was added to a final concentration of 0.2% to dissolve the cell membrane. Cells were incubated on ice for 90 s and gently vortexed for 30 s four times. The nuclei were pelleted by centrifugation, resuspended in IT buffer supplemented with 50% glycerol, and frozen at −80 °C. Chromatin fiber extraction from the HeLa nuclei was conducted as described using MNase (Worthington) concentrations of 0.045 units/350 μg of chromatin for 5 min at 37 °C or 0.3 units/350 μg of chromatin for 30 min at 0 °C (58). The digestion was stopped by the addition of EDTA to a final concentration of 10 mM. The cell nuclei were sedimented, and the soluble chromatin fiber fraction in the supernatant was used for further experiments. Linker histone depletion was conducted essentially as described previously (47). The monovalent salt concentration of the fiber preparation was raised with sodium chloride to 0.35 M followed by incubation for 2 h on ice. Chromatin was loaded on a Sepharose CM 25 fast flow column equilibrated in 10 mM Tris, pH 7.5, 0.35 M NaCl, 1 mM EDTA. Flow-through fractions containing the chromatin fibers were collected, checked on 15% SDS-PAGE, and dialyzed against 10 mM Tris, pH 7.5, 50 mM KCl, 1 mM EDTA overnight at 4 °C. Recombinant histones were overexpressed, purified, and fluorescently labeled with either Alexa Fluor 488 or 633 C5 maleimide (Molecular Probes Europe BV, Leiden, Netherlands) as described previously (59, 60). Recombinant mononucleosomes were reconstituted by salt dialysis using a 146-bp DNA template containing the *Xenopus borealis* 5 S RNA positioning sequence (59) and histone H2A12C labeled with the Alexa 488 fluorophore referred to as $H2A^f$. Linker histone H1 from *Bos tauris* was purchased from Roche Diagnostics and purified as described previously (59). Histone H1 was labeled at the N terminus by mixing with Alexa Fluor 488 carboxylic acid and 2,3,5,6-tetraflourophenyl ester at molar stoichiometry in 20 mM Hepes, pH 8.0, followed by incubation at 20 °C for 1 h. Further purification with Bio-Rex 70 resin was conducted as described previously (60, 61). Labeled H1 was dialyzed against water and concentrated. Yeast NAP1 with an N-terminal His tag was overexpressed in *Escherichia coli* from plasmid pET28-yNAP1 and purified as described (60). Total RNA was extracted and purified as described previously from HeLa cells (62) and was kindly provided by Olaf Thürigen. The two most prominent bands are 18 S and 28 S rRNA of ≈2000 and ≈5000 nt long, respectively.

Analytical Ultracentrifugation—AUC experiments were carried out on a Beckman Instruments Optima XL-A with absorbance optics. The sedimentation velocity data for the chromatin samples were recorded at 20 °C in a buffer containing 10 mM Hepes, pH 8.0, 50 mM potassium acetate, 10 mM EDTA, and 0.6% (v/v) glycerol. Data were acquired at 260 nm, with a radial step size of 0.003 cm and 15,000 rpm in continuous scan mode. A partial specific volume of $\bar{\nu} = 0.644$ ml·g^{-1} at 20 °C was calculated for the HeLa chromatin fibers from values of 0.746 ml·g^{-1} (histones) and 0.55 ml·g^{-1} (DNA) and the relative molecular weight fractions. The molecular weight of one chromatosome unit comprises DNA (126.7 kDa) for an average nucleosome repeat length of 192 bp in HeLa cells (7), the histone octamer (108.5 kDa), and the linker histone H1 (~24 kDa). This corresponds to an extinction coefficient of ϵ_{260} = 2,514,550 M^{-1}·cm^{-1} per chromatosome calculated with an ϵ_{260} = 6500 M^{-1}·cm^{-1} per DNA nucleotide (ϵ_{260} = 2,496,000 M^{-1}·cm^{-1} for a 192-bp DNA duplex), ϵ_{260} = 17,200 M^{-1}·cm^{-1} for the histone octamer, and ϵ_{260} = 1350 M^{-1}·cm^{-1} for linker histone H1. The buffer density of ρ = 1.004 g·ml^{-1} and the viscosity η = 1.023 mPa/s at 20 °C were calculated with SEDNTERP version 1.05 by J. Philo, D. Hayes, and T. Laue (www.jphilo.mailway.com/download.htm) (see Ref. 63). Velocity sedimentation data were plotted with the program dc/dt+ version 1.16 by J. Philo (64). Sedimentation coefficients were determined with SEDPHAT version 2.0 (www.analyticalultracentrifugation.com) (65). Sedimentation equilibrium experiments were analyzed with the program Ultrascan 6.2 by B. Demeler (www.ultrascan.uthscsa.edu/). For the AUC experiments, chromatin samples were diluted with a buffer containing 10 mM Hepes, pH 8.0, 50 mM potassium acetate, and 10 mM EDTA to an absorbance of A_{260} ≈1 (0.4 μM nucleosome). Where indicated, NAP1 was added to the chromatin fiber sample at concentrations of 2.4 or 3.5 μM monomer, corresponding to a ratio of about 0.75 and 1.1 NAP1 per core histone. Three different samples of NAP1 and chromatin fibers were analyzed by AUC as follows. (i) NAP1 was added directly to the chromatin fiber preparation. (ii) Chromatin fibers were preincubated with NAP1 for 1 h on ice. The histone H1 was then titrated to a concentration of 1 histone H1/2–3 NAP1. (iii) NAP1 was incubated with chromatin fibers for 1 h on ice followed by a stepwise titration of H2A·H2B dimer to a ratio of 1 histone/1 NAP1.

The complexes of $H1^f$ with NAP1 were characterized with sedimentation velocity and equilibrium experiments. $H1^f$ was mixed with NAP1 at a monomer ratio of 1:2 in 10 mM Tris, pH 7.5, 10 mM KCl, and data were recorded at 494 nm for sedimentation velocity runs and 494 and 280 nm in sedimentation equilibrium experiments.

Gel Electrophoretic Analysis of NAP1-Histone Interactions—The relative $H2A^f$·H2B dimer binding affinities of NAP1 and RNA were compared. $H2A^f$·H2B dimer was preincubated with NAP1 at a molar ratio of 1 NAP1 monomer/histone monomer in 15 mM Tris-HCl, pH 7.5, 50 mM KCl, 3% glycerol, and 0.33 mM dithiothreitol. NAP1 binds the $H2A^f$·H2B dimer with a nanomolar dissociation constant at a stoichiometry of 1 NAP1 monomer/histone (60, 66). Increasing amounts of RNA were titrated to the NAP1-$H2A^f$·H2B complex (ranging from 39 to 1560 ng), and transfer of the dimer was analyzed on 1% agarose gels. Bands were visualized by illumination with a UV light box at 302 nm and detection by a CCD camera exploiting the $H2A^f$ fluorescence. To follow the removal of histone H2A·H2B dimer from the nucleosome, reconstituted mononucleosomes (~200 nM) containing labeled $H2A^f$·H2B dimer were incubated with different NAP1 (from 0.9 to 5.1 μM) or RNA (from 7.8 to 57 ng/μl) concentrations for 2–4 h at room temperature and were analyzed by gel shift experiments. The binding stoichiometry between histone H1 and NAP1 was determined by titrating a 1 μM histone $H1^f$ solution in 10 mM Tris, pH 7.5, 36 mM KCl with increasing amounts of NAP1 (0–4 μM). The relative affinities of H2A·H2B dimer and H1 for NAP1 were compared by titrating a saturated NAP1-$H2A^r$·H2B dimer complex ($H2A^r$, Alexa 633 labeled H2A) with increasing concentrations of $H1^f$. The competitive binding of $H2A^r$·H2B and $H1^f$ to NAP1 was analyzed on 1% agarose gels as described above.

Biochemical Characterization of Chromatin Fibers—To determine which proteins were displaced by NAP1 from chromatin, 20 μl of chromatin with an absorbance of A_{260} = 3.6 (~1.5 μM nucleosomes) was incubated with 13 μM NAP1 for 3 h at room temperature and then

centrifuged for 90 min at 13,000 rpm and 20 °C in a tabletop centrifuge. The pellet was resuspended in 2× SDS loading buffer. The proteins of the supernatant were precipitated with 15% trichloroacetic acid for 30 min on ice and centrifuged at 13,000 rpm for 15 min at 4 °C. The pellet was washed with acetone, air-dried, and resuspended in 2× SDS loading buffer. Samples were analyzed on 15% SDS-PAGE. For MNase digestions, native and H1-depleted chromatin was prepared as described above. Fibers at a concentration of $A_{260} = 6$ were supplemented with 3 mM $CaCl_2$ and digested with 0.1 unit/μl MNase at 37 °C for various time points. The reaction was stopped by the addition of EDTA and SDS. Proteins were digested by proteinase K, and DNA was phenol/chloroform-extracted, ethanol-precipitated, and analyzed on 6% native polyacrylamide gels. For NAP1-treated fibers, chromatin at a nucleosome concentration of ~2.7 μM was incubated with ~23 μM NAP1 for 3 h at room temperature before digestion with MNase.

SFM Imaging and Data Analysis—SFM imaging of air-dried samples was conducted with a Nanoscope IV Multimode SFM from Veeco Instruments in "tapping mode" as described previously (59). As free NAP1 bound efficiently to the mica surface and obscured the imaging, it was removed by passing the sample through a 1-ml Bio-Spin 50 microcolumn (Bio-Rad) filled with nickel-nitrilotriacetic acid-agarose (Qiagen, Hildesheim, Germany) and equilibrated with 10 mM Hepes, pH 8.0, 50 mM potassium acetate. Directly before imaging, the eluate was diluted in the same buffer to a final concentration of A_{260} ≈0.02, and 10 μl was pipetted on freshly cleaved mica. The mica was washed with distilled water and dried with nitrogen flow. The control chromatin fibers were purified and deposited identically.

For an automatic quantitative analysis of the SFM images, algorithms were developed using MATLAB version 6.5.1 (Mathworks, Natick, MA) and the ALEX program written by C. Rivetti and M. Young (see Ref. 67). The software automatically computed the position and size of each individual nucleosome and mean width, volume, area, perimeter, and height of the whole chromatin fibers. In the air-dried images, the nucleosomes appeared as spheres of about 2 nm height. To measure the area covered by the chromatin fibers, a contour line was plotted at a height of 0.2 nm above the background (Fig. 5*B*). The area within this contour line was considered to belong to the chromatin fiber. From this, the area covered by the fiber was calculated. The position of the nucleosomes was determined by detecting the local height maxima inside the segmented chromatin fibers. To account for noise in the topography signal, which could obscure the identification, additional constraints were implemented. First, a threshold for minimal height of a nucleosome was set to 0.4 nm. Second, the distance between two neighboring nucleosomes had to be at least 8 nm. Third, the exact positions of the nucleosome centers were determined by taking out each nucleosome of the chromatin image and by subsequent cross-correlation with a rotated copy. With this procedure, the positions of the nucleosome centers and the total number of nucleosomes of the chromatin fiber could be identified reliably as shown in Fig. 5*B*. The total area occupied by the chromatin fiber (see *contour line* in Fig. 5*B*) was divided by the number of nucleosomes. By approximating the area occupied by a nucleosome as a circle, the average distance between nucleosomes was calculated. In addition the distance of a given nucleosome to its nearest neighboring nucleosome was determined. A total of 1063 chromatin fibers with 36,261 nucleosomes were evaluated. The data for the average distance between nucleosomes were fit to a Gaussian distribution (Fig. 5*C*), whereas the distribution of nearest neighbor distances d (Fig. 5*D*) was fitted to the product of a Gaussian and $\cos^2$

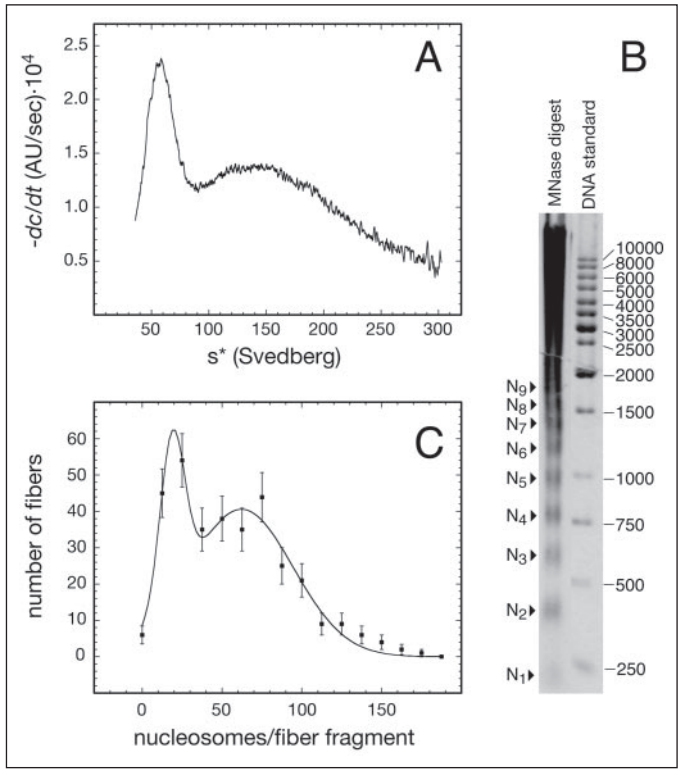

FIGURE 1. **Characterization of the chromatin fiber preparation.** *A,* distribution of sedimentation coefficients derived by the dc/d*t* method from AUC runs for the chromatin fiber sample studied. Averaging 11 different chromatin preparations yielded two major peaks at 46 ± 6 S and 166 ± 13 S. *B,* chromatin samples were analyzed on a 1% agarose gel after mild micrococcal nuclease digestion. The digestion pattern revealed the existence of a regular nucleosome spacing characteristic for native chromatin. DNA bands corresponding to fragments with 1–9 nucleosomes (N_1 to N_9) are marked. *C,* distribution of the number of nucleosomes per single chromatin fiber fragment determined on SFM images.

to account for the observed periodicity of peaks as shown in Equation 1.

$$p(d) = c_1 \cdot \exp\left(\frac{(d-\bar{d})^2}{2\cdot\sigma^2}\right)\cdot(\cos^2(c_2\cdot d + c_3) + 4) \quad \text{(Eq. 1)}$$

In Equation 1 $\bar{d}$ is the average distance between nearest neighboring nucleosomes; σ is the standard deviation, and c_1, c_2, and c_3 are constants.

RESULTS

NAP1 Reversibly Alters the Hydrodynamic Shape of Native Chromatin Fibers—Analytical ultracentrifugation was used to determine the sedimentation properties of native chromatin fibers from HeLa cells in the presence of NAP1. These fibers were analyzed by sedimentation velocity ultracentrifugation. From averaging 11 different chromatin preparations, values of $s_{20,w}$ = 46 ± 6 S and $s_{20,w}$ = 166 ± 13 S were derived for the two main peaks as shown in Fig. 1*A* (sedimentation coefficients ($s_{20,w}$) at standard conditions of water, 20 °C). These *s* values correspond to chromatin fiber fractions of different lengths. The isolated chromatin fibers were analyzed by partial MNase digestion and showed regular spacing, which demonstrates the integrity of the fiber preparation (Fig. 1*B*). In order to determine the length distribution of the fiber fragments, the number of nucleosomes per fiber was counted on scanning force microscopy images, and a bimodal distribution with two peaks at 19 ± 2 and 62 ± 5 nucleosomes was observed when fitted with the sum of two Gaussians (Fig. 1*C*). The two distributions had standard deviations of 7 and 32 nucleosomes, respectively. Previous

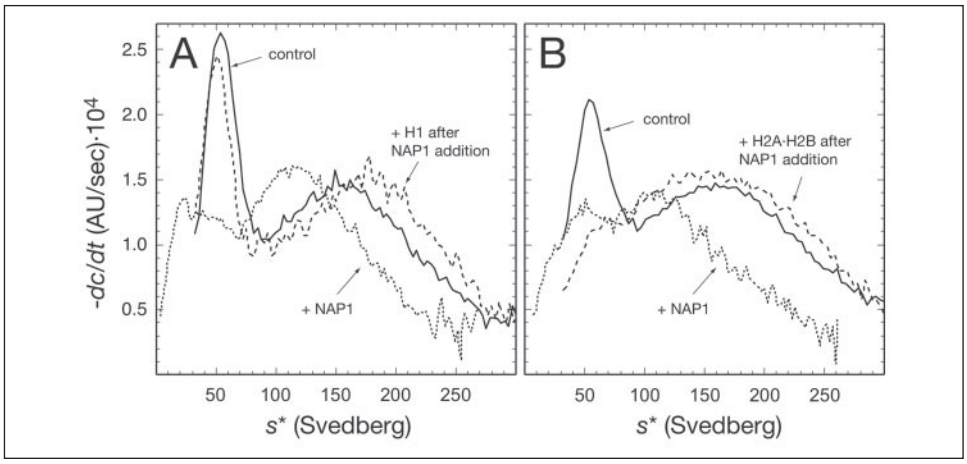

FIGURE 2. **Effect of NAP1 on the sedimentation coefficients distribution of chromatin fibers.** Representative examples for the different type of experiments are shown. All samples contained chromatin fibers at an $A_{260} \approx 1$. For the chromatin control samples, an average sedimentation distribution with two peaks at 46 ± 6 S and 166 ± 13 S was obtained. The sedimentation distribution for NAP1-incubated chromatin yielded two peaks with average values of 25 ± 3 S and 116 ± 6 S. *A* and *B,* the control chromatin fibers are shown as *solid lines*, the fibers incubated with NAP1 as *dotted lines,* and the NAP1 incubated fibers that were either titrated with H1 or H2A·H2B dimer as *dashed lines*. *A,* chromatin fibers were incubated with NAP1 at a concentration of 2.4 μM for 2 h. Then histone H1 was added in small aliquots to an end concentration of 0.8 μM. The resulting sedimentation distribution displayed two peaks with average values of 40 ± 3 S and 160 ± 16 S. *B,* chromatin fibers that were preincubated with 3.5 μM NAP1 were titrated stepwise to a final concentration of 1.7 μM H2A·H2B dimer. The distribution at the titration end point had two peaks with average values of 40 ± 7 S and 157 ± 19 S.

work showed that chromatin fibers with ~20 and 45 nucleosomes have a sedimentation coefficient of ~50 and 110 S under similar salt concentrations (68). As the number of nucleosomes measured by SFM is in excellent agreement with these results, the 50 S peak could be assigned to chromatin fiber fragments with ~20 nucleosomes and the 160 S species to chromatin fibers with ~60 nucleosomes.

To examine the effect of NAP1 on chromatin conformation, isolated fibers were preincubated with NAP1 for at least 1 h on ice and subsequently analyzed by sedimentation velocity experiments. As shown in Fig. 2, *A* and *B*, the sedimentation profile changes dramatically upon incubation with NAP1. The sedimentation coefficients of the main species were significantly shifted to lower *s* values, and two maxima at 25 ± 3 and 116 ± 6 S ($n = 4$ experiments) were obtained. This corresponds to a 45 and 30% decrease of the sedimentation coefficients for the two peaks, as compared with the control chromatin fibers. The peak at around 25 S was also reduced in height, indicating that the total amount of molecules with this sedimentation coefficient was decreased. The changes in the sedimentation profile could be reversed by the addition of either H1 (Fig. 2*A*) or H2A·H2B dimer (Fig. 2*B*). The two main peaks in the sedimentation coefficient profile were found at 40 ± 3 and 160 ± 16 S upon addition of H1 ($n = 4$ experiments, Fig. 2*A*) and at 40 ± 7 and 157 ± 19 S after titration with H2A·H2B dimer ($n = 3$ experiments, Fig. 2*B*).

NAP1 Removes the Linker Histone H1 from Native Fibers Leaving the Nucleosome Core Unaltered—To identify which histone proteins were displaced by NAP1, the protein composition was determined after separating the chromatin fibers from NAP1 by centrifugation (Fig. 3A). NAP1 induced the transition of histone H1 from the chromatin-containing pellet to the NAP1-containing supernatant. No core histones were found in the NAP1-containing supernatant, indicating that the core histones were not displaced by NAP1 from the chromatin fiber. The same experiments were also conducted with chromatin fibers that were depleted of linker histone H1. The stripped fibers also showed no significant displacement of core histone proteins from chromatin (Fig. 3*A*, *lane 13*). Only very small amounts of histone H2A·H2B dimer were found in the NAP1-containing fraction. Thus, NAP1 removes the linker histone H1 from native chromatin fibers and does not mobilize significant amounts of the core histones.

To analyze whether NAP1 alters the nucleosome spacing or the length of DNA protected by the nucleosome, MNase digestions were performed (supplemental Fig. S1). Upon NAP1 incubation, a single DNA band of ~146 bp was visible indicating the displacement of linker histones from chromatin.

NAP1 and RNA Mediated H2A·H2B Dimer Extraction—Because NAP1 was not able to extract significant amounts of core histones from native chromatin fibers, it was analyzed whether NAP1 can remove the H2A·H2B dimer from reconstituted mononucleosomes. Gel shift experiments were conducted with mononucleosomes containing fluorescently labeled histone H2A. In addition, RNA as a high affinity but bona fide unspecific histone binding partner was used to extract histone dimers from the mononucleosomes. The NAP1-$H2A^f$·H2B or RNA-$H2A^f$·H2B complexes were clearly separated from the mononucleosome band on standard agarose gels allowing the visualization of the transfer of $H2A^f$·H2B dimers from nucleosomes into a complex with NAP1 or RNA (Fig. 3*B*). To determine the relative binding affinities of NAP1 and RNA to the $H2A^f$·H2B dimer, the NAP1-$H2A^f$·H2B complex was titrated with increasing amounts of RNA (Fig. 3*B*, *lanes 1–7*). A competition with RNA for $H2A^f$·H2B in complex with NAP1 was evident, and equivalent concentrations of RNA and NAP1 were determined. Then mononucleosome solutions of about 200 nM were incubated with different amounts of NAP1 or RNA for 2–4 h at room temperature. Fig. 3*B*, *lanes 8–14*, shows the redistribution of the fluorescence signal from the mononucleosome band with increasing concentrations of NAP1 or RNA. In these experiments an additional fluorescent band was visible below the mononucleosome. This band could be assigned to a nucleosome complex with a histone hexamer core as it contained the $H2A^f$ fluorescence, and ethidium bromide staining indicated the presence of DNA. This hexasome was the predominant species formed upon incubation of mononucleosomes with NAP1 or RNA, with some complete dissociation observed at high concentrations when using a 146-bp DNA template (Fig. 3*B*, *lane 21*). For control experiments unlabeled mononucleosomes were also incubated with NAP1, resulting in equivalent dimer extraction as similar ethidium bromide staining pattern was apparent, indicating that fluorescence labeling did not alter nucleosome stability (data not shown). Both RNA and NAP1

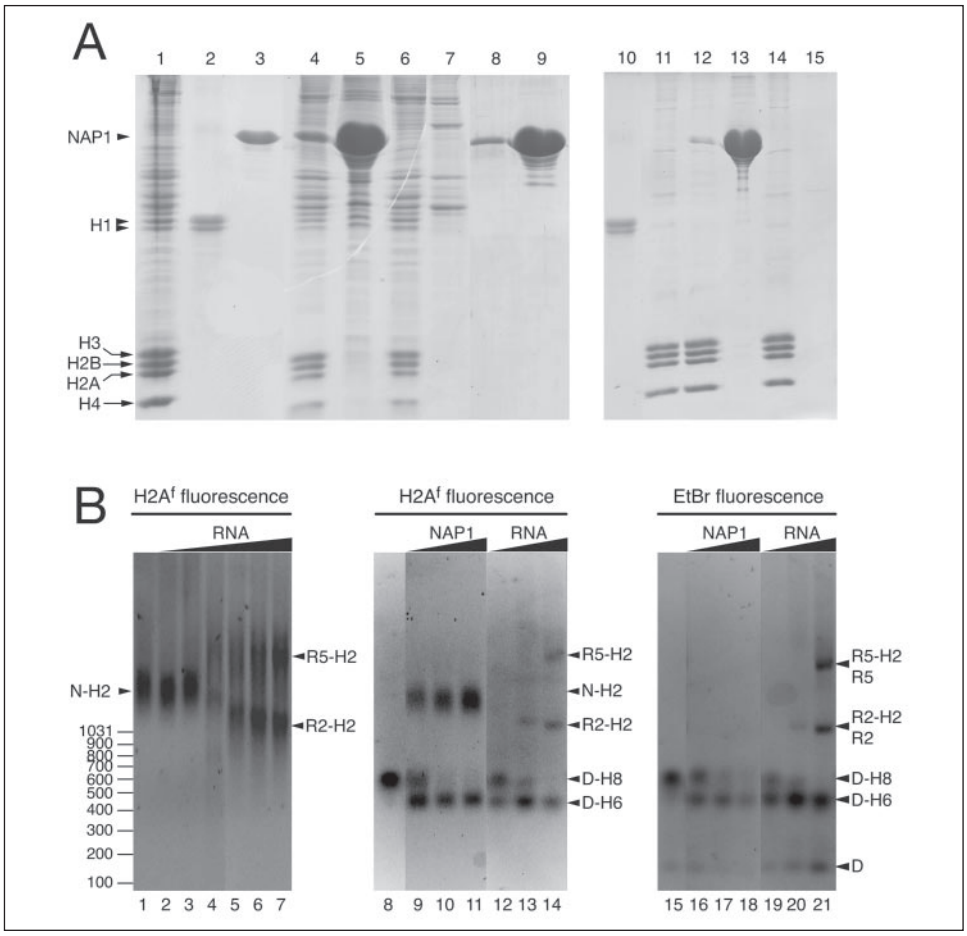

FIGURE 3. **Characterization of the proteins displaced from chromatin fiber and mononucleosomes by NAP1.** *A,* SDS-PAGE of native HeLa chromatin treated with NAP1. Chromatin was incubated with NAP1 and then pelleted to separate soluble NAP1 and interacting proteins from chromatin. *Left panel,* analysis of native chromatin fibers (*lanes 1–9*). *Lane 1,* whole chromatin sample; *lane 2,* H1; *lane 3*, NAP1; *lane 4*, pellet of chromatin incubated with NAP1; *lane 5,* supernatant of chromatin incubated with NAP1; *lane 6,* pellet of chromatin without added NAP1; *lane 7,* supernatant of chromatin without added NAP1; *lane 8*, pellet of NAP1 alone; *lane 9,* supernatant of NAP1 alone. *Right panel,* analysis of chromatin fibers that were stripped of linker histone H1 (*lanes 10–15*). *Lane 10,* H1; *lane 11,* whole H1-stripped chromatin sample; *lane 12,* pellet of chromatin incubated with NAP1; *lane 13,* supernatant of chromatin incubated with NAP1; *lane 14,* pellet of chromatin without added NAP1; *lane 15,* supernatant of chromatin without added NAP1. *B,* removal of $H2A^f$·H2B dimers from reconstituted mononucleosomes by NAP1 and RNA analyzed by gel electrophoresis. The following abbreviations are used to assign the bands: *D*, free 146-bp DNA; *H2*, $H2A^f$·H2B dimer; *D-H6*, nucleosome with histone hexamer core, where one H2A·H2B dimer is missing; *D-H8*, complete mononucleosome; *N-H2*, complex of NAP1 with $H2A^f$·H2B dimer; *R2,* free 18 S rRNA (≈2000 nt); *R5,* free 28 S rRNA (≈5000 nt); *R2-H2*, complex of 18 S rRNA with $H2A^f$·H2B dimer; *R5-H2,* complex of 28 S rRNA with $H2A^f$·H2B dimer. *Left panel* (*lanes 1–7*), complex of NAP1 (6 μM) and $H2A^f$·H2B dimer (3 μM) was titrated with increasing amounts of RNA and visualized by recording the $H2A^f$ fluorescence. RNA concentrations: *lane 1,* no RNA; *lane 2,* 6.5 ng/μl; *lane 3,* 13 ng/μl; *lane 4,* 30 ng/μl; *lane 5,* 70 ng/μl; *lane 6,* 120 ng/μl; *lane 7,* 240 ng/μl. At increased RNA concentrations a transition of $H2A^f$·H2B from a NAP1-$H2A^f$·H2B complex into an RNA-$H2A^f$·H2B complex was observed. *Center panel* (*lanes 8–14*): recombinant mononucleosomes (200 nM) reconstituted with $H2A^f$ were incubated with increasing NAP1 and RNA concentrations: *lane 8,* no NAP1 and RNA; *lane 9,* 0.9 μM NAP1; *lane 10,* 3.3 μM NAP1; *lane 11,* 5.1 μM NAP1; *lane 12,* 7.8 ng/μl RNA; *lane 13,* 18 ng/μl RNA; and *lane 14,* 58 ng/μl RNA. Samples were visualized by detection of the $H2A^f$ fluorescence. *Right panel* (*lanes 15–21*), same sample composition as in *lanes 8–14,* but visualization of DNA bands was via ethidium bromide staining.

seemed to be similarly efficient in extracting one histone $H2A^f$·H2B dimer from the mononucleosome complex at the concentrations used.

Scanning Force Microscopy Analysis of Chromatin Fibers—The structural changes caused by the incubation of chromatin fibers with NAP1 were further analyzed by scanning force microscopy. As shown on the images in Fig. 4, A–*D*, the isolated native chromatin fibers adopted various conformational states. In contrast to other studies, these fibers were not treated by fixation agents and were deposited to the mica surface by a procedure that leads to minimal disturbance of the sample. Some of the molecules had a fiber-like structure, although others were more condensed and hence probably represent chromatin fragments that are folded beyond the 30-nm fiber. According to the chromonema model, an additional compaction of the 30-nm fiber is achieved by its folding into 60–80- and 100–130-nm chromonema fibers (69–71). Analysis of the fiber height profiles revealed that in almost all regions only a single layer of nucleosomes was present. This suggests that upon binding of the fiber to the surface, its three-dimensional organization is rearranged so that all nucleosomes can contact the surface, in an equilibration process similar to the one that has been observed for long DNA fragments (72). Thus, the number and position of all nucleosomes present in the fiber could be determined. A total of 36,261 nucleosomes in 1063 fibers were evaluated. It is noted that the quantification of the nucleosome number per individual fiber on the SFM images agreed with the observed sedimentation behavior of the chromatin fibers (Fig. 1).

To elucidate the effects of NAP1 on the chromatin conformation, fibers incubated with NAP1 were examined. Incubation of chromatin with NAP1 did not have drastic effects on the conformation, which was apparent by simple visual inspection of the SFM images (Fig. 4, *E–H*). To compare with the linker histone-depleted chromatin conformation, H1-stripped chromatin fibers were imaged with the SFM. The overall folding in these fibers did not change significantly (Fig. 4, *I–L*). However, the quantification of the average internucleosomal distances within the chromatin fibers revealed distinct changes upon NAP1 treatment. A total of 125 control fibers (9550 nucleosomes), 753 fibers without H1

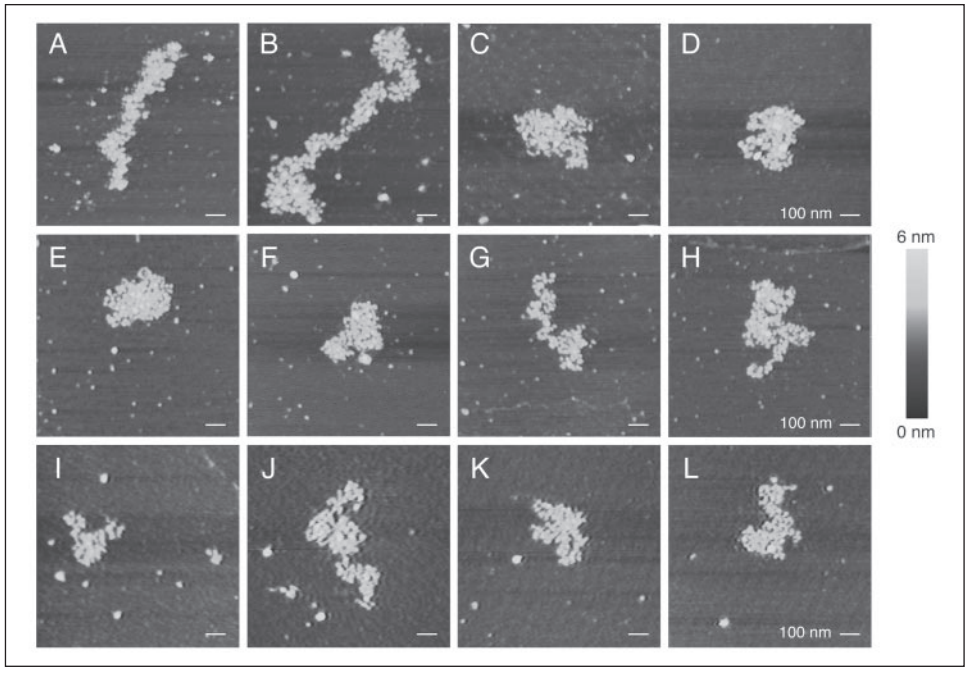

FIGURE 4. **SFM images of chromatin fibers (1 × 1 μm images).** *A–D,* single chromatin fiber fragments. *E–H,* chromatin fibers incubated with NAP1. *I–L,* chromatin fibers depleted of linker histone H1.

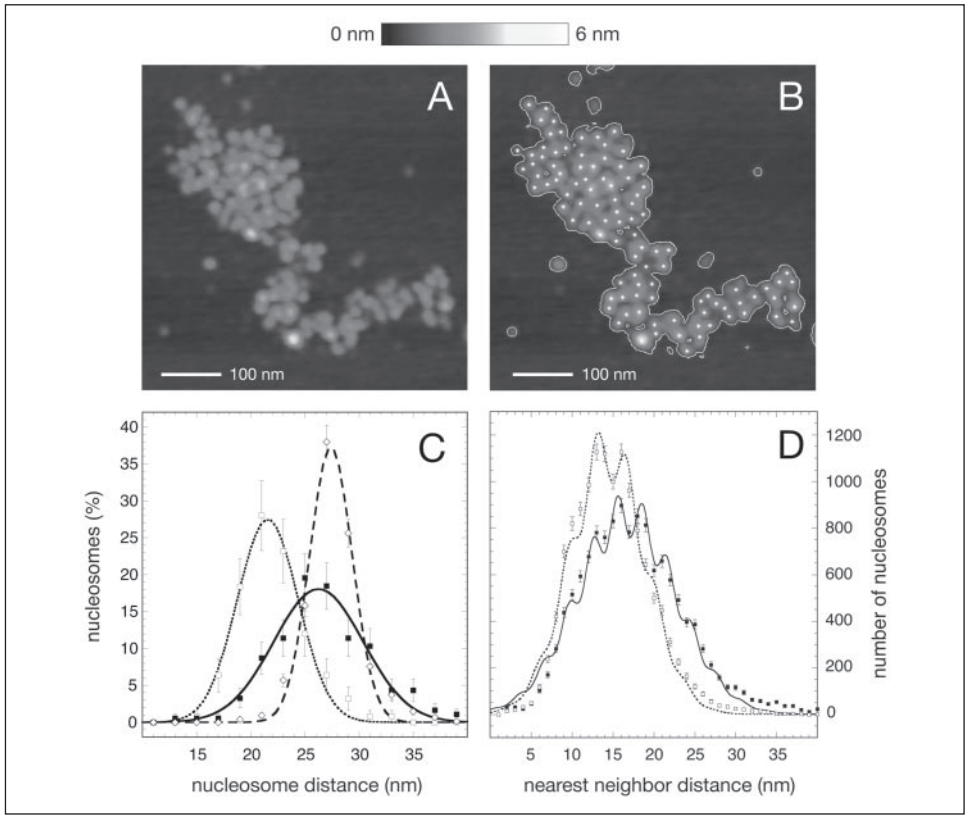

FIGURE 5. **Image analysis of chromatin fibers to determine internucleosomal distances.** *A,* original SFM image, 550 × 550 nm scan. *B,* the area of the chromatin fiber was segmented as indicated by a contour line around the fiber. Centers of the individual nucleosomes were automatically identified and are depicted in the image with *white asterisks*. *C,* histogram of the average internucleosomal distance within control chromatin fibers (*open squares*), chromatin fibers incubated with NAP1 (*black squares*) and fibers without H1 (*open diamonds*). The average value for the distance distribution increased from 22.3 ± 0.4 to 27.6 ± 0.6 nm upon removal of histone H1 by NAP1. In addition, the distribution of distances became broader with standard deviations of 2.5 for the control and 4.2 nm for the NAP1-treated fibers. For chromatin fibers stripped of linker histones, an average distance of 27.4 ± 0.8 nm was obtained. *D,* distribution of distances of a given nucleosome to its nearest neighbor nucleosome. Both control fibers (*open squares*) and chromatin fibers incubated with NAP1 (*black squares*) displayed peaks with a periodicity of 2.9 nm that is likely to reflect the three-dimensional folding of the nucleosome chain in the 30-nm chromatin fiber. Accordingly, the data were fitted with a modified Gaussian distribution (see Equation 1).

(13441 nucleosomes), and 184 chromatin fibers (13,280 nucleosomes) incubated with NAP1 from 4 or 5 different sample depositions were evaluated. Fig. 5*C* shows the histogram of the internucleosomal distances for control chromatin fibers, the H1-stripped fibers, and those incubated with NAP1. The average distance between the nucleosomes increased from 22.3 ± 0.4 nm for the control to 27.6 ± 0.6 nm in the presence of NAP1. The difference of 5.3 ± 0.7 nm would correspond to ~17-bp DNA released from the nucleosome. This increased nucleosomal distance is also found in the linker histone-stripped fibers that showed mean distances of 27.4 ± 0.8 nm. The distribution of the internucleosomal distances for the NAP1 incubated fibers was also broadened compared with control chromatin as apparent from the different standard deviations of 2.5 to 4.2 nm. This may be due to the increased heterogeneity in nucleosome composition of the resulting fiber. In order to characterize the organization of individual nucleosomes, the distance between a given nucleosome and its nearest neighbor was measured. The corresponding relation is shown in Fig. 5*D*. Again the whole distribution was shifted to larger distances by 2.7 nm and showed

some broadening with average values of 14.9 ± 0.1 and 17.6 ± 0.1 nm and standard deviations of 4.6 and 6.0 nm in the absence and presence of NAP1. Most interestingly, the two distributions were not of a simple Gaussian shape but showed several peaks/shoulders at about 10.4, 13.2, 16.4, and 19.4 nm for the control and at 10.0, 12.8, 15.6, 18.6, 21.4, and 24.2 nm in the presence of NAP1. This corresponds to a periodical distance of 2.9 ± 0.1 nm between peaks for the two samples. This nearest neighbor distance distribution of the surface-bound fibers reflects the three-dimensional organization of the repeating unit of the chromatin fiber, and its relation to different fiber geometries is currently being evaluated.[3] In the presence of NAP1, the periodicity of the peaks was preserved, but the distribution on an average shifted by 2.7 nm. This suggests that the overall organization of the chromatin fibers was maintained upon removal of histone H1 by NAP1, while the distance between the nucleosomes increased.

[3] G. L. Heuvelman, G. Wedemann, J. F. Kepert, and K. Rippe, manuscript in preparation.

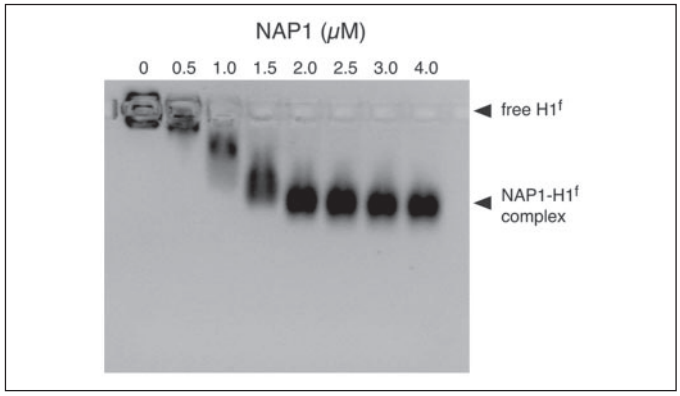

FIGURE 6. **Gel shift analysis of NAP1 with histone H1^f.** Increasing amounts of NAP1 (0.5, 1, 1.5, 2.0, 2.5, 3, and 4 μM) were mixed with 1 μM histone H1^f. Histone H1^f was completely shifted into a NAP1 containing complex at a concentration of 2 μM NAP1, indicating a 2:1 complex of NAP1 and histone H1.

NAP1 Binds the Linker Histone H1^f with a 2:1 Stoichiometry and with a Comparable Affinity as the H2A·H2B Dimer—By electrophoretic gel mobility shift analysis, the binding stoichiometry of NAP1 to H1^f was determined. First histone H1^f was titrated with increasing amounts of NAP1 showing the formation of a distinct complex at a stoichiometry of 2 ± 0.5 NAP1 monomer/histone monomer (Fig. 6). In order to compare the binding affinities of H2A·H2B dimer and H1 to NAP1, a saturated H2A^r·H2B dimer-NAP1 complex was titrated with H1^f (r and f = labeling with Alexa 633 and 488, respectively). H1^f was capable of competing with histone H2A^r·H2B dimer for NAP1 binding. Because histone H2A^r·H2B and H1^f were labeled with different dyes and migrated slightly different in their complexes with NAP1, the two complexes could be separated on agarose gels and visualized with UV excitation light (data not shown). H1^f seemed to be efficient in binding to NAP1 as titrated H1^f bound to NAP1 that was previously saturated with H2A^r·H2B dimer.

The molecular weights and association states of the NAP1-H1^f complexes were determined by sedimentation equilibrium experiments under low salt conditions (10 mM Tris, pH 7.5, and 10 mM KCl; see Fig. 7, *A* and *B*). Initial analysis showed that the data could only be fitted poorly to a one-component model, with a mean molecular mass between 200 and 400 kDa, indicating the presence of higher order complexes. The absorbance profiles at three different protein concentrations and two different wavelengths could be fitted most accurately with a model of a monomer-tetramer equilibrium (Fig. 7, *A* and *B*). The molecular weight for the monomer was fixed to 126 kDa during fitting, which corresponds to a complex consisting of two NAP1 and one H1^f. The oligomerization of the $NAP1_2$-H1^f complex in a monomer-tetramer equilibrium was further confirmed by sedimentation velocity

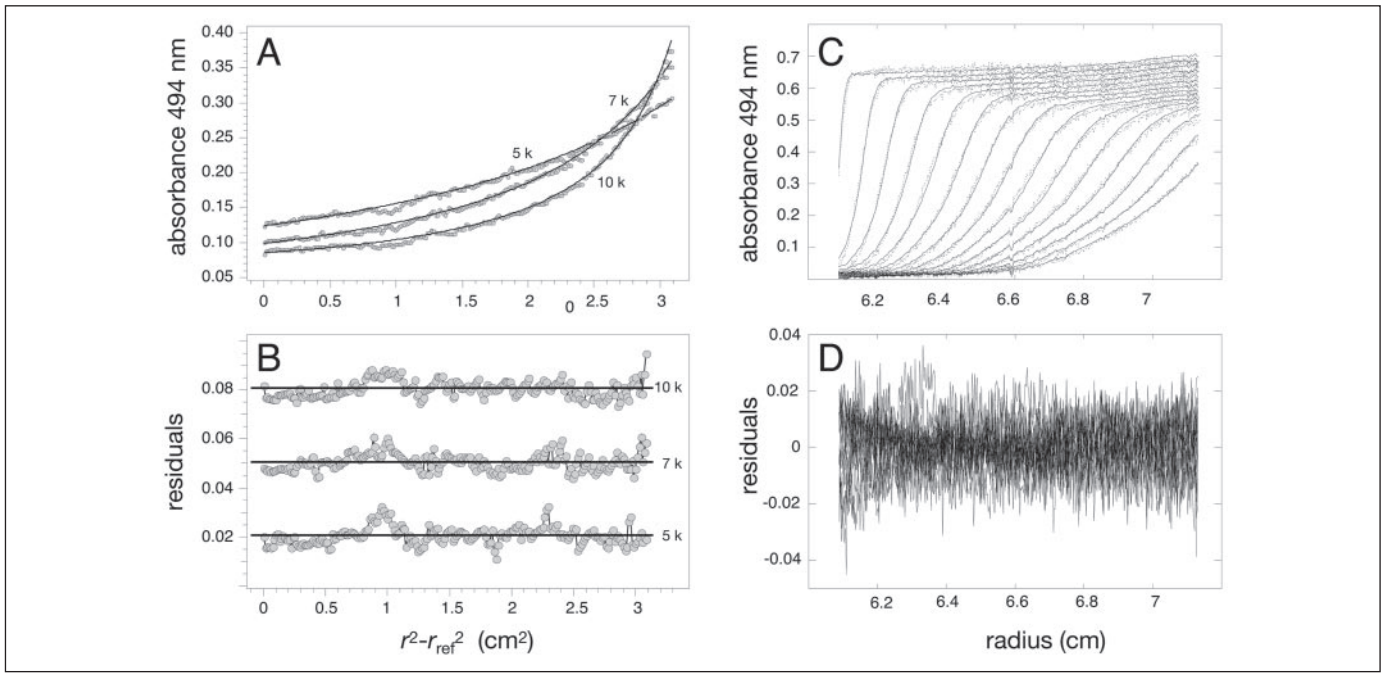

FIGURE 7. **AUC analysis of NAP1 complexes with histone H1^f.** NAP1 samples between 8 and 16 μM were mixed with histone H1^f in a 2:1 ratio (monomer NAP1: monomer H1^f). *A,* sedimentation equilibrium analysis of NAP1-H1^f complexes. Data were recorded at 5000, 7000, and 10,000 rpm at 494 nm. The fits of a monomer-tetramer model to the absorbance profiles are shown by *solid lines*. The monomer represents a complex of a NAP1 dimer with one H1 and a molecular mass of 126 kDa. *B,* residuals of the fitted function to the absorbance data shown under *A*. *C,* sedimentation velocity analysis. NAP1 at 16 μM was mixed with 8 μM H1^f, and data were recorded at 494 nm, 37,000 rpm, and 20 °C in a continuous scan mode. As in *A,* a monomer-tetramer equilibrium model was fitted to the absorbance data (*solid line*, every sixth scan is shown), with a $(NAP1)_2$-H1 complex as monomer. *D,* residuals for the fit presented in *C*.

experiments. As shown in Fig. 7, *C* and *D*, the velocity sedimentation profiles could be fitted well with a monomer-tetramer model yielding sedimentation coefficients of 6.1 ± 0.1 S and 10.5 ± 1 S for the monomer and tetramer, respectively. Again the molecular mass for the monomer was fixed to 126 kDa during fitting.

DISCUSSION

NAP1 was initially described as a factor that facilitates nucleosome assembly (24). In later reports it has been also linked to other cellular processes like histone transport, gene expression, and nucleosome remodeling (18, 21, 27, 34, 73). Here we examined how NAP1 affects the chromatin fiber organization. A NAP1-induced transition to an extended fiber conformation was observed by AUC and SFM. Our results show that NAP1 binds to histone H1 with high affinity. This leads to the reversible removal of linker histones from chromatin.

The chromatin fibers studied were isolated from HeLa cells and showed hydrodynamic and structural properties comparable with earlier studies (38, 47, 58, 74). Incubation with NAP1 changed the chromatin sedimentation profile significantly as apparent from the 30–45% decrease of the sedimentation coefficient distribution. This predominantly reflects an extension of the chromatin fiber shape and to a smaller extent an up to ~10% reduction of the molecular weight because of the loss of H1. The latter effect would correspond to an equal decrease in the sedimentation coefficient if the frictional coefficient remained constant. Thus, a 20–35% reduction of the *s* value distribution was due to a change of the chromatin conformation to a more extended shape. This is consistent with previous reports on the effect of linker histone binding to chromatin where similar changes in the sedimentation coefficient have been reported (37, 75, 76). For the first maximum of around 50 S (~20 nucleosomes) some height reduction and broadening were observed in the presence of NAP1 in addition to the shift of the maximum (Fig. 2*A*). Apparently, nucleosomes are more accessible in these shorter chromatin fibers, and linker histones could be extracted more easily as compared with the second peak of the distribution at 160 S (~60 nucleosomes). This might be due to a folding of longer chromatin fibers into higher order structures of 60–130 nm diameter (69–71), in which additional internucleosomal contacts are present that could stabilize the chromatosome structure.

The additional compaction beyond the 30-nm chromatin fiber was apparent also on the SFM images. On these images the chromatin conformation changes induced by NAP1 could be examined on the single nucleosomal level. The NAP1-treated fibers retained a similar organization, and no large differences were visible from a simple inspection of the images (Fig. 4). However, quantitative analysis revealed an increase in the internucleosomal distance by about 5 nm from 22.3 ± 0.4 to 27.6 ± 0.6 nm upon incubation with NAP1. This can be explained by the partial release of DNA from the chromatosome in the DNA entry-exit region. The control with H1-stripped fibers had an average distance of 27.4 ± 0.8 nm, which further confirmed that the NAP1-induced changes were because of linker histone displacement. It has been reported previously that linker histone extraction changes the center to center distances between nucleosomes in the chromatin fiber and induces an opening of the chromatin fiber (47, 48). Most interestingly, the DNA hypermethylation of chromatin, which has been correlated with a more compact and biologically inactive conformation, induced a similar decrease of the internucleosomal distance by ~4 nm, from 28 to 24 nm, although the overall fiber conformation was also preserved (52). Thus, we conclude that the chromatin fiber organization can accommodate changes of the internucleosome distance of 4–5 nm. Such a nucleosome distance reduction appears to be characteristic for the transition of the chromatin fiber between transcriptionally active and more repressive conformations.

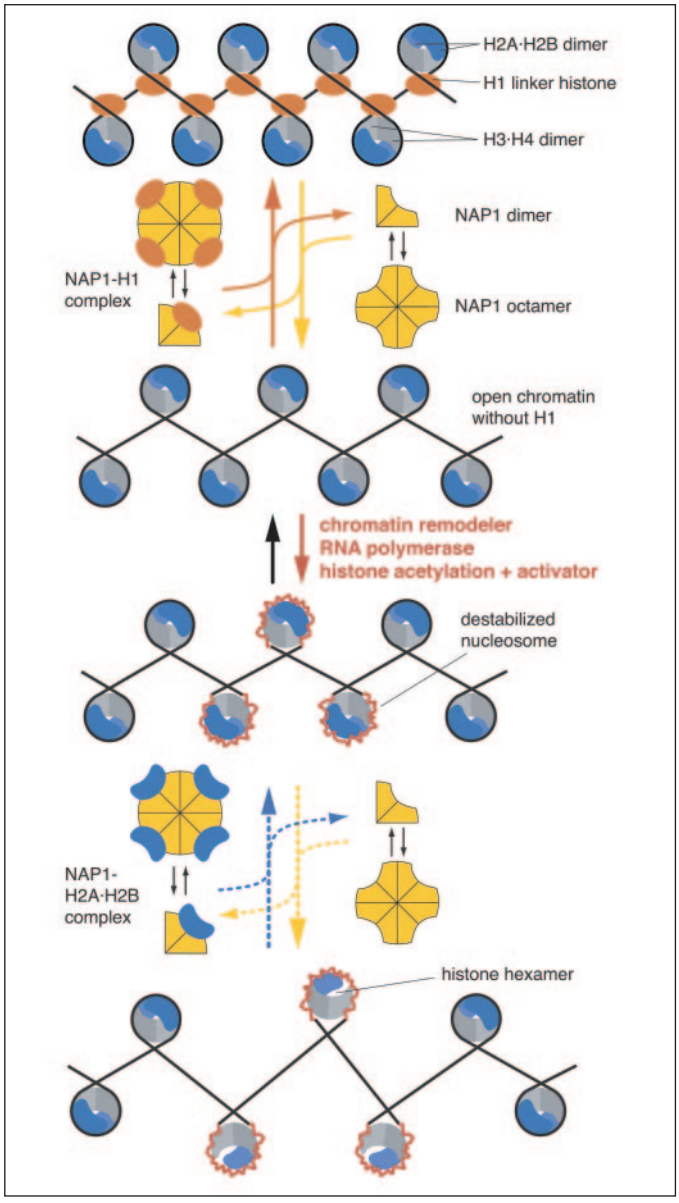

FIGURE 8. **Effects of NAP1 on the chromatin fiber conformation.** NAP1 is in a dimer-octamer equilibrium as described in a previous study (60) and binds linker histone H1 from chromatin fibers. This induces a more open and extended chromatin conformation with an increased internucleosome distance. In the absence of additional protein factors, NAP1 will not remove H2A·H2B dimer from H1-depleted fibers (Fig. 3*A*), but it can do so with mononucleosomes as described previously (28) (see also Fig. 3*B*). Furthermore, it has been reported that NAP1 is involved in H2A·H2B dimer exchange on nucleosomal arrays by the SWR1 chromatin remodeling complex (18) or in an *in vitro* system with acetylated histones and the transcriptional activator GalVP16 (30). NAP1-related histone chaperone activities have also been identified in the context of RNA polymerase II transcription where nucleosomes with a histone hexamer core form that are lacking one H2A·H2B dimer (19, 31–34, 77, 82, 83). Accordingly, a NAP1-mediated removal of one H2A·H2B dimer that requires destabilization of the nucleosome structure due, for example, to chromatin remodeling or RNA polymerase activity has been included in the scheme. As indicated by the *dashed arrows*, the occurrence of this reaction with chromatin fibers remains to be demonstrated.

The binding stoichiometry of linker histone H1 with NAP1 and the molecular composition of the resulting complexes were analyzed by AUC and gel shift experiments. In the gel shift analysis, a binding stoichiometry of two NAP1 monomers per histone H1 monomer was observed, which was also consistent with the AUC experiments where H1 was titrated to chromatin fibers preincubated with NAP1 in order to reverse the NAP1-induced conformation changes. As inferred from the

AUC sedimentation velocity and sedimentation equilibrium experiments, a complex of one NAP1 dimer with one H1 is formed, which was in equilibrium with a complex of a NAP1 octamer associated with four H1 molecules (504 kDa). This was very similar to the association properties of NAP1 in complexes with the H2A·H2B dimer (60). In addition, Shintomi *et al.* (35) reported recently that NAP1 binds to the H1 analogue B4 in *Xenopus* egg and acts as a linker histone chaperone. The authors estimated a NAP1:B4 binding stoichiometry of 2:1 and observed that the complex of NAP1-B4 migrated in native polyacrylamide gels with an apparent molecular mass of ~230 kDa and an additional band of ~500 kDa, which is also indicative of the formation of higher order association states.

NAP1 has been related previously to histone exchange and was proposed to be involved in transcription (18, 28, 34). Transcription elongation is facilitated by factors that alter nucleosomes in order to allow RNA polymerase to proceed along the template (31, 33, 77–81). One of these factors, the FACT complex, has histone chaperone activity that facilitates the movement of RNA polymerases along the template by extracting H2A·H2B dimers from the nucleosome complexes (19, 31–33). The resulting nucleosomes with a hexameric histone core appear to be intermediates of transcription through chromatin (19, 77, 82, 83). Accordingly, histone chaperones like NAP1 have been proposed to be involved in the transient removal of the H2A·H2B dimer from the octamer, while preserving most of the overall nucleosomal structure as opposed to a complete removal and subsequent *de novo* assembly of nucleosomes (34). This activity has been demonstrated in *in vitro* experiments where NAP1 was sufficient for extracting and exchanging the H2A·H2B dimer from a mononucleosome (28). Here, we also observed that NAP1 as well as RNA are capable of extracting the H2A·H2B dimer at the mononucleosomal level. However, NAP1 failed to do so in the context of native chromatin fibers. Because RNA has a strong histone binding affinity but has not been reported to interact specifically with nucleosomes, it seems likely that both NAP1 and RNA bind histones that have already dissociated from the nucleosome (84). This process would not require a specific interaction with nucleosomes, which is in agreement with the observation that NAP1 binds H2A·H2B dimer and histone H1 tightly with dissociation constants in the nanomolar range but has low affinity to nucleosomes (60, 85). The dissociation of the H2A·H2B dimer appears to occur only at a very slow rate with chromatin fibers in the absence of additional factors. In contrast, the linker histone H1 displays a much higher mobility and exchange rate *in vivo* than the core histones as reviewed in Ref. 86.

An inhibition of transcription by linker histone H1 has been reported in a number of studies, and it is clear that the transition of chromatin to a transcriptionally active state has to involve the removal of linker histones (10, 11, 76, 87, 88). Binding to NAP1 would provide a mechanism of how this can be established. A recent study described the interaction of the acidic nuclear protein parathymosin with H1 (9). This protein has only a modest affinity for linker histone H1 with a dissociation constant in the μM range but nevertheless induces chromatin decondensation *in vivo*. Thus, it seems likely that NAP1 as a binding partner for H1 with a nanomolar dissociation constant can exert the same effect on chromatin.

In summary, we propose that NAP1 can induce a more open chromatin conformation via the pathway depicted in Fig. 8. NAP1 is present in a dimer-octamer equilibrium and can bind both H1 and the H2A·H2B dimer with high affinity as shown here and in Ref. 60. In the absence of additional factors, NAP1 will extract only linker histones from chromatin fibers. The H2A·H2B dimer remained stably bound in the nucleosomes, even if fibers devoid of H1 were examined. Thus, the removal/exchange of the H2A·H2B dimer by NAP1 observed with mononucleosomes (28) requires an additional destabilization of the chromatin fiber/nucleosome structure, possibly due to the activity of chromatin remodelers (18), RNA polymerase (34), or histone acetylation and a transcriptional activator (30). These factors could facilitate the removal of a single histone H2A·H2B dimer by NAP1 or a related histone chaperone activity to form chromatin-containing nucleosomes with a histone hexamer core that has been reported to be an intermediate of actively transcribed chromatin (19, 31–34, 77, 82, 83). On the other hand, it is demonstrated here that the high affinity binding of NAP1 and H1 occurs readily with chromatin fibers. The physiological relevance of this process is supported by the recent observation that NAP1 interacts *in vivo* with the H1 analogue B4 in *Xenopus* eggs (35). As the absence of H1 is an essential feature of transcriptionally active chromatin, the formation of a NAP1-H1 complex might be the origin for the global effects of NAP1 on gene expression (27).

Acknowledgments—We thank Peter Lichter, Malte Wachsmuth, Gernot Längst, Olaf Thürigen, Claudio Rivetti, and Lutz Ehrhardt for help and discussions and Karolin Luger and Tom Owen-Hughes for providing plasmid vectors. The insightful comments of the anonymous reviewer of a previous manuscript version are gratefully acknowledged.

REFERENCES

1. Vermaak, D., Ahmad, K., and Henikoff, S. (2003) *Curr. Opin. Cell Biol.* **15,** 266–274
2. Felsenfeld, G., and Groudine, M. (2003) *Nature* **421,** 448–453
3. Gilbert, N., Boyle, S., Fiegler, H., Woodfine, K., Carter, N. P., and Bickmore, W. A. (2004) *Cell* **118,** 555–566
4. Weintraub, H., and Groudine, M. (1976) *Science* **193,** 848–856
5. Wu, C., Wong, Y. C., and Elgin, S. C. (1979) *Cell* **16,** 807–814
6. Bellard, M., Kuo, M. T., Dretzen, G., and Chambon, P. (1980) *Nucleic Acids Res.* **8,** 2737–2750
7. van Holde, K. E. (1989) *Chromatin*, Springer-Verlag, Heidelberg
8. Dillon, N. (2004) *Biol. Cell* **96,** 631–637
9. Martic, G., Karetsou, Z., Kefala, K., Politou, A. S., Clapier, C. R., Straub, T., and Papamarcaki, T. (2005) *J. Biol. Chem.* **280,** 16143–16150
10. Bednar, J., Horowitz, R. A., Grigoryev, S. A., Carruthers, L. M., Hansen, J. C., Koster, A. J., and Woodcock, C. L. (1998) *Proc. Natl. Acad. Sci. U. S. A.* **95,** 14173–14178
11. Zlatanova, J., Caiafa, P., and Van Holde, K. (2000) *FASEB J.* **14,** 1697–1704
12. Grummt, I., and Pikaard, C. S. (2003) *Nat. Rev. Mol. Cell. Biol.* **4,** 641–649
13. Fischle, W., Wang, Y., and Allis, C. D. (2003) *Curr. Opin. Cell Biol.* **15,** 172–183
14. Hebbes, T. R., Clayton, A. L., Thorne, A. W., and Crane-Robinson, C. (1994) *EMBO J.* **13,** 1823–1830
15. Lachner, M., O'Carroll, D., Rea, S., Mechtler, K., and Jenuwein, T. (2001) *Nature* **410,** 116–120
16. Fan, J. Y., Gordon, F., Luger, K., Hansen, J. C., and Tremethick, D. J. (2002) *Nat. Struct. Biol.* **9,** 172–176
17. McKittrick, E., Gafken, P. R., Ahmad, K., and Henikoff, S. (2004) *Proc. Natl. Acad. Sci. U. S. A.* **101,** 1525–1530
18. Mizuguchi, G., Shen, X., Landry, J., Wu, W. H., Sen, S., and Wu, C. (2004) *Science* **303,** 343–348
19. Sims, R. J., III, Mandal, S. S., and Reinberg, D. (2004) *Curr. Opin. Cell Biol.* **16,** 263–271
20. Haushalter, K. A., and Kadonaga, J. T. (2003) *Nat. Rev. Mol. Cell. Biol.* **4,** 613–620
21. Loyola, A., and Almouzni, G. (2004) *Biochim. Biophys. Acta* **1677,** 3–11
22. Tyler, J. K. (2002) *Eur. J. Biochem.* **269,** 2268–2274
23. Adams, C. R., and Kamakaka, R. T. (1999) *Curr. Opin. Genet. Dev.* **9,** 185–190
24. Ishimi, Y., Hirosumi, J., Sato, W., Sugasawa, K., Yokota, S., Hanaoka, F., and Yamada, M. (1984) *Eur. J. Biochem.* **142,** 431–439
25. Walter, P. P., Owen-Hughes, T. A., Cote, J., and Workman, J. L. (1995) *Mol. Cell. Biol.* **15,** 6178–6187
26. Chen, H., Li, B., and Workman, J. L. (1994) *EMBO J.* **13,** 380–390
27. Ohkuni, K., Shirahige, K., and Kikuchi, A. (2003) *Biochem. Biophys. Res. Commun.* **306,** 5–9
28. Park, Y. J., Chodaparambil, J. V., Bao, Y., McBryant, S. J., and Luger, K. (2005) *J. Biol. Chem.* **280,** 1817–1825
29. Redon, C., Pilch, D., Rogakou, E., Sedelnikova, O., Newrock, K., and Bonner, W. (2002) *Curr. Opin. Genet. Dev.* **12,** 162–169
30. Ito, T., Ikehara, T., Nakagawa, T., Kraus, W. L., and Muramatsu, M. (2000) *Genes Dev.* **14,** 1899–1907

31. Belotserkovskaya, R., Oh, S., Bondarenko, V. A., Orphanides, G., Studitsky, V. M., and Reinberg, D. (2003) *Science* **301,** 1090–1093
32. Orphanides, G., Wu, W. H., Lane, W. S., Hampsey, M., and Reinberg, D. (1999) *Nature* **400,** 284–288
33. Belotserkovskaya, R., Saunders, A., Lis, J. T., and Reinberg, D. (2004) *Biochim. Biophys. Acta* **1677,** 87–99
34. Levchenko, V., and Jackson, V. (2004) *Biochemistry* **43,** 2359–2372
35. Shintomi, K., Iwabuchi, M., Saeki, H., Ura, K., Kishimoto, T., and Ohsumi, K. (2005) *Proc. Natl. Acad. Sci. U. S. A.* **102,** 8210–8215
36. Ramos, I., Prado, A., Finn, R. M., Muga, A., and Ausio, J. (2005) *Biochemistry* **44,** 8274–8281
37. Ausio, J. (2000) *Biophys. Chem.* **86,** 141–153
38. Wang, X. Y., He, C., Moore, S. C., and Ausio, J. (2001) *J. Biol. Chem.* **276,** 12764–12768
39. Carruthers, L. M., and Hansen, J. C. (2000) *J. Biol. Chem.* **275,** 37285–37290
40. Dorigo, B., Schalch, T., Bystricky, K., and Richmond, T. J. (2003) *J. Mol. Biol.* **327,** 85–96
41. Hansen, J. C., and Turgeon, C. L. (1999) *Methods Mol. Biol.* **119,** 127–141
42. Hansen, J. C., Ausio, J., Stanik, V. H., and van Holde, K. E. (1989) *Biochemistry* **28,** 9129–9136
43. Carruthers, L. M., Schirf, V. R., Demeler, B., and Hansen, J. C. (2000) *Methods Enzymol.* **321,** 66–80
44. Garcia-Ramirez, M., Rocchini, C., and Ausio, J. (1995) *J. Biol. Chem.* **270,** 17923–17928
45. Schwarz, P. M., and Hansen, J. C. (1994) *J. Biol. Chem.* **269,** 16284–16289
46. Garcia-Ramirez, M., Dong, F., and Ausio, J. (1992) *J. Biol. Chem.* **267,** 19587–19595
47. Leuba, S. H., Yang, G., Robert, C., Samori, B., van Holde, K., Zlatanova, J., and Bustamante, C. (1994) *Proc. Natl. Acad. Sci. U. S. A.* **91,** 11621–11625
48. Zlatanova, J., Leuba, S. H., and van Holde, K. (1998) *Biophys. J.* **74,** 2554–2566
49. Leuba, S. H., Bustamante, C., van Holde, K., and Zlatanova, J. (1998) *Biophys. J.* **74,** 2830–2839
50. Leuba, S. H., Bustamante, C., Zlatanova, J., and van Holde, K. (1998) *Biophys. J.* **74,** 2823–2829
51. Yodh, J. G., Lyubchenko, Y. L., Shlyakhtenko, L. S., Woodbury, N., and Lohr, D. (1999) *Biochemistry* **38,** 15756–15763
52. Karymov, M. A., Tomschik, M., Leuba, S. H., Caiafa, P., and Zlatanova, J. (2001) *FASEB J.* **15,** 2631–2641
53. Bash, R., Wang, H., Yodh, J., Hager, G., Lindsay, S. M., and Lohr, D. (2003) *Biochemistry* **42,** 4681–4690
54. Wang, H., Bash, R., Yodh, J. G., Hager, G. L., Lohr, D., and Lindsay, S. M. (2002) *Biophys. J.* **83,** 3619–3625
55. Bash, R. C., Yodh, J., Lyubchenko, Y., Woodbury, N., and Lohr, D. (2001) *J. Biol. Chem.* **276,** 48362–48370
56. Yodh, J. G., Woodbury, N., Shlyakhtenko, L. S., Lyubchenko, Y. L., and Lohr, D. (2002) *Biochemistry* **41,** 3565–3574
57. d'Erme, M., Yang, G., Sheagly, E., Palitti, F., and Bustamante, C. (2001) *Biochemistry* **40,** 10947–10955
58. Giannasca, P. J., Horowitz, R. A., and Woodcock, C. L. (1993) *J. Cell Sci.* **105,** 551–561
59. Kepert, J. F., Fejes Tóth, K., Caudron, M., Mücke, N., Langowski, J., and Rippe, K. (2003) *Biophys. J.* **85,** 4012–4022
60. Fejes Tóth, K., Mazurkiewicz, J., and Rippe, K. (2005) *J. Biol. Chem.* **280,** 15690–15699
61. Lee, K. M., and Hayes, J. J. (1997) *Proc. Natl. Acad. Sci. U. S. A.* **94,** 8959–8964
62. Neben, K., Tews, B., Wrobel, G., Hahn, M., Kokocinski, F., Giesecke, C., Krause, U., Ho, A. D., Kramer, A., and Lichter, P. (2004) *Oncogene* **23,** 2379–2384
63. Laue, T. M., Shah, B. D., Ridgeway, T. M., and Pelletier, S. L. (1992) in *Analytical Ultracentrifugation in Biochemistry and Polymer Science* (Harding, S. E., Rowe, A. J., and Horton, J. C., eds) pp. 90–125, Royal Society of Chemistry, Cambridge, UK
64. Philo, J. S. (2000) *Anal. Biochem.* **279,** 151–163
65. Schuck, P. (2003) *Anal. Biochem.* **320,** 104–124
66. McBryant, S. J., Park, Y. J., Abernathy, S. M., Laybourn, P. J., Nyborg, J. K., and Luger, K. (2003) *J. Biol. Chem.* **278,** 44574–44583
67. Rivetti, C., and Codeluppi, S. (2001) *Ultramicroscopy* **87,** 55–66
68. Ausio, J., Borochov, N., Seger, D., and Eisenberg, H. (1984) *J. Mol. Biol.* **177,** 373–398
69. Sedat, J., and Manuelidis, L. (1978) *Cold Spring Harbor Symp. Quant. Biol.* **42,** 331–350
70. Belmont, A. S., and Bruce, K. (1994) *J. Cell Biol.* **127,** 287–302
71. Tumbar, T., Sudlow, G., and Belmont, A. S. (1999) *J. Cell Biol.* **145,** 1341–1354
72. Rivetti, C., Guthold, M., and Bustamante, C. (1996) *J. Mol. Biol.* **264,** 919–932
73. Kellogg, D. R., and Murray, A. W. (1995) *J. Cell Biol.* **130,** 675–685
74. Rabbani, A., Iskandar, M., and Ausio, J. (1999) *J. Biol. Chem.* **274,** 18401–18406
75. Zlatanova, J., and van Holde, K. (1996) *Prog. Nucleic Acids Res. Mol. Biol.* **52,** 217–259
76. Carruthers, L. M., Bednar, J., Woodcock, C. L., and Hansen, J. C. (1998) *Biochemistry* **37,** 14776–14787
77. Studitsky, V. M., Walter, W., Kireeva, M., Kashlev, M., and Felsenfeld, G. (2004) *Trends Biochem. Sci.* **29,** 127–135
78. Studitsky, V. M., Kassavetis, G. A., Geiduschek, E. P., and Felsenfeld, G. (1997) *Science* **278,** 1960–1963
79. Orphanides, G., LeRoy, G., Chang, C. H., Luse, D. S., and Reinberg, D. (1998) *Cell* **92,** 105–116
80. Orphanides, G., and Reinberg, D. (2000) *Nature* **407,** 471–475
81. Squazzo, S. L., Costa, P. J., Lindstrom, D. L., Kumer, K. E., Simic, R., Jennings, J. L., Link, A. J., Arndt, K. M., and Hartzog, G. A. (2002) *EMBO J.* **21,** 1764–1774
82. Nacheva, G. A., Guschin, D. Y., Preobrazhenskaya, O. V., Karpov, V. L., Ebralidse, K. K., and Mirzabekov, A. D. (1989) *Cell* **58,** 27–36
83. Hartzog, G. A., Speer, J. L., and Lindstrom, D. L. (2002) *Biochim. Biophys. Acta* **1577,** 276–286
84. Peng, H. F., and Jackson, V. (1997) *Biochemistry* **36,** 12371–12382
85. McQuibban, G. A., Commisso-Cappelli, C. N., and Lewis, P. N. (1998) *J. Biol. Chem.* **273,** 6582–6590
86. Misteli, T. (2001) *Science* **291,** 843–847
87. Zlatanova, J. (1990) *Trends Biochem. Sci.* **15,** 273–276
88. Crane-Robinson, C. (1999) *BioEssays* **21,** 367–371
89. Levchenko, V., Jackson, B., and Jackson, V. (2005) *Biochemistry* **44,** 5357–5372
90. Bruno, M., Flaus, A., Stockdale, C., Rencurel, C., Ferreira, H., and Owen-Hughes, T. (2003) *Mol. Cell* **12,** 1599–1606
91. Krogan, N. J., Dover, J., Wood, A., Schneider, J., Heidt, J., Boateng, M. A., Dean, K., Ryan, O. W., Golshani, A., Johnston, M., Greenblatt, J. F., and Shilatifard, A. (2003) *Mol. Cell* **11,** 721–729

THE JOURNAL OF BIOLOGICAL CHEMISTRY
Vol. 280, No. 18, Issue of May 6, pp. 18442–18451, 2005
Printed in U.S.A.

Reconstitution of Nup157 and Nup145N into the Nup84 Complex*[S]

Received for publication, November 11, 2004, and in revised form, January 28, 2005
Published, JBC Papers in Press, March 1, 2005, DOI 10.1074/jbc.M412787200

Malik Lutzmann‡, Ruth Kunze‡, Karin Stangl‡, Philipp Stelter‡, Katalin Fejes Tóth§, Bettina Böttcher¶, and Ed Hurt‡‖

From the ‡Biochemie-Zentrum der Universität Heidelberg, Im Neuenheimer Feld 328, 69120 Heidelberg, Germany, the ¶European Molecular Biology Laboratory, D-6900 Heidelberg, Germany, and the §Kirchhoff-Institut für Physik, Universität Heidelberg, 69120 Heidelberg, Germany

About 30 different nucleoporins (Nups) constitute the nuclear pore complex. We have affinity-purified 28 of these nuclear pore proteins and identified new nucleoporin interactions by this analysis. We found that Nup157 and Nup170, two members of the large structural Nups, and the Gly-Leu-Phe-Gly nucleoporin Nup145N specifically co-purified with members of the Nup84 complex. In addition, Nup145N co-enriched during Nup157 purification. By *in vitro* reconstitution, we demonstrate that Nup157 and Nup145N form a nucleoporin subcomplex. Moreover, we show that Nup157 and Nup145N bind to the heptameric Nup84 complex. This assembly thus represents approximately one-third of all nucleoporins. To characterize Nup157 structurally, we purified and analyzed it by electron microscopy. Nup157 is a hollow sphere that resembles a clamp or a gripping hand. Thus, we could reconstitute an interaction between a large structural Nup, an FG repeat Nup, and a major structural module of the nuclear pore complex.

Nucleocytoplasmic transport occurs through nuclear pore complexes (NPCs),[1] highly elaborate supramolecular assemblies within the double nuclear membrane (1, 2). The core structure of the NPC is formed by a spoke complex, which is sandwiched between a cytoplasmic and a nuclear ring. The eight spoke units, as part of the 8-fold symmetrical NPC array, surround the center of the NPC through which active nucleocytoplasmic transport is thought to take place. Moreover, a nuclear basket and short cytoplasmic fibrils, which are attached to the nuclear ring and the cytoplasmic ring of the NPC, respectively, can be visualized by high resolution electron microscopy (3–5).

About 30 different nucleoporins constitute the NPC in yeast and higher eukaryotes (6, 7). Nucleoporins exist in 8-, 16- and 32-fold copies per NPC and, thus, this ~50-MDa structure is assembled from a relatively low number of components (6). Nucleoporins are grouped into two major classes, one class with FG repeats that functions directly in nucleocytoplasmic transport by binding the soluble transport receptors (8, 9), and another class that is devoid of FG repeat sequences and is considered as representing the predominant structural constituents of the NPC. Moreover, a few of the structural nucleoporins should mediate integration in the double nuclear membrane or organize the repeat-containing nucleoporins to form the active transport channel (for review, see Refs. 2 and 10).

In past years, significant progress has been made in the biochemical analysis of the NPC composition and organization of individual nucleoporins within NPC subcomplexes (1, 2, 10). Moreover, immuno-electron microscopy has revealed the relative location of nucleoporins within the overall NPC framework. Thus, the first models have emerged from these studies that discuss how nucleoporins could perform their distinct roles in NPC structure and nucleocytoplasmic transport (11–13).

One of the best characterized subcomplexes of the NPC is the Nup84 complex in yeast (14–16). This assembly is composed of seven subunits and was shown to perform several essential roles, including functions in nuclear envelope organization, NPC biogenesis, and mRNA export. Because none of the members of the Nup84 complex contain FG repeat sequences, which bind to the shuttling transport receptors, it is intriguing how this complex can specifically affect the nuclear export of poly(A)$^+$ RNA. A vertebrate Nup107-Nup160 complex (17–19), which is homologous to the yeast Nup84 complex, was also shown to be essential for the postmitotic nuclear pore assembly (19–21).

Recently, we have reported that the Nup84 complex could be reconstituted *in vitro* from its recombinant seven subunits and exhibits a Y-shaped structure in the electron microscope, which is indistinguishable from the native complex (16). Thus, the Nup84 complex can self-assemble in a modular way from distinct smaller nucleoporin construction units. Motivated by these findings, we sought to extend the Nup84 complex further by searching for new interaction partners and successively assembling them *in vitro* into the pre-existing complex. A nucleoporin interaction analysis has been performed recently (22). Protein interactions that occur at individual FG Nups were sampled using immobilized nucleoporins and yeast extracts. This study showed that several FG Nups also captured the hexameric Nup84 complex.

Here, we conducted a proteomic approach to unravel additional nucleoporin interactions. We found that Nup157 and Nup145N are specifically associated with purified members of the Nup84 complex. In agreement with these findings, Nup157 and Nup145N could be reconstituted into the heptameric Nup84 complex. We examined purified Nup157 in the electron microscope and found that it has a characteristic clamp-like structure. Our data thus show the interaction of a large struc-

* The costs of publication of this article were defrayed in part by the payment of page charges. This article must therefore be hereby marked "*advertisement*" in accordance with 18 U.S.C. Section 1734 solely to indicate this fact.

[S] The on-line version of this article (available at www.jbc.org) contains supplemental Fig. 1 (growth analyses of yeast strains expressing TAP-tagged nucleoporins), Fig. 2 (peptide mass fingerprinting of newly identified protein interactions), and Fig. 3 (sedimentation equilibrium ultracentrifugation of Nup145N).

‖ Supported by Deutsche Forschungsgemeinschaft Grant SFB 638/B2 and a grant from Fonds der Chemischen Industrie and to whom correspondence should be addressed. Tel.: 49-6221-544173; Fax: 49-6221-544369; E-mail: cg5@ix.urz.uni-heidelberg.de.

[1] The abbreviations used are: NPC, nuclear pore complex; GST, glutathione *S*-transferase; MALDI-TOF, matrix-assisted laser desorption/ionization-time of flight; Nup, nucleoporin; ProtA, protein A; TAP, tandem affinity purification; TEV, tobacco etch virus.

tural Nup with the Nup84 complex, a key structural module of the NPC.

EXPERIMENTAL PROCEDURES

Microbiological Techniques and DNA Manipulations—Microbiological techniques (growth and transformation of *Escherichia coli* and yeast) and standard DNA manipulations (cloning, PCR amplification, and ligation) were performed as described previously (16, 23).

Insertion of Yeast Nucleoporin Genes into E. coli Expression Vectors and Yeast 2μ Plasmids and Genomic Integration of the Tandem Affinity Purification (TAP) Tag—For expression in *E. coli*, the open reading frames of *Nup145N* and *Nup157* were amplified by PCR and cloned into pPROEXHT-GST-TEV (16). For bicistronic expression of GST-*Nup157* and GST-*Nup120*, the open reading frame of *Nup120* was amplified with a 5′ second ribosomal binding site and cloned downstream of the *Nup157* (16). Bicistronic expression of GST-*Nup84* and GST-*Nup157* was performed in a similar way. For overexpression in yeast, the open reading frames of *NUP157* and *NUP188* were cloned into the pNOPPATA2L 2μ plasmid (24) and transformed into yeast strains genomically disrupted for the gene of interest. For TAP tagging of the yeast nucleoporins, the cassette harboring the TAP tag was genomically integrated at the 3′-end of the genes as described (25).

Overexpression of Proteins in E. coli and Yeast—All recombinant protein expression in *E. coli* was done with the BL21 codon plus RIL strain (Stratagene) and performed as described previously (16), except that bicistronic expression of GST-*Nup157*/GST-*Nup120* was performed overnight at 16 °C and induced with 0.1 mM isopropyl-1-thio-β-D-galactopyranoside. Yeast cells overexpressing ProtA-tagged Nups were grown in 2–6 liters of SDC-Leu medium at 30 °C to an OD of ~3.5. After pelleting the cells by centrifugation, the pellet was washed in cold water and NB buffer (150 mM NaCl, 50 mM KOAc, 20 mM Tris, pH 7.5, 2 mM $Mg(OAc)_2$, and 0.15% Nonidet P-40). The cell pellet was frozen in liquid nitrogen and stored at −20 °C.

Affinity Purification of Chromosomally TAP-tagged Yeast Nucleoporins and Mass Spectrometry Analysis—Affinity purification of nucleoporins from 2–6 liters of yeast cultures grown at 30 °C in YPD (1% yeast extract, 2% peptone, and 2% dextrose) medium to an OD of ~3.5 was performed as described (26). Only the first affinity purification step of the TAP method (TEV elution) was applied. The second step (*i.e.* calmodulin-Sepharose) was omitted, because it was found to be disruptive for some nucleoporin interactions (*e.g.* Nup133 dissociated from the Nup84 complex upon incubation with calmodulin-Sepharose.[2] Affinity purification of Nup53 and Nup59 were not successful. TEV-eluted nucleoporins were analyzed on Novex SDS 4–12% gradient polyacrylamide gels (Invitrogen) and stained with colloidal or normal Coomassie R250 (both from Sigma). Mass spectrometry using tryptic digests of bands excised from a Coomassie-stained SDS-polyacrylamide gel was performed according to (27). Analysis was performed on a Bruker Reflex III MALDI-TOF instrument. Identification of protein bands was achieved by peptide mass fingerprints using Mascot (Matrix Science) and the MSDB mass spectrometry protein data base.

Affinity Purification of GST- and ProtA-tagged Proteins—Purification of GST-tagged proteins from *E. coli* was performed in NB buffer containing 10% glycerol as described (16). Overexpressed ProtA-tagged Nup157 and Nup188 were affinity-purified in NB buffer, which was supplemented with 0.15% Nonidet P-40 and a mixture of protease inhibitors during cell lysis. After cell breakage and centrifugation, the soluble fraction was incubated with 0.5 ml of IgG-Sepharose (Amersham Biosciences) per 2 liters of culture, and beads were washed with 30 volumes of NB buffer plus 0.5 mM dithiothreitol. TEV cleavage was performed for 2 h at 16 °C in 150 μl of Luria-Bertani medium with 0.5 mM dithiothreitol and 10 μl of TEV protease (1 mg/ml). Ion exchange (Mono Q HR5/5; Amersham Biosciences) and gel filtration chromatography (Superose 6 HR10/30 and Superdex 200 HR10/30; Amersham Biosciences) were performed on an ÄKTA basic system (Amersham Biosciences). All gel filtration chromatography and binding assays of Nup145N, Nup157, and the Nup84 complex were performed in NB buffer. The heptameric Nup84 complex was reconstituted as described (16).

Electron Microscopy and Image Processing—For negative staining, 5 μl of sample were placed on a freshly glow-discharged, carbon-coated grid and then washed four times with water, stained with uranyl formate (2% w/v), and dried. Electron microscopy was carried out on a Philips CM120 BioTwin electron microscope equipped with a tungsten filament operating at 100 kV. Micrographs of selected areas were recorded with a wide angle charge-coupled device camera (DV300W1; Gatan) at a nominal magnification of 93,000.

For image processing, micrographs of Nup157 were taken at a calibrated magnification of 50,000 and scanned with the Zeiss Scai Scanner at a step size of 21 μm/pixel, which corresponded to 4.2 Å at specimen level. 5,000-particle images were selected and boxed using the MRC image-processing package (28). Boxed particle images were imported to the IMAGIC 5 package (29), which was used for all further steps. Particles were normalized and band pass-filtered with a low frequency cutoff of 1/170 $Å^{-1}$ and a high frequency cutoff of 1/9 $Å^{-1}$. The box size of the extracted particle images was 50 × 50 pixels. For initial alignment the alignment by classification strategy was chosen. After a few rounds of refinement the class averages stabilized. Relative spatial orientations of the class averages were determined by sinogram correlation. This process was started several times, beginning with different class averages for the initial determination of Euler angles. Three-dimensional maps were calculated using the exact weighted back projection algorithm. Determination of Euler angles and calculation of three-dimensional maps were repeated until the map converged into a stable shape from which projections could be generated that were similar to all of the initially observed class averages. A three-dimensional map was further refined by projection matching. This process was repeated several times. Resolution of the final map was estimated by Fourier shell correlation (FSC). The FSC was 0.5 at a spatial frequency of 1/17.5 $Å^{-1}$ and crossed the 3 σ curve at 1/14 $Å^{-1}$.

Analytical Ultracentrifugation—Analytical sedimentation equilibrium ultracentrifugation was carried out at 4 °C on a Beckman Optima XL-A analytical ultracentrifuge equipped with absorbance optics and an An60 Ti rotor. From the amino acid sequence of Nup145N, a molecular mass of 64.8 kDa, an extinction coefficient at 280 nm of $\epsilon = 3.14 \cdot 10^4$ $M^{-1} \cdot cm^{-1}$, and a partial specific volume of $\bar{\nu} = 0.7114$ $ml \cdot g^{-1}$ at 4 °C were calculated from the amino acid composition with the program SEDNTERP version 1.08.[3] Nup145N was analyzed in a buffer containing 150 mM NaCl, 50 mM potassium acetate, 20 mM Tris-HCl, pH 7.5, and 2 mM magnesium acetate with a density of $\rho = 1.0093$ $g \cdot ml^{-1}$ as calculated with SEDNTERP. Sedimentation equilibrium ultracentrifugation runs were performed with protein concentrations of 1.6, 3.2, and 7.4 μM and at angular velocities of 7,000 and 10,000 rpm. Equilibrium was obtained after 24 h. Absorbance data were collected at 280 and 230 nm by averaging 10 scans with radial increments of 0.001 cm in step mode. The molecular mass of Nup145N was determined by global fitting of the data to an ideal single component model with the software UltraScan version 6.2 (www.ultrascan.uthscsa.edu).

RESULTS

Proteomic Analysis of Nucleoporin Interactions—To obtain a more comprehensive picture of nucleoporin interactions in the NPC, we sought to affinity-purify all yeast Nups in a comparative way and identify stoichiometrically and sub-stoichiometrically co-purifying bands. Therefore, *NUP* genes were chromosomally tagged with the TAP construct (26). Functionality of the TAP-tagged nucleoporins, which are essential for cell growth or whose deletion causes a slow growth phenotype, was tested by growth analysis (supplemental Fig. 1*A*, available in the on-line version of this article). In the case of non-essential Nups whose deletion does not cause a growth inhibition, growth analyses did not reveal whether the TAP tag impairs nucleoporin function; however, all of these yeast Nups had already been tagged at the carboxyl terminus by ProtA or a green fluorescent protein and were shown to be assembled into the NPCs (6, 30).

Subsequently, TAP-modified nucleoporins were affinity-purified from whole cell lysates under standardized conditions (see "Experimental Procedures"). We applied only the first affinity purification step of the TAP method (*i.e.* proteolysis-mediated elution from IgG-Sepharose by the TEV protease) but omitted the second step (*i.e.* calmodulin-Sepharose), which was found to be disruptive for some known nucleoporin interactions.[2] The TEV eluates from the various nucleoporin purifications were analyzed by SDS-PAGE, and distinct bands discern-

[2] R. Kunze and M. Lutzmann, unpublished results.

[3] Developed by J. Philo, D. Hayes, and T. Laue; www.jphilo.mailway.com/download.htm.

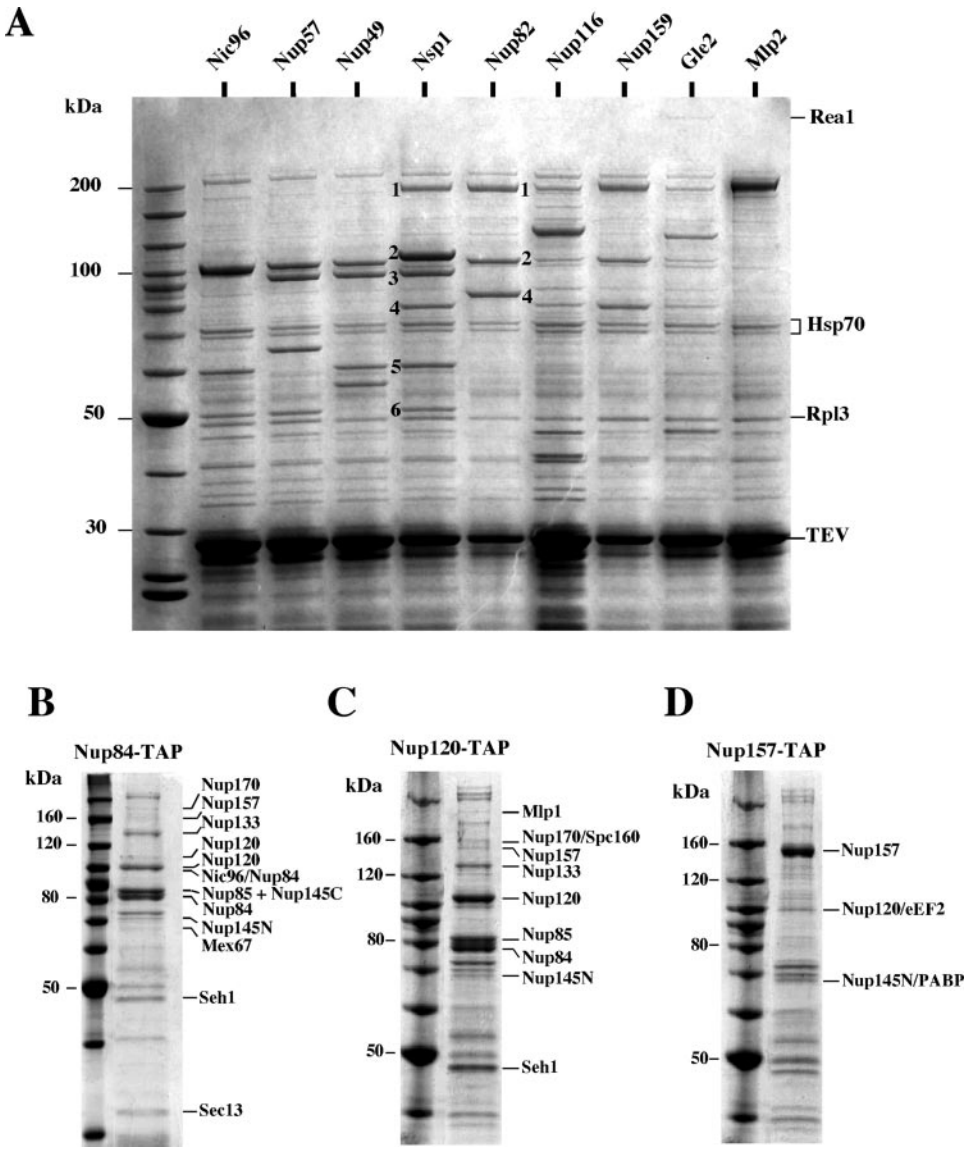

FIG. 1. ***In vivo* interactions between yeast nucleoporins.** *A*, affinity purification of the indicated TAP-tagged Nups by IgG-Sepharose and TEV elution followed by SDS-PAGE and Coomassie staining. For Nsp1 and Nup82 purifications, the co-purifying nucleoporins are indicated in the columns as follows: *band(s) 1*, Nup159; *band(s) 2*, Nsp1; *band 3*, Nic96; *band(s) 4*, Nup82; *band 5*, Nup57; and *band 6*, Nup49. Note that the calmodulin binding tag present on the bait protein increases the molecular mass by ~5 kDa. Protein bands were identified by mass spectrometry (see Table I). Marked on the right are prominent contaminants (*e.g.* Hsp70 and Rpl3) and the TEV protease. Interestingly, Rea1 was detected in the Gle2 and Nup116 preparations. *B–D*, affinity purification of Nup84-TAP (*B*), Nup120-TAP (*C*), and Nup157-TAP (*D*). Only the nucleoporin bands identified by mass spectrometry, but not contaminants, are labeled on the *right*. Shown are also molecular mass markers.

ible by Coomassie staining were excised and analyzed by MALDI-TOF mass spectrometry (see "Experimental Procedures" and supplemental Fig. 2, available in the on-line version of this article). Because of the omission of the second affinity purification step, all of the nucleoporin purifications were contaminated by common impurities (*e.g.* heat shock proteins, fatty acid synthetase, translation factors, ribosomal proteins, etc.) that tend to stick to IgG-Sepharose. Nevertheless, side-by-side comparison of the different nucleoporin preparations allowed us to identify specific co-purifying bands (Fig. 1). This comprehensive analysis confirmed many of the known nucleoporin interactions and convincingly revealed the three major structural modules of the NPC, namely the Nic96 complex (Nsp1-Nup57-Nup49-Nic96), the Nup82 complex (Nup82-Nsp1-Nup159-Nup116-Gle2), and the Nup84 complex (Nup84-Nup85-Nup120-Nup133-Nup145C-Seh1-Sec13) (Fig. 1 and Table I) (for cross references, see Refs. 1 and 2).

Nup170, Nup157, and Nup145N Associate in Vivo with the Nup84 Complex—Importantly, our systematic nucleoporin purifications revealed several new interactions. Thus, we found Sac3 in the Nup60 preparation (Table I and supplemental Fig. 2). These data are consistent with previous observations that the pore-associated mRNA export factor Sac3 interacts functionally with Nup60 and Nup1 (31). Moreover, we could detect Kap123 in the Nic96 preparation along with low amounts of the Rea1 AAA^+-type ATPase, which is associated with nucleoplasmic pre-60 S ribosomal subunits (32), in the TAP-purified Gle2 and Nup116 purifications (Fig. 1, Table I, and supplemental Fig. 2).

Additionally, several members of the Nup84 complex co-enriched a specific set of nucleoporins not previously known to interact. Affinity-purified Nup84, Nup120, and Nup145C all contained sub-stoichiometric amounts of Nup170, Nup157, and Nup145N (Fig. 1, *B* and *C*, Table I, and supplemental Fig. 2). In addition, we found Nic96 and Mex67 in the Nup84 preparation and Mlp1 in the Nup120 purification (supplemental Fig. 2). It was recently suggested that Mlp1 is bound via Nup60 and Nup145 to the NPC (33) and that the mRNA export receptor

TABLE I

Proteomic analysis of yeast nucleoporin interactions

TAP-tagged proteins are indicated in the top row (Bait). Co-purifying proteins identified by mass spectrometry are listed in the far left column (Found) and indicated by shaded (medium and dark gray) rectangles in the column below the name of each bait protein. Previously known nucleoporin interactions found in this study are denoted by dark gray rectangles. Signified by light gray rectangles are the bait proteins, which were also identified by mass spectrometry.

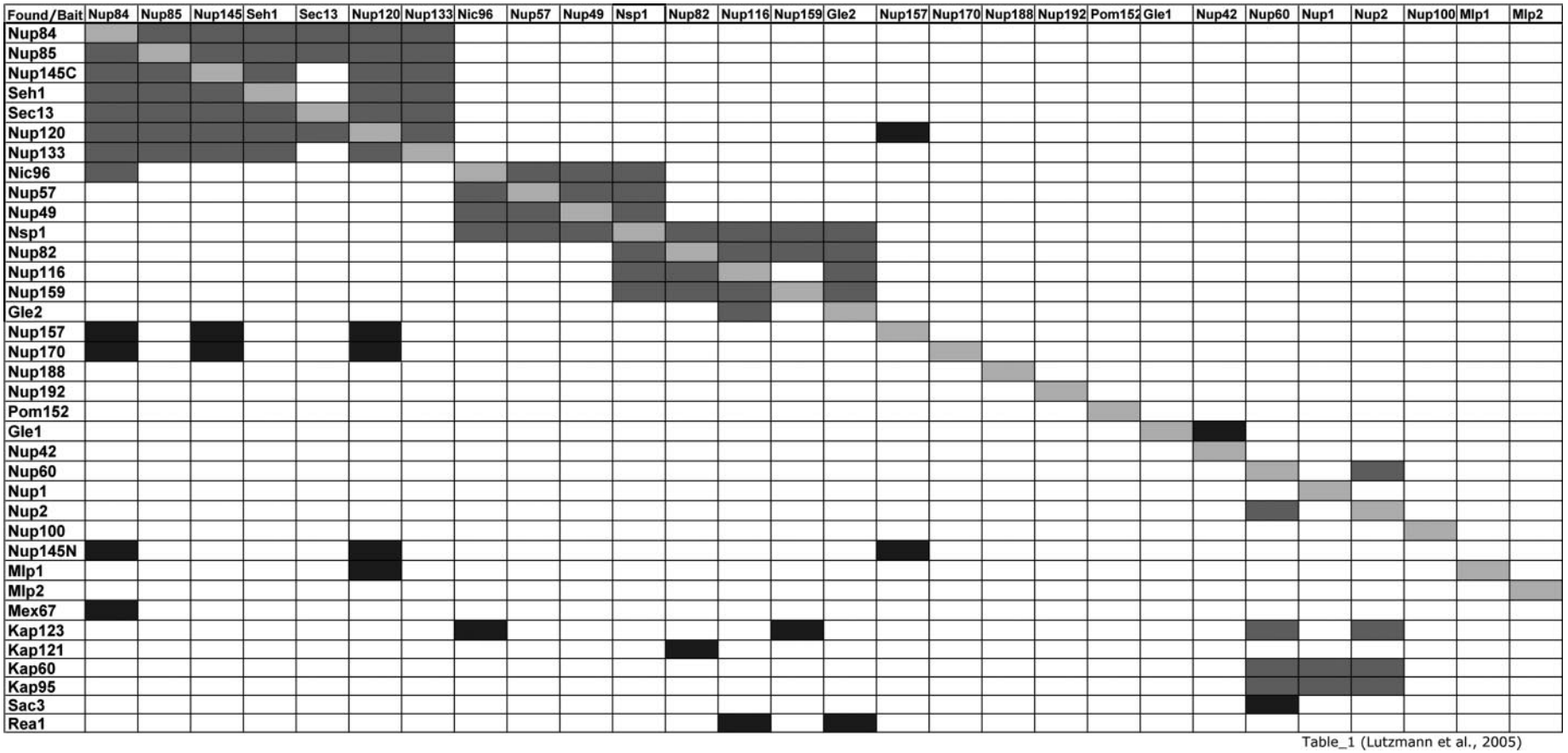

Table_1 (Lutzmann et al., 2005)

Mex67 interacts with Nup85 (23). Moreover, Nup98 (the vertebrate counterpart of Nup145N) was described to interact with the Nup107-Nup160 complex (the vertebrate counterpart of the Nup84 complex; Refs. 18 and 34). Further biochemical analysis and *in vitro* reconstitution are required to show that these observed protein interactions are direct.

Consistent with the findings described above, affinity-purified Nup157 also revealed the presence of Nup120 and Nup145N (Fig. 1*D*). It is not clear why only Nup120 but not the other members of the Nup84 complex was found in the Nup157 preparation (see "Discussion"). Moreover, we could not detect members of the Nup84 complex in the Nup170 preparation (Table I). This may not be significant, as Nup170-TAP could not be affinity-purified in satisfactory levels.[4] Altogether, the data suggested that Nup170, Nup157, and Nup145N could be in physical contact with the Nup84 complex.

In Vitro Reconstitution of the Nup157-Nup145N Heterodimer—To further study the interactions of Nup157 and Nup145N with the Nup84 complex, we performed *in vitro* reconstitution. First, we analyzed whether Nup157 and Nup145N can directly bind to each other. To perform this experiment, GST-tagged Nup145N was expressed in *E. coli* and purified to homogeneity by GST-affinity purification, TEV cleavage, and gel filtration chromatography. Nup145N, which has a calculated M_r of ~65,000, eluted from the gel filtration column in a relatively sharp peak with an apparent M_r of ~200,000 (Fig. 2*A*).

Analytical ultracentrifugation was conducted to analyze the association state of Nup145N in greater detail (supplemental Fig. 3, available in the on-line version of this article). The apparent molecular mass of Nup145N was determined to be 61.4 kDa from a fit to a single component model. No systematic deviations could be detected as evident from inspection of the residuals in supplemental Fig. 3. This demonstrates that the model describes the data accurately and that only one component was present. The molecular mass of Nup145N calculated from its primary sequence is 64.8 kDa, which comes close to the value determined by analytical ultracentrifugation. Thus, Nup145N exists as a monomer under physiological buffer conditions and the protein concentrations used. We assume that the unusual elution of purified Nup145N from the gel filtration column is due to the presence of GLFG repeats. It was recently reported that FG repeat domains within nucleoporins are natively unstructured and induce atypical elution during gel filtration (35).

In contrast to Nup145N, expression of Nup157 in *E. coli* yielded mostly insoluble protein (data not shown). Therefore, we sought to exploit yeast as an expression system and overexpressed ProtA-tagged Nup157 from a high copy number (2 μ) plasmid. The protein was affinity-purified on IgG-Sepharose and eluted by TEV protease cleavage. The eluate was then applied to a gel filtration column yielding highly purified Nup157 that eluted at ~200 kDa (Fig. 2*B*).

To analyze whether purified Nup145N and Nup157 proteins can form a complex *in vitro*, GST-Nup145N immobilized on GSH beads was incubated with purified Nup157 from yeast. As shown in Fig. 2*C*, Nup157 bound to Nup145N in a ~1:1 stoichiometric ratio, as judged from the intensity of the Coomassie-stained bands. To show the specificity of this interaction, we tested whether Nup157 binds to GST alone. Only trace amounts of Nup157 were bound to GST beads (Fig. 2*C*). Moreover, we tested whether another large nucleoporin, Nup188, can interact with Nup145N *in vitro*. Similar to Nup157, ProtA-tagged Nup188 was expressed in yeast from a 2μ plasmid and purified by IgG-Sepharose and gel filtration chromatography. However, only very small amounts of Nup188 were seen to bind to GST-Nup145N (Fig. 2*C*).

To further characterize complex formation between Nup145N and Nup157, we mixed partially purified Nup145N and Nup157 in solution and monitored heterodimerization by gel filtration chromatography. The reconstituted Nup157-Nup145N complex eluted at ~400 kDa, which is two fractions earlier than the single subunits (compare Fig. 2*D* with *panels A* and *B*). Thus, Nup157 and Nup145N constitute a novel nucleoporin subcomplex.

In Vitro Reconstitution of Nup157 and Nup145N into the Nup84 Complex—Our next aim was to assemble the Nup157-Nup145N heterodimer into the heptameric Nup84 complex. For these reconstitution studies, the pre-assembled Nup84 complex, which consists of seven subunits (Nup84, Nup85, Nup120, Nup133, Nup145C, Seh1, and Sec13), was immobilized on GSH-Sepharose via the GST-tagged Nup145C subunit (see Ref. 16). Then, highly purified Nup157 from yeast (see Fig. 2*B*) and Nup145N purified from *E. coli* (see Fig. 2*A*) were incubated with the immobilized Nup84 complex. After a washing step to remove unbound material, proteins were eluted and analyzed by SDS-PAGE and Coomassie staining. As shown in Fig. 3*A*, Nup157 and Nup145N bound in a ~1:1 stoichiometry to the Nup84 complex, yielding an assembly of nine subunits with a calculated molecular mass of 820 kDa. However, when this supercomplex was subjected to gel filtration chromatography, most of it dissociated into the separate subcomplexes (data not shown). This suggests that the interaction between the Nup157-Nup145N heterodimer and Nup84 complex is not very strong. These *in vitro* findings are consistent with the observation that only small amounts of Nup157 and Nup145N were co-enriched during Nup84 complex purification from yeast lysates (see Fig. 1, *B–D*). In further reconstitution studies we showed that Nup157 (Fig. 3*B*) or Nup145N alone (data not shown) can bind to the pre-assembled Nup84 complex. This suggests that both Nup157 and Nup145N have separate binding sites on the Nup84 complex.

Interaction of Nup157 with Nup120-containing Subcomplexes—Our proteomic analysis showed that affinity-purified Nup157 contained Nup120, which is a member of the Nup84 complex (see Fig. 1*D*). Hence, we wanted to analyze whether Nup157 and Nup120 interact directly. To this end, GST-tagged Nup157 and untagged Nup120 were co-expressed from a bicistronic construct in *E. coli*. Significantly, Nup120 (identified by mass spectrometry) co-enriched with affinity-purified GST-Nup157 (Fig. 3*C*). However, *E. coli* heat shock proteins were also bound to beads, which could mean that Nup157 and/or Nup120 are not completely folded or that they expose hydrophobic binding sites. In contrast, bicistronic co-expression of another GST-tagged Nup (GST-Nup84), together with Nup157 in *E. coli*, did not reveal any co-enrichment of Nup157 during GST-Nup84 affinity purification (Fig. 3*C*). This suggests that Nup157 *per se* is not a sticky protein.

To obtain further evidence for a Nup157-Nup120 interaction, we tested the binding of soluble Nup157 purified from yeast to different *in vitro* reconstituted subcomplexes of the Nup84 complex immobilized on GSH-Sepharose (see Ref. 16). These analyses revealed that Nup157 was bound to the pentameric Nup120-Nup85-Seh1-Nup145C-Sec13 complex and the trimeric Nup120-Nup85-Seh1 complex (Fig. 3*D*). Importantly, Nup157 did not bind to complexes that lack Nup120 (*e.g.* the Nup85-Seh1, Nup145C-Sec13, and Nup133-Nup84 complexes). We conclude from these studies that Nup120 exhibits a binding site for Nup157 within the Nup84 complex.

Electron Microscopic Analysis of Purified Nup157—Because Nup157 and Nup145N could be efficiently purified and ob-

[4] K. Stangl, unpublished data.

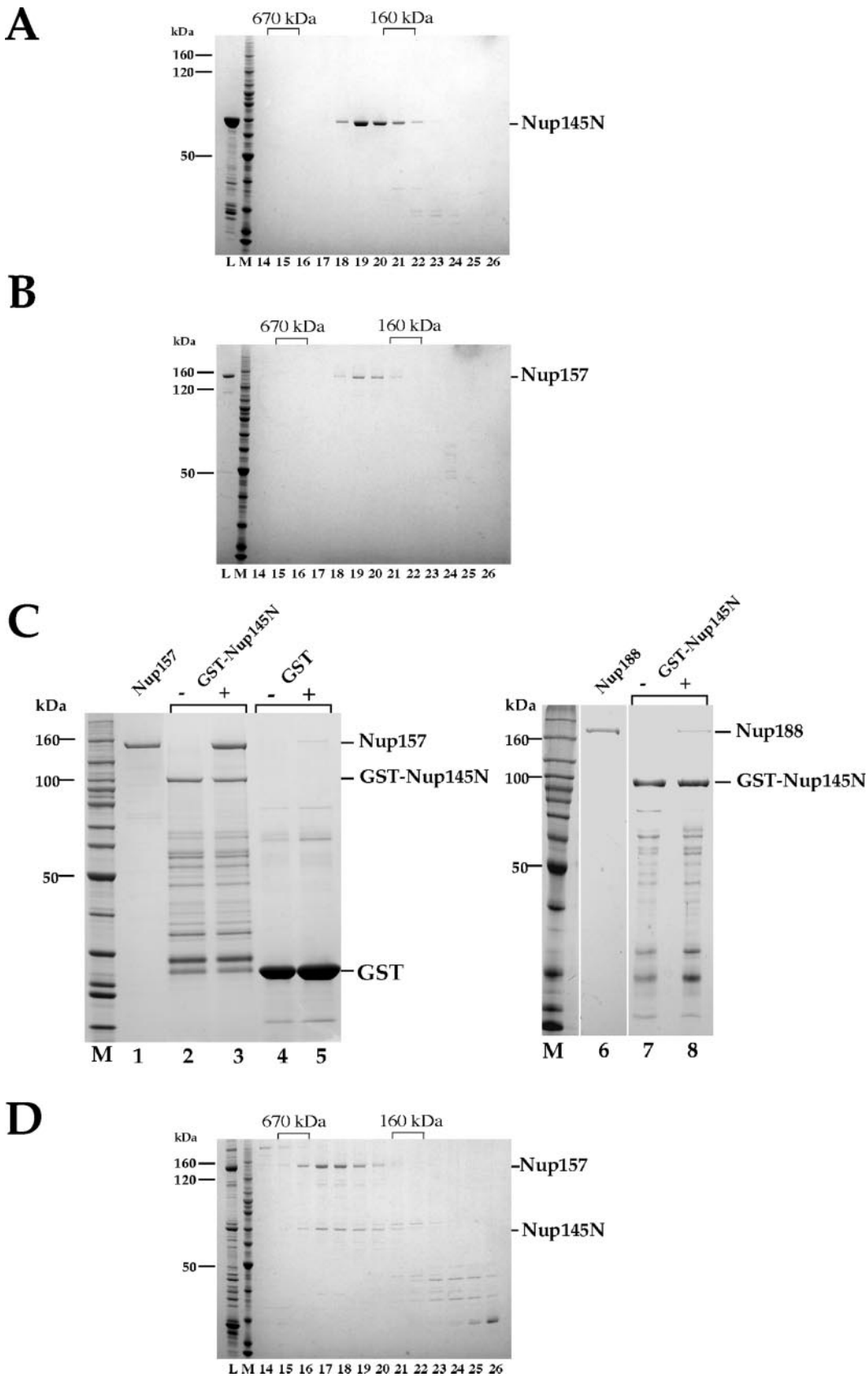

FIG. 2. **Nup157 and Nup145N form a heterodimer.** *A* and *B*, gel filtration of Nup145N purified from *E. coli* (*A*) and Nup157 purified from yeast (*B*) on a Superdex 200 HR column. Shown are the loaded proteins (*L*), a protein standard (*M*), and fractions 14–26. The column was calibrated with molecular mass markers (Bio-Rad) of 670, 158, 44, and 17 kDa (indicated on the *top*). *C*, *in vitro* binding of Nup157 to immobilized GST-Nup145N and GST. *Lane 1*, purified Nup157; *lane 2*, GST-Nup145 incubated with buffer; *lane 3*, GST-Nup145 incubated with purified Nup157; *lane 4*, GST incubated with buffer; *lane 5*, GST incubated with purified Nup157; *lane 6*, purified Nup188; *lane 7*, GST-Nup145 incubated with buffer; *lane 8*, GST-Nup145 incubated with purified Nup188; *M*, protein standard. *D*, gel filtration of the Nup157-Nup145N complex on Superdex 200 HR. Shown are the loaded proteins (*L*), a protein standard (*M*), and *fractions 14–26*. Indicated on the *right* are the positions of Nup157 and Nup145N.

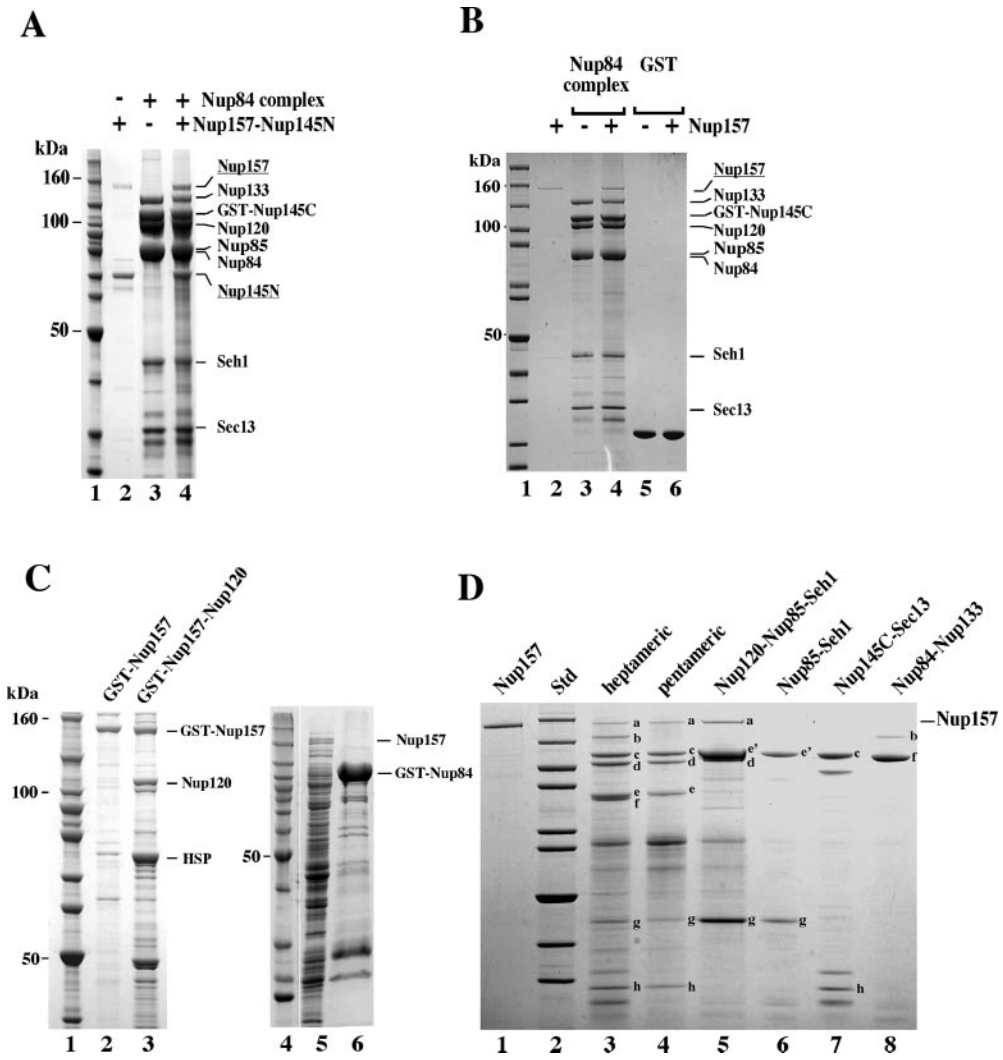

FIG. 3. **Reconstitution of a nine-subunit assembly between Nup157-Nup145N and the Nup84 complex.** *A*, *In vitro* binding of purified Nup157 and Nup145N to the reconstituted Nup84 complex. Purified and mixed Nup157 and Nup145N (*lane 2*) were incubated with the heptameric Nup84 complex immobilized on GSH beads via GST-Nup145C (*lane 4*). A molecular mass marker (*lane 1*) and buffer control (*lane 3*) are also shown. Bound proteins were analyzed by SDS-PAGE and Coomassie staining. *B*, *in vitro* binding of Nup157 to the reconstituted Nup84 complex. Purified Nup157 (*lane 2*) was incubated with the immobilized Nup84 complex (*lane 4*) or GST (*lane 6*). Buffer controls (*lanes 3* and *5*) are also shown. Bound proteins were analyzed by SDS-PAGE and Coomassie staining. Indicated on the *right* are the positions of the Nup proteins. *C*, Nup157 and Nup120 bind directly to each other. Molecular mass markers (*lanes 1* and *4*), GST-Nup157 (*lane 2*), GST-Nup157 co-expressed with Nup120 (*lane 3*), and GST-Nup84 co-expressed with Nup157 (*lane 6*) were purified from *E. coli* and TEV eluates analyzed by SDS-PAGE and Coomassie staining. *Lane 5* shows the *E. coli* lysate containing GST-Nup84 and Nup157. *D*, binding of soluble Nup157 purified from yeast to different *in vitro* reconstituted subcomplexes. Purified Nup157 (*lane 1*) was incubated with the immobilized complexes heptameric Nup84-Nup85-Nup120-Nup133-Nup145C-Seh1-Sec13 (*lane 3*), pentameric Nup85-Nup120-Nup145C-Seh1-Sec13 (*lane 4*), trimeric Nup85-Nup120-Seh1 (*lane 5*), dimeric Nup85-Seh1 (*lane 6*), dimeric Nup145C-Sec13 (*lane 7*), and dimeric Nup84-Nup133 (*lane 8*). Bound proteins were analyzed by SDS-PAGE and Coomassie staining. Bands were labeled as follows: *a*, Nup157; *b*, Nup133; *c*, GST-Nup145C; *d*, Nup120; *e*, Nup85; *e'*, GST-Nup85; *f*, Nup84; *g*, Seh1; and *h*, Sec13.

tained in pure form, we sought to study their morphology by transmission electron microscopy. For the purified Nup145N we could not see a discernible structure in the electron microscope.[5] This is most likely due to the small size of the Nup145N molecule and the presence of GLFG repeats, which are not structured and thus may not be contrasted enough by negative staining.

For negative staining of Nup157, we used fractions of the final gel filtration column that contained essentially pure protein (Fig. 4*A*). In the electron microscope, Nup157 showed a globular morphology with a diameter of ~12 nm. A significant number of Nup157 molecules exhibited an indentation (Fig. 4*A*). To find out whether the structure of overexpressed Nup157 differs from endogenous Nup157, we affinity-purified Nup157 from yeast that expressed chromosomally TAP-tagged *NUP157*. However, authentic Nup157 was indistinguishable from overproduced Nup157 (Fig. 4*A*).

Because micrographs of negatively stained Nup157 showed a homogeneous spread of particles, we could perform image processing to reveal more details of the Nup157 structure. By calculating the three-dimensional map of the protein, it became apparent that Nup157 was hollow and looked like a clamp or a gripping hand (Fig. 4*B*; see also "Discussion"). The outer dimensions of the clamp were 12 nm in the long direction and ~7–8 nm in the shorter direction.

DISCUSSION

From the ~30 yeast nucleoporins, about two-thirds are organized in biochemically stable NPC subcomplexes. However, the direct interacting partners for the remaining Nups are still unidentified (for review, see Refs. 2, 10, and 36). Moreover, it is not known how the stable NPC subcomplexes interact with

[5] M. Lutzmann, unpublished results.

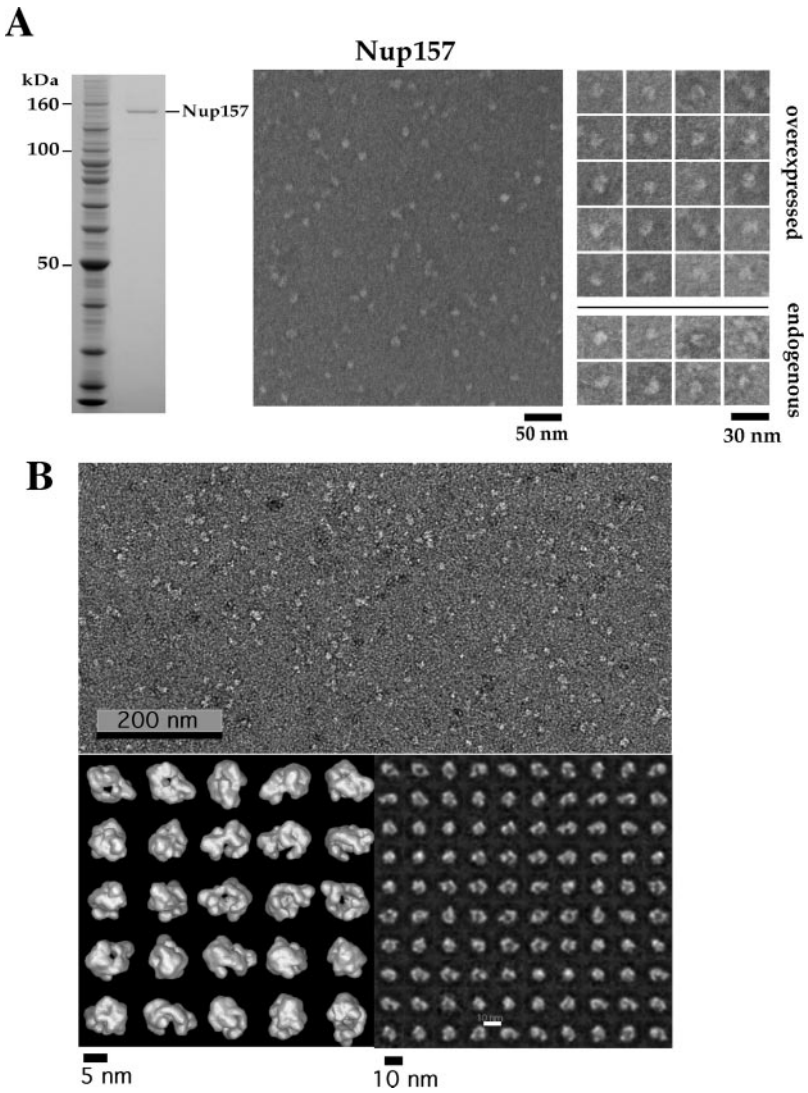

FIG. 4. **Electron microscopic analysis of purified Nup157.** *A*, purified Nup157, which was analyzed by SDS-PAGE and Coomassie staining (*left*), was used for electron microscopy analysis. An overview electron micrograph of the negatively stained Nup157 (*middle*) and a gallery of selected particles of overexpressed or endogenous Nup157 (*right*) are shown. *B*, image processing of Nup157. Charge-coupled device image of Nup157 stained with 2% uranyl acetate. Different views of the surface representation of the three-dimensional map of Nup157 at ~17-Å resolution are shown. The threshold was chosen such that the volume accounted for 160 kDa. Different characteristic projections of Nup157 were derived from projection matching.

each other and which nucleoporins bridge between them. By reinvestigation of nucleoporin interactions, we identified several possible new Nup interactions and could reconstitute two of them *in vitro*. The observation that some of the interactions found *in vivo* were not reciprocal in the TAP purifications could be due to the possibility that a substoichiometric association does not always reveal a clear cut band on the SDS-polyacrylamide gel (please note that the TEV eluates from the various nucleoporin purifications were analyzed by SDS-PAGE and that only distinct bands discernible by Coomassie staining were excised and analyzed by MALDI-TOF mass spectrometry). The finding that only Nup120 was detected in the Nup157 preparation by mass spectrometry, but not the other subunits of the Nup84 complex, is not clear. However, Nup120 was found only as second hit in the peptide mass fingerprint analysis (see Fig. 1*D* and supplemental Fig. 2; the first hit was elongation factor eEF2, a possible contaminant) and, thus, its amount on the SDS-polyacrylamide gel cannot be estimated. Thus, we suspect that the other smaller subunits of the Nup84 complex were also present in purified Nup157, but because of a reduced Coomassie staining these subunits were not seen as distinct bands and therefore not analyzed by mass spectrometry.

Because of the observed substoichiometric interactions between Nup157, Nup145N, and the Nup84 complex, we performed *in vitro* reconstitution. In this way, we could reconstitute the interactions between nine nucleoporins, an assembly that represents 30% of all yeast nuclear pore proteins. However, the nine-subunit assembly, formed *in vitro* between the robust heptameric Nup84 and the dimeric Nup157-Nup145N complexes, is not stable enough for performing further biochemical purification. Thus, for a complete *in vitro* reconstitution of the NPC, low affinity interactions between NPC subcomplexes as described here could pose a problem. On the other hand, it is conceivable that several low affinity contacts as part of the entire NPC structure will stabilize the overall assembly.

We also wanted to analyze the structure of the Nup84 complex bound to Nup157 in the electron microscope. However, images of the Nup84 complex with bound Nup157 were not homogenous, and in only a few cases could contact between Nup157 molecules and the Y-shaped Nup84 complex be discerned.[6] We suspect that during specimen preparation for electron microscopy the unstable assembly of the Nup84 complex with Nup157 largely dissociated. Further work is required to reveal the structural details of how Nup157 is bound to Nup84 complexes.

Taking our biochemical data together, it is tempting to speculate that Nup157 (together with other structural Nups like Nup170) could link Nup84 complexes together, generating a higher structural assembly. A single Nup157 molecule, the structure of which resembles a clip with two spars, might

[6] M. Lutzmann, unpublished data.

access two separate Nup84 complexes. The Nup84 complex was estimated to occur in 16 copies per NPC and was suggested to represent a major part of the octagonal spoke-ring complex (2). However, other scenarios of interaction are also conceivable. Thus, the Nup157-Nup145N dimer could form a dual interface between two Nup84 complexes or Nup157 bridges between a Nup84 complex module and another structural Nup.

In addition to the *in vitro* reconstituted interactions of Nup157 and Nup145N with the Nup84 complex, we also describe in this work how Nup170 (homologue of Nup157), Mlp1, and Nic96 exhibit physical connections to the Nup84 complex. Because all of these nucleoporins except Nup145N lack FG repeat sequences, the identified contacts may be important for the structural organization of the NPC. The observation that Nic96 was found to be associated with purified Nup84 suggests that two key structural modules of the NPC, namely the stable Nic96 complex composed of Nic96, Nup57, Nup49, and Nsp1 (37) (see also Table I) and the Nup84 complex, could come in direct contact.

The *in vitro* finding that the Nup157-Nup145N heterodimer forms an assembly with the Nup84 complex, which can be easily dissociated, could reflect an *in vivo* requirement for a dynamic NPC biogenesis and/or organization. Notably, the conserved Nup145 is made as a precursor that is posttranslationally cleaved into two functionally separated domains, Nup145N and Nup145C in yeast (38, 39) or Nup98 and Nup96 in mammals (34, 40). The autoproteolytic cleavage of Nup145 is not essential in yeast but becomes essential in cells lacking Nup188 (38, 39). Moreover, self-cleavage of the Nup98-Nup96 precursor in mammals is crucial for NPC assembly (34, 40). Our work has revealed that both Nup145C and Nup145N have physical contact with the Nup84 complex, but the way these subunits interact with this NPC structural module is different. Whereas the Nup145C domain is a stable subunit of the Nup84 complex, the Nup145N domain is only loosely associated. It is possible that Nup145N has to be cleaved off from Nup145C to allow a dynamic interaction with the Nup84 complex.

Interesting in this context are recent studies showing that the binding dynamics between structural nucleoporins govern NPC permeability and affect channel gating (41). Notably, Goldfarb and colleagues observed that yeast cells lacking Nup170 exhibit a reversible dissociation of several structural nucleoporins (including members of the Nup84 complex) from NPCs upon the addition of aliphatic alcohols or chilling (41). Thus, dynamic rearrangements of structural NPC modules may be important not only for NPC assembly but also during translocation of large cargo through the transport channel, which may not be possible with a rigid NPC structure. Linker nucleoporins, which connect structural modules, could regulate this structural flexibility.

Finally, we report in this study the first structural analysis of a so-called large Nup (Nup157) that, like Nup188, is thought to be a structural constituent of the spoke-ring complex of the NPC (42–45). Isolation of this and other large Nups (*e.g.* Nup188 and Nup192) in *E. coli* was limited because of their low solubility. Thus, we developed a method to overexpress these large Nups in yeast followed by subsequent affinity purification and conventional chromatography. Because these three large Nups could be obtained in reasonable (microgram) amounts and pure form, we could perform the first biochemical and electron microscopy analyses (not shown in this study is the electron microscopy structure of Nup188 and Nup192).

The observation that Nup157 is not an elongated molecule but forms a hollow sphere is interesting in the structural context of the subunits of the Nup84 complex. Within the Nup84 complex, Nup120, Nup145C, and Nup85 exhibit elongated structures as shown by electron microscopy (15, 16). Notably, using computational and biochemical methods, several subunits of the yeast Nup84 complex (Nup120, Nup145C, and Nup85) and homologous vertebrate Nup107–160 complex were suggested to be elongated because they contain β-propeller/α-solenoid arrangements (46). Similarly, human Nup133 contains two domains, a carboxyl-terminal domain responsible for its interaction with its subcomplex through Nup107, and an amino-terminal domain whose crystal structure reveals a seven-bladed β-propeller (47). The N-terminal domain of Nup159 had been crystallized and was shown to contain an unusually asymmetric seven-bladed β-propeller (48). X-ray analysis of Nup157 or domains thereof should reveal which structural motifs occur in these large Nups.

Acknowledgments—We are grateful to Daniela Roser for technical assistance in TAP-tagging the yeast nucleoporins, Dr. Katja Strässer for the Nup60-TAP purification, Denise Lau for the high copy number ProtA-Nup192 plasmid, Sabine Merker and Petra Ihrig, under the supervision of Dr. J. Lechner (BZH, Heidelberg, Germany), for performing mass spectrometry, and Karsten Rippe (Kirchhoff-Institut für Physik, Heidelberg University) for help in analytical ultracentrifugation.

REFERENCES

1. Fahrenkrog, B., and Aebi, U. (2003) *Nat. Rev. Mol. Cell Biol.* **4,** 757–766
2. Suntharalingam, M., and Wente, S. R. (2003) *Dev. Cell* **4,** 775–789
3. Goldberg, M. W., and Allen, T. D. (1992) *J. Cell Biol.* **119,** 1429–1440
4. Ris, H. (1997) *Scanning* **19,** 368–375
5. Stoffler, D., Feja, B., Fahrenkrog, B., Walz, J., Typke, D., and Aebi, U. (2003) *J. Mol. Biol.* **328,** 119–130
6. Rout, M. P., Aitchison, J. D., Suprapto, A., Hjertaas, K., Zhao, Y., and Chait, B. T. (2000) *J. Cell Biol.* **148,** 635–651
7. Cronshaw, J. M., Krutchinsky, A. N., Zhang, W., Chait, B. T., and Matunis, M. J. (2002) *J. Cell Biol.* **158,** 915–927
8. Rexach, M., and Blobel, G. (1995) *Cell* **83,** 683–692
9. Bayliss, R., Littlewood, T., and Stewart, M. (2000) *Cell* **102,** 99–108
10. Fabre, E., and Hurt, E. (1997) *Annu. Rev. Genet.* **31,** 277–313
11. Rout, M. P., Aitchison, J. D., Magnasco, M. O., and Chait, B. T. (2003) *Trends Cell Biol.* **13,** 622–628
12. Ribbeck, K., and Görlich, D. (2001) *EMBO J.* **20,** 1320–1330
13. Ben-Efraim, I., and Gerace, L. (2001) *J. Cell Biol.* **152,** 411–417
14. Siniossoglou, S., Wimmer, C., Rieger, M., Doye, V., Tekotte, H., Weise, C., Emig, S., Segref, A., and Hurt, E. C. (1996) *Cell* **84,** 265–275
15. Siniossoglou, S., Lutzmann, M., Santos-Rosa, H., Leonard, K., Mueller, S., Aebi, U., and Hurt, E. C. (2000) in *J. Cell Biol.* **149,** 41–54
16. Lutzmann, M., Kunze, R., Buerer, A., Aebi, U., and Hurt, E. (2002) *EMBO J.* **21,** 387–397
17. Fontoura, B. M. A., Dales, S., Blobel, G., and Zhong, H. (2001) *Proc. Natl. Acad. Sci. U. S. A.* **98,** 3208–3213
18. Vasu, S., Shah, S., Orjalo, A., Park, M., Fischer, W. H., and Forbes, D. J. (2001) *J. Cell Biol.* **155,** 339–3354
19. Belgareh, N., Rabut, G., Bai, S. W., van Overbeek, M., Beaudouin, J., Daigle, N., Zatsepina, O. V., Pasteau, F., Labas, V., Fromont-Racine, M., Ellenberg, J., and Doye, V. (2001) *J. Cell Biol.* **154,** 1147–1160
20. Harel, A., Orjalo, A. V., Vincent, T., Lachish-Zalait, A., Vasu, S., Shah, S., Zimmerman, E., Elbaum, M., and Forbes, D. J. (2003) *Mol. Cell* **11,** 853–864
21. Walther, T. C., Alves, A., Pickersgill, H., Loiodice, I., Hetzer, M., Galy, V., Hulsmann, B. B., Kocher, T., Wilm, M., Allen, T., Mattaj, I. W., and Doye, V. (2003) *Cell* **113,** 195–206
22. Allen, N. P., Huang, L., Burlingame, A., and Rexach, M. F. (2001) *J. Biol. Chem.* **276,** 29268–29274
23. Santos-Rosa, H., Moreno, H., Simos, G., Segref, A., Fahrenkrog, B., Panté, N., and Hurt, E. (1998) *Mol. Cell. Biol.* **18,** 6826–6838
24. Hellmuth, K., Lau, D. M., Bischoff, F. R., Künzler, M., Hurt, E. C., and Simos, G. (1998) *Mol. Cell. Biol.* **18,** 6364–6386
25. Gavin, A.-C., Bösche, M., Krause, R., Grandi, P., Marzioch, M., Bauer, M., Schultz, J., Rick, J. M., Michon, A.-M., Cruciat, C. M., Remor, M., Höfert, C., Schelder, M., Brajenovic, M., Ruffner, H., Merino, A., Klein, K., Hudak, M., Dickson, D., Rudi, T., Gnau, V., Bauch, A., Bastuck, S., Huhse, B., Leutwein, C., Heurtier, M.-A., Copley, R. R., Edelmann, A., Querfurth, E., Rybin, V., Drewes, G., Raida, M., Bouwmeester, T., Bork, P., Seraphin, B., Kuster, B., Neubauer, G., and Superti-Furga, G. (2002) *Nature* **415,** 141–147
26. Rigaut, G., Shevchenko, A., Rutz, B., Wilm, M., Mann, M., and Séraphin, B. (1999) *Nat. Biotechnol.* **17,** 1030–1032
27. Bassler, J., Grandi, P., Gadal, O., Lessmann, T., Tollervey, D., Lechner, J., and Hurt, E. C. (2001) *Mol. Cell* **8,** 517–529
28. Crowther, R. A., Henderson, R., and Smith, J. M. (1996) *J. Struct. Biol.* **116,** 9–16
29. van Heel, M., Harauz, G., Orlova, E. V., Schmidt, R., and Schatz, M. (1996) *J. Struct. Biol.* **116,** 17–24
30. Huh, W. K., Falvo, J. V., Gerke, L. C., Carroll, A. S., Howson, R. W., Weissman, J. S., and O'Shea, E. K. (2003) *Nature* **425,** 686–691
31. Fischer, T., Strässer, K., Racz, A., Rodriguez-Navarro, S., Oppizzi, M., Ihrig, P., Lechner, J., and Hurt, E. (2002) *EMBO J.* **21,** 5843–5852

32. Nissan, T. A., Bassler, J., Petfalski, E., Tollervey, D., and Hurt, E. C. (2002) *EMBO J.* **21,** 5539–5547
33. Galy, V., Olivo-Martin, J., Scherthan, H., Doye, V., Rascalou, N., and Nehrbass, U. (2000) *Nature* **403,** 108–112
34. Fontoura, B. M. A., Blobel, G., and Matunis, M. J. (1999) *J. Cell Biol.* **144,** 1097–1112
35. Denning, D. P., Patel, S. S., Uversky, V., Fink, A. L., and Rexach, M. (2003) *Proc. Natl. Acad. Sci. U. S. A.* **100,** 2450–2455
36. Rout, M. P., and Aitchison, J. D. (2001) *J. Biol. Chem.* **276,** 16593–16596
37. Grandi, P., Doye, V., and Hurt, E. C. (1993) *EMBO J.* **12,** 3061–3071
38. Teixeira, M. T., Fabre, E., and Dujon, B. (1999) *J. Biol. Chem.* **274,** 32439–32444
39. Teixeira, M. T., Siniossoglou, S., Podtelejnikov, S., Bénichou, J.-C., Mann, M., Dujon, B., Hurt, E., and Fabre, E. (1997) *EMBO J.* **16,** 5086–5097
40. Rosenblum, J. S., and Blobel, G. (1999) *Proc. Natl. Acad. Sci. U. S. A.* **96,** 11370–11375
41. Shulga, N., Mosammaparast, N., Wozniak, R., and Goldfarb, D. S. (2000) *J. Cell Biol.* **149,** 1027–1038
42. Aitchison, J. D., Rout, M. P., Marelli, M., Blobel, G., and Wozniak, R. W. (1995) *J. Cell Biol.* **131,** 1133–1148
43. Kosova, B., Panté, N., Rollenhagen, C., and Hurt, E. (1999) *J. Biol. Chem.* **274,** 22646–22651
44. Zabel, U., Doye, V., Tekotte, H., Wepf, R., Grandi, P., and Hurt, E. C. (1996) *J. Cell Biol.* **133,** 1141–1152
45. Nehrbass, U., Rout, M. P., Maguire, S., Blobel, G., and Wozniak, R. W. (1996) *J. Cell Biol.* **133,** 1153–1162
46. Devos, D., Dokudovskaya, S., Alber, F., Williams, R., Chait, B. T., Sali, A., and Rout, M. P. (2004) *PLoS Biol.* **2,** e380
47. Berke, I. C., Boehmer, T., Blobel, G., and Schwartz, T. U. (2004) *J. Cell Biol.* **167,** 591–597
48. Weirich, C. S., Erzberger, J. P., Berger, J. M., and Weis, K. (2004) *Mol. Cell* **16,** 749–760

SUPPLEMENTAL FIGURES

Supplemental FIG. 1. *A*, Growth analyses of yeast strains expressing TAP-tagged nucleoporins. Wild-type haploid yeast strain and derived strains carrying the indicated TAP-tagged nucleoporin genes were analyzed by growth on YPD. Cells were spotted in 10^{-1} dilutions on YPD plates and it was grown for 2 days at 30°C or 3 days at 37°C.

Supplemental FIG. 2. Information on peptide mass fingerprinting for newly identified protein interactions. For a newly identified band (*identif. band*) in the indicated TAP-purification (*bait*), we show the hit number (*Hit-No.*), the *Probability Based Mowse Score* and the number of peptides, which were found for this band (*peptides found*). When the newly identified band was only found as second hit, also the first hit band and its MS data are given (in squared brackets).

Supplemental FIG. 3. Analytical sedimentation equilibrium ultracentrifugation of Nup145N. Absorbance scans at 280 nm recorded at 7000 rpm (curves 1, 3 and 5) and 10000 rpm (curves 2, 4 and 6) and at three different protein concentrations of 1.6 μM (curves 1 and 2), 3.2 μM (curves 3 and 4) and 7.4 μM (curves 5 and 6) are shown. The top panel displays the experimental data points and the fitted curve to a single component model with a molecular weight of 61.4 kDa. At the bottom the residuals of the fits are plotted.

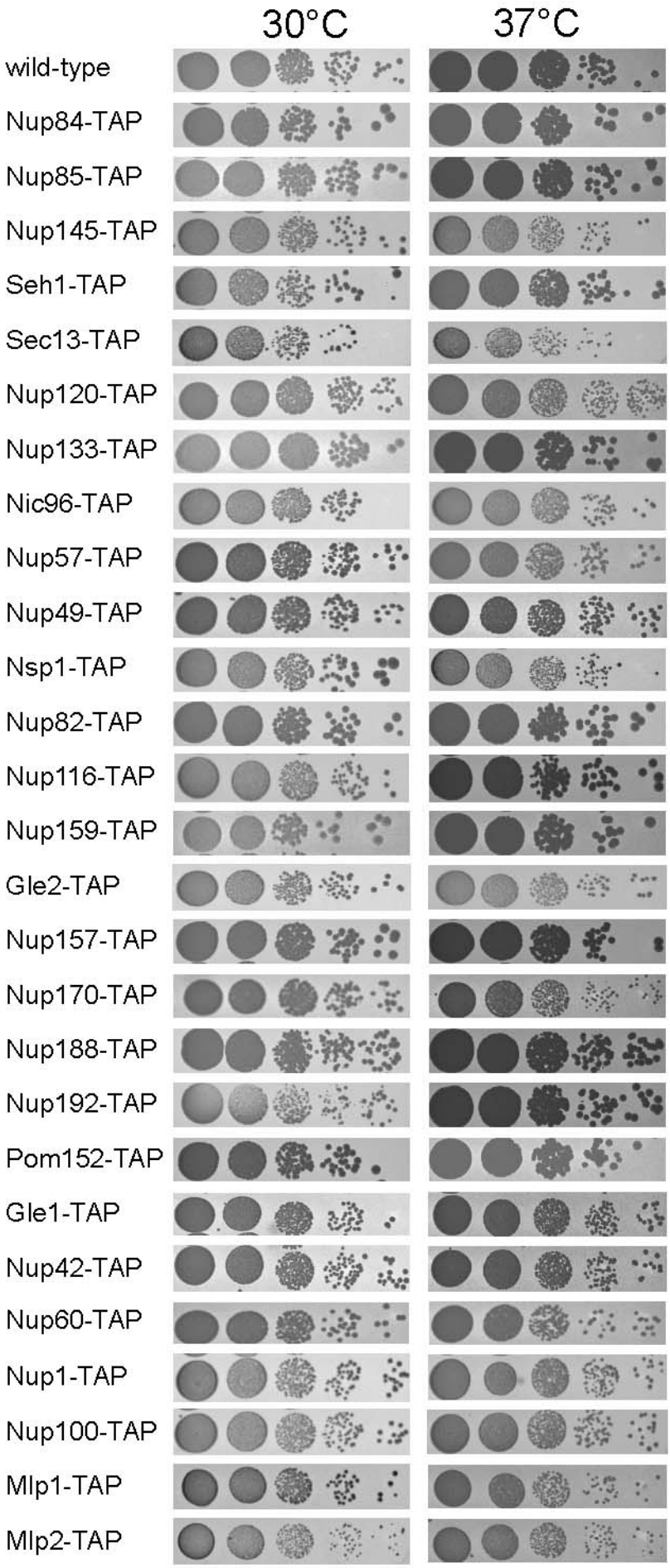

Supplemental Fig. 1 (Lutzmann et al., 2005)

Bait	*identif. Band*	*Hit-No.*	*Probability Based Mowse Score*	*Peptides found*
Gle2-TAP	Rea1-band	1	288	45
Nup116-TAP	Rea1-band	1	71	18
Nic96-TAP	Kap123-band	1	72	10
Nup145-TAP	Nup170-band	1	96	11
	Nup157-band	1	205	21
Nup84-TAP	Nup157-band	1	137	14
	Nup170-band	1	83	9
	Nup145N-band	1	53	7
	Mex67-band	1	88	9
	Nic96-band	2	61	7
	[Nup84	1	64	8]
Nup120-TAP	Nup157-band	1	92	12
	Nup170-band	2	33	5
	[Scp160	1	34	6]
	Nup145N-band	1	59	7
	Mlp1-band	1	42	12
Nup157-TAP	Nup120-band	2	60	12
	[eEF2	1	180	27]
	Nup145N-band	2	114	15
	[PABP	1	96	16]
Nup42-TAP	Gle1-band	1	247	25
Nup60-TAP	Sac3-band	1	71	12

Supplemental Fig. 2 (Lutzmann et al., 2005)

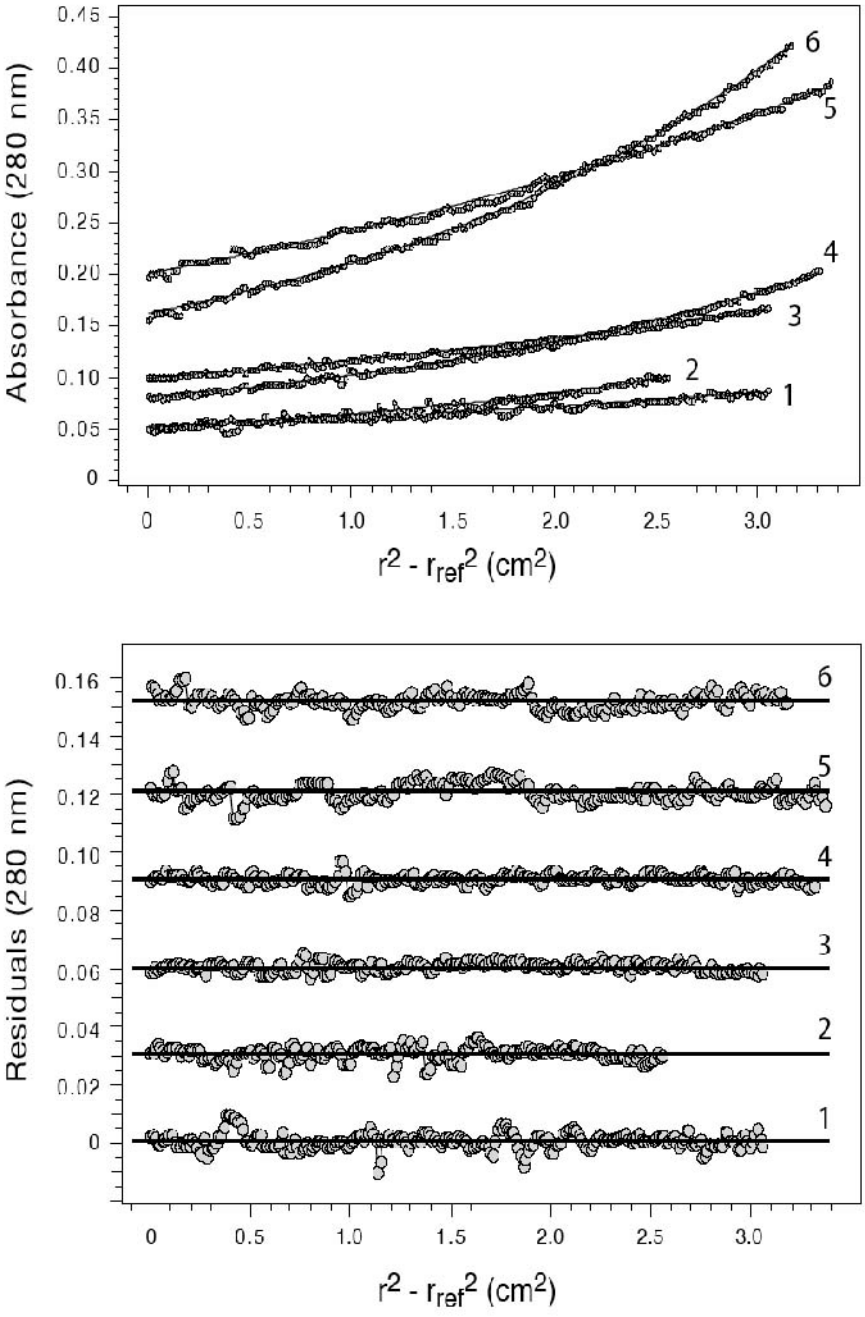

Supplemental Fig. 3 (Lutzmann et al., 2005)